Bacteria-Responsive Biomaterials for Prevention, Detection, and Treatment of Infections

by

Dahlia Alkekhia

B.S., Massachusetts Institute of Technology, 2011

A dissertation submitted in partial fulfillment of the requirements for the degree of Doctor of Philosophy in Biomedical Engineering at Brown University

PROVIDENCE, RI

February 2020

Dedicated to my parents, Majd and Mayda,

and my sisters, Tala and Zeena

This dissertation by Dahlia Alkekhia is accepted in its present form by the Biomedical Engineering at Brown University graduate program as satisfying the dissertation requirement for the degree of Doctor of Philosophy.

Date: _____ _____

Anita Shukla, Ph.D., Advisor

Recommend to the Graduate Council

Date: _____ _____

Anubhav Tripathi, Ph.D., Reader

Date: _____ _____

Edith Mathiowitz, Ph.D., Reader

Date: _____ _____

Beth Fuchs, Ph.D., Reader

Date: _____ _____

Jason Sello, Ph.D., Reader

Approved by the Graduate Council

Date: _____ _____

Andrew Campbell, Ph.D., Dean of the Graduate School

Curriculum Vitae

Dahlia Alkekhia

EDUCATION

Doctor of Philosophy, Biomedical Engineering *Sept 2014 – Jan 2020*
Brown University, Providence, RI
Advisor: Anita Shukla, PhD
Thesis: Bacteria-responsive biomaterials for prevention, detection, and treatment of infections
National Science Foundation Graduate Research Fellow

Bachelor of Science, Biological Engineering *June 2011*
Massachusetts Institute of Technology (MIT), Cambridge, MA

HONORS AND AWARDS

- Biomedical Engineering Society 2018 National Meeting Student Travel Award *Oct 2018*
  1 of 20 awarded conference attendees
- Nominated by Biomedical Engineering Department to present research at the Brown University/University of Tokyo joint symposium *Nov 2017*
- Presented on behalf of Dr. Anita Shukla at the Office of Naval Research (ONR) Annual Review *July 2015, 2017*
- Presented on behalf of Dr. Anita Shukla at the Battelle-ONR Kick-off Meeting *Oct 2015*
- National Science Foundation Graduate Research Fellowship Award (NSF GRFP) *2015*

ACADEMIC RESEARCH EXPERIENCE

Biomedical Engineering, Brown University, Providence, RI *Sept 2014 – Jan 2020*
PhD Candidate, Advisor: Anita Shukla, PhD
Thesis Title: Bacteria-responsive biomaterials for prevention, detection, and treatment of infections

Specific Aim 1: Develop multilayer antibacterial polymer films using layer-by-layer self-assembly. Demonstrate influence of polymer molecular weight on its mobility within films and in turn on film stability and extended antibacterial efficacy.

Specific Aim 2: Synthesize chromogenic β-lactamase substrate-polymer conjugates for the development of diagnostic biomaterials with visual detection of β-lactamase-producing antibiotic resistant bacteria.

Specific Aim 3: Develop β-lactamase-degradable hydrogels as a platform for bacteria triggered antibiotic delivery. Investigate effects of material properties on hydrogel responsiveness and drug release kinetics.

Systems Biology, Harvard Medical School, Boston, MA *Sept 2013 – Aug 2014*
Research Fellow, Advisor: Peter Sorger, PhD

- Quantified cytokine production by osteoclast progenitor cells using Luminex assays and single-cell imaging
- Utilized data-driven models to correlate signaling and endogenous cytokine production with proliferation and differentiation to extrapolate biological mechanisms

Department of Biology, MIT, Cambridge, MA *July 2009 – Dec 2010*
Undergraduate Researcher, Advisor: Laurie Boyer, PhD

- Investigated the role of acetylation of histone variant, H2AZ, on its redistribution during cell differentiation
- Created mutant H2AZ embryonic stem cells using site-directed mutagenesis and transfection
- Researched how 3D chromatin interactions and polycomb-group proteins regulate gene expression and ultimately cell fate in the HoxD region in mice

- Quantified HoxD gene expression in embryonic stem cells using RT-qPCR; demonstrated differences pre- and post-differentiation
- Set up fluorescence in situ hybridization to study 3D chromatin interactions (first time assay was run in the lab)

INDUSTRY RESEARCH EXPERIENCE

Merrimack Pharmaceuticals, Inc., Cambridge, MA *Jan 2012 – Aug 2013*
Research Associate, R&D Department

- Optimized a novel immunofluorescence high-content imaging assay to quantitatively study signaling and phenotypic characteristics during differentiation of primary progenitor cells
- Assay development facilitated rapid testing of hypothesis and data generation
- Develop, in a team of 3, prototype drug delivery osteoarthritis therapeutics and optimized loading dosage by analyzing *in vitro* and *in vivo* samples by ELISA
- Presented results at two company-wide conferences and at weekly group meetings; shared data and experimental plans with international collaborators

Saudi Aramco, Dhahran, Saudi Arabia *June 2010*
Intern, R&D Department

- Taught a new hire, with no biology background, common molecular biology experimental tools
- Participated in screening for best-fit algae for carbon capture and bacteria for biodesulfurization

PUBLICATIONS

Published or accepted

1. **Alkekhia D**., Hammond P., and Shukla A., *Layer-by-Layer Biomaterials for Drug Delivery*, Annual Review of Biomedical Engineering, 22 (2020). In press.

2. Yu, C., **Alkekhia D**., Shukla A., *β-lactamase responsive supramolecular hydrogels with "host-guest" self-healing capability*, ACS Applied Polymer Materials, 2, 1, 55-65 (2019).

3. **Alkekhia D.**, Shukla A., *Influence of poly-L-lysine molecular weight on antibacterial efficacy in polymer multilayer films*. Journal of Biomedical Materials Research Part A, 107, 1324-1339 (2019).

4. Kopesky P.*, Tiedemann K.*, **Alkekhia D.**, Zechner C., Millard B., Schoeberl B., Komarova SV., *Autocrine signaling is a key regulatory element during osteoclastogenesis.* Biology Open, 3, 8, 767-76 (2014).

In preparation

5. **Alkekhia D**., LaRose C., Shukla A., *β-lactamase responsive hydrogels for bacteria triggered antibiotic delivery*. In preparation (2020).

6. **Alkekhia D**.,* Safford H.,* Shukla S., Shukla A., *A chromogenic β-Lactamase substrate for diagnostic biomaterials*. Editing manuscript (2020).

7. Wang S.,* Battigelli A.,* Fairman A., **Alkekhia D**., Yang W., Antoci V., Moore D., and Shukla A., *Polyelectrolyte multilayer films for controlled delivery of chemotherapeutics.* Editing manuscript (2020).

* Authors contributed equally

PATENTS

Shukla A., **Alkekhia D.**, Shukla S., Safford H., *A Chromogenic β-lactamase Substrate*, Provisional U.S. Patent Application No.: 62/698,695.

PRESENTATIONS

1. **Alkekhia D.**, Shukla A., *Effect of Poly-L-Lysine Molecular Weight on Antibacterial Activity of Polyelectrolyte Multilayer Coated Surfaces*. American Institute of Chemical Engineers (AIChE) Annual Meeting, Pittsburgh, PA, October 2018. Oral.

2. Wang S., **Alkekhia D.**, Battigelli A., Yang W., Moore D., Antoci V., Shukla A., *Polyelectrolyte Multilayer Films for Controlled Delivery of SHP2 Inhibitor, SHP099,* Sigma Xi Annual Meeting & Student Research Conference, San Francisco, CA, October 2018. **Awarded best poster in engineering division*

3. Safford H., **Alkekhia D.**, Shukla S., Shukla A., *A Novel Chromogenic & β-lactamase Substrate for Bacteria Detection,* Biomedical Engineering Society (BMES) Annual Meeting, Atlanta, GA, October 2018. Poster.

4. Wang S., **Alkekhia D.**, Battigelli A., Yang W., Moore D., Antoci V., Shukla A., *Polyelectrolyte Multilayer Films for Controlled Delivery of SHP2 Inhibitor, SHP099*, Biomedical Engineering Society (BMES) Annual Meeting, Atlanta, GA, October 2018. Poster.

5. **Alkekhia D.**, Shukla A., *Influence of Poly-L-lysine Molecular Weight on Antibacterial Activity of Polyelectrolyte Films*, Biomedical Engineering Society (BMES) Annual Meeting, Atlanta, GA, October 2018. Poster. **Received Biomedical Engineering Society (BMES) 2018 Student Travel Award*

6. **Alkekhia D.**, Shukla A., *Effect of Poly-L-lysine Molecular Weight on Antibacterial Activity in Polyelectrolyte Multilayer Assemblies*, American Chemical Society (ACS) National Meeting, Boston, MA, August 2018. Oral.

7. **Alkekhia D.**, Shukla A., *β-lactamase Responsive Biomaterials for the Detection and Treatment of Bacterial Infections*, Brown University/University of Tokyo GPLLI Joint Student Symposium, Brown University, Providence, RI, November 2017. Oral. **Nominated by the graduate program to present at symposium*

8. **Alkekhia D.**, Shukla S., Shukla A., *β-lactamase Responsive Biomaterials for the Detection and Treatment of Bacterial Infections*, Institute for Molecular and Nanoscale Innovation's 10th Anniversary Poster Session, Brown University, Providence, RI, September 2017. Poster.

9. **Alkekhia D.**, Shukla S., Shukla A., *Antimicrobial Internal Coating for the ACCSIL Advanced Field Dressing*, Force Health Protection Pillar, Future Naval Capability: Science and Technology Program Review, Office of Naval Research, Arlington, VA, July 2017. Oral.

10. Adrianzén-Fonseca MI, **Alkekhia D**, Shukla S, Vera-González NA, Sheybani R, Shukla A. Thermoresponsive Hydrogels for Triggered Drug Delivery. New England Science Symposium, Boston, MA, March 2017. Poster.

11. Hollingsworth N., Cowles S., **Alkekhia D.**, de Queiroz Ribeiro N., Rossoni R., Fuchs B., and Shukla A. *Bacteria-responsive hyaluronic acid-penicillin conjugates as highly effective, versatile antibacterial polymers.* Materials Research Society Annual Fall Meeting, Boston, MA, November – December 2016. Oral

12. **Alkekhia D.**, Shukla A., *Multilayer Polymeric Films Exhibiting Controlled & β-lactamase-triggered Antibiotic Release*, Biomedical Engineering Society (BMES) Annual Meeting, Minneapolis, MN, October 2016. Oral.

13. **Alkekhia D.**, Shukla A., *Antimicrobial Internal Coating for the ACCSIL Advanced Field Dressing*, Battelle-ONR ACCSIL Kick-off Meeting: Planning the Way Forward, Battelle, Columbus, OH, October 2015. Oral.

14. **Alkekhia D.**, Shukla A., *Antimicrobial Internal Coating for the ACCSIL Advanced Field Dressing*, Force Health Protection Pillar, Future Naval Capability: Science and Technology Program Review, Office of Naval Research, Arlington, VA, July 2015. Oral.

15. **Alkekhia D.**, *Understanding RANK and CXCR1/2 Signaling in Osteoclastogenesis*, Merrimack Pharmaceuticals Inc. Internal Presentations, Cambridge, MA USA, June 2013. Oral.

16. Kopesky P., **Alkekhia D.**, *Progenitor Cells and Network Biology: Designing a Bone Regeneration Therapeutic,* Merrimack Pharmaceuticals Inc. Internal Presentations, Cambridge, MA USA, July 2012. Oral.

TECHNICAL SKILLS

Instrumentation: High performance liquid chromatography (HPLC), nuclear magnetic resonance (NMR), matrix assisted laser desorption ionization time-of-flight (MALDI-TOF) mass spectroscopy, quartz crystal microbalance-dissipation (QCM-D), Fourier transform infrared spectroscopy (FTIR), atomic force microscopy (AFM), dynamic light scattering (DLS), profilometery, ellipsometry, fluorescence spectroscopy, confocal laser scanning microscopy (CLSM)
Techniques: Hydrogel photo- and chemical polymerization, micelle and liposome formulation, thin-layer chromatography (TLC), column chromatography, size exclusion chromatography (SEC), bacterial culture, mammalian and stem cell culture, immunocytochemistry, fluorescence in situ hybridization (FISH), ELISA, Luminex assays, RT-qPCR, site-directed mutagenesis, SDS-PAGE, western blots, DNA extraction and sequencing, transfection, transformation

MENTORSHIP EXPERIENCE

Undergraduate and Master's Students Research Advisor
Shukla Laboratory, Brown University, Providence, RI

1. Alexis Fairman, Sc.M. Candidate, Biomedical Engineering (Master's student) *2018 – 2020*
2. Selena Nikki Tully, Sc.B Candidate, Biomedical Engineering (Rising Senior) *2018 – 2019*
3. Sorathan Munckong, Sc.B Candidate, Biomedical Engineering (Junior) *2018*
4. Victor Addonizio, Sc.B. Candidate, Chemical & Biochemical Engineering (Senior) *2017 – 2018*
5. Hannah Safford, Sc.B. Candidate, Biomedical Engineering (Sophomore – Senior) *2017 – 2019*
   Received of Undergraduate Teaching Research Award
   Presented at Biomedical Engineering Society National Meeting (poster)
   Presented at Society for Biomaterials National Meeting (poster)
   Honors Thesis
6. Soobin Wang, Sc.B. Candidate, Biomedical Engineering (Sophomore – Senior) *2017 – 2019*
   Received Undergraduate Teaching Research Award
   Presented at Biomedical Engineering Society National Meeting (poster)
   Awarded best poster at Sigma Xi Annual Meeting & Student Research Conference
   Honors Thesis
7. Marina Adrianzen, Sc.B. Candidate, Biomedical Engineering (Senior) *2016 – 2017*
   Presented at New England Science Symposium (poster)
   Honors Thesis
8. William O'Gara, Sc.B. Candidate, Mechanical Engineering (Rising Junior) *Summer 2016*
9. Zakir Tahiry, Sc.B. Candidate, Biomedical Engineering (Rising Sophomore) *Summer 2016*
10. Grant Menon, Sc.B. Candidate, Biomedical Engineering (Sophomore – Junior) *2015 – 2016*

PROFESSIONAL AFFILIATIONS

American Institute of Chemical Engineers Member *2018*
American Chemical Society Member *2018*
Biomedical Engineering Society National Member *2016, 2018*
Materials Research Society National Member *2016*

LEADERSHIP ACTIVITIES

Judge at Rhode Island Science and Engineering Fair,
Community College of Rhode Island *2017, 2019*
Panelist at Biomedical Engineering Society Grad School Panel, Brown University *2019*
Board Member, Graduate Biomedical Engineering Society, Brown University *2016*

Prior to Brown University

President, Arab Students Organization (ASO), MIT *2010 – 2011*
Organizer, ASO 8th Science and Technology Awards Banquet, MIT *2011*
Co-director/Presenter,
ASO College Admissions Arab Mentorship Program, MIT & Saudi Arabia *2009, 2010*
Team Member, MIT Development Lab,
Resource Development International NGO, Cambodia *2011*
Volunteer, Sanad Children's Cancer Support Society, Saudi Arabia *2008, 2009*

Acknowledgements

I want to start off by thanking my advisor, Dr. Anita Shukla, who has always believed in me, trusted me, and allowed me to venture into the world of chemistry which we both had very little experience with, and then gave me the opportunity to persevere until I was able to develop what we had envisioned. You have helped me grow in multiple ways as a researcher, mentor, and communicator. Thank you for always pushing me to be confident and proud. I would also like to thank my committee, Dr. Anubhav Tripathi, Dr. Edith Mathiowitz, Dr. Jason Sello, and Dr. Beth Fuchs for their generosity, time, advice, and kind encouragement. I have enjoyed learning through your different perspectives and expertise.

I especially want to thank every Shukla Lab member, past and present, you have made this journey enjoyable and worthwhile. It has been wonderful seeing the lab grow over the years. Thank you Yingying, Chao, Akram, Lexie, Quentin, Cassi, Ronnie, Roya, and especially, Nisha, Bethany, Shashank, Christina, Noel, Alessia, and Carly - I would not have been able to do this without you. Thank you for the chats about science and everything else, the laughs in and out of lab, celebrating the big stuff as well as the small victories (#diditgel), indulging my coffee cravings, and for the endless amount of chocolate, donuts, and cake. I have learned from each and every one of you and I am going to miss working with you all. Your friendships have meant everything and are the best of what I will be taking with me. To all my undergrads (especially Grant, Soobin, and Hannah), it was so much fun working with you and such a pleasure watching you grow as independent researchers.

To all my friends, near and far, and all over the world, thank you for the good times, for our travels and memories, for pushing me to take breaks, helping me shake off stress, and encouraging me and being proud of me. To my Bolt Coffee friends, thank you for the amazing coffee, the warm hellos and chats, and for making Providence feel like home from day one.

To my family who never stopped asking me when I was going to be done with school, I am done! Thank you for your encouragement throughout my life and for always being proud of me. To the women in my family, Teta, Nana, Aunti Dima, and mom, you have always inspired me with how graciously and tirelessly you do it all - truly superwomen. To my sisters, Tala and Zeena, my best friends and number one supporters, I cannot thank you enough. I can always count on you for the effortless laughs and for always being there for me (thanks for helping me format my thesis). Lastly, to my parents, none of this would have been possible without you. I am so grateful for all the opportunities you have provided me and for your unconditional love and support. I am who I am because of you.

I am so lucky to have you all on this journey with me.

Thank you,

Dahlia

Contents

List of Tables

List of Figures

List of Schemes

Abstract

Bacterial infections can be difficult to treat and potentially lethal due to the rising global threat of antibiotic resistance. Systemic administration and overuse of antibiotics exacerbate antibiotic resistance. There is a need for therapeutic approaches to protect against infections, detect the presence of antibiotic resistant bacteria, and provide highly controlled delivery of antibacterial agents, to reduce development of antibiotic resistance. This thesis focused on developing 1) coatings to prevent and treat device associated bacterial infections, 2) biomaterials with facile colorimetric indication of antibiotic resistant bacteria, and 3) bacteria-responsive biomaterials as a platform for spatiotemporally controlled delivery of antibacterial agents to limit unnecessary exposure to drugs. Natural and synthetic polymers, including newly developed responsive polymers, were utilized to formulate these biomaterials. Layer-by-layer self-assembly was used to form multilayer polymeric films with hyaluronic acid and poly-L-lysine (PLL), an antibacterial polypeptide. These coatings reduced bacterial attachment to surfaces (critical for biofilm prevention) and inhibited planktonic cell growth. PLL mobility, governed by molecular weight, influenced coating stability, antibacterial mechanism of action, and extended efficacy over repeated exposure to bacteria. Additionally, in this thesis, β-lactamases (βLs), the most prevalent cause of antibiotic resistance, were used as enzymatic triggers for bacteria-responsive biomaterials. To develop biomaterials with a facile, colorimetric indication of bacterial infection, a chromogenic βL substrate was synthesized and covalently tethered to polymers. The polymer conjugates and hydrogels formulated using these conjugates changed color from clear to yellow specifically in the presence of βLs and βL-producing bacteria. A βL cleavable compound was also synthesized and used to crosslink poly(ethylene glycol) hydrogels encapsulating a model drug carrier (polystyrene nanoparticles). βL-producing bacteria specifically degraded these hydrogels triggering cargo release. Our studies demonstrated how hydrogel properties (polymer density) and environmental factors (βL concentration and specificity, bacterial growth conditions) influence rates of hydrogel degradation and cargo release. The biomaterials developed here have the potential to prevent, detect, and treat bacterial infections.

Chapter 1

Introduction

1.1 Motivation: Bacterial Infections and Antibiotic Resistance

Antibiotic resistance is one of the greatest global health threats. Microbial infections are becoming more and more difficult to treat due to the rise in multi-drug resistant species, also known as super bugs.[1] The Centers for Disease Control and Prevention (CDC) issued the first report on antibiotic resistance threats in the United States in 2013 to bring attention to the severity of this global health challenge.[2] Recently, in 2019, another report was issued,[3] indicating that deaths caused by antibiotic resistant microbes decreased by 18% since the 2013 report, suggesting prevention protocols in hospitals were helping. However, the burden of antibiotic resistance is still very high. Better data sources available for the 2019 report indicated that the initial reported number of deaths was underestimated by almost a half. The CDC now estimates over 2.8 million infections and 35,000 deaths caused by resistant microbes annually in the US alone. There are also concerns about rising resistant infections in the community, and the emergence and spread of new forms of resistance.[3]

Penicillin was discovered by Alexander Fleming in 1928 in his messy laboratory, and was later proven to be a miracle in medicine, saving countless of lives.[4] However, penicillin resistant strains were reported soon after the antibiotic was used in the healthcare system in the 1940s, at the end of World War II. With every new antibiotic introduced, bacteria eventually caught up. As shown in Figure 1.1b, resistant strains evolve within less than 60 years after initial use of the antibiotic, and have been reported for every class of antibiotics available.[5] Overuse and misuse of antimicrobials, including antibiotics, has been associated with increased risk of antibacterial resistance development.[6]

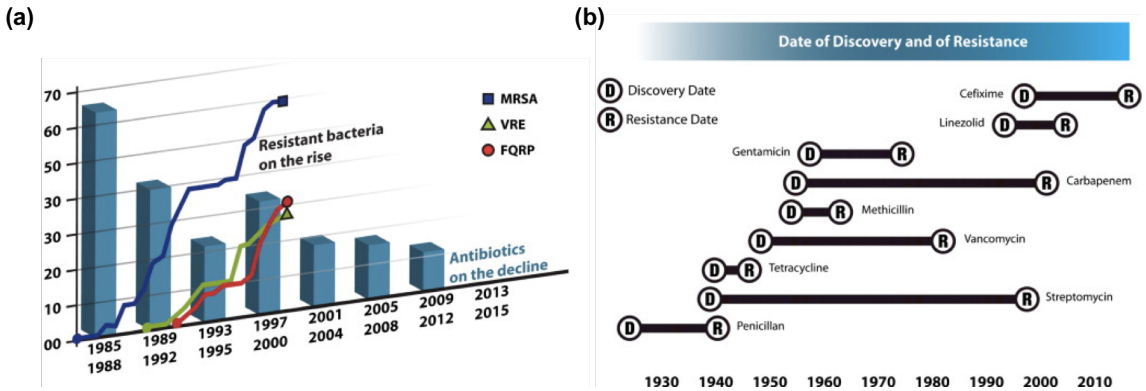

Figure 1.1: Rise in bacterial antibiotic resistance.(a) An increase in the prevalence of antibiotic resistant strains over the years is accompanied by a decrease in the number of new antibiotics. (b) Timeline of antibiotic resistance development after the first introduction of a new antibiotic. Modified from Reference [5] with permission.

The CDC reports propose four core actions to fight antibiotic resistance:

1. Preventing infections from occurring and resistant bacteria from spreading
2. Tracking resistant bacteria
3. Improving the use of antibiotics
4. Promoting the development of new antibiotics and new diagnostic tests for resistant bacteria

Innovation in tackling this global threat is needed from all fronts, from public health initiatives and societal changes to developing technologies that can enhance detection and treatment of infections. However, due to the high cost of drug discovery and the eminent development of drug resistance, companies are leaving the space of antibiotics development, resulting in very few new antibiotics being introduced into the clinic (Figure 1.1a).[5] Researches have been investigating different approaches to overcome resistance: developing alternatives like antimicrobial peptides and polymers[7–9] and bacteriophage,[10] repurposing drugs,[11,12] enhancing efficacy of current antibiotics through co-delivery with resistance inhibitors (e.g., anti-quorum sensors,[13] β-lactamase inhibitors[14]), or enhancing antibiotic uptake by bacteria.[15]

Our aim in this thesis was to develop biomaterials that can help tackle bacterial infections from multiple avenues, which encompass some of the core actions proposed by the CDC: prevention, detection, and improved use of antibacterial agents. We used natural and synthetic polymers, and those that we functionalized with small molecules, to formulate biomaterials of different scales (polymeric conjugates, thin films, hydrogels) that are designed and well characterized for the enhanced management of infections. We investigated how an antibiotic alternative, a cationic polypeptide, poly-L-lysine (PLL), incorporated in multilayer films renders these films antibacterial. Used as coatings, the films can aid in preventing infections *via* different mechanisms: by inhibiting attachment to surfaces and by releasing PLL into the surrounding solution to prevent planktonic bacterial growth. For infection detection and improved use of antibacterial agents, we chemically modified polymers to incorporate biological responsiveness to develop bacteria triggered biomaterials. We synthesized a bacteria cleavable chromophore that was incorporated into biomaterial to provide a visual, colorimetric indication of infection by antibiotic resistant bacteria. We also formulated bacteria degradable hydrogels to be used as a platform for localized, on-demand antibiotic delivery. The goal is to limit unnecessary exposure to antibiotics, especially late-stage and broad spectrum drugs, by selectively targeting drug-resistant bacteria while reducing damage to microbiota.

In search of appropriate bacterial triggers, we looked at common antibiotic resistance mechanisms. There are multiple resistance mechanisms that bacteria have evolved, including alteration of the antibiotic target site, reducing the permeability of antibiotics, or excreting drugs through efflux pumps.[16] However, the most common mechanism is the production of β-lactamases (βL), which are enzymes that cleave the β-lactam ring present in antibiotics such as penicillins, cephalosporins, and carpabenems, inactivating these antibiotics.[17,18] The enzymes are produced by many gram-positive and gram-negative bacteria, including *Staphylococcus aureus*,[19] *Mycobacterium tuberculosis*,[20] *Bacillus cereus*,[21] *Pseudomonas aeruginosa*,[22,23] and *Klebsiella pneumoniae*,[24] and have been implicated in

the drug resistance of biofilms.[22] Given the prevalence of βLs, their specificity to bacteria (since they are not produced by mammalian cells), and the selectivity and efficiency of enzymatic reactions, this thesis focused on βLs as the bacterial trigger for diagnostic and triggered antibacterial biomaterials.

In this thesis, we also conducted structure-function relationship studies to investigate material properties that govern their efficacy. For example, we studied how the molecular weight (MW) of PLL in the antibacterial multilayer coatings affect their antibacterial mechanism and extended efficacy, or which modifications to a chromogenic βL substrate allow its conjugation to polymers without losing its responsiveness, or how structural and environmental properties affect bacteria-responsive hydrogel degradation and cargo release rates.

1.2 Biomaterials for Prevention, Detection, and Treatment of Bacterial Infections

Biomaterials of different scales have played a large role in management of infections. Hydrogels,[25] nano- and microparticles (liposomes, polymersomes, micelles, metal nanoparticles (NPs)),[26] and coatings,[27] have been developed for the prevention, detection, and treatment of infections. These material have been developed using a range of polymers both natural and synthetic. Natural polymers, such as hyaluronic acid (HA), alginate, and chitosan, are biocompatible, biodegradable, and can mimic tissues providing biofunctionality. Synthetic polymers, such as poly(ethylene glycol) (PEG), poly(lactic-co-glycolic acid) (PLGA), poly(caprolactone), and polyurethane, on the other hand, are more easily and consistently synthesized and readily modified, allowing higher control over their properties, and in many cases their biocompatibility has been well established. One of the most commonly used polymers for countless biomedical applications is PEG. PEG's high hydrophilicity lends it many favorable characteristics that it can transfer to biomaterials

of different scale (nano to macroscale), including increased solubility, stealth properties and enhanced circulation, and reduced protein fouling, and excellent biocompatibility *in vivo*.[28] Therefore, it has been conjugated to drugs,[29] decorated particles,[30] coated surfaces, and used to formulate hydrogels.[31] Its facile modification led to the prevalence of PEG macromers of different shapes and sizes with various functionalities that are commercially available or can be easily synthesized.[28]

In this thesis, we conjugated PEG to a hydrophobic chromogenic βL indicator to increase its solubility and to form diagnostic hydrogels (chapter 4). We also used PEG as the backbone of our engineered βL degradable hydrogels (chapter 5). Additionally, we exploited the ability of some polymers to self-assembly into well defined structures, such as polyelectrolytes for creating antibacterial films (chapter 3), and β-lactam-PEG conjugates that we synthesized to form micelle-like NPs (Appendix chapter A)

1.2.1 Antibacterial Coatings for Infection Prevention

With advancements in surgical procedures and implantable medical devices come the risks of infections. At least half of nosocomial (hospital acquired) infections, which constitute a large portion of infections, involve medical devices.[32,33] To further complicate the situation, bacteria can form biofilms on surfaces, including medical devices,[34,35] which are very difficult to treat,[34,36] and can release planktonic bacteria leading to infection recurrence.[37] This community of cells is enclosed in a polysaccharide matrix, evading the immune system and retarding the diffusion of antibacterial agents to cells, reducing drug concentration and increasing risk of their hydrolysis by βLs.[24] The first step of biofilm formation is bacterial adhesion to the surface, therefore, inhibiting bacteria attachment is critical.[36]

Antibacterial coatings have been used clinically to coat a range of medical surfaces

including catheters,[38] implant nails,[39,40] wound dressings,[41] and pacemakers.[42] They can prevent biofilm formation and device-associated infections typically by one of three main mechanisms: anti-adhesion, contact killing, or release-based killing.[43] Polymers with their versatility and tunability are excellent candidates for forming coatings with these properties. Some requirements for these coatings include their stability, meaning they remain intact for an extended amount of time, but also that the antibacterial mechanism remains effective, whether it is loaded or tethered antibiotics or contact killing polymers. The infection microenvironment must be considered; the pH could affect the ionization of antibacterial polymers and proteins could adhere to the coating, eliminating its antibacterial effect. For contact killing surfaces, a self-cleaning mechanism is also important (such as erodible layers or anti-adhesive properties) to reduce accumulation of dead bacteria on the surface, which might promote protein and then live bacteria adhesion. Additionally, if the coating elutes antibiotics, careful consideration of the concentration accumulating at the site is critical as to not promote resistance development due to prolonged release of low concentration of antibiotics.[5,44] For many implantable devices, tissue integration is also important, therefore, in addition to biocompatibility, an ideal coating would help tissue cells win the "race to the surface" against bacteria by promoting their selective adhesion.[45] These considerations emphasize the importance of characterizing antibacterial coatings from multiple perspectives, including polymer structure-function studies and drug release profiles.

Layer-by-layer self-assembly is a facile, aqueous technique that has been used to form various types of thin films for biomedical applications.[46] The versatile nature of LbL allows combining different types of building blocks into one film, which could provide the film multiple advantageous properties, such as combining polycationic polymers that are inherently antibacterial,[47] antifouling polymers,[27,46] in addition to antibiotics either as a building block,[48] encapsulated within the films,[49] or tethered to the polymers.[50] Examples of such systems, and how they address the considerations mentioned above are reviewed in chapter 2. In chapter 3, we demonstrate how the physicochemical proprieties of LbL multilayer

coatings assembled using the cationic polypeptide, PLL, and a polyanion, HA, affect the antibacterial mechanisms and efficacy of the coatings. PLL was used as a structural element, but also as an antibacterial agent alternative to antibiotics. Antibacterial polymers and polypeptides have demonstrated efficacy against gram-positive and gram-negative bacteria, as well as resistant strains, through bacterial cell wall disruption.[7,47,51] Due to their mechanism of action, they are also hypothesized to be less susceptible to resistance development in bacteria.[52] Our studies suggest the coatings are antibacterial *via* the anti-adhesive properties of hydrophilic HA, contact-killing by PLL, and release killing by PLL, which is able to diffuse within and out of the multilayer films, providing the films with extended antibacterial efficacy.

1.2.2 Bacterial Infection Diagnostics

Bacterial infections are conventionally diagnosed after culturing the bacteria, which is time consuming. Enzyme-linked immunosorbent assay (ELISA) and polymerase chain reaction (PCR) have been used to detect bacteria; they are faster than conventional culturing, sensitive, reproducible, and can detect low concentrations of bacteria, allowing early detection of infection, even in sepsis.[53] Although these characterization techniques, including next generation sequencing and whole genome sequencing, will be important for monitoring the spread and development of antibiotic resistant bacteria,[54] they still require labor-intensive sample preparation, expensive equipment, and specialized knowledge, which is not ideal for an initial quick indication of an infection. Additionally, these issues limit the accessibility of these assays, especially in developing countries and poorer communities, which is why there has been efforts in developing point of care diagnostics.[55] Examples of such technologies include paper diagnostics[56] and microfluidic devices[57] with colorimetric or electrochemical readouts. These systems are rapid and can selectively detect pathogens in different clinical samples, but many of them cannot yet distinguish antibiotic

resistant bacterial strains. Detecting antibiotic resistant bacteria is critical for informing the appropriate treatment and for aiding in monitoring hospital and community outbreaks and preventing spread of resistant bacteria.

There have been increasing reports in the literature on systems developed to detect βLs as an indicator of resistant bacterial infections. Many of the approaches are based on the selective cleavage of a probe by βLs that produces a fluorescent signal.[58–61] Other systems are based on luminescent[62] or fluorescence resonance energy transfer (FRET)-based probes.[63] However, many of these systems do not provide a visual readout to enable easily interpreted diagnosis without specialized equipment. Additionally, one of the goals of this thesis is to develop solutions which can be engineered into various types of biomaterials or integrated into multifunctional biomaterial, such as wound dressings, for example, that are applied to protect a wound but can also present an indication of antibiotic resistant infections if they arise, even before a test is prescribed by a doctor. Therefore, we synthesized a βL chromogenic substrate that can be conjugated to polymers to formulate biomaterials that change color in the presence of βL producing bacteria (chapter 4).

1.2.3 Antibiotic Delivery for the Treatment of Infection

In most scenarios antibiotics are administered systemically, which raises multiple issues that can exacerbate antibiotic resistance. These challenges include low concentrations of the antibiotic reaching the infected tissue, which could exert pressure on the bacteria to develop resistance. Another issue is off-target toxicity, which could harm the host microbiome, allowing opportunistic resistant bacteria to flourish.[64] Localized delivery could address some of these issues, and has been utilized in the delivery of antibiotics, especially in dentistry and orthopedics.[65] Yet, controlled delivery of effective concentrations even from localized systems is critical. For many applications, a high initial concentration of antibiotic followed by a sustained release to inhibit any resurgent infection is ideal,[44,66] but in

all cases, concentrations above the minimum inhibitory concentration (MIC) are required, as to not promote development of resistance. Enhanced formulations with controlled delivery have revolutionized treatments in multiple diseases. These approaches rely heavily on the physicochemical properties of polymers and their modifications. The next sections describe some of the approaches utilized to control drug delivery focusing on hydrogels, but many of these concepts have been used to design other biomaterials such as particles and coatings.

Stimuli Responsive Biomaterials

"Smart" biomaterials that can respond to exogenous or endogenous stimuli have gained considerable attention for different applications such as diagnostics, drug delivery, and regenerative medicine.[67] Responsiveness can be acquired through the use of compounds or polymers that undergo a physical and/or chemical change upon change in pH, temperature, ionic strength, or under the influence of light, magnetic field, electric field, enzymes, or in response to a combination of inputs.[68]

For infection detection and treatment, there has been an explosion in the literature on stimuli responsive biomaterials for both exogenous and endogenous stimuli.[69] The potential advantages of such systems is the spatiotemporal control over release, which can help limit unnecessary exposure to antibiotics, increasing concentration at the site of infection, while reducing off-target toxicity. All of the above have the potential to decrease susceptibility to resistance. Most interesting are biomaterials that respond to the bacterial infection environment with the aim of forming self-defensive systems. Common examples include antibiotic-loaded, polymeric nanoparticles activated by low pH,[70–72] which is characteristic of some bacterial infections.[73] Other triggers include bacterial toxins,[74] lipases,[75] phosphatases and phospholipases.[76] In this thesis work, we focus on enzymatic triggers, namely, βLs (chapter 4 and chapter 5) and hyaluronidases (HAse) (chapter 3), since enzyme reac-

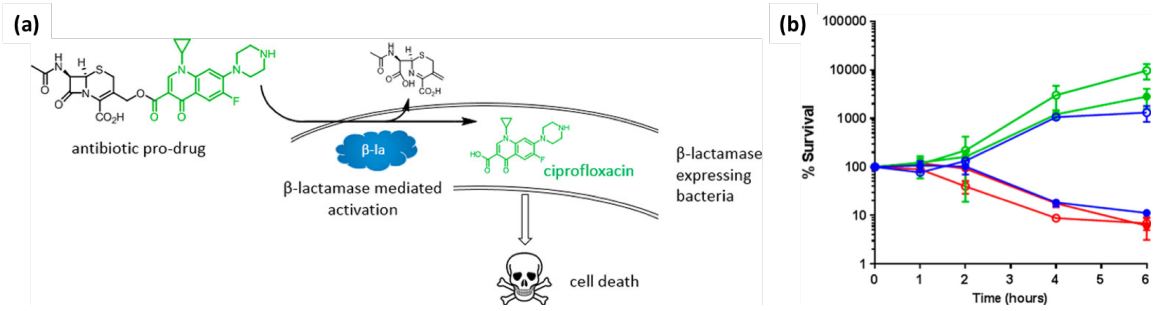

Figure 1.2: βL triggered activation of an antibiotic prodrug. (a) Scheme of ciprofloxacin prodrug and its activation by βL producing bacteria. (b) Percent survival of the βL-producing *E. coli* (filled circle) and non-βL-producing *E. coli* (empty circle) with no treatment (green), free ciprofloxacin (red), or prodrug (blue). Modified from Reference [79] under the Creative Commons Attribution 4.0 International license.

tions are highly selective and efficient and can regulate biomaterial responses (e.g., enzyme concentration dependent surface erosion) for superior control over antibiotic release rates. As mentioned earlier, due to the specificity of βLs to bacteria, they were specifically chosen as a trigger for diagnostic biomaterials (chapter 4) and degradable biomaterials as platforms for bacteria-activated release of antibiotics (chapter 5). Examples of βL triggered antibacterial therapeutics in literature are mostly of pro-drugs, such as those triggered to activate nitric acid,[77] a prochelator,[78] antibiotics,[15,79] or photosensitizers for targeted photodynamic therapy.[80] Figure 1.2a presents a schematic of a cephalosporin-based ciprofloxacin prodrug and its activation by βL-producing bacteria. As show in Figure 1.2b, the prodrug exhibits selective bactericidal activity against βL-producing *E. coli* (blue, filled circle) compared to non-βL-producing *E. coli* (blue, empty circle), and in comparison to treatment with free ciprofloxacin which killed both types of bacteria (red). Another example is of βL degradable polymeric vesicles that disassemble in the presence of the enzymes and deliver the loaded antibiotics.[81] Our aim was to develop hydrogels that can be gelled *in situ* in wounds or at other sites, and can be degraded by βL-producing bacteria to develop a platform for localized, bacteria triggered antibiotic delivery.

Hydrogels for Drug Delivery

Hydrogels are highly water-swollen, three-dimensional, polymeric networks. The physicochemical properties of hydrogels are highly tunable; by changing the polymers molecular weight, concentration, crosslinking mechanism or density, the pore size, equilibrium swelling, mechanical properties, and consequently, the functionality of the hydrogels can be tailored.[82] For these reasons, hydrogels have been designed for many biomedical applications, including drug delivery. Drugs can be encapsulated or loaded into these hydrogels, forming a drug depot where matrix properties contribute to the release mechanisms.[82,83]

A range of antibacterial hydrogels have been developed,[84] and some are used clinically in management of infections, especially in treatment of wounds, which are prone to infections.[25,85] Hydrogels' high water content make them an excellent candidate for hydrating the wound, taking up some exudate, filling deep and irregular wounds, and allowing gaseous exchange; all important factors for wound healing.[85] Other desirable functions of a wound dressing include preventing bacterial infections, which can be complicated by biofilm formation and polymicrobial infections, and delivery of growth factors to promote healing.[25] Examples of antibiotic containing hydrogels include muporocin loaded ointments[86] and silver impregnated modern wound dressings.[25,87]

However, prophylactic treatments and release of "sub-inhibitory" concentrations of antibiotics have been linked to increased risk in antibiotic resistance development.[5,44] Therefore applying hydrogels that can provide most of the benefits mentioned above, and are loaded with antibiotics but restrict their delivery to cases when an infection arises, has the potential to improve management of infections and reduce susceptibility to antibiotic resistance. Additionally, a facile colorimetric indication of the presence of resistant bacteria by such hydrogels would promote better wound care and potentially restrict the spread of

resistant bacteria.

There are many different gelation mechanisms utilized to form hydrogels with various properties and functionalities. The crosslinks could be covalent, ionic, or supramolecular, where noncovalent interactions such as hydrogen bonding, electrostatic interaction, host-guest interactions, etc., come together to form hydrogels with potentially reversible properties. In this thesis, we have formulated covalently crosslinked PEG hydrogels (chapter 4, chapter 5) since they can withstand changes in pH, ionic strength or temperature (unless engineered otherwise), and therefore, can be designed to degrade under very specific conditions, such as the presence of certain enzymes. Many different types of chemistries have been utilized to crosslink hydrogels; the most commonly used include light initiated free-radical polymerization,[88] and click chemistry like azide-alkyne or Michael-type addition.[89] We used maleimide-thiol Michael-type addition to form end-linked matrices, which has been shown to produce more unifrom matrices, and can be used for *in situ* gelation.[31] The reaction also proceeds at near-physiological pH and temperatures, with selective reactivity of maleimide towards thiols on PEG, preserving cargo activity.[90]

Gelation conditions were optimized to achieve efficient crosslinking and reduce matrix defects, which is important to formulate hydrogels with a predictable average mesh size, mechanical properties, and degradation and drug release profiles. The polymerization reaction is carried until the material transitions from liquid to gel phase, which is reached when a critical number of linkages have reacted (the gelation point can be predicted via Flory-Stockmayer theories).[91] The latter is governed by the probability of finding crosslinking points during gelation, which is influenced by stoichiometric ratio, polymer density, but also in our reaction, the ratio of thiolates (reactive species) to thiols, which is dictated by their pK_a and solution pH.[92–94] Therefore, the reaction rate needs to be optimized so that there is sufficient time to allow adequate mixing of the building blocks, yet the reaction still proceeds efficiently to achieve a high yield of crosslinks by the time the gelation point

is reached.

Drug Delivery Mechanisms

There are different drug loading methods which depend on the drug and polymer properties, gelation technique, and desired release profile. Generally, drugs can be loaded either by entrapment during gelation, loading post-gelation via swelling and/or diffusion, encapsulation into a secondary carrier, or even chemical tethering to the hydrogel backbone. Release of cargo is typically controlled by diffusion, swelling, or a chemical stimulus; in a lot of cases, more than one mechanism is at play.

Many factors need to considered when choosing the material and gelation conditions to achieve desired cargo release profiles. Matrix mesh size plays a large role in dictating drug release and can be estimated for chemically crosslinked swollen gels using the Peppas-Miller expression based on the Flory–Rehner theory.[67,95] Other factors that will influence the diffusivity of the drug include its size, hydrophilicity, solubility, any polymer-drug interactions, and potential swelling of the hydrogel.

One of the main concerns of drug release systems is a burst release, which could lead to cytotoxicity and prematurely deplete the drug reservoir. Furthermore, extended drug release is usually necessary for effective treatment. Repeated dosing could lead to oscillating drug concentration which might fall outside the therapeutic range, meaning below the minimum effective concentration (MEC) or above the maximum toxic concentration (MTC) as shown in Figure 1.3a. Patient compliance is also another issue with repeated and extended drug administration. Therefore, in many scenarios zero-order release is the most desirable, where a burst release is avoided and the drug is released at a constant rate (Figure 1.3b), which could help achieve a constant concentration at the tissue that is designed to fall within the therapeutic range (which is also dependent on the drug elimination rate) (Figure 1.3a).

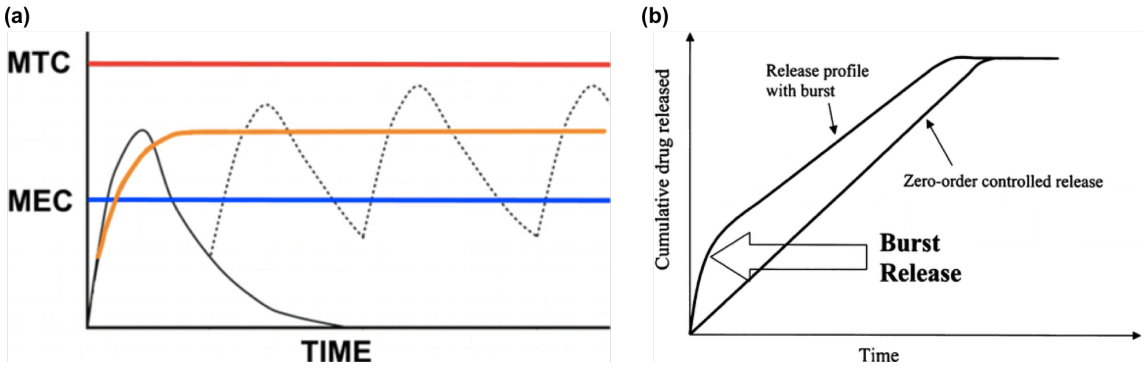

Figure 1.3: Drug concentrations resulting from burst release or zero-order controlled release profiles. (a) In systems with rapid clearance of drug from plasma or the tissue, multiple dosing (black lines) could lead to concentrations outside of the therapeutic range which lies between the minimum effective concentration (MEC) and above the maximum toxic concentration (MTC). Zero-order release (orange line) can lead to a constant concentration of drug designed to lie in the therapeutic range. (b) Example drug release profiles caused by burst release and zero-order controlled release. Reprinted with permission from Reference [96], Copyright 2001 Elsevier B.V. (a) and from Reference [97], Copyright 2016 American Chemical Society (b).

Consequently, many approaches have been investigated and used in the clinic to control drug release (over hours, days, or weeks).[98] One approach is tuning the matrix mesh size to decrease or prevent the diffusion of cargo from the hydrogels. This can be achieved in multiple ways such as optimizing polymer MW, polymer density, and crosslinking density.[99] Another approach to delay drug release is the incorporation of polymers or compounds that can interact with the drug through electrostatic, hydrophobic, or host-guest interactions, for example.[98] We have demonstrated an example of the latter approach for loading and release of a chemotherapeutic in LbL films assembled with polymeric β-cyclodextrins as the host in Appendix chapter B.

An alternative approach is to prevent diffusion and engineer systems where release is only degradation based, which could be achieved by tethering the drug via a cleavable linker or encapsulating the drug in a degradable hydrogel. Figure 1.4 demonstrates examples from literature of drug delivery systems and how their release mechanisms affect drug burst release and half-life ($t_{1/2}$), where it is apparent that degradable systems can provide

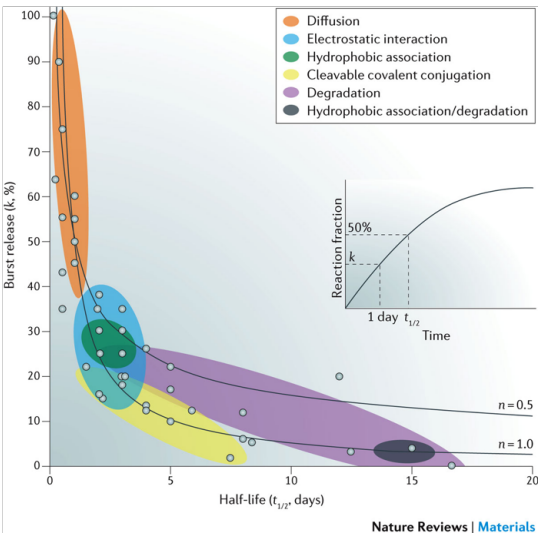

Figure 1.4: Effect of release mechanism on drug burst release and half-life. Each dot represents the drug burst release and half-life from release systems reported in the literature. Colored circles indicate different drug release mechanisms. The half-life ($t_{1/2}$, in days) is determined by the time when the fraction of released drug reaches 50% and the burst release parameter (k, %) is determined by the drug release fraction at 24 hours as shown in a representative release profile in the inset. Reprinted from Reference [98] with permission.

enhanced controlled release of drugs with lower burst release and longer half-lives.

In degradable hydrogels, release is controlled via degradation kinetics, and the erosion process is the rate-limiting step. Most chemically degradable hydrogels contain labile moieties in the matrix's backbone or crosslinkers that are either hydrolytically (e.g. esters) or enzymatically (e.g. peptide) cleaved. Degradation could be *via* surface or bulk erosion, depending on the hydrophilicity of the polymer and the rate of water or enzyme diffusion into the hydrogel matrix compared to the degradation at the surface. Bulk erosion is usually accompanied with an increase in hydrogel swelling over time as the matrix in the center of the hydrogel is cleaved, increasing hydrogel porosity, potentially affecting drug release rate and causing a delayed burst release due to hydrogel late-stage sudden dissolution.[100]

Surface erosion can potentially provide more controlled and predictable drug delivery. For enzyme degradable hydrogels, erosion rate is governed by enzyme concentration, access to the cleavage site, and kinetics of cleavage of the labile moiety. This can be further

modulated by changing hydrogel properties, such as crosslinking density, concentration of cleavable sites or in other words ratio of degradable to non-degradable polymer.[101–103] In addition to erosion rate, drug release is also dependent on concentration of loaded drug and the geometry and size of the biomaterial. Zero-order drug release can be achieved with surface erosion with certain hydrogel geometries such as thin disks where degradation is approximately from one plane and surface area is constant over time. Enzyme degradable hydrogels thus have the potential to provide selective degradation and controlled cargo release, and therefore have been engineered to release drugs in response to specific cues to achieve on-demand delivery.

One example of a treatment that showed extremely positive results *in vivo*, outcompeting prophylactic antibiotic therapy in terms of infection clearance and bone repair in infected, implant fixed, mouse femoral fractures, is an injectable PEG hydrogel that adheres to tissue and fractures and degrades in the presence of proteases, releasing lysostaphin, an antibacterial enzyme.[104] Figure 1.5 illustrates the hydrogel components and treatment of femur fractures (Figure 1.5b), and demonstrates the dramatic reduction in bacterial infection treated with lysostaphin loaded hydrogels compared to soluble lysostaphin (no hydrogel) or systemically administered oxacillin (Figure 1.5b).

1.3 Summary and Research Overview

With the increasing risk of infections by antibiotic resistant bacteria, there is a critical need to develop innovative solutions that can both improve antibacterial treatment and reduce susceptibility to the spreading or development of antibiotic resistance. This thesis focuses on developing biomaterials with translatable potential to aid in enhancing management of bacterial infections through prevention, detection, and treatment. Our studies also include characterization of the physicochemical properties of the biomaterials because

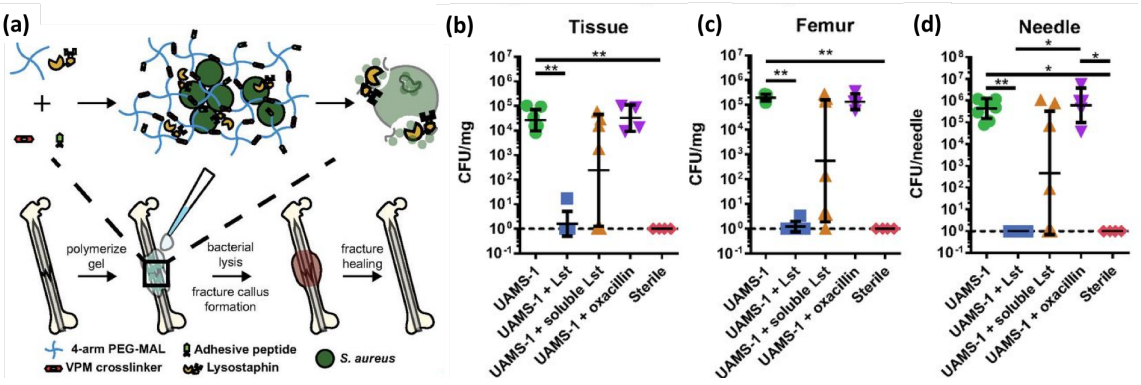

Figure 1.5: Healing of infected mouse femur fractures by injectable, protease cleavable, lysostaphin (Lst) releasing PEG hydrogels. (a) Scheme of hydrogel components and treatment of femur fractures. Quantification of *S. aureus* UAMS-1 recovered from the (b) tissue surrounding the femur, (c) femur bone, and (d) stabilization needle 7 days postfracture under the conditions of: no treatment, treatment with Lst loaded hydrogels, soluble Lst, prophylactic systemically administered antibiotic (oxacillin), or no infection. Dashed line indicates detection limit. *P $<$ 0.05, **P $<$ 0.01. Kruskal–Wallis test with Dunn's multiple comparisons test. Modified from Reference [104] under the Creative Commons Attribution-Non Commercial-No Derivatives License 4.0 (CC BY-NC-ND).

fundamentally understanding the structure-function relationships is crucial to better design "smart" biomaterials for any application.

Chapter 2 briefly discusses the fundamentals driving layer-by-layer self-assembly, then reviews recent publications (in the last 6 years) that exemplify the use of LbL in biomedical engineering, specifically in the areas of cancer treatment, bacteria infection prevention and treatment, and mediating cellular responses. The emphasis of the review is demonstrating how the versatility and modularity of LbL self-assembly allows high levels of control over the biomaterials' physicochemical properties and in turn functionality to achieve enhanced therapeutic potential (such as targeting, triggered responses, and cargo protection). Appendix chapter B presents an example of LbL multilayered coatings developed for loading and local delivery of a cancer therapeutic.

Chapter 3 presents the first characterization of the inherent antibacterial properties of (PLL/HA) multilayer films and their potential use as antibacterial coatings. This work also investigated the effect of PLL molecular weight (MW) on the antibacterial efficacy of the

coatings, revealing that the diffusion of PLL within the films, which is governed by its MW, affected film stability and the number of possible repeated uses of the antibacterial coatings. The findings also demonstrated that the films' antibacterial activity stems from three different mechanisms: release of PLL, contact killing, and anti-adhesion. This combination led to both complete inhibition of planktonic bacteria growth and a reduction in the attachment or growth of bacteria on the coated surfaces, which is critical for preventing biofilm formation.

In chapter 4, we describe the synthesis of a chromogenic βL substrates which was successfully conjugated to polymers and incorporated into biomaterials without compromising its responsiveness to βLs to provide a visual colorimetric indication of infection by antibiotic resistant bacteria. The compound contained a chromogenic leaving group on one end which was cleaved off in the presence of βL, causing a color change from clear to bright yellow. On the other end, the substrate was functionalized with a reactive group that can be used for facile conjugation to polymers, without chemically modifying the carboxylate enzyme recognition site or the chromophore. Tethering of the substrate to a linear PEG chain increased its solubility, and the conjugate demonstrated the color change when incubated with βL-producing bacteria. The substrate was also attached to multi-arm PEG to then be covalently tethered in hydrogels, which also changed color in the presence of βLs. This color change provides a facile visual detection of resistant bacteria without the need for specialized instrumentation or knowledge, extending its utility to homes, low-income communities, and military fields.

Chapter 5 presents βL responsive hydrogels that we developed as a platform for triggered antibiotic delivery. By incorporating a cephalosporin that is cleaved by βLs into PEG matrices as the crosslinker, we formed hydrogels that degrade specifically by βLs and βL-producing bacteria. Fluorescent NPs encapsulated into the hydrogels as model cargo were only released from responsive hydrogels in the presence of βLs, tracking hydrogel degra-

dation rates, indicating the potential of utilizing these hydrogels for on-demand antibiotic delivery. This triggered release provides spatiotemporal control over antibiotic delivery, limiting antibiotic exposure to pathogenic bacteria without causing collateral damage to the microbiome. Our studies also demonstrated the effect of hydrogel properties, such as polymer density, and environmental conditions including type and concentration of βL and bacterial growth conditions on hydrogel degradation rates. Additionally, Appendix chapter A introduces a similar conjugate, β-lactam-PEG, that was synthesized and utilized to form micelle-like NPs to be loaded with antibiotics in the NPs' hydrophobic core and potentially be released in the presence of βLs.

Lastly, chapter 6 concludes the thesis and provides a summary and future perspectives for each of the main areas discussed here, focusing on considerations and tests needed to bring these technologies closer to the clinic.

Chapter 2

Layer-by-Layer Biomaterials for Drug Delivery: A Review

Chapter 2 has been previously published as an original review article:

Alkekhia, D., Hammond P., and Shukla, A., "Layer-by-Layer Biomaterials for Drug Delivery", Annual Review of Biomedical Engineering, 22, 2020.

2.1 Abstract

Controlled drug delivery formulations have revolutionized treatments for a range of health conditions. Over decades of innovation, layer-by-layer (LbL) self-assembly has emerged as one of most versatile fabrication methods used to develop multifunctional controlled drug release coatings. The numerous advantages of LbL include its ability to incorporate and preserve biological activity of therapeutics, coat multiple substrates of all scales (e.g., nanoparticles to implants), and exhibit tuned, targeted, and/or responsive drug release behavior. The functional behavior of LbL films can be related to their physicochemical properties. In this review, we highlight recent advances in the development of LbL engineered biomaterials for drug delivery, demonstrating their potential in the fields of cancer therapy, microbial infection prevention and treatment, and directing cellular responses. We focus on discussing the various advantages of the LbL biomaterial design for a given application as demonstrated through *in vitro* and *in vivo* studies.

2.2 Introduction: Layer-by-layer Self-assembly

Layer-by-layer (LbL) self-assembly is a versatile technique used to fabricate functional surface coatings typically utilizing aqueous assembly conditions. LbL assembly involves alternating deposition of multivalent compounds with complementary interactions (Figure 2.1), leading to the assembly of a multilayered structure. First demonstrated with charged colloids[105], the use of LbL for different applications gained traction dramatically once Decher and Hong introduced the method for polyelectrolytes in 1991[106]. Among the many advantages of LbL assembly, particularly for biomedical applications, is the ability to readily and conformally coat substrates with a range of physicochemical properties and geometries without damaging the substrate[107,108]. LbL assembly can be used to coat large surface areas efficiently[109], while still allowing for nanoscale resolution, which is critical for pre-

cise control over biological surface interactions. Furthermore, the mild, aqueous assembly conditions make it possible to incorporate small molecules and biologics while avoiding solvents, temperatures, pH and ionic strengths that can destabilize these compounds. The conceivable applications of LbL in the field of biomaterials are limitless. Researchers have already explored the use of LbL biomaterials for cellular engineering[110,111], tissue engineering and regenerative medicine[112], biosensors (e.g., detecting cholesterol[113] or glucose[114]), antifouling and antimicrobial materials[46], vaccines[115], and drug delivery systems[116] among other applications.

This review highlights recent advances (particularly in the last 6 years) in the area of LbL self-assembled biomaterials for applications in drug delivery. First, we introduce factors that influence LbL film physicochemical properties and thus their functional behavior. This brief discussion will be followed by a review of LbL drug delivery systems that fall under three application areas where LbL has proven especially promising: cancer therapy, bacterial infection prevention and treatment, and directing cellular responses. We aim to demonstrate how the modularity of LbL assembly has been exploited to develop multifunctional delivery systems that enhance treatment efficacy.

2.3 LbL Fundamentals: Factors that Influence LbL Assembly

LbL assembly is most commonly driven by electrostatic interactions between oppositely charged compounds. Hydrophobic, van der Waals, hydrogen bonding, covalent bonding, host-guest and bio-specific interactions, can all contribute to film growth and may even serve as the primary driver for film assembly[122]. Multilayers are commonly assembled via dipping[123], spraying[109], and spin-coating[124]; other LbL fabrication methods such as electromagnetic[125] and fluidic assembly[126–128], 3D printing[129], and micropatterning[130,131] have also been explored. A multitude of components have been assembled

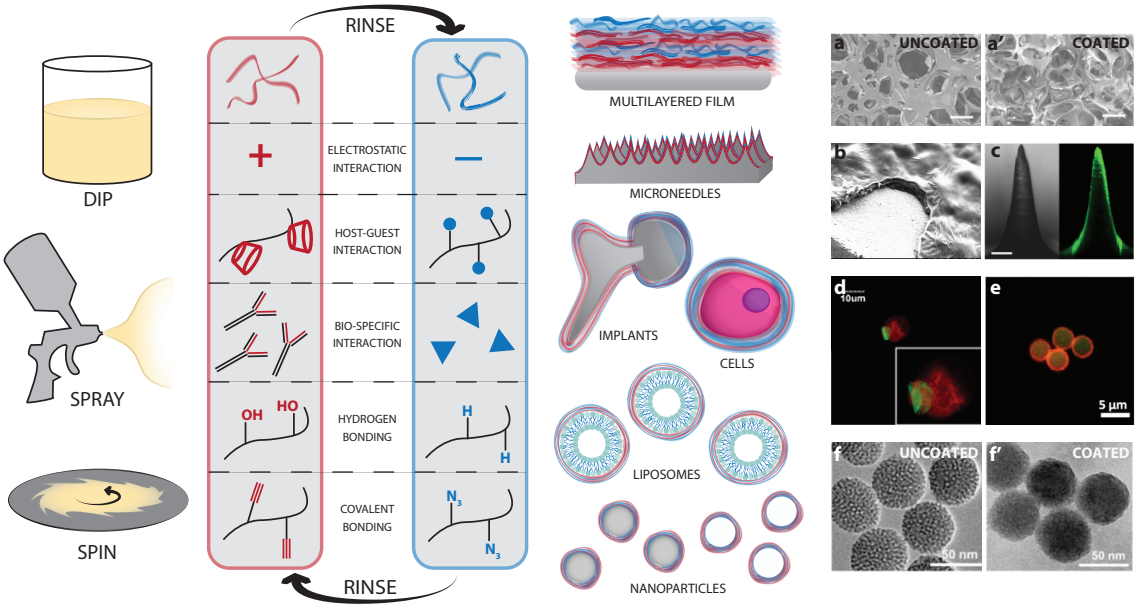

Figure 2.1: Schematic of common LbL approaches, common interactions exploited in LbL self-assembly, and examples of substrates coated for biomedical applications. Examples of biomaterials functionalized via LbL self-assembly: *(a, a')* gelatin sponge[117], *(b)* TiO_2[118], *(c)* microneedle[119], *(d)* monocyte (red) wrapped with LbL backpack (green)[120], *(e)* microcapsules with payloads in wall and core[121], *(f, f')* MSNs[49]. Images modified with permissions from corresponding references. Copyright (2012, 2015) American Chemical Society.

in LbL architectures. Polyelectrolytes are most commonly utilized including synthetic polymers (e.g., polyethylenimine (PEI), poly(diallyldimethylammonium chloride) (PDADMAC), poly-L-lysine (PLL), poly(sodium 4-styrenesulfonate) (PSS), and poly(acrylic acid) (PAA)) and naturally derived polymers (e.g., chitosan (CHI), hyaluronic acid (HA), and alginate (ALG)). Other macromolecules such as proteins, micro- and nanoparticles (NPs), and inorganic materials like clay and graphene, have also been incorporated into multilayer films. Richardson et al. recently reviewed the range of LbL assembly methods and innovations in materials incorporated and characterization techniques that have been developed over the years[132,133].

Multiple studies in the 1990s and early 2000s investigated the effects of assembly parameters on growth and stability of LbL films. Assembly conditions including temperature[134], ionic strength[135,136], and pH[137] influence the physicochemical properties of

macromolecules and in turn their interactions, which govern film assembly and ultimately functional behavior. Other factors that influence film properties include molecular weight (MW)[138,139], species concentration[135], incubation time[140], and assembly method[124]. Studies over the last few years have delved deeper into quantitatively explaining and in some cases revising some previously well-accepted theories of polyelectrolyte complexes and coacervates and LbL self-assembly using more sensitive characterization techniques and molecular dynamics simulations[141–143].

The self-assembly of polyelectrolytes is an ion-exchange phenomena where charged polymer segments replace associated counterions. The main driving force for assembly is the entropic release of counterions and water molecules[144]; there is a small enthalpic contribution due to rearrangement of water[141]. Counterions have been observed throughout the bulk LbL film and not only the film surface during assembly[141]. Increasing salt concentrations can lead to ionic shielding and formation of denser films[145,146]; however, above a certain threshold, too high a salt concentration can prevent interactions between film components and disable film growth[136,146].

Ionization of polyelectrolytes, dictated by their pK_a and solution pH, plays a critical role in film assembly. The amount of polymer adsorbed is self-regulated due to electrostatic repulsion, while surface charge reversal upon each complementary deposition enables film growth. It has been widely accepted that overcompensation or overcharging is necessary at each adsorption step; however, a more recent study using accurate measurement of radiolabeled counterions showed that charge overcompensation does not necessarily occur for each adsorbed component. In a study of PDADMAC and PSS multilayers, overcompensation only occurred when the PDADMAC polycation was adsorbed, while the PSS polyanion simply compensated the positive surface charge of the previous layer[142]. Recent studies monitoring the diffusion of ions, PDADMAC, and PSS in (PDADMAC/PSS) multilayers using isotopic labeling showed that the apparent diffusion coefficients of extrinsic

sites (i.e., charged polyelectrolyte repeat units and their associated counterions), are at least two orders of magnitude greater than the diffusivity of PDADMAC and PSS[143]. Diffusion of PDADMAC extrinsic sites is faster than PSS sites[143], which explains the difference in charge overcompensation observed between PDADMAC and PSS layers[142]. It was previously thought that in the exponential multilayer film growth regime, "loosely bound" polymer diffuses "in and out" of the film during assembly resulting in exponential growth in comparison to linear growth where there is a constant thickness increment per bilayer[139]. Under the new perspective, if extrinsic sites (which diffuse much faster than polymers) are able to diffuse throughout the multilayers during adsorption, the films will grow exponentially[143]. By improving our understanding of film growth mechanisms and component interactions, LbL films with optimal properties for specific biological applications can be designed.

2.4 The Potential of LbL Self-assembly in Drug Delivery

The versatility of the LbL technique, with its plethora of advantages for biological applications, has led to its use in drug delivery. In addition to cytocompatibility, engineering the drug loading capacity, stability of films, and protection of the therapeutic payload and its controlled release are of paramount importance to the successful translation of LbL drug delivery systems.

2.4.1 Loading Therapeutic Agents

LbL assembly has been used in drug delivery applications to form conformal coatings on substrates including macroscopic materials such as bandages[147], textiles[148], and implants[149], as well as micro- and nanomaterials including micro- and nanoparticles (NPs)[150] and cells[111]. Particles including mesoporous silica NPs (MSNs), liposomes, polymersomes,

gold NPs, etc., have been coated using LbL, while hollow capsules have been developed by selectively removing a sacrificial core upon LbL coating[150–152].

Therapeutic cargo incorporated into LbL films vary from small molecules, to nucleic acids, to large macromolecules like proteins and enzymes, to cells. Depending on the molecule's physical and chemical characteristics (e.g., charge, hydrophobicity) and the desired release profile (e.g., rapid, sustained, triggered), the cargo can be encapsulated during or post-assembly. Cargo loading methods include noncovalent binding to the film components[153], encapsulation within a secondary carrier that is incorporated in the film[49], and covalent attachment to the polymer backbone which is then incorporated into the film[50].

Multilayer films are capable of high drug loadings due to the multivalent interactions with film components. Charged drugs may interact with ionized groups on film building blocks through ionic and hydrogen bonding. For example, gentamicin (Gen) has been layered with PAA[153] or with tannic acid[48], leading to an impressive $\sim$45 and $\sim$30 weight (wt) % drug loading. Drug loading can also be readily tuned by changing the number of layers[154]. For some therapeutics, functional groups with specific affinity to the drug can be incorporated into the films. One example are cyclodextrins (CDs), which are cyclic oligosaccharides with a hydrophobic core and hydrophilic exterior that have been used to encapsulate, solubilize, protect, and deliver small hydrophobic or neutral drugs via host-guest complexation[155]. Polymeric CDs consisting of ionic CD repeat units[118,156] or CDs conjugated to common LbL polyelectrolytes (e.g., HA[49,157] or PAA[158]) have been recently used to form LbL coatings on 2D substrates[158], hollow shell capsules[157], and core-shell particles[49]. Furthermore, cargo can be encapsulated in the core of micro- and NPs, which are then incorporated as film components by alternating adsorption with a complementary polyion[159–161]. Interesting functional behavior has also been realized with the incorporation of multiple therapeutics within different layers of the LbL film architecture[66,162].

2.4.2 Increasing Stability and Biocompatibility of the Therapeutic Payload

Polyelectrolyte multilayer films have the ability to protect cargo from different environmental factors that can lead to therapeutic degradation. For example, multiple studies of have shown that small interfering RNA (siRNA) protected in LbL film NP coatings can resist nuclease degradation *in vitro*[163]. Pharmacokinetic studies in animals have also shown that LbL coated NPs prolong the half-life of their cargo and reduce clearance rates[164,165], which may be attributed partially to the anionic and antifouling capabilities of certain polymers (e.g., HA), which reduces protein adsorption and opsonization[164,166]. Beyond protecting cargo in circulation, LbL coated NPs have also protected cargo from enzymatic degradation during intracellular trafficking and aided in endosomal escape and delivery to the nucleus or cytosol[165,167,168]. Even during storage, LbL films have been shown to stabilize drugs, such as vancomycin[169] or vaccines[170], enhancing therapeutic shelf-life and reducing dependence on the "cold chain".

LbL coated surfaces and NPs have generally shown minimal toxicity *in vitro*[171,172] and *in vivo*[49,173]. Furthermore, use of natural polyelectrolytes in LbL coatings can enhance biocompatibility. For example, (ALG/CHI) coatings drastically reduced the hemolytic toxicity of bare MSNs towards human red blood cells *in vitro* ($<$1% hemolysis vs. 67% for bare MSNs) and coated Dox-loaded MSNs eliminated cardiotoxicity associated with free Dox[165]. The LbL approach has also alleviated toxicity associated with polycations used in DNA delivery[174,175].

2.4.3 Therapeutic Payload Delivery

Drug release rate from LbL films can be limited by the rate of diffusion of the drug through the film or the rate of film dissolution or degradation. LbL films can potentially deconstruct over time due to ion exchange with surrounding counter ions, film swelling, and mobility of film components[136,176]. Controlled delivery enables improved efficacy at lower drug concentrations, reduces off-site toxicity, and can improve overall therapeutic index of the drug. Many advancements have been made that increase sophistication of drug release mechanisms. Figure 2.2 presents some of the strategies employed for controlled drug delivery in LbL films.

Often a sustained release of the therapeutic is desirable; this can be achieved by increasing film thickness[118], controlling film dissolution or degradation rate[177], or covalently tethering therapeutic cargo to polymers[50]. Researchers have stabilized multilayers by covalently crosslinking the film during or post-assembly[157]. Various strategies have been employed to obtain staged release of multiple therapeutic agents at different rates, taking advantage of the stratified LbL film architecture[66,178,179]. In other scenarios, triggered release of therapeutics is needed. By incorporating responsive film components that cause conformational changes to the film in response to specific stimuli, on demand drug delivery can be achieved[180]. Both physical (e.g., light, temperature, magnetic fields) and chemical (e.g., pH, ionic strength, enzymes) stimuli have been explored. The responsive functionality could be an inherent quality of the polymers used in the LbL film (e.g., weak polyelectrolytes exhibit change in ionization in response to pH changes[153,159]), responsive elements could be incorporated into the polymer backbone[177], or drugs could be attached to the polymers via responsive linkers[172]. Drug delivery can also be targeted by enhancing selective uptake by certain cells through incorporation of polymers that naturally target receptors of interest (e.g., HA which targets CD44 receptors upregulated in cancer cells[181]) or polymers that are functionalized with targeting moieties (e.g., antibodies[173], ligands[182]) into the LbL

film. Intracellular targeting can be achieved using polymers that mediate endosomal escape, cargo release, and delivery to the sub-cellular target (e.g., poly-L-arginine (PAR)[168], polyamidoamines[183]) or pH responsive particles that disassemble in acidic endo/lysosomal environments, releasing cargo[167]. With LbL assembly, it is entirely possible to combine multiples of these approaches to develop advanced biomaterials, with targeted, responsive delivery of one or more therapeutics while also incorporating other capabilities, such as disease detection. The remainder of this review will describe examples of recent advances (limited to the last 6 years) in LbL controlled delivery for applications in cancer therapy, treatment of infectious diseases, and cellular engineering. Table 1 summarizes a selection of examples discussed here.

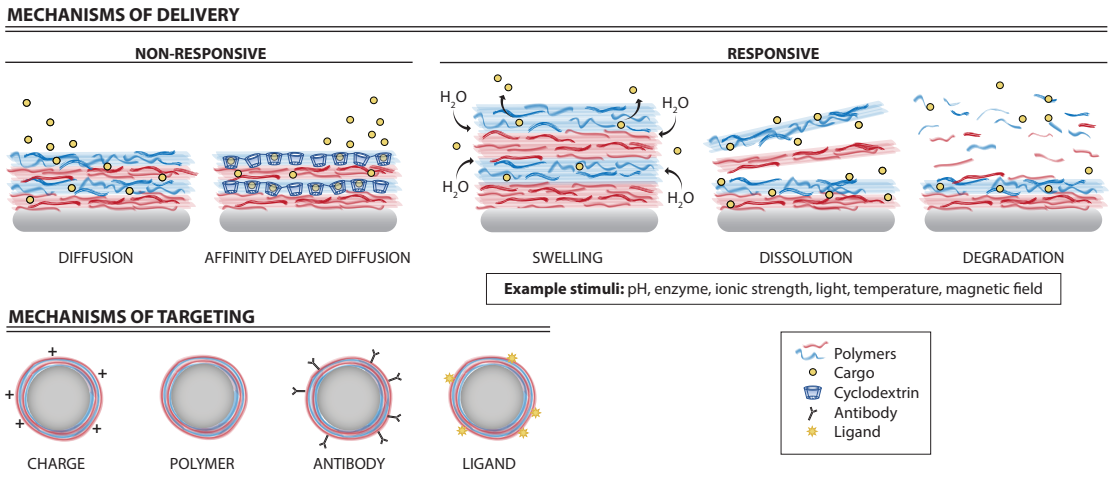

Figure 2.2: An overview of payload delivery mechanisms in non-responsive and stimuli-responsive LbL films and approaches utilized for active targeting.

2.5 LbL Biomaterials for Cancer Therapy

Cancer is the second leading cause of death in the United States[184]. There are over 1.7 million new cancer cases and over 600,000 cancer deaths projected for 2019 in the US alone[184], with an estimated cost of $173 billion in 2020[185]. Despite advances in chemotherapeutic formulations, these drugs still suffer from significant toxicity to non-cancerous

cells[186]. With most chemotherapeutics being administered systemically, drug delivery can be enhanced and toxicity reduced by actively targeting the therapeutic[173], triggering drug release specifically at the target site[49], enhancing uptake by cancer cells[166], promoting intracellular trafficking to the site of action[165], and co-delivery of multiple therapeutics[168,187]. LbL films have been widely explored in this context with extremely promising *in vitro* and *in vivo* results[188].

2.5.1 Targeted Delivery

NP accumulation at tumor sites is often aided by the enhanced permeation and retention effect, which causes passive targeting of nanomaterials through leaky tumor vasculature. However, it is noted that many studies have questioned the relevance of this kind of passive targeting mechanism in human tumors, while others have validated it in clinical studies. Although passive targeting may assist in some cases, the use of specific interactions such as high affinity ligand-receptor interactions, which can be incorporated by LbL coatings, can provide increased uptake of NPs by tumor cells. Furthermore, the hydrated nature of LbL coatings can be used to extend blood plasma half-life, which further increases the opportunity for tumor accumulation, and may also be used to induce tumor-responsive behavior.

The CD44 cell surface receptor, which is highly overexpressed on a number of solid epithelial tumor cell types[189], has been explored for molecular targeting. HA, a glycosoaminoglycan abundant in the human body, binds CD44 and is internalized via endocytosis[190]. There are multiple examples of successful tumor targeting and uptake of LbL film coated NPs incorporating HA via CD44 interactions[49,157,166,173,181]. For example, a multifunctional NP system encapsulating a photosensitizer, $TPPS_4$, into the LbL shell of NPs incorporating HA showed enhanced uptake of $TPPS_4$ *in vitro* by two tumorigenic cell lines expressing CD44 compared to free $TPPS_4$, and compared to uptake by CD44 negative

normal kidney fibroblasts. Similar HA-CD44 mediated selective uptake was reported for HA and PLL condensed polymerized DNA NPs by ovarian cancer cells[181] and (PLL/HA) LbL coated polystyrene NPs by breast cancer cells[166]. This enhanced uptake was significantly reduced by siRNA-directed CD44 gene silencing[166] or when cells were pre-treated with excess free HA, indicating that NP uptake is indeed CD44 mediated[49]. HA-CD44 targeting has also been demonstrated *in vivo*. Histological analysis of excised non-small cell lung carcinoma xenografts showed co-localization of (PLL/HA) NPs with the CD44 receptor. These NPs achieved 4-fold higher accumulation in breast carcinoma xenografts, and 2-fold reduction in liver accumulation in non-cancer-bearing mice compared to control NPs of comparable size and charge with dextran sulfate outer layers instead of HA[166].

In another LbL system aimed at hematologic malignancies, dual targeting was designed by conjugating antibodies against CD20 (a well-known blood cancer marker[191]) to HA (to aid in CD44-mediated endocytosis). An siRNA cocktail aimed at B-cell lymphoma 2 (a pro-survival protein) (siBCL2) was layered onto negatively charged PLGA NPs with the polycation, PAR, and this HA-CD20 conjugate ((PAR/siBCL2/PAR/HA-CD20)) (Figure 2.3*a,b*). In an orthotopic non-Hodgkin's lymphoma murine model, 100% and 80% of mice treated with dual (CD44/CD20) and single (CD44) targeted NPs survived over the 46-day experiment, respectively (Figure 2.3*c*). Significantly reduced leukemia cell proliferation (Figure 2.3*c,d*), lower expression of BCL2, and an increase in apoptosis associated markers was observed (Figure 2.3*e*), again with greater success with dual-targeting compared to single-targeting[173].

Yet another recent receptor-mediated targeting approach combined sugar-lectin interactions to assemble a bioenspired LbL MSN coating with a capping layer of transferrin (Tr) to bind receptors overexpressed by cancer cells. (Concanavalin A/glycogen) LbL coated, Dox-loaded MSNs incorporating Tr exhibited higher uptake by liver carcinoma cells overexpressing Tr receptor, more effective killing of cancer cells, and reduced toxicity against

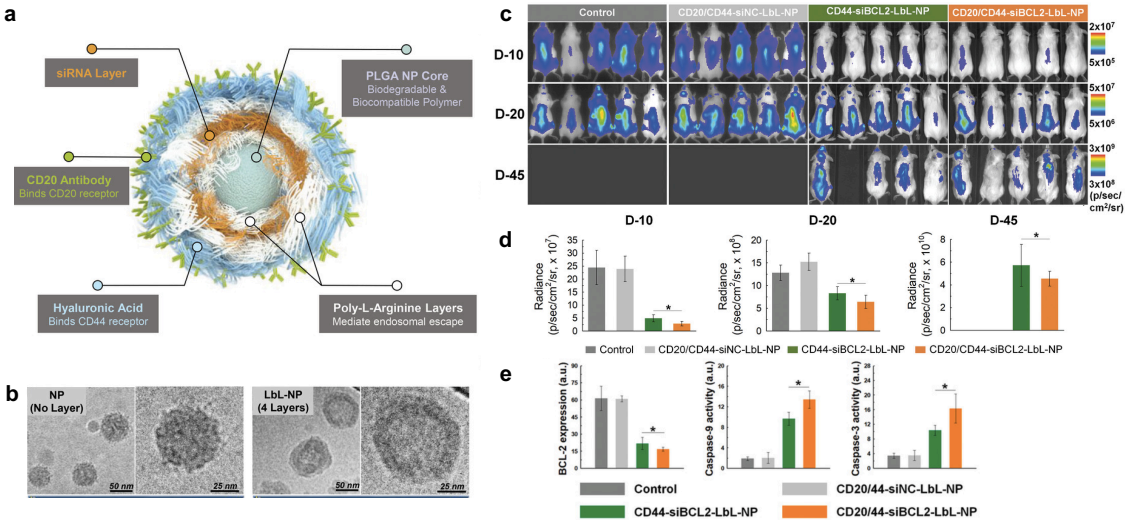

Figure 2.3: Enhanced siRNA precision targeting, internalization, and gene downregulation, leading to anticancer efficacy mediated by dual-targeted LbL NPs. (*a*) Schematic of a CD20/CD44 dual-targeted LbL NP for siRNA delivery. (*b*) Cryogenic transmission electron microscopy images of poly(lactic-co-glycolic acid) (PLGA) NPs without (left) and with LbL coating (right). (*c*) *In vivo* whole-body bioluminescent imaging of luciferase expressing leukemia cells in mice treated with saline, CD44-targeted siBCL2 LbL NPs, CD20/CD44 dual-targeted siBCL2 LbL NPs, or CD20/CD44 dual-targeted siNC vehicle LbL NPs. (*d*) Quantitative analyses of luminescence intensities from leukemia cells in mice after 10, 20, and 45 days of treatment. (*e*) Quantitative analyses of immunohistochemistry images of tumor sections harvested from euthanized mice and stained for BCL2 and apoptosis associated markers, caspase-9 and caspase-3 ($*p < 0.05$). Adapted from Reference [173] with permission.

non-cancerous cells *in vitro*, compared to non-Tr-targeted NPs. This enhanced efficacy was reduced when Tr receptors were competitively inhibited by soluble Tr[167].

Alternative targeting approaches, such as matrix targeting, have also been explored. In one such example of LbL targeting to osteosarcoma, a bisphosphonate (alendronate), which is known to bind strongly to bone matrix, was conjugated to PAA. (PAA-alendronate/PLL) coated quantum dots (QD) demonstrated rapid particle accumulation in bone tissue, and at later timepoints, high accumulation and long retention in osteosarcoma xenografts in mice, while non-targeted QD controls showed little or no tumor accumulation. Similarly coated liposomes containing Dox achieved multi-fold decrease in tumor growth and even complete tumor remediation in some animals *in vivo*, in direct comparison to untargeted

liposomal carriers[182].

2.5.2 Theranostics

The importance of tracking chemotherapeutics in the body to monitor their accumulation at the tumor site and their cellular uptake has motivated the development of NPs with both drug delivery and imaging capabilities. Theranostics can also aid in personalizing treatment, monitoring disease progression and treatment efficacy, and/or providing imaging aided site-specific treatment, such as photodynamic therapy (PDT)[192]. Commonly used imaging agents include QDs[182] and magnetic resonance imaging (MRI) contrast agents, like gadolinium-III (GD^{3+})[49]. In the study by Chen et al. described earlier[49], GD^{3+} was chelated with the photosensitizer ($TPPS_4$) and incorporated into multilayer MSN coatings via host-guest interactions with CD-modified HA. Real-time and *ex vivo* near infrared (NIR) fluorescence monitoring of xenograft tumor-bearing mice injected with these NPs showed greater $TPPS_4$ accumulation at the tumor than in any other organ, which was not observed with free $TPPS_4$. MRI enabled image-guided PDT.

Monitoring sub-cellular localization of NPs or their cargo can enable tracking of endosomal escape and delivery to the nucleus and/or cytosol. A recent LbL theranostic approach utilized Cy3 dye labeled siRNA, which acted as a fluorescence resonance energy transfer (FRET) acceptor, and was electrostatically bound to (PAA/PEI) layered upconversion NPs (UCNPs), which acted as the FRET donor. Along with delivering the siRNA therapeutic, NIR-initiated FRET enabled simultaneous monitoring of the cargo's intracellular fate[163]. The fluorescence of the siRNA and the UCNPs, as well as the resulting FRET between the pair allowed initial detection of siRNA coated NP entering cells *in vitro*. After 24 hours, a loss of FRET indicated siRNA disassociation from the NPs.

2.5.3 Stimuli-Responsive Drug Release

To further enhance the precision delivery of therapeutics at the tumor site, several stimuli-responsive systems have been investigated, such as those that respond to external triggers including light,[193] magnetic field,[194] and temperature.[161] Here we present selected examples of LbL films that respond to the most commonly studied trigger in stimuli-responsive cancer therapies, pH. The hypoxic and slightly acidic environment of tumors (pH 6.4-6.8[195]) has been exploited as a trigger for drug delivery or selective uptake by cancer cells[166] and for intracellular drug release in acidic endosomes and lysosomes (pH 4.5-5.5[196])[167,197].

The uptake of the (PLL/HA) coated NPs described earlier[166] was hypothesized to be enhanced via the hypoxic and acidic tumor environment, in addition to HA-CD44 interactions. These coated NPs underwent chemical and structural changes at tumor pH including swelling and loss of negative charge, which may explain increased uptake observed in *in vitro* cell experiments. In an *in vivo* breast carcinoma xenograft mouse model, immunofluorescence microscopy of excised tumors showed co-localization of the NPs with hypoxia-inducable factor 1-α, suggesting accumulation of the NPs in tissue regions with low oxygen partial pressure.

The importance of pH responsiveness for intracellular delivery of cargo has also been demonstrated. (ALG/CHI) coated aminated MSNs loaded with Dox demonstrated a drastic increase in Dox release at pH 5.2 compared to pH 7.4 (48.6% vs. 7.5%, respectively, in 132 hours). As pH is lowered, the amino groups on the aminated MSNs and CHI become more ionized, increasing electrostatic repulsion with Dox, while the carboxyl groups on ALG become less ionized, reducing interaction with Dox, thus leading to greater Dox release from the MSNs. Intracellular tracking studies in cervical cancer cells suggest that Dox delivery via the LbL NPs leads to more gradual but prolonged accumulation of Dox

in the nucleus, which could be beneficial in extending therapeutic efficacy compared to free Dox. Free Dox was observed to rapidly enter the nucleus. In contrast, the LbL NPs are endocytosed, following which, the acidic microenvironment of endosomes/lysosomes triggers the release of Dox from the NPs, which can then translocate to the nucleus[165]. The sugar-lectin multilayer films coating Dox-loaded MSNs described earlier for Tr targeting to cancer cells[167] also showed pH responsive intracellular delivery. *In vitro* studies showed multilayer stability at pH 7.4 and triggered Dox release at pH 5.0 due to reduced sugar-lectin binding at low pH.

2.5.4 Tackling Multidrug Resistance: Co-delivery of Anticancer Therapeutics via LbL Systems

Delivery of multiple therapeutics from a single LbL-engineered NP has shown great potential in treating multidrug resistant (MDR) cancers. For example, co-encapsulation of two chemotherapeutics in LbL coated NPs, simultaneously targeting multiple cell signaling pathways known to have crosstalk and feedback, exhibited synergistic killing of cancer cells *in vitro*. The coated NPs enhanced tumor volume reduction in mice and did not exhibit dose-limiting hepatic toxicity associated with the free drug combination[187]. In another approach, chemotherapeutic-loaded liposomes were coated with an LbL shell containing siRNA that is delivered first to silence MDR related gene expression, resensitizing cancer cells to the encapsulated chemotherapeutic, resulting in enhanced treatment efficacy in tumor-bearing mice[168,198].

2.6 LbL Biomaterials for Antibacterial Therapy

Bacterial infections are among the leading causes of death worldwide[1]. Infection of implants and biomedical devices are of critical concern, accounting for half of all hos-

pital acquired (or nosocomial) infections[33]. To prevent the formation of biofilms, which severely complicate treatment, it is necessary to inhibit bacteria growth and attachment on these surfaces[36]. LbL assembly can be used to develop antimicrobial coatings on implants and biomedical devices that exhibit anti-adhesion, contact killing, release-based killing, or arguably the most effective, a combination of more than one of these approaches[43,199]. With the ability to incorporate a plethora of molecules and macromolecules with varying properties in LbL films, several studies have demonstrated the vast potential of LbL for antibacterial coatings[46]. Here we focus on discussing some recent examples of LbL films that include loading and release of antibacterial therapeutics.

2.6.1 Stimuli-Responsive Drug Release

With recent concerns over rising rates of antibiotic resistance and a lack of new therapeutic development[200,201], it has become crucial to develop new controlled antibiotic delivery approaches. Effective antibiotic concentrations must be delivered at appropriate time scales while limiting unnecessary exposure. Over the last few years there has been a dramatic increase in publications on stimuli-responsive antibacterial biomaterials[69], including LbL architectures, which provide superior control over antibiotic release and exposure. External triggers have been used to initiate antibacterial functionality in LbL films including light (e.g., ultra-violet light triggered reactive oxygen species (ROS) delivery[160]), temperature (e.g., polymer brushes switching from bactericidal to cell-repellent[202]), and magnetic field (e.g., directed biofilm penetration[171]). More recently, the native bacterial microenvironment is being exploited to design self-defensive coatings[48,153,154,159,172].

pH

The most common self-defensive antibacterial LbL films are pH responsive, taking advantage of the secretion of lactic and acetic acid by various bacteria, reducing the microenvironmental pH[73]. pH responsiveness can be imparted by the incorporation of an acid labile polymer-drug linker (e.g., ALG-dialdehyde-Gen[172]), or an acid labile polymer, or simply by the use of weak polyelectrolytes which undergo pH-dependent changes in ionization[153,159]. An example of the latter approach includes an LbL film assembled from the weak polyacid, PAA, and micelles loaded with the antibiotic, triclosan, formulated from a methoxy-poly(ethylene glycol)-poly(ϵ-caprolactone)-CHI block polymer[159]. In addition to enabling a sustained release *in vitro* (up to 7 days) compared to triclosan micelles alone ($\sim$8 hours), the LbL films exhibited a more rapid killing of *Staphylococcus aureus* when present in non-buffered (NaCl) versus buffered (phosphate buffered saline; PBS) solutions. These results are explained by the pH responsiveness of PAA and CHI, which causes an enhanced release of triclosan under acidic conditions (pH 5.5) and in the presence of *S. aureus* relative to non-pathogenic conditions (pH 7.4). These LbL films also successfully reduced the infection incidence rate compared to uncoated subcutaneous implants (16.7% vs. 83.3%, respectively) in a rabbit *S. aureus* infection model[159].

Sukhishvili and coworkers developed pH responsive antibacterial LbL films exhibiting high levels of stability and sequestration of antibiotics for at least 35[48] and 45 days[153], until a burst release was triggered by pH reduction. In one LbL film, 3 different antibiotics were incorporated with high drug loading ($\sim$30% wt) by ionic and hydrogen bonding with tannic acid. Fundamental studies found that change in pH was correlated with the fraction of antibiotic released and that the release rate was also affected by antibiotic hydrophilicity. These coatings inhibited both the attachment and growth of gram-positive and gram-negative bacteria on the surface and in the surrounding solution *in vitro*[48]. In another system, an interesting loading and release mechanism was designed using films assembled

with inorganic montmorillonite clay nanoplatelets (MMT) and PAA. To reduce electrostatic repulsion between MMT and PAA, films were assembled at pH 2.2. The films showed a high degree of swelling with increasing pH due to ionization of the PAA carboxylic acids (Figure 2.4*a*). Loading of the antibiotic, Gen, at pH 7.5 led to a 15-fold deswelling and an increase in dry film thickness due to high drug loading ($\sim$45 wt %). A dual antibacterial mechanism was observed: triggered release with decreasing pH (Figure 2.4*b*) and potential long term contact killing due to Gen that was strongly bound to MMT. Gen-loaded (MMT/PAA) coatings killed bacteria and reduced their adhesion under flow conditions (Figure 2.4*c*), in which case, Gen release would be attributed to local acidification[153]. A recent study confirmed the acidity of the bacteria microenvironment with direct visualization using a pH-sensitive fluorescent probe attached to LbL-assembled poly(methacrylic acid) (PMAA) films (Figure 2.4*d*)[154].

Enzymes

LbL coatings have been designed to degrade specifically in the presence of bacteria virulence factors, including enzymes such as hyaluronidases (HAses)[203]. HAses, which cleave HA into oligosaccharides[204], are produced by a variety of bacteria and thought to assist in spreading and acquiring nutrients[205]. We have previously examined the HAse triggered degradation of (PLL/HA) films, and the concomitant release of PLL, which plays both a structural and antibacterial role in these films. Film stability and extended antibacterial efficacy was influenced by PLL diffusion within the films, which is governed by PLL MW. When incubated with HAse, the films degraded faster than dissolution in buffer, suggesting that these films may potentially release PLL more rapidly in the presence of virulent HAse-producing bacteria[199]. Beyond polypeptide release, HAses can also trigger antibiotic release from LbL films. Wang et al. developed Gen loaded (MMT/HA) films and showed that higher amounts of Gen were released in the presence of higher concentrations of HAse

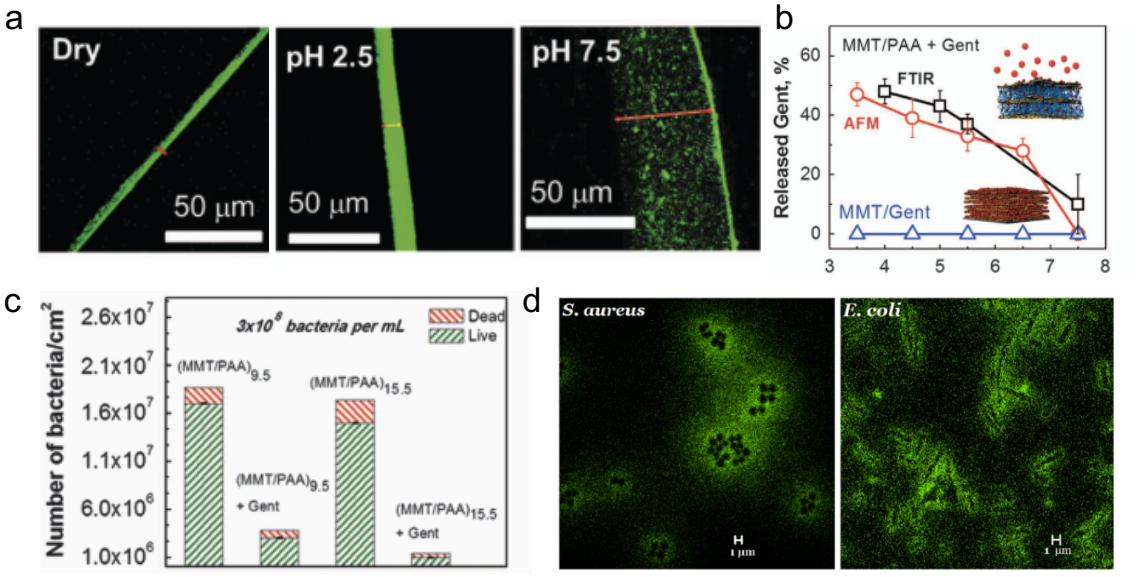

Figure 2.4: pH-responsive self-defensive antibacterial LbL coatings. *(a)* Confocal laser scanning microscopy (CLSM) images of Alexa-488-stained (MMT/PAA) films dried (left) or hydrated in 0.2 M NaCl/0.01 M PBS at pH 2.5 (middle) or pH 7.5 (right). *(b)* Influence of pH on percent Gen released from (MMT/PAA + Gen) or (MMT/Gen) films evaluated using atomic force microscopy (AFM) or Fourier transform infrared spectroscopy (FTIR). *(c)* Number of live and dead *S. aureus* cells adhering to the surface of Gen-free and Gen-loaded (MMT/PAA) films after a constant 2-hour flow of 3 x 10^8 bacteria/mL suspensions in PBS. *(d)* CLSM images of a pH-responsive-probe-labeled PMAA coating showing fluorescence surrounding *S. aureus* (left) and *E. coli* (right) due to local acidification. Adapted from Reference [153] *(a-c)* and Reference [154] *(d)* with permission.

or increasing concentrations of *S. aureus* or *E. coli*. In an *in vivo* rabbit infection model, subcutaneous polydimethylsiloxane (PDMS) implants coated with these films showed a reduction in live bacteria and increase in dead bacteria on the surface, as well as a much lower number of live bacteria and healthier tissue surrounding the implant, compared to uncoated implants. The authors noted that potential microenvironmental factors *in vivo* (e.g., proteins, macrophages) reduced film efficacy compared to *in vitro* results, underlining the importance of *in vivo* investigation[206].

An additional advantage of enzymatic degradation is the stimuli-responsive removal of film layers which strips off any attached bacteria. This self-cleaning mechanism is critical in reducing accumulation of dead bacteria on the surface, which prevents protein ad-

sorption, increases antibacterial efficacy, and may prevent biofilm formation[207]. With Gen loaded (MMT/PLL) films, which degraded in the presence of chymotrypsin or bacteria, LIVE/DEAD staining after 4 hours showed the same number of bacteria adhered on the film's surface as on uncoated or Gen-free (MTT/PLL) coated PDMS, albeit the majority were dead. However, after 24 hours, a large portion of the dead bacteria had been removed from the coated surfaces likely due to the removal of layers by enzymatic degradation[208].

2.6.2 Combination Therapy

The innate versatility of LbL assembly allows the incorporation of more than one treatment or functionality, such as combining therapeutics with different modes of action. Multiple examples of systems combining cationic polymers or peptides with antibiotics for synergistic bacteria killing have been reported[209], and have been demonstrated with LbL systems as well. For example, MSNs loaded with amoxicillin coated with positively charged lysozyme, followed by HA, and then a cationic polymer showed improved antibacterial efficacy against amoxicillin-resistant *S. aureus* and *E. coli in vitro* compared to control formulations lacking one or more of the therapeutic components. The enhanced antibacterial effect of the LbL systems was demonstrated in an *in vivo* murine *S. aureus* wound infection model compared to co-delivery of free lysozyme and amoxicillin. The polycation and lysozyme can electostatically interact with and damage the bacterial membrane, while the HA provides HAse responsive cleavage and delivery of the loaded antibiotic, amoxicillin[210].

Some LbL systems have been designed to respond to multiple stimuli enabling different bacterial killing mechanisms. In one example, magnetic NPs were coated with Gen, tannic acid, silver NPs, and then HA. This film exhibited dual-responsive release of Gen and Ag^{+} in the presence of HAse and at low pH, while magnetic field navigation enabled enhanced penetration of the NPs into biofilms, improving biofilm disruption and dramat-

ically eliminating live bacteria (0.01% vs. 71% with and without external magnetic field, respectively). These films offer ways to tackle difficult to treat bacterial infections[171].

2.6.3 Engineering the Microbiome: LbL Delivery of Probiotics

With a recent explosion of interest in the gastrointestinal (GI) microbiome and its roles in homeostasis and pathology and appreciation of the therapeutic potential of probiotics, LbL assembly has garnered attention for the effective delivery of these beneficial bacteria to the GI tract. Probiotic delivery vehicles must protect the cells from the enzymes and acidic environment of the gut, and promote adhesion and growth on intestinal surfaces. Different bacteria have been coated using LbL films such as (carboxymethyl cellulose/k-carrageenan)[211] or (CHI/sodium phytate)[212], and have shown improved survival *in vitro* under simulated gastric conditions. Anselmo et al. encapsulated *Bacillus coagulans* in $(CHI/ALG)_2$ bilayers, significantly improving cell survival under *in vitro* GI mimicking conditions compared to uncoated or single bilayer coated bacteria. The terminal ALG layer shrinks and forms an insoluble layer in GI conditions, and was hypothesized to limit diffusion of protons and bile salts to the probiotics, thus increasing survival. The LbL layers also enhanced the adhesion and growth of the coated cells to *ex vivo* porcine small intestine tissue ($\sim$1.5-fold greater than uncoated bacteria), and in a live human intestine-mimicking tissue *in vitro* model ($\sim$3-fold higher after 1 hour compared to uncoated bacteria) due to the mucoadhesive properties of CHI and ALG. These advantages led to an over 6-fold increase in bioluminescence in the GI tract emitted from coated bacteria compared to uncoated bacteria administered to mice via oral gavage. These results are highly promising for future translation of a facile LbL probiotic delivery technology[213].

2.7 LbL Biomaterials for Directing Cellular Responses

Beyond delivery of chemotherapuetics and antibacterials, LbL assembly has been used extensively to develop functional biomaterials that mimic the *in vivo* microenvironment, providing scaffolds and signaling molecules for cells, preserving activity of sensitive biomolecules[214–216], and overcoming many of the challenges facing vaccine delivery to antigen presenting cells (APCs)[115]. Here, we briefly review some of the latest developments in LbL assembly for such applications.

2.7.1 Tissue Regeneration While Preventing Infection

For many medical implants a key concern is promoting cell adhesion and tissue integration while preventing bacterial attachment[45]. To address this "race to the surface", the Cao group took advantage of LbL assembly to conformally coat pH[172] and HAse[217] responsive antibacterial LbL films onto osteogenic growth factor (bone morphogenetic protein; BMP-2) loaded titania nanotubes. These coatings successfully reduced bacterial attachment and growth and promoted osteoblast differentiation *in vitro*. Even in a *S. aurues* and osteoblast co-culture, the pH-responsive coatings allowed osteoblast growth and spreading and reduced bacterial growth compared to controls[172].

Other work has examined utilizing LbL assembly to achieve tailored release of antibiotics and growth factors by developing distinct upper and lower multilayer segments containing poly(β-amino esters) that undergo hydrolytic degradation at different rates[66]. This LbL film provided early Gen release, which eradicated an established *S. aureus* biofilm in a rat tibial osteomyelitis model, followed by a sustained Gen release to prevent infection over 8 weeks. BMP-2 in the lower layers exhibited a sustained release, important to prevent burst associated risks such as bone cancer and to promote tissue growth. Alter-

natively, staged release of Gen and BMP-2 was achieved by incorporating laponite clay barrier layers to reduce interlayer diffusion[179]. The time to release 99% of BMP-2 from a single component film was 19 days, which was extended to 33 days with the addition of Gen containing layers on top, while coatings incorporating a single or double clay barrier interlayer extended the release to 47 and 55 days, respectively. Compared to single component films, extended BMP-2 release enabled significantly greater osteoblast differentiation over 4 or more weeks.

2.7.2 Delivery of Cells

Delivery of cells for transplantation, cell therapy, and tissue engineering requires the use of carriers (e.g., scaffolds, vesicles) to aid in cell survival, growth, and potentially differentiation. LbL assembly has been used as a mechanism to provide an ultrathin extracellular matrix (ECM) for individual cells or cell aggregates, mimicking *in vivo* conditions[111,216]. Fakuda et al. demonstrated the potential of this approach by LbL coating single mouse β-cells with bilayers of ECM components, fibronectin and gelatin, which promoted integrin-mediated cell-ECM interactions, facilitating rapid fabrication of dense β-cell spheroids. These spheroids produced greater levels of insulin *in vitro* compared to spheroids assembled from non-LbL-coated cells or 2D cultured cells. When the LbL spheroids were transplanted into diabetic mice, blood glucose levels were quickly reduced and glucose sensitivity after intraperitoneal glucose simulation was improved[112].

LbL cell coatings can also themselves be loaded with therapeutics to promote cell function upon release. For example, dermal papilla cells (DPCs), specialized mesenchymal cells found in hair follicles, were coated with fibroblast growth factor-2 (FGF-2) containing LbL films, (gelatin/ALG + FGF-2/gelatin). These films mimicked the native cellular microenvironment and delivered FGF-2, which is known to play an important role in hair regeneration, over 6-7 days. These coatings promoted higher proliferation, viability, and

expression of intrinsic markers in DPCs compared to non-FGF-2 loaded coatings. When tested on nude mice, subcutaneous delivery of FGF-2 LbL coated DPCs with epithelial cells resulted in *de novo* hair generation with higher induced hair follicle density, maturity, and organized 3D cellular structure compared to non-FGF-2 containing treatments or uncoated DPCs. These approaches may be useful for treatment of conditions such as alopecia[218].

2.7.3 Delivery of Vaccines

DNA vaccine delivery is another recent area in which LbL assembly has shown tremendous promise in addressing some of the critical challenges associated with nucleic acid vaccine delivery[115]: providing higher cargo loading[219], controlling delivery duration and uptake by APCs[220,221], protecting cargo[170], and co-delivering antigen and adjuvant to enhance the immune response[219,221]. Zhang et al. developed LbL films composed of just immune signals (increasing loading and eliminating potential immune response elicited by synthetic polymers) by layering a cationic peptide antigen and anionic nucleic acid adjuvant (poly-riboinosinic:polyribocytidylic (poly(I:C))) on gold NPs. Confocal imaging showed a high degree of co-localization between poly(I:C) and the peptide in the extranuclear region in dendritic cells (DCs) treated with LbL NPs *in vitro*. The LbL NPs activated DCs *in vitro* and in mice, eliciting more potent antigen-specific T cell expansion and recall than soluble antigen and adjuvant[219].

Again taking advantage of the ability of LbL to coat a range of substrates, combining the substrate's beneficial properties with LbL functionality to enhance treatment, pain-free, LbL microneedle (MN) mediated transdermal vaccination into skin (rich with APCs) has been explored[220–222]. For this approach, LbL films loaded with model antigens or adjuvants are coated onto MNs with a stimuli-responsive LbL film or responsive base layer to achieve rapid lift-off or release of the films once the MNs are implanted in the skin, leading to sustained cargo release. He et al. developed MNs coated with (PEI/poly(I:C)) LbL films on

top of a pH responsive polymer base layer, which resulted in quick release upon implantation (over 15 minutes) into mouse ears. Similar LbL coated microneedles showed efficient uptake of poly(I:C) by 37% of APCs in human *ex vivo* skin tissue within 20 minutes of implantation[222]. Further innovation has led to LbL MNs that shorten application time to 1 minute, using pH-induced charge-invertible micelles as a base layer, followed by multilayers of model antigen, chicken ovalbumin (OVA) and a synthetic polycation. Despite this rapid administration, LbL MN vaccination of mice generated OVA-specific antibody levels 9-fold and 160-fold higher than intramuscular and subcutaneous injections, respectively[220].

Duong et al. demonstrated the potential of using these vaccine coated MNs for DNA-based cancer immunotherapy, in which the goal is to generate immune cells with specificity against cancer cells. Polycarbonate MNs were coated by alternating deposition of poly(I:C) and an ultra-pH-responsive oligo sulfamethazine conjugated poly(β-amino ester urethane) polymer (OSM-(PEG-PAEU)) that forms polycationic micelles at pH 4. Finally, a polyplex of pOVA (plasmid DNA) vaccine with a polycation (DA3; branched-PEI deoxycholic acid conjugates), was deposited. The positively charged OSM-(PEG-PAEU) sequestered poly(I:C) and pOVA with minimal release at pH 4.0 in comparison to 90% release at pH 7.4 resulting from pH-responsive coating disassembly (Figure 2.5*a*). FITC labeled polyplexes delivered subcutaneously on the back skin of mice rapidly diffused into blood capillaries while MN patch administration showed that polyplexes persisted at the site (Figure 2.5*b*). This difference in polyplex retention at the implantation site resulted in low and high OVA protein expression three days after subcutaneous and MN administration, respectively. Macrophages and DCs took up the antigen and adjuvant and effectively activated B cells for humoral immunity, and $CD8^+$ T cells for cellular immunity. The concentration of anti-OVA antibodies produced by co-delivery of antigen and adjuvant via the LbL MN array was greater than controls as presented in Figure 2.5*c*, as was the population of IFN-γ secreting $CD8^+$ T cells. This enhanced immune response activation by adjuvant containing LbL coated MNs translated to significantly higher suppression of tumor growth

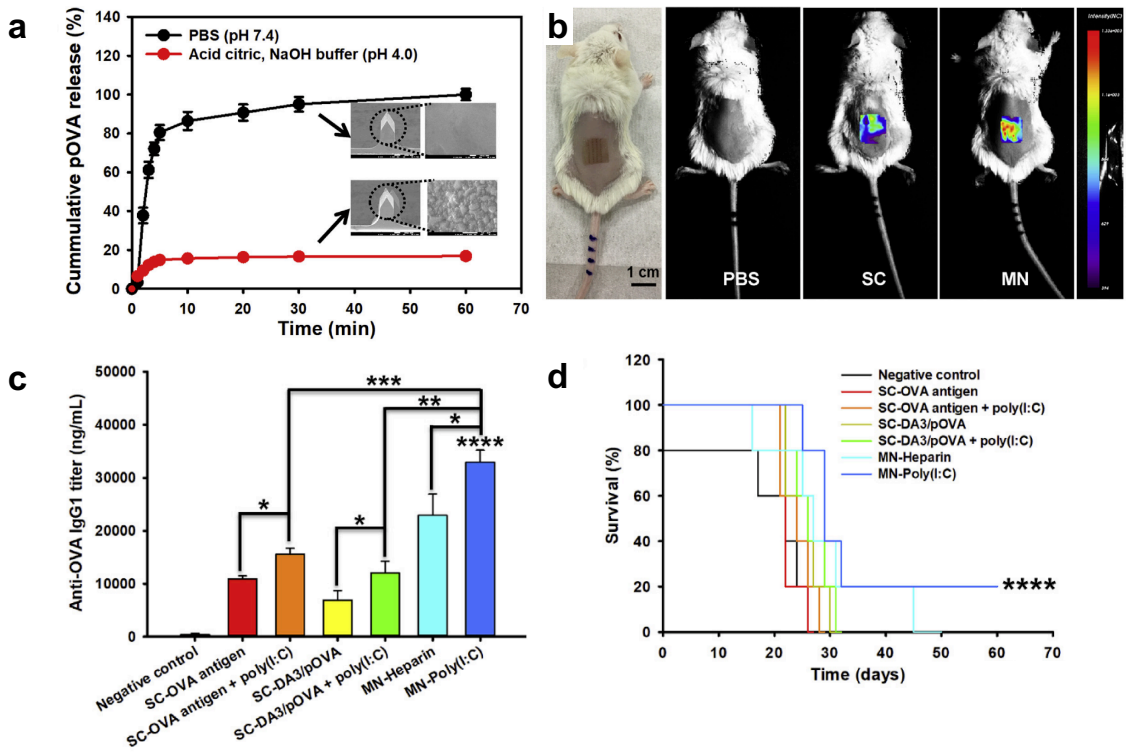

Figure 2.5: LbL coated MN arrays co-deliver DNA vaccine antigen and adjuvant for cancer immunotherapy. *(a)* Percent cumulative release of pOVA from MN arrays coated with layers of ultra-pH-responsive OSM-(PEG-PAEU) and poly(I:C) at pH 4.0 and 7.4. Insets shows scanning electron microscopy images of the corresponding MN arrays after incubation. *(b)* Distribution of FITC labeled polyplexes in the back skin of mice 30 minutes after subcutaneous (SC) or MN array patch administration. *(c)* Anti-OVA IgG1 titer in blood samples of mice immunized with various formulations through either SC or MN administration. *(d)* Survival curves of mice 60 days after various treatments ($*p < 0.05$, $**p < 0.01$, $***p < 0.001$, $****p < 0.0001$). Adapted from Reference [221] with permission.

in a lung metastasis murine model compared to control formulations, with 20% of mice still alive 60 days post administration (Figure 2.5*d*)[221].

2.8 Conclusions and Perspectives

This review highlighted the advantages of LbL self-assembly for applications in drug delivery. Using LbL, materials of different size (e.g., small molecules, proteins, polymers, cells) can be combined under benign aqueous assembly conditions to develop smart

biomaterials. LbL has been used to engineer multifunctional drug carriers which better mimic *in vivo* biological microenvironments, providing cargo protection, precision targeting, stimuli-responsive delivery, and improved spatiotemporal co-delivery of multiple therapeutics. Future studies focusing on investigating interactions between LbL biomaterials and cells in an *in vivo* environment and the factors that might affect stability, responsiveness, and drug release from LbL systems (e.g., enzyme concentrations, local pH, presence of proteins and marcophages, etc.) will move these systems closer to the clinic. In the applications presented here, this need for further preclinical studies is especially clear for antimicrobial LbL biomaterials, where *in vivo* work appears less prevalent than other LbL application areas. Additional systematic and in-depth biocompatibility studies, especially in the newer areas of LbL coatings applied to cells and regenerative medicine, are also critical for future advancement. Finally, a deeper understanding of the underlying mechanisms of interaction between film components could help further the advancements in engineering biological-tailored systems and predicting their responses. With continuous innovation in LbL, we have only just scratched the surface of potential advancements in LbL drug delivery.

2.9 Disclosure Statement

The authors are not aware of any affiliations, memberships, funding, or financial holdings that might be perceived as affecting the objectivity of this review.

2.10 Acknowledgements

The authors acknowledge financial support from Brown University, the Office of Naval Research (N000141712120 and N000141712651 awarded to AS), and the National Science Foundation Graduate Research Fellowship (grant number 1644760 awarded to DA). We

also thank graduate student, Carly Deusenbery, of Brown University for her assistance with figure preparation.

Chapter 3

Influence of poly-L-lysine molecular weight on antibacterial efficacy in polymer multilayer films

---

Chapter 3 has been previously published as an original article:

Alkekhia, D. and Shukla, A. "Influence of poly-L-lysine molecular weight on antibacterial efficacy in polymer multilayer films", J. Biomed. Mater. Res. Part A, 107: 1324-1339, 2019.

3.1 Abstract

Antibacterial coatings can prevent and treat medical device-associated infections. We examined the antibacterial properties of coatings assembled from poly-L-lysine (PLL) and hyaluronic acid (HA). (PLL/HA) films were fabricated using layer-by-layer assembly with three different PLL MWs, differentiated by number of repeat units, i.e., 33, 91, and 407 (denoted PLL^{30}, PLL^{90}, and PLL^{400}). Films assembled with all three PLL MWs completely inhibited the growth of planktonic, gram-positive *Staphylococcus aureus* and methicillin resistant *S. aureus* and gram-negative *Pseudomonas aeruginosa* and *Escherichia coli*, over a 24-hour exposure. All three film architectures also inhibited *S. aureus* attachment by approximately 60 to 70% compared to non-film coated surfaces, likely attributed to significant film hydration and electrostatic repulsion due to HA. The true differences in antibacterial efficacy between different PLL MWs were observed upon repeated exposures of (PLL/HA) to *S. aureus* every 24-hours. We found that PLL^{400} films lost the ability to inhibit planktonic *S. aureus* growth after one use while PLL^{30} and PLL^{90} films were effective over 4 to 5 and 9 to 13 repeated exposures, respectively. Our experiments indicated that differences in efficacy were related to low in-film mobility of PLL^{400} and also agreed with dissolution timescales for PLL^{30} and PLL^{90} films.

3.2 Introduction

Bacterial infections are among the leading causes of death worldwide. These infections are becoming increasingly difficult to treat due to rising antibiotic resistance and stagnant antimicrobial development and approval.[223,224] Resistant bacteria lead to more than 23,000 deaths annually in the United States alone[225] and an estimated 700,000 deaths worldwide.[226] Many of these infections are acquired in hospital settings.[1] At least half of nosocomial infections involve medical devices.[32,227] Medical devices are often prone to

bacterial attachment and biofilm formation,[35] which can severely complicate treatment.[34,36] Biofilms are capable of evading antibiotic therapies, causing recurring infections, and leading to further dissemination of planktonic bacteria.[37,228] Antibacterial surface coatings aid in preventing biofilm formation and device-associated infections and have been used clinically to coat a range of medical surfaces including catheters,[38] implant nails,[39,40] wound dressings,[41] and pacemakers.[42] The primary mechanisms of antibacterial activity of these coatings include release-based killing (e.g., silver eluting surfaces[229,230]), contact killing (e.g., hydrophobic polycation coated surfaces[231,232]), and anti-adhesion (e.g., hyaluronic acid coated surfaces[233]). Multifunctional coatings integrating different antibacterial approaches that are capable of both inhibiting bacterial attachment (the first step of biofilm formation) and killing surrounding planktonic bacteria have the potential to mitigate serious infection related complications.[43]

With a minimal arsenal of newly approved antibiotics to combat common infections, antimicrobial polymers and polypeptides have gained interest as alternative therapeutics.[7,47,51,234] These macromolecules typically act by disrupting bacterial cell membranes and are potentially less susceptible to resistance development in bacteria.[52] Additionally, many of these polymers have been shown to be active against gram-negative bacteria,[7,47] which are often more difficult to treat than gram-positive species,[223,235–237]. Moreover, the size and charge of antimicrobial polymers make them good candidates for coating surfaces without the use of complex covalent grafting methods.[238] An example of these polymers, α-poly-L-lysine (PLL), is a synthetic polypeptide whose cationic nature imparts an intrinsic antibacterial functionality. PLL has most commonly been used in non-antimicrobial therapy related applications including DNA[239] and drug delivery[240] and enhancing cell attachment to surfaces.[241] PLL in solution, ranging in molecular weight (MW) between 4 to 30 kDa, has been found to be effective against different bacteria species including *Staphylococcus aureus*, *Escherichia coli*, and *Pseudomonas aeruginosa*.[242–245] PLL has been combined with other biomaterials to provide or enhance antibacterial efficacy. For exam-

ple, graphene-PLL composites showed improved antibacterial efficacy compared to either graphene or PLL alone;[246] similar results were seen with chitosan-PLL conjugates.[247] PLL has also been conjugated to prophycenes[248] and porphyrins[249] to render these photosensitizers effective in killing gram-negative and gram-positive bacteria. Despite PLL's potential as an effective antimicrobial, studies on its use as a stand-alone antibacterial agent are highly limited. Here we have demonstrated that PLL incorporated in polyelectrolyte multilayer surface coatings renders these films antibacterial without any further modification, incorporation of antibiotics, or additional antimicrobial polymers. We formulated these coatings using layer-by-layer (LbL) self-assembly. LbL assembly is a versatile, aqueous film assembly method based on alternating adsorption of multivalent species with complementary interactions,[122] typically via dipping, spraying, or spin-coating.[132] Among its many advantages is the ability to coat a wide range of materials and substrate geometries while retaining critical substrate functional and/or morphological properties.[107,117] LbL assembly has been used to fabricate polyelectrolyte multilayers for many different applications,[110,250,251] including coatings containing other antimicrobial components.[46,252,253] PLL has been used to assemble LbL films,[254–256] often with hyaluronic acid (HA),[139,241,257–259] an anionic natural polysaccharide abundant in connective tissue. These (PLL/HA) multilayer films have been used primarily in investigating mechanisms of LbL film growth.[139,257,258] Use of (PLL/HA) films for biomedical applications including vesicle formation for drug delivery[259] or development of cell culture surfaces[241,260] has also been studied. PLL has previously been incorporated in antibacterial coatings, (HA/chitosan)-(HA/PLL) composite LbL films,[261] and LbL films composed of photocrosslinked PLL and photoreactive vinyl-modified HA.[262] In the (HA/chitosan)-(HA/PLL) composite films, the (HA/PLL) layers underwent enzymatic degradation, reducing bacterial attachment, while the remaining (HA/chitosan) layers provided bactericidal activity. In the photocrosslinked PLL containing films, the elasticity of the multilayer films was tuned via changing crosslinking parameters to investigate the influence of film stiffness on bacterial attachment and growth. To the best of our knowl-

edge, (PLL/HA) multilayer films lacking covalent modifications and the incorporation of additional antimicrobial components, have not yet been examined for their antibacterial efficacy. Lichter et al. reported the importance of polycation mobility in dictating LbL film antibacterial efficacy.[263] Mutschler et al. found that the length of poly(arginine), a cationic polypeptide, in (poly(arginine)/HA) LbL films played a key role in the antibacterial effect of these films. Lower molecular weight (MW) poly(arginine) consisting of 30 repeat units was hypothesized to diffuse to the surface of the film and interact with surface exposed bacteria due to enhanced mobility compared to 100 and 200 repeat unit poly(arginine) films.[264] Based on the intrinsic antibacterial properties of PLL and the findings of these previous studies, we hypothesized that (PLL/HA) assemblies may serve as antibacterial coatings that inhibit planktonic bacterial growth and bacterial surface attachment by a mechanism influenced by PLL mobility.

In this work, we examined the role of PLL MW in determining (PLL/HA) film antibacterial properties. Three different MWs of PLL were examined (33, 91, or 407 repeat units; i.e., 6.9, 19, and 85.1 kDa, which we refer to as PLL^{30}, PLL^{90}, and PLL^{400}, respectively). We investigated the physicochemical properties of these films including growth and PLL loading, swelling behavior and wettability, PLL mobility within these films, and PLL release properties. We also investigated the growth inhibition of planktonic bacteria and inhibition of bacterial attachment on film coated surfaces, finding that all three film architectures reduced bacterial attachment and inhibited planktonic bacterial growth. However, these films exhibited differences in efficacy over repeated bacterial exposures, which were attributed to several PLL MW dependent characteristics of the films including differences in PLL mobility and in film stability. The (PLL/HA) films we have examined in this work could be assembled on different medical devices including implants, wound dressings, sutures, and vascular grafts to prevent bacterial infections with a multifunctional approach via their antiadhesive properties, localized PLL release, and contact killing activity.

3.3 Materials and Methods

3.3.1 Materials

α-Poly-L-lysine hydrobromide (PLL) of different repeat units (RU) and hence MW were obtained from Alamanda Polymers (Huntsville, AL) (PLL^{10}: 10 RU, MW 2.1 kDa, polydispersity index (PDI) not reported; PLL^{30}: 33 RU, MW 6.9 kDa, PDI 1.02; PLL^{90}: 91 RU, MW 19 kDa, PDI 1.07; PLL^{400}: 407 RU, MW 85.1 kDa, PDI 1.02). Hyaluronic acid sodium salt from Streptococcus equi (HA, MW $\sim$1.65 MDa), poly(sodium 4-styrenesulfonate) (SPS, MW $\sim$70 kDa), hyaluronidase from Streptomyces hyalurolyticus (HAse), human plasma fibronectin, bovine calf serum, high glucose Dulbecco's Modified Eagle's Medium (DMEM), Dulbecco's phosphate buffered saline without calcium or magnesium (PBS, 10$\times$), sodium bicarbonate, sodium dodecyl sulfate, anhydrous dimethyl sulfoxide (DMSO), and methanol were obtained from Sigma-Aldrich (St. Louis, MO). Linear poly(ethyleneimine) (LPEI, MW $\sim$45 kDa) was obtained from Polysciences, Inc. (Warrington, PA). Silicon wafers were obtained from WAFERPRO (San Jose, CA). 2,4,6-Trinitrobenzene Sulfonic Acid (TNBSA, 5% in methanol solution), sodium hydroxide (NaOH, 1 N), hydrochloric acid (HCL, 1 N), borosilicate glass slides, 5/6-carboxyfluorescein succinimidyl ester (NHS-fluorescein), dye removal columns, and Slide-A-Lyzer 3.5 kDa molecular weight cut off (MWCO) dialysis cassettes were obtained from Thermo Fisher Scientific (Waltham, MA). Normal goat serum (NGS) and Alexa Fluor 594 goat anti-rabbit IgG were purchased from Life Technologies (Eugene, OR). Rabbit anti-fibronectin antibody was purchased from Invitrogen (Carlsbad, CA). LIVE/DEAD BacLight Bacterial Viability Kit L7007 was obtained from Molecular Probes (Eugene, OR). Cell counting kit-8 (CCK8) was purchased from Dojindo Molecular Technologies, Inc. (Rockville, MD). NIH 3T3 murine fibroblasts (CRL-1658), *Staphylococcus aureus* 25923, methicillin-resistant *S. aureus* (MRSA) MW2 (BAA-1707), *Pseudomonas aeruginosa*

27853, and *Escherichia coli* 25922 were obtained from ATCC (Manassas, VA). Cation-adjusted Mueller Hinton Broth (CMHB) and CMHB agar plates with 5% sheep's blood were obtained from BD Biosciences (San Jose, CA). Trypsin and penicillin-streptomycin were obtained from Caisson (North Logan, UT). Ultra high purity nitrogen gas (99.999%) was obtained from Corp Brothers, Inc. (Providence, RI). Ultrapure water (18.2 MΩ·cm MilliQ, EMD Millipore, Taunton, MA) was used in all experiments.

3.3.2 Characterizing (PLL/HA) Film Physicochemical Properties

Layer-by-Layer Film Assembly

Silicon and glass substrates (∼7 x 25 mm) were prepared for assembly by rinsing in methanol three times, followed by three water rinses, and drying with air before plasma etching using air in a Harrick PDC-32G plasma cleaner operated at high radio frequency level (12 MHz) for one or five minutes for silicon and glass, respectively. Immediately following plasma etching, the substrates were submerged in LPEI (10 mM, pH 4.25) for at least 15 minutes. All substrates were initially coated with 10 (LPEI/SPS) bilayers assembled by submerging substrates in LPEI (10 mM, pH 4.25) followed by SPS (10 mM, pH 4.75) and repeating, using an adapted Zeiss-Microm DS-50 programmable slide stainer, as previously described.[253] Following $(LPEI/SPS)_{10}$ assembly, $(PLL/HA)_n$ films were assembled using a Biolin Scientific KSV Nima dip coater, where n represents the number of bilayer repeats assembled. For all other experiments $(PLL/HA)_{50}$ films assembled with all three PLL MWs examined were utilized unless otherwise stated. Substrates were first submerged into PLL^{30}, PLL^{90}, or PLL^{400} (1 mg/mL in 1× PBS, pH 7.4) for 15 minutes, followed by a 5 minute rinse with gentle agitation in 1× PBS, pH 7.4. This PLL adsorption step was followed by an analogous HA adsorption step. The substrates were submerged into HA (1 mg/mL in 1× PBS, pH 7.4) for 15 minutes, followed by a 5 minute rinse

with gentle agitation in 1× PBS, pH 7.4. This process was repeated n times to build up $(PLL/HA)_n$. Polymer solutions were refreshed after 25 bilayers. Film or complex formed on the non-plasma treated surface of the substrate was removed with 1 M NaOH. Films were dried under nitrogen and stored at 4°C prior to use in subsequent experiments.

Film Growth Characterization

$(PLL/HA)_n$ film growth was examined by measuring dry film thickness for n = 5, 10, 15, 20, 30, and 50 bilayers. Films with thicknesses below 200 nm were measured using a J.A. Woollam M-2000 ellipsometer, while thicker films were examined using a Veeco Dektak 3 surface profilometer. For ellipsometry measurements, a 632.8 nm laser was used at three incidence angles: 55, 65, and 75 degrees. The refractive index for the polymer films was set to 1.55. Measurements were taken at six different locations on the substrate. For profilometry measurements, films were scratched at three different locations and the average step height between the uncoated surface and the film was determined. Scan lengths of 2000 μm were utilized.

Film Swelling

Dry $(PLL/HA)_{50}$ films assembled on glass were hydrated in 1× PBS at 4°C for 18 hours and incubated with fluorescein-labeled PLL (1 mg/mL PLL^F) (see Section 2.2.4 for PLL^F labeling protocol) for 15 minutes at 25°C. These films were imaged using a Zeiss LSM 800 confocal laser scanning microscope (CLSM) with a C-Apochromat 40×/1.2 W Korr objective (0.44 μm Z-sections). A 488 nm laser (0.1% power) was used to image PLL^F in the films, while a 640 nm laser (1.2% power) was used to detect the position of the glass substrates via reflection. The hydrated thickness of the film was measured by examining thickness of a rendered Z-stack of these films using ZEISS ZEN software (some level of fluorescence from PLL^F was visible throughout the entire film thickness for each PLL MW

examined). This hydrated thickness was then compared to the dry film thickness obtained via profilometry to obtain a percent swelling using equation 3.1:

$$\% \, Swelling = \frac{film \, hydrated \, thickness \; - \; film \, dry \, thickness}{film \, dry \, thickness} \tag{3.1}$$

Examining PLL Mobility Within $(PLL/HA)_{50}$ Films

In order to examine PLL mobility within $(PLL/HA)_{50}$ films, PLL was first fluorescently labeled with fluorescein (PLL^{F}) generally following the NHS-fluorescein vendor protocol. Briefly, PLL^{30F}, PLL^{90F}, and PLL^{400F}, were synthesized by mixing the appropriate MW PLL (2 mg/mL) with NHS-fluorescein (10 mg/mL in anhydrous DMSO) at a 1:0.025 molar ratio of PLL RU to fluorescein in 0.1 M sodium bicarbonate (pH 8.5) for 18 hours at 25°C. Free fluorescein was removed using a dye removal column and the conjugate was dialyzed in water for 12 hours at 25°C using a 3.5 kDa MWCO membrane. Conjugation and purity were confirmed using size exclusion chromatography (SEC; Agilent 1260 Infinity high precision liquid chromatograph).

Dry $(PLL/HA)_{50}$ coated glass slides were hydrated in 1× PBS at 4°C for 18 hours. Hydrated films were then incubated in PLL^{F} of matching PLL MW as PLL used in the film assembly for 15 minutes, followed by a 1× PBS rinse for 5 minutes. These films, denoted $(PLL/HA)_{50}$-PLL^{F}, were subsequently imaged using CLSM as described in Section 2.2.3. $(PLL/HA)_{25}$-(PLL^{F}/HA)-$(PLL/HA)_{24}$ films were also assembled with PLL^{F} sandwiched in the middle of the (PLL/HA)50 film. Following 25 bilayers, a PLL^{F} adsorption and rinse step was performed identical to PLL adsorption steps, followed by the remaining 24 bilayers of (PLL/HA). Again, the same PLL^{F} MW was utilized as the rest of the PLL in the film. Dry $(PLL/HA)_{25}$-(PLL^{F}/HA)-$(PLL/HA)_{24}$ films were hydrated in 1× PBS at 4°C for 18 hours before they were imaged using CLSM as described in Section 2.2.3.

Fluorescence recovery after photobleaching (FRAP) experiments were also conducted using a Zeiss LSM 800 CLSM with a C-Apochromat 40×/1.2 W Korr objective on $(PLL/HA)_{50}$-PLL^{F} films. Circular regions (20 μm diameter) were bleached with a 488 nm laser until fluorescence intensity reached ∼30% of the initial intensity. Average fluorescence was then monitored in the bleached region over 15 minutes and corrected using the intensity of a non-bleached region of the same size to account for gradual photobleaching during imaging; this corrected average fluorescence was normalized to the intensity pre-bleaching. Measurements were conducted in the center of the films to reduce substrate-film and PBS-film effects. FRAP experiments were repeated using three coated substrates per condition with at least two FRAP experiments per substrate.

Measuring $(PLL/HA)_{50}$ Film Stability

$(PLL/HA)_{50}$ Film Dissolution in Bacteria Media

$(PLL/HA)_{50}$ coated silicon wafers were sterilized via exposure to ultraviolet light in a Nuaire Class II Type A2 biosafety cabinet for 15 minutes per side and then incubated in 1 mL of CMHB at 37°C shaking at 100 rpm. Every 24 hours, the substrates were rinsed twice with 1× PBS and then added to fresh CMHB. The substrates were dried with nitrogen following the rinse step either every 24 hours for PLL^{30} and PLL^{90} films or every 4 days for PLL^{400} films, and dry film thickness was measured using a Veeco Dektak 3 surface profilometer (as described in Section 2.2.2).

Degradation of $(PLL/HA)_{50}$ in HAse and Quantification of Released PLL

$(PLL/HA)_{50}$ coated silicon wafers were incubated coating side facedown in 0.5 mL of 1× PBS, pH 7.4 or HAse dissolved in 1× PBS at different concentrations (2.5, 5, and 10 U/mL) at 37°C. Every hour until one of the film architectures completely degraded, all

films were removed from their incubation solution, dried with nitrogen and dry thicknesses were measured using a Veeco Dektak 3 surface profilometer (as described in Section 2.2.2). Films were then incubated in fresh 1× PBS or HAse. Incubation solutions were stored at -20°C until their PLL content was quantified. TNBSA was used to quantify the amount of PLL in each incubation solution by taking advantage of its colorimetric reaction with the primary amines of PLL. The assay was modified from the vendor protocol and previously published protocols.[265,266] Briefly, 50 μL of the film incubation solution or controls of blank 1× PBS were transferred to a 96-well plate (UV-transparent) and mixed with 25 μL of diluted TNBSA solution (0.01% in sodium bicarbonate, pH 8.5) and left rocking for 30 minutes at 37°C. To stop the reaction, 12.5 μL of 1 M HCl was added followed by 25 μL of 10% SDS, and the absorbance was measured at 335 nm using a BioTek® Cytation 3 plate reader. Standard curves of PLL at each MW studied were produced to quantify the PLL release results. HAse was confirmed to produce no interfering signal. Total PLL loading in $(PLL/HA)_{50}$ films was similarly examined by completely degrading films in 10 U/mL HAse for 22 hours at 37°C and subsequently quantifying the PLL present using TNBSA.

3.3.3 Antibacterial Activity of PLL and $(PLL/HA)_{50}$ Coatings

Investigating PLL Minimum Inhibitory Concentration (MIC)

Antibacterial activity of PLL was tested against *S. aureus* using a modified microdilution assay based on previously established protocols.[267] PLL^{30}, PLL^{90}, PLL^{400} were dissolved in CMHB at 256 μg/mL and filtered using a 0.22 μm sterile syringe filter. PLL solutions were serially diluted 1:2 with CMHB in 96-well plates. Bacteria in its logarithmic growth phase was added at a final concentration of 10^5 CFU/mL. Positive controls of bacteria cultured without any treatment and negative controls of CMHB without bacteria were included. After 16 to 18 hours of shaking at 100 rpm and 35°C, the optical density

at 600 nm (OD_{600}) was measured using a BioTek® Cytation 3 plate reader. Normalized bacteria density was calculated using Equation 3.2.

$$Normalized\ bacteria\ density = \frac{sample\ abs\ -\ negative\ control\ abs}{positive\ control\ abs\ -\ negative\ control\ abs} \quad (3.2)$$

The MIC of PLL was taken as the range of sample concentrations over which the normalized bacteria density transitioned from 0 to greater than 0.

Measuring Planktonic Bacteria Growth Inhibition by $(PLL/HA)_{50}$ Films

The capability of $(PLL/HA)_{50}$ coated silicon wafers to inhibit growth of *S. aureus*, MRSA, *E. coli*, and *P. aeruginosa* was examined. Film coated substrates and controls of uncoated silicon were sterilized via exposure to ultraviolet light in a Nuaire Class II Type A2 biosafety cabinet for 15 minutes per side. Samples were placed in 12-well plates with 1 mL of 10^5 CFU/mL bacteria in its logarithmic growth phase. After a 24-hour incubation with shaking at 100 rpm and 37°C, 100 μL of media was removed from each well. The OD_{600} was measured using a BioTek® Cytation 3 plate reader to examine bacterial growth. Normalized bacterial density was calculated using Equation 2, where the positive control was bacteria cultured without any treatment and the negative control was CMHB without bacteria added. Normalized bacteria density was examined similarly for film coated substrates that were repeatedly challenged with fresh *S. aureus* at 10^5 CFU/mL in its logarithmic growth phase every 24 hours. Substrates were removed from the 12-well plates every 24 hours, rinsed with 1 mL of 1× PBS twice and incubated with fresh bacteria if no bacterial growth was apparent. This repeated exposure was continued until normalized bacteria growth greater than 0 was observed. Film incubation solutions were stored at -20°C prior to PLL quantification. Due to interference from CMHB, TNBSA was not utilized

to directly quantify PLL in these incubation solutions. Instead, a modified microdilution assay was utilized as described in Section 2.4.1. These incubation solutions were serially diluted with CMHB and the number of dilutions to reach the MIC range were compared to the MIC of non-film incorporated PLL^{30}, PLL^{90}, or PLL^{400} to calculate the potential lower and upper range of PLL release in these film-CMHB incubation solutions.

Examining Bacteria Attachment Inhibition on $(PLL/HA)_{50}$ Films

The ability of the $(PLL/HA)_{50}$ films to inhibit the attachment of *S. aureus* was examined using film coated glass substrates and comparing to uncoated glass. Substrates were sterilized via exposure to ultraviolet light in a Nuaire Class II Type A2 biosafety cabinet for 15 minutes per side, placed in 6-well plates, and incubated with 2.5 mL of 10^6 CFU/mL *S. aureus* in its logarithmic growth phase. After 2 hours at 37°C without shaking, substrates were rinsed with 2 mL of 1× PBS twice and either examined via a LIVE/DEAD BacLight Bacterial Viability Kit or placed coating side facedown onto agar plates (CMHB agar with 5% v/v sheep's blood). For the agar plate assay, the presence of bacterial colonies was examined after 16 to 18 hours incubation at 37°C, indicating bacteria attachment and growth, via a Canon PowerShot s110 digital camera. For substrates examined via a LIVE/DEAD assay, samples were incubated for 15 to 30 minutes with the LIVE/DEAD dye mixture (15 μL of component A and B per 1 mL 1× PBS). These substrates were imaged with a Nikon TiE inverted fluorescence microscope using a 470/40 excitation and 525/50 emission (FITC) filter for live cells and a 545/30 excitation and 620/60 emission (TRITC) filter for dead cells with a Plan Fluor 10×/0.3 objective. 10 images per substrate were taken, with 3 to 6 repeats per coated substrate type, and 15 repeats for uncoated substrates. CellProfiler™ was used to quantify the average surface area covered by bacteria per field of view. Percent area covered with live or dead cells was normalized to the percent area covered with live or dead cells on uncoated glass controls.

3.3.4 Examining $(PLL/HA)_{50}$ Films Cytocompatibility

Cytocompatibility of $(PLL/HA)_{50}$ film release components was measured for NIH 3T3 murine fibroblasts. NIH 3T3 cells were cultured in DMEM (containing 4 mM L-glutamine, 4500 mg/L glucose, 1 mM sodium pyruvate, and 1500 mg/L sodium bicarbonate) with 10% calf bovine serum and 1% penicillin-streptomycin at 37°C and 5% CO_2. Film coated and uncoated silicon substrates were incubated in 1 mL of DMEM at 37°C in 5% CO_2 for 24 hours. Subsequently, 100 μL of these incubation solutions or solutions in which non-film incorporated HA (1000 μg/mL) or PLL (32, 16, and 32 μg/mL for PLL^{30}, PLL^{90}, and PLL^{400}, respectively) were dissolved were incubated with NIH 3T3 cells seeded in tissue cultured treated 96-well plates at 10^4 cells/cm^2 for 24 hours at 37°C. Cell viability was measured using CCK8 following the vendor's protocol. Briefly, incubation solutions were removed and 150 μL of CCK8 reagent was added. After two hours of incubation at 37°C, absorbance at 450 nm was measured using a BioTek® Cytation 3 plate reader. Normalized cell viability was calculated using Equation 3.3. Positive controls of cells grown in DMEM and negative controls lacking cells were included.

$$Normalized\ cell\ viability = \frac{sample\ abs\ -\ negative\ control\ abs}{positive\ control\ abs\ -\ negative\ control\ abs} \tag{3.3}$$

3.3.5 Statistical Analysis

Results are reported as means $\pm$ standard deviations. All experiments were repeated with three or more samples. Statistical significance was calculated using one-way and two-way analysis of variance (ANOVA; α = 0.05) with Tukey's post-hoc analysis on GraphPad PRISM™ or MATLAB™; *, $p < 0.05$; **, $p < 0.01$; ***, $p < 0.001$; ****, $p < 0.0001$.

Label	DP_n[b]	M_n[b]	PDI[b]	MIC against *S. aureus*[a]	
				μg/mL	μM
PLL^{10}	10	2.1	n/a	64	30.5
PLL^{30}	33	6.9	1.02	8	1.2
PLL^{90}	91	19	1.07	8	0.4
PLL^{400}	407	85.1	1.02	16	0.2

[a] MIC Minimum inhibitory concentration against *S. aureus* 25923.
[b] DP_n Number average degree of polymerization, measured by NMR. M_n Number average molecular weight in kDa, measured by NMR. PDI Polydispersity index, measured by GPC. All polymer specifications reported by manufacturer.

Table 3.1: PLL specifications and antibacterial efficacy in solution

3.4 Results

3.4.1 Effect of Molecular Weight on PLL MIC

Here we used PLL with varying number of RUs (10, 33, 91, and 407) denoted as PLL^{10}, PLL^{30}, PLL^{90}, and PLL^{400}, respectively, to assemble $(PLL/HA)_n$ multilayer films as shown in Figure 3.1(A). Prior to film incorporation, we investigated the antibacterial activity of non-film incorporated PLL by determining the MIC of these specific PLL MWs against *S. aureus*. We found that the MIC of PLL/textsuperscript10, PLL^{30}, PLL^{90}, and PLL^{400} against *S. aureus* was 64.0, 8.0, 8.0 and 16.0 μg/mL (i.e., 30.5, 1.2, 0.4, and 0.2 μM, respectively). Table 1 summarizes PLL RU, MW, PDI, and MIC. We also confirmed that HA had no inhibitory effect against *S. aureus* up to at least 1000 μg/mL; therefore, any antibacterial activity reported in our studies is attributed to PLL.

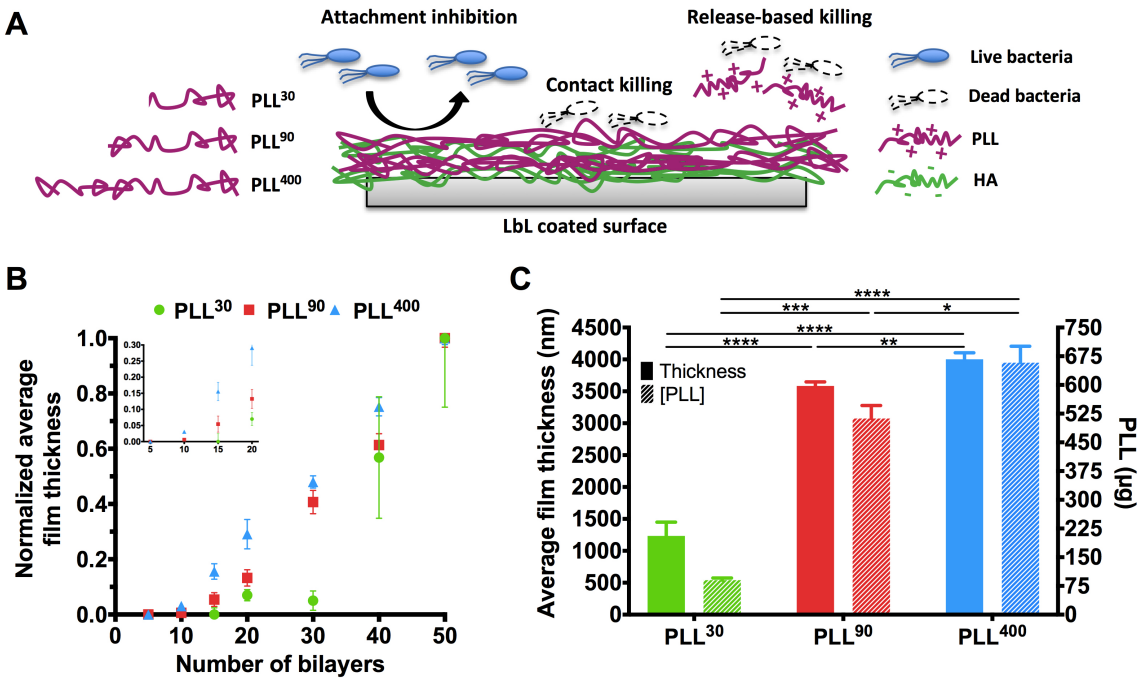

Figure 3.1: $(PLL/HA)_n$ film thickness and PLL loading. A) Schematic of $(PLL/HA)_n$ multilayer coatings and potential mechanisms of antibacterial activity. B) Average film thickness versus number of bilayers (n) for $(PLL/HA)_n$ films assembled using PLL^{30}, PLL^{90}, or PLL^{400} normalized to average film thickness of $(PLL/HA)_{50}$ (n = 3 repeats). Inset zooms in on average film thicknesses for n = 5, 10, 15, and 20 bilayers. Note, average thickness of PLL^{30} films with n = 5 and 10 bilayers was not measurable. C) Thickness of $(PLL/HA)_{50}$ films (solid bars, left axis; n = 12 repeats) and total amount of PLL incorporated in these films (striped bars, right axis; n = 3 repeats). Results are shown as mean ± standard deviation. Statistical significance was examined using two-way ANOVA with Tukey's post-hoc analysis; * $p < 0.05$; ** $p < 0.01$, *** $p < 0.001$; **** $p < 0.0001$.

Film characteristics	PLL^{30}	PLL^{90}	PLL^{400}
Total dry thickness (nm)	1233±216	3585±64	4002±103
Total PLL loading (μg)	90±5	512±34	657±43
PLL/nm thickness (ng/nm)	73±4	143±9	164±11
Total hydrated thickness (μm)	4.6±1.0	16.2±7.3	21.2±1.4

Table 3.2: $(PLL/HA)_{50}$ Film Thickness and PLL Loading Based on PLL MW

3.4.2 Investigating $(PLL/HA)_{50}$ Multilayer Film Physical Properties

$(PLL/HA)_n$ Film Assembly and PLL Loading

To investigate the influence of PLL MW on multilayer film antibacterial efficacy, we assembled $(PLL/HA)_n$ films with PLL^{30}, PLL^{90}, and PLL^{400}. Attempts at assembling $(PLL/HA)_n$ films utilizing PLL/textsuperscript10 did not result in film growth, likely due to severe MW mismatch between PLL and HA (2.1 kDa versus 1.65 MDa), which has previously been shown to hinder film buildup.[138] We monitored film growth with increasing number of bilayers, as shown in Figure 3.1(B), and observed exponential film growth, characteristic of (PLL/HA) films.[257,258,268] $(PLL/HA)_{50}$ films built with PLL^{30} resulted in an average thickness of 1233 $\pm$ 216 nm, significantly thinner than the 3585 $\pm$ 64 nm and 4001 $\pm$ 103 nm thickness observed for PLL^{90} and PLL^{400} films, respectively (Fig. 3.1(C)). $(PLL/HA)_{50}$ films had a large swelling capacity as observed by CLSM imaging of PLL^{F} incubated films. Percent swelling of initially dry films in 1$\times$ PBS was found to be approximately 430 $\pm$ 36%, 349 $\pm$ 204%, and 281 $\pm$ 99% for PLL^{400}, PLL^{90}, and PLL^{30} films, respectively.

In order to quantify the total amount of PLL contained in these 50 bilayer films, the films were completely degraded using HAse, an enzyme which degrades the HA polysaccharide into oligosaccharides,[204] followed by quantification of the PLL amino groups. Incubating films in HAse led to complete film disassembly. The amount of PLL loaded in

the different films was proportional to the difference in film thickness between PLL MWs. PLL^{30}, PLL^{90}, and PLL^{400} $(PLL/HA)_{50}$ films contained approximately 90 $\pm$ 5, 512 $\pm$ 34, and 657 $\pm$ 43 μg of PLL, respectively (Fig. 3.1(C)). Table 2 summarizes $(PLL/HA)_{50}$ thickness and PLL loading characteristics.

Effect of PLL MW on PLL Mobility Within $(PLL/HA)_{50}$ Films

To characterize the diffusion of PLL at the specific MWs explored in this work, we first conjugated fluorescein to the three different PLLs, yielding PLL^{30F}, PLL^{90F}, and PLL^{400F}. Using SEC, PLL was detected using refractive index but showed no absorbance at 492 nm. After fluorescein conjugation, an absorbance signal was detected at the aforementioned wavelength indicating successful tethering to PLL (data not shown). SEC also confirmed successful purification of the PLL^F product by removal of non-conjugated fluorescein using a dye removal column. PLL^F was either deposited on top of the 50 bilayer films, denoted $(PLL/HA)_{50}$-PLL^F, or embedded within the films during film assembly, denoted $(PLL/HA)_{25}$-(PLL^F/HA)-$(PLL/HA)_{24}$. We then examined these films using CLSM. Rendered cross sectional images show that PLL^{30F} and PLL^{90F} were able to diffuse throughout the entirety of the film for both $(PLL/HA)_{50}$-PLL^F and $(PLL/HA)_{25}$-(PLL^F/HA)-$(PLL/HA)_{24}$ (Fig. 3.2(A)). We noted that the fluorescence intensity was lower for $(PLL/HA)_{25}$-(PLL^F/HA)-$(PLL/HA)_{24}$ than films capped with PLL^F, possibly due to PLL^F exchange with non-fluorescent PLL during film assembly. For the PLL^{400F} capped film, PLL^{400F} remained primarily in the top portion of the film and did not diffuse considerably into the lower layers (Fig. 3.2A). When incorporated mid-film assembly, PLL^{400F} remained primarily in the center of the film, appearing as a bright fluorescent band (Fig. 3.2A). Z-profiles of the fluorescence intensity for both $(PLL/HA)_{50}$-PLL^F (Fig. 3.2B) and $(PLL/HA)_{25}$-(PLL^F/HA)-$(PLL/HA)_{24}$ films (Fig. 3.2C) showed PLL^{30F} and PLL^{90F} homogeneously distributed throughout the entire thickness of the film, while PLL^{400F} is observed

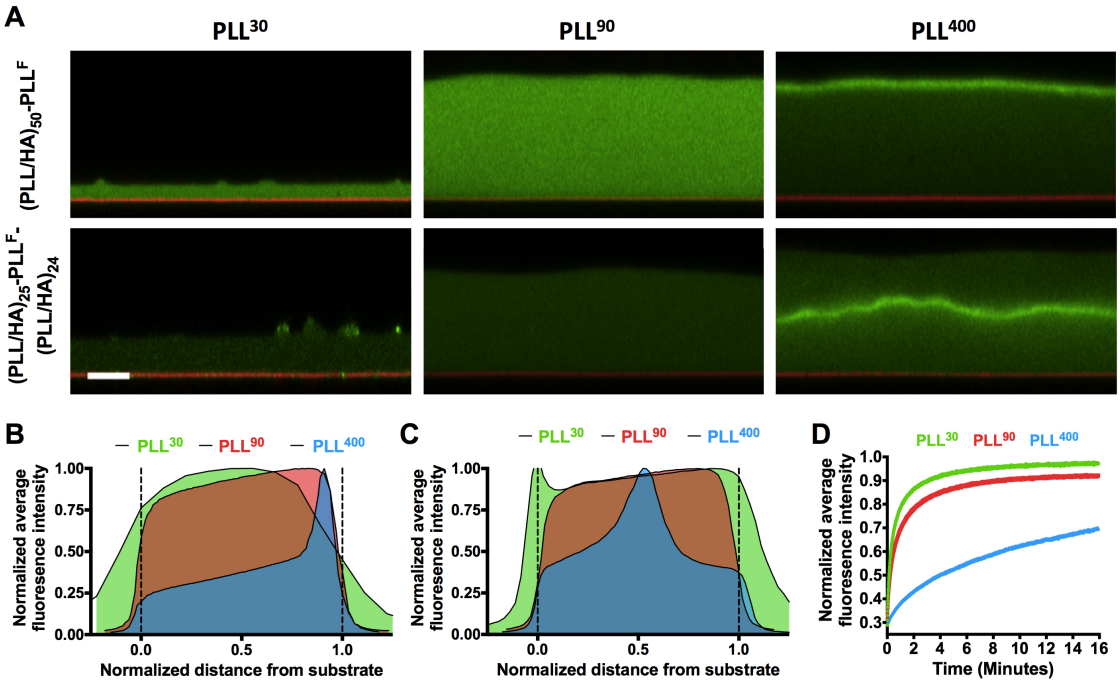

Figure 3.2: Examining PLL mobility within $(PLL/HA)_{50}$ films. CLSM and FRAP experiments. A) Representative cross-sectional CLSM images of $(PLL/HA)_{50}$-PLL^F (top) and $(PLL/HA)_{25}$-(PLL/textsuperscriptF/HA)-$(PLL/HA)_{24}$ films (bottom) assembled with PLL^{30}, PLL^{90}, or PLL^{400} (left to right). Green indicates PLL^F and red indicates the glass substrate. The scale bar represents 10 μm. Normalized average fluorescence intensity across film z-profiles in (B) $(PLL/HA)_{50}$-PLL^F and (C) $(PLL/HA)_{25}$-(PLL^F/HA)-$(PLL/HA)_{24}$ films. Dotted lines indicate the bottom of the film (i.e., the glass substrate at a normalized distance of 0) and the top of the film (i.e., at a normalized distance of 1). D) Recovery of fluorescence in a photobleached area in $(PLL/HA)_{50}$-PLL^F films assembled with PLL^{30}, PLL^{90}, or PLL^{400} tracked over time. Average fluorescence intensity is normalized to the initial fluorescence before bleaching. Time = 0 corresponds to the end of the photobleaching step. At least 2 FRAP experiments were conducted per substrate, with 3 repeats per condition. CLSM images and intensity z-profiles are representative of at least 3 imaged substrates.

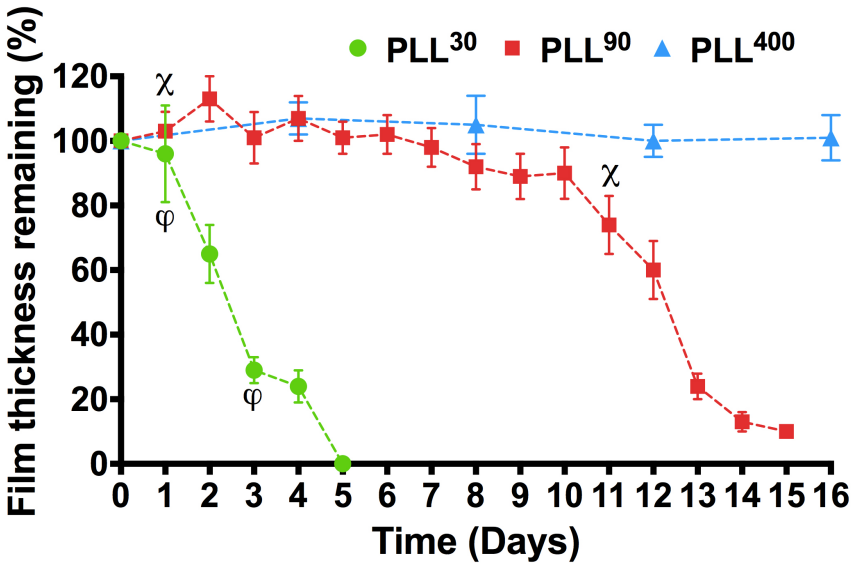

Figure 3.3: $(PLL/HA)_{50}$ film stability over time in bacteria media. Dry thickness of films assembled using PLL^{30}, PLL^{90}, or PLL^{400} over time incubated in CMHB at 37°C. Results are shown as mean ± standard deviation. Symbols indicate the first timepoint that change in dry film thickness was observed to be significantly different from the first day based on one-way ANOVA and Tukey's post-hoc analysis; $p < 0.0001$; $n = 3 – 6$.

at either the surface or centered in the film depending on the deposition method. FRAP experiments showed a much slower fluorescence recovery for photobleached regions of $(PLL/HA)_{50}$-PLL^F films assembled with PLL^{400} compared to PLL^{30} and PLL^{90}, indicating a significantly lower mobility of PLL^{400} compared to PLL^{30} and PLL^{90}.

Effect of PLL MW on $(PLL/HA)_{50}$ Film Stability

$(PLL/HA)_{50}$ Film Dissolution in Bacterial Media

We monitored the change in dry film thickness of $(PLL/HA)_{50}$ films incubated in CMHB over time as shown in Figure 3.3. PLL^{30} films underwent a gradual and relatively linear dissolution over five days. In contrast, PLL^{90} films remained stable over 10 days, following which film thickness began decreasing. The thickness of these films fell to approximately 10% of the original thickness by approximately 15 days. At this point, it

was difficult to accurately measure remaining film thickness on subsequent days. On the other hand, PLL^{400} films remained stable over at least 16 days, with no change in dry film thickness observed.

$(PLL/HA)_{50}$ Film Enzymatic Degradation and PLL Release

To test the responsiveness to HAse and the subsequent release of PLL, $(PLL/HA)_{50}$ films were incubated with different concentrations of HAse in 1× PBS, pH 7.4 at 37°C. Higher HAse concentrations caused faster degradation of the films, as observed by monitoring dry film thickness (Fig. 3.4, A-C). PLL MW also affected the rate of degradation with films built with lower MW PLL degrading more quickly; 10 U/mL HAse degraded PLL^{30}, PLL^{90}, and PLL^{400} films completely within 3, 4, and 5 hours, respectively. We also observed that PLL90 and PLL^{400} films did not degrade in the lowest concentration of HAse tested (2.5 U/mL) within the timeframes we examined. PLL release was also quantified by measuring primary amines in solution via their interaction with TNBSA. The amount of PLL released as the films degraded was concomitant with decrease in film thickness (Fig. 3.4, D-F), suggesting that PLL is present throughout the film, and is released as the film degrades. As expected, for PLL^{90} and PLL^{400}, there was negligible PLL release with the lowest HAse concentration.

3.4.3 Evaluating Antibacterial Properties of $(PLL/HA)_{50}$ Films

Antibacterial Efficacy of $(PLL/HA)_{50}$ Films Against Planktonic Bacteria

We tested the efficacy of $(PLL/HA)_{50}$ coated substrates in inhibiting planktonic bacterial growth for films assembled using PLL^{30}, PLL^{90}, and PLL^{400}. We examined activity against gram-positive bacteria, *S. aureus* and MRSA, as well as gram-negative bacteria, *E.*

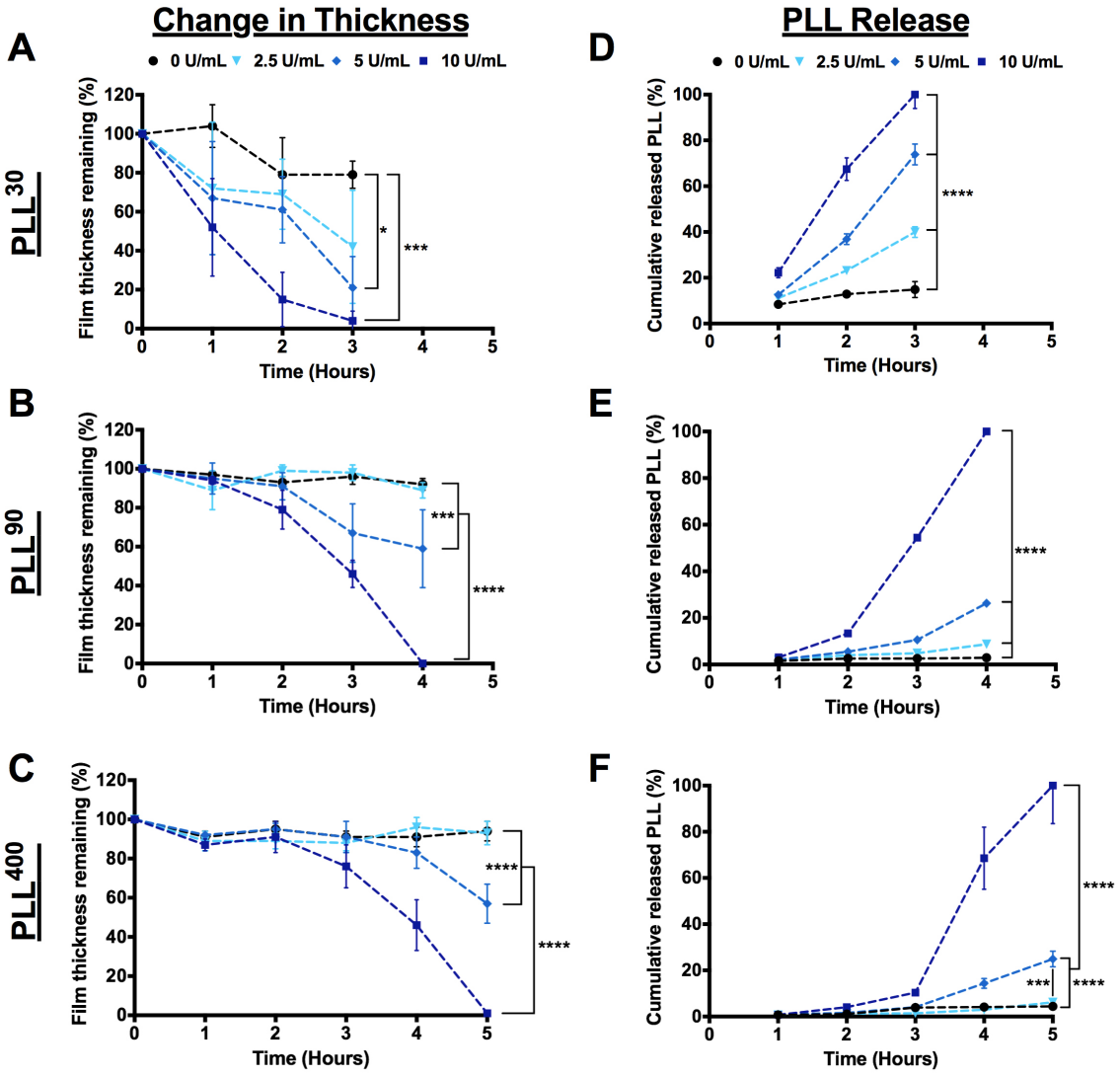

Figure 3.4: Film degradation and PLL release in response to HAse. $(PLL/HA)_{50}$ films assembled with PLL^{30} (A, D), PLL^{90} (B, E), or PLL^{400} (C, F) incubated in 1× PBS (0 U/mL) or different concentrations of HAse (2.5, 5, or 10 U/mL) at 37°C over time. (A-C) Percent dry film thickness remaining normalized to the initial dry film thickness and (D-F) percent PLL released normalized to total PLL loading over time. Results are shown as mean ± standard deviation. Statistical significance between different HAse concentrations and time points was examined using two-way ANOVA and Tukey's post-hoc analysis. Significance between HAse concentrations at the last time points are shown; * $p < 0.05$, *** $p < 0.001$; **** $p < 0.0001$; n = 3.

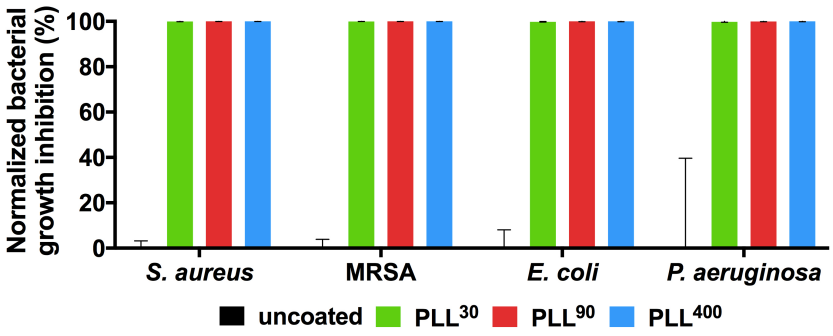

Figure 3.5: Planktonic bacterial growth inhibition. Bacterial density was measured after $(PLL/HA)_{50}$ coated or uncoated substrates were incubated in gram-positive *S. aureus* and MRSA and gram-negative *E. coli* and *P. aeruginosa* for 24 hours and normalized to uncoated substrates. Results are shown as mean $\pm$ standard deviation; n = 3.

coli and *P. aeruginosa* by quantifying optical density of bacterial suspensions incubated with $(PLL/HA)_{50}$ films for 24 hours at 37°C. The normalized bacterial growth inhibition is shown in Figure 3.5. We observed that $(PLL/HA)_{50}$ films completely inhibited bacterial growth (>99.8% inhibition) for all four bacterial strains at all three PLL MWs tested. Next, we investigated the possibility of repeated usage of these coatings against *S. aureus*. Every 24 hours, if the coatings were successful in inhibiting bacterial growth, they were rinsed and challenged with a fresh inoculum of *S. aureus*. We observed a PLL MW dependence on antibacterial efficacy for repeated $(PLL/HA)_{50}$ use. Figure 3.6A represents this information as a survival curve of $(PLL/HA)_{50}$ films, showing the percentage of coated substrates still effective at completely inhibiting *S. aureus* after each repeated bacterial exposure. For all films tested, PLL^{400} films were only effective for a single use, while PLL^{30} and PLL^{90} films could be effectively utilized for 4 to 5 and 9 to 13 uses, respectively.

We also quantified PLL in the $(PLL/HA)_{50}$ bacteria incubation solutions collected during repeated bacterial exposure for repeats in which the films were effective against *S. aureus*. It was expected that PLL concentration would be at or above the MIC range of the PLL MW incorporated in the film against *S. aureus*. Due to interference from CMHB, direct quantification of PLL as we had done when examining PLL release in the presence

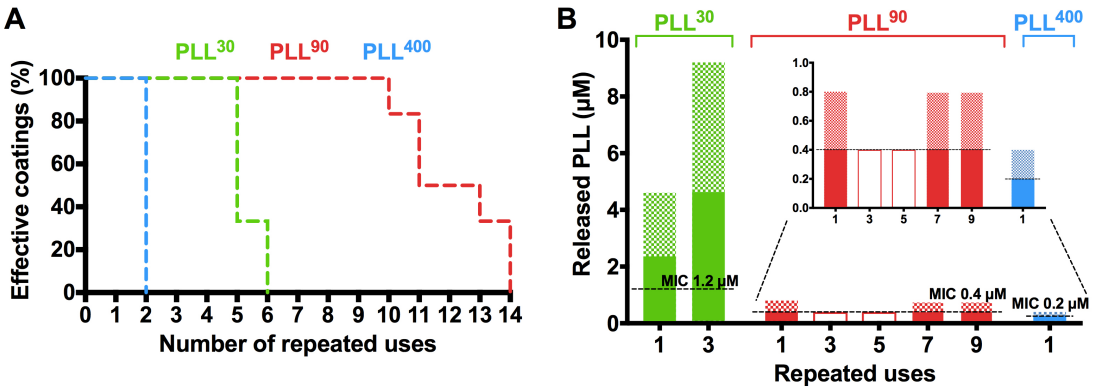

Figure 3.6: Planktonic bacterial growth inhibition upon repeated bacterial exposures. A) Percent of $(PLL/HA)_{50}$ films that remained effective at completely inhibiting the growth of *S. aureus* upon repeated exposure to fresh *S. aureus* inocula every 24 hours. B) Concentration of PLL released from $(PLL/HA)_{50}$ films into incubation solutions during repeated bacterial exposures. Minimum concentration is represented as a solid bar and the possible upper range is shown as a shaded bar. Empty bars indicate no bacterial inhibition was observed. Horizontal dashed lines indicate the MIC for each PLL MW. Inset zooms in on the release from PLL^{90} and PLL^{400} films. Experiments were conducted on 6 repeats.

of HAse, was not possible. Instead, we utilized a microdilution assay approach in which the film incubation solution was serially diluted 1:2 with fresh media and exposed to *S. aureus*. We determined how many dilutions were needed to observe a transition from complete *S. aureus* growth inhibition to a lack of complete inhibition (i.e., the MIC of PLL against *S. aureus*). Using the PLL^{30}, PLL^{90}, and PLL^{400} MIC ranges we had determined against *S. aureus* (as summarized in Table 1) and the number of dilutions of film incubation solutions required to reach the MIC range, we determined the amount of PLL present in the $(PLL/HA)_{50}$ bacteria incubation solutions. As a validation of the method, we compared TNBSA quantification of PLL^{90} in HAse film degradation in PBS to a microdilution assay of the same solution and found that the measured PLL concentration range agreed with the TNBSA results (Fig. 3.10). Figure 3.6B shows the PLL release concentration in $(PLL/HA)_{50}$ film-*S. aureus* incubation solutions over repeated 24-hour exposures. As the MIC is a range, the release quantity is also shown as a range lying between the possible lowest (solid bar) and highest (shaded bar) concentrations of PLL released during that substrate use. Note, empty bars are shown for samples that did not lead to any bacterial growth

inhibition when tested in the microdilution assay. The released PLL concentrations are generally at or above MIC in samples where films were observed to be effective. For example, PLL^{30} films showed a PLL release above the PLL^{30} MIC against *S. aureus* at 1 and 3 repeated uses, over which we had observed all tested substrates to be effective at completely inhibiting *S. aureus* growth (Fig. 3.6A). Similarly, PLL^{400} concentrations were at or above the PLL^{400} MIC against *S. aureus* at one use. PLL^{90} films were generally more variable, showing at or above PLL^{90} MIC release for some of the effective incubation solutions but not others. For example, incubation solutions from the 3rd and 5th repeated use showed PLL^{90} concentrations below the MIC. These results suggest that the method of measuring PLL release may have some discrepancies or that additional modes of antibacterial activity in addition to released PLL activity may be at play, including contact killing through the interaction of bacteria with PLL at the interface of the $(PLL/HA)_{50}$ coatings.

Bacterial Anti-Attachment Efficacy of $(PLL/HA)_{50}$ Films

Given its importance in preventing biofilm formation, the ability of $(PLL/HA)_{50}$ films to inhibit bacterial attachment was also examined. We incubated $(PLL/HA)_{50}$ coated glass substrates with *S. aureus* for two hours for films formulated with PLL^{30}, PLL^{90}, and PLL^{400}. The substrates were then either stained with LIVE/DEAD dyes to quantify attached bacteria, or plated coating side facedown onto agar for 18 hours to examine growth of potentially attached bacteria. Figure 3.7A shows representative images of LIVE/DEAD staining of glass versus $(PLL/HA)_{50}$ coated glass incubated with *S. aureus*. Figure 3.7B reports the percent of surface covered by live bacteria normalized to uncoated glass substrates. PLL^{30}, PLL^{90}, and PLL^{400} coatings reduced attachment by live bacteria by $85 \pm 3\%$, $74 \pm 5\%$, and $83 \pm 4\%$, respectively, relative to uncoated glass. We also observed an increase in dead bacteria on the $(PLL/HA)_{50}$ surface relative to uncoated glass (approximately 2 to 3 times larger area covered by dead bacteria). Overall, a large decrease in total bacteria at-

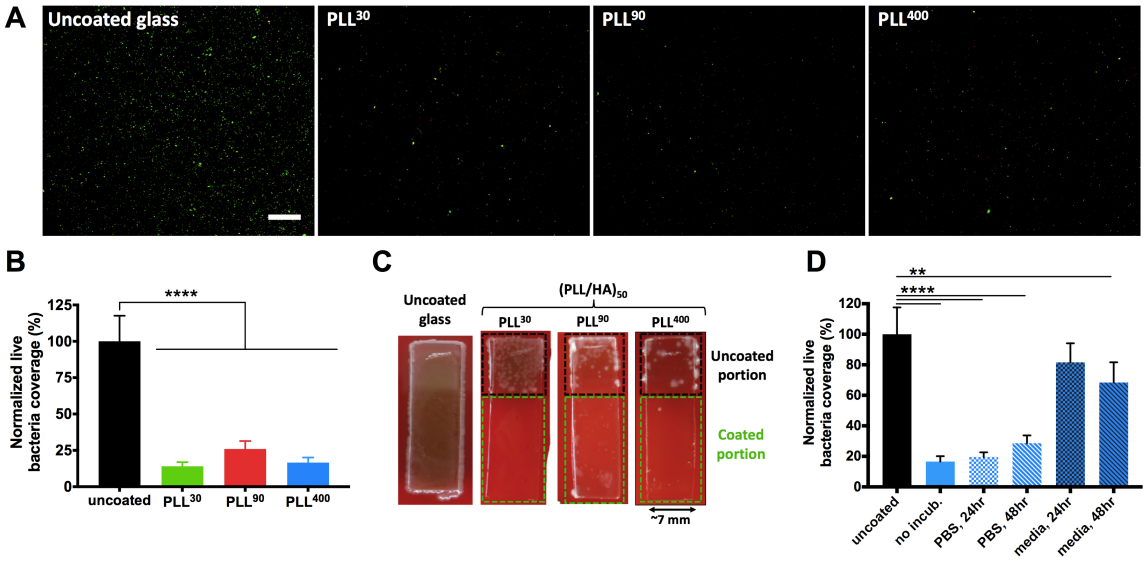

Figure 3.7: Bacterial attachment to $(PLL/HA)_{50}$ coated and uncoated substrates. A) Representative images of LIVE/DEAD staining of adherent S. aureus on uncoated and $(PLL/HA)_{50}$ coated glass. B) Percent area covered with live bacteria normalized to percent area of uncoated glass with live bacteria attached. C) Images of $(PLL/HA)_{50}$ coated glass and uncoated glass after a 2 hour incubation in S. aureus followed by rinsing and plating coating side down onto CMHB agar for 18 hours. D) Percent area covered with live bacteria normalized to percent area of uncoated glass with live bacteria attached for PLL^{400} film coated glass preconditioned or not in PBS or media for 24 or 48 hours. Scale bar represents 200 μm. Results are shown as mean $\pm$ standard deviation. Statistical significance was examined using one-way ANOVA and Tukey's post-hoc analysis; ** $p < 0.01$; **** $p < 0.0001$; n = 3 – 6 for film coated glass, n = 15 for uncoated glass. Images of substrates on agar are representatives of at least 3 repeats.

tached compared to uncoated glass (72 $\pm$ 7%, 60 $\pm$ 7%, 62 $\pm$ 6% reduction for PLL^{30}, PLL^{90}, and PLL^{400} coatings, respectively) was observed. Examining substrates incubated on agar upon exposure to *S. aureus*, we observed that bacteria were unable to grow on the $(PLL/HA)_{50}$ coated portion of the glass at all PLL MWs (Fig. 3.7C). In contrast, bacterial growth was observed on uncoated regions of the film coated substrates, albeit to a lesser degree than plain glass. As PLL^{400} films were only able to inhibit planktonic bacteria growth once, we examined whether they were able to reduce bacterial attachment beyond one use. For this study, we tested the attachment of *S. aureus* to PLL^{400} coatings that had been preconditioned in bacteria media for 24 or 48 hours, at which point we had observed them to be unable to inhibit planktonic *S. aureus* growth (Fig. 3.6). As shown in Figure 3.7D, LIVE/DEAD staining indicated that the coatings were not as effective in inhibiting bacteria attachment as non-preconditioned films, showing only an 18 $\pm$ 12% and 31 $\pm$ 13% reduction in live bacteria attachment on coatings preconditioned for 24 and 48 hours, respectively. In contrast, when PLL^{400} coatings were preconditioned in 1$\times$ PBS instead of bacteria media for 24 and 48 hours, LIVE/DEAD staining showed a reduction in live bacteria attachment similar to what was observed with non-preconditioned films (80 $\pm$ 3% and 71 $\pm$ 5% reduction by coatings preconditioned for 24 and 48 hours, respectively).

Investigating $(PLL/HA)_{50}$ Film Cytocompatibility

The cytocompatibility of $(PLL/HA)_{50}$ films assembled with PLL^{30}, PLL^{90}, and PLL^{400} was tested using NIH 3T3 fibroblasts. NIH 3T3 cells were cultured in media in which these films or uncoated controls had been incubated for 24 hours. The effect of the release solution on cell viability was observed using a CCK8 assay. Figure 3.8 shows NIH 3T3 viability normalized to cells cultured in untreated growth media. Release media from PLL^{30} and PLL^{90} films as well as uncoated controls did not reduce cell viability compared to untreated growth media. However, the release media from PLL^{400} films were highly

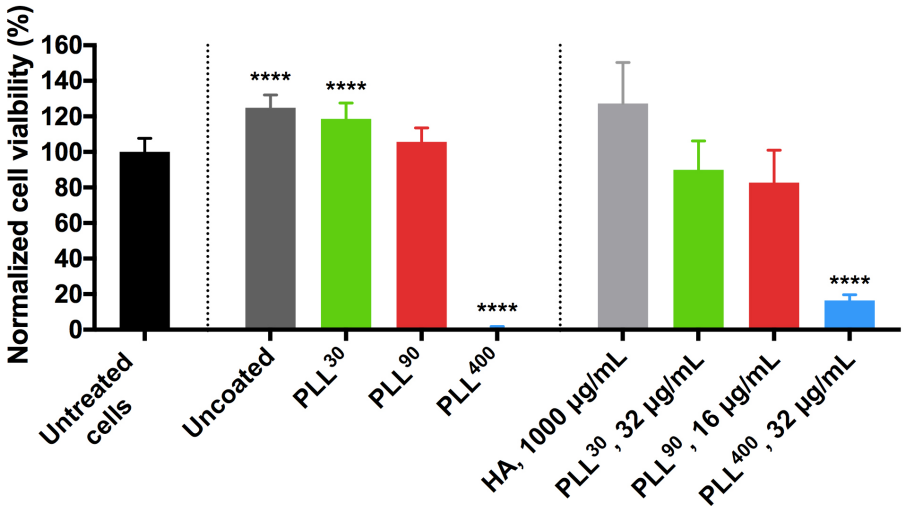

Figure 3.8: Fibroblast cytocompatibility with $(PLL/HA)_{50}$ film release components. Viability of NIH 3T3 cells incubated for 24 hours with media in which $(PLL/HA)_{50}$ coated silicon substrates were incubated for 24 hours or with solutions of HA or PLL. Viability and statistical significance is shown relative to untreated cells. Statistical significance was examined using one-way ANOVA and Tukey's post-hoc analysis; **** $p < 0.0001$; n = 3.

cytotoxic, completely reducing viability. To confirm this reduction in cell viability was due to PLL released into the solution, we examined the cytotoxicity of non-film incorporated PLL^{400} and HA (Fig. 3.8). NIH 3T3 cells were cultured in media containing HA dissolved at film assembly concentrations (1 mg/mL) or PLL^{400} at the maximum PLL release concentration estimated from bacterial growth inhibition experiments (i.e., 32 μg/mL). PLL^{30} and PLL^{90} were similarly examined for their effect on NIH 3T3 cells at the maximum estimated concentration from repeated use studies (32 and 16 μg/mL, respectively) (Fig. 3.8). No statistical difference between NIH 3T3 viability was observed for non-film incorporated HA, PLL^{30}, and PLL^{90} compared to untreated growth media. PLL^{400} at a concentration of 32 μg/mL, significantly reduced normalized viability to $16 \pm 3\%$.

3.5 Discussion

Antibacterial polymers have great potential to be utilized in antibacterial coatings for the prevention and treatment of nosocomial infections. These coatings can function in several different ways to prevent bacterial attachment and/or kill planktonic or surface-attached bacteria, including contact killing and release-based killing or other physicochemical interactions that prevent attachment (Fig. 3.1A).[27,234,269,270] In this work, we explored the properties of coatings developed using a promising antibacterial polymer, PLL, incorporated in LbL assembled films along with a biocompatible polyanion, HA. We examined the effect of PLL MW on the antibacterial properties of these $(PLL/HA)_{50}$ multilayer films. To the best of our knowledge this is the first study that performs a systematic investigation of the effect of PLL MW on antibacterial properties in multilayer films. PLL has been shown to have antibacterial activity against a range of gram-positive and gram-negative bacteria.[242–245,271] The antibacterial effect of PLL has been attributed to its disorganization of the outer bacterial cell membrane by releasing lipopolysaccharides.[271,272] In our studies, we utilized PLL of varying but uniform MW (PLL^{10}, PLL^{30}, PLL^{90}, and PLL^{400}). We found that non-film incorporated PLL showed an initial decrease in MIC against *S. aureus* as the MW increased between PLL/textsuperscript10 and PLL^{30}, indicating improved antibacterial efficacy with the higher MW PLL (Table 1). This observation is similar to previous reports on the antibacterial properties of ε-PLL, a homopolymer produced by bacteria and used as a food preservative; ε-PLL requires a minimum of 10 RU to exhibit antibacterial activity against *E.f coli*.[244] With PLL^{30} and higher MWs, we observed a similarity in the μg/mL MIC but decrease in μM MIC, indicating that the number of protonated amino groups ($NH3^{+}$) on the PLL backbone is the key determinant of antibacterial activity and the same effect can be achieved with a lower number of molecules of longer polymer chains. However, the antibacterial activity decreased for PLL^{400}. Structure-activity relationship studies have shown that some antibacterial polycations, including guanidinylated polycarbonates (8 to

30 kDa)[273] and guanylated polymethacrylates (3 to 20 kDa),[274] are more effective at lower than higher MW. This difference has been attributed to the sieving effect of the bacterial membrane, reducing the ability of larger polymers to penetrate the membrane.[275] It is likely that PLL^{400} is similarly unable to effectively penetrate the bacterial cell wall. When considering $(PLL/HA)_n$ LbL films, PLL MW could affect several different factors including film growth, stability, and polymer mobility within the film. All of these factors, in addition to PLL MIC, are capable of influencing the antibacterial functionality of $(PLL/HA)_n$ multilayer films. Therefore, we investigated the impact of PLL MW on the film physiochemical properties. $(PLL/HA)_n$ films have previously been shown to exhibit exponential growth, due to the ability of PLL to diffuse within the film,[257,258,268] followed by a transition to a linear growth regime after a certain number of layers.[139,276] The specific MWs of PLL and HA utilized in this work, led to similar growth behavior (Fig. 3.1B). Influence of polyelectrolyte MW on film final thickness has been attributed to the crossover to the exponential growth regime,Kujawa2005 and has shown to also affect the onset of the linear regime,[139] which both happen at a lower number of layers with higher MW polymers. PLL^{30}, PLL^{90}, and PLL^{400} films transitioned to the linear phase of growth at approximately 30, 20, and 10 bilayers, respectively. The differences in growth behavior led to large differences in the final thickness and PLL loading of $(PLL/HA)_{50}$ films, with films assembled using PLL^{90} and PLL^{400} being approximately 3 times thicker and containing 6 to 7 times more PLL, respectively, than PLL^{30} films (Table 2 and Fig. 3.1C). In the case of PLL^{30}, the significant difference in MW between PLL and HA may have led to slower film growth due to "stripping off" of PLL^{30} when the growing film was exposed to HA during film assembly.[138] Gram-positive bacteria, *S. aureus* and MRSA, as well as gram-negative bacteria, *E. coli* and *P. aeruginosa*, are among the most common pathogens encountered in medical device-associated infections.[37,236,277–280] $(PLL/HA)_{50}$ coatings assembled from all three PLL MWs examined successfully inhibited planktonic bacterial growth for each of these bacteria over 24 hours (Fig. 3.5); these films are highly promising for use as device coatings. In certain

clinical scenarios including recurrent infections,[281] bacterial growth inhibition is required over extended time periods upon multiple exposures. Therefore, we tested repeated usage of the coatings in inhibiting *S. aureus* growth, and interestingly, large differences appeared between films assembled with different MW PLL. While PLL^{400} coatings were only effective at inhibiting bacterial growth for one 24-hour use, PLL^{30} and PLL^{90} coatings could be used repeatedly multiple times (Fig. 3.6A). In order to elucidate the mechanism of bacterial growth inhibition and understand the differences in the repeated use efficacy of the different PLL MW assemblies, we measured the concentration of PLL released into bacteria solutions incubated with these films. We found that PLL was generally released at high enough concentrations to inhibit bacterial growth (Fig. 3.6B), suggesting that PLL release plays an important role in bacterial growth inhibition over repeated exposures.

We hypothesized that the large differences observed in the number of effective repeated uses for PLL^{30}, PLL^{90}, and PLL^{400} films is due to the reduced mobility of higher MW PLL within the $(PLL/HA)_{50}$ films. This effect of MW has been reported for weak polycations that diffuse within LbL films, including PLL in (PLL/HA) films fabricated at MWs different from those examined in this work[139] and chitosan in (chitosan/HA) films.[282] Within the 24-hour bacteria-film incubation periods, higher amounts of PLL were released from films with lower MW PLL (Fig. 3.6B), supporting our hypothesis. PLL^{400} films released between 16 to 32 μg of PLL within the first incubation of the films with *S. aureus* before they lost efficacy. However, this amount of PLL is equivalent to only approximately 2.5 to 5% of the total PLL^{400} load within the $(PLL/HA)_{50}$ films, indicating that a large amount of PLL remains entrapped within the film. We used CLSM along with FRAP to more directly examine the mobility of fluorescein-tagged PLL within $(PLL/HA)_{50}$ (Fig. 3.2). As expected, PLL^{30F} was found to be the most mobile within a PLL^{30} film, followed closely by PLL^{90F} in PLL^{90} films. PLL^{400F} was the least mobile, diffusing through only approximately 16% of the film thickness when added to the top of the PLL^{400} film (i.e., $(PLL/HA)_{50}$-PLL^{F}). These findings suggest that "loosely bound" mobile PLL^{400} is only present in the upper portion of

the film. This stratification has been attributed to the formation of a "non-diffusive zone" below the upper "diffusion zone" during film buildup and restructuring,[134,276,283] and has been demonstrated for high MW PLL in (PLL/HA) multilayer films.[139] We hypothesize that once all of the mobile PLL in the upper portion of PLL^{400} films has been released (within the first 24-hour use of the film), there is a lack of mobile PLL that can be released into the solution at high enough concentrations during subsequent bacterial exposures, limiting the use of PLL^{400} films in inhibiting planktonic bacterial growth to one 24-hour use. In contrast, PLL^{30} and PLL^{90} films have a reservoir of mobile PLL throughout a much larger portion of the film, resulting in longer-term PLL release, allowing repeated uses for effective bacterial growth inhibition.

The number of effective repeated uses of $(PLL/HA)_{50}$ films can also be impacted by film stability over time. Film swelling, ion exchange, mobility of film components,[136,176] and potential interactions with proteins and cells could result in gradual destabilization of the films;[284] and the rate of dissolution has been shown to be influenced by polyelectrolyte MW.[285] Studies have shown that (PLL/HA) films formulated with 40 to 60 kDa PLL and 64 kDa HA dissolved in approximately 16 days in 1× PBS,[286] while (PLL/HA) multilayers built with 30 kDa PLL but higher MW HA (400 kDa) were stable in sodium chloride solution for several months and for at least two weeks in contact with cells and culture media.[287] For PLL^{30} and PLL^{90} films, the number of effectives uses correlated with the film stability in media (Fig. 3.3). PLL^{30} films completely eroded over 5 days, consistent with their loss in efficacy following the fourth to fifth use (corresponding to 4 to 5 days). The thickness of PLL^{90} films began to decrease significantly around day 10, also around the time when some films began to lose efficacy in inhibiting bacterial growth upon repeated exposure. Interestingly, the thickness of PLL^{400} films remained highly stable over time, with no significant change in thickness detected by the second day, which is when PLL^{400} films are no longer able to inhibit planktonic bacterial growth. The lack of efficacy of the higher MW PLL films following the first bacterial exposure is thus not influenced

by loss in film stability, but primarily to lack of PLL^{400} release or diffusion to the film's surface following the first use. Film stability in the presence of HAse was also examined. HAses are commonly produced by different bacteria strains, and believed to be a virulence factor that allows host tissue penetration.[205,288–290] The HAse film degradation was dose dependent and PLL MW dependent. Faster degradation and consequently PLL release resulted with higher HAse concentrations and lower MW PLL films (Fig. 3.4). HAse triggers have been used to develop bacteria responsive antibacterial systems including HA nanocapsules containing polyhexanide,[291] HA-gentamicin conjugates multilayered with montmoillonite,[292] and HA-antimicrobial peptide conjugates layered with chitosan.[293] The films developed here may also respond specifically to the presence of HAse producing virulent bacteria, degrading and releasing higher concentrations of PLL faster than via diffusion alone. In addition to eliminating planktonic bacteria, inhibition of bacterial attachment on surfaces is critical in preventing the formation of bacterial biofilms. These complex surface-attached three-dimensional bacterial structures are very difficult to treat.[37,228] We observed that $(PLL/HA)_{50}$ coatings formulated with all three PLL MWs, reduced *S. aureus* attachment by approximately 60 to 70% compared to uncoated surfaces according to LIVE/DEAD staining. Attached bacteria were unable to grow further on these surfaces when incubated on agar for 18 hours (Fig. 7A-C). The significant reduction in bacterial attachment could be attributed to multiple factors including film hydration and elasticity. The significant hydration of HA-containing multilayers has been shown to repel mammalian cells and proteins important for cell attachment.[294–297] The gel-like characteristics of HA containing coatings provides high elasticity,[297] and multiple studies have shown that substrate elasticity also plays an important role in bacteria attachment. Tuning the stiffness of poly(ethylene glycol) hydrogels[298,299] and poly(dimethylsiloxane) hydrogels[300] has shown that fewer bacteria adhere on softer substrates. Less bacteria were also found to adhere to softer (poly(acrylic acid)/poly(allylamine hydrochloride)) LbL films.[301] The $(PLL/HA)_{50}$ films developed in this work all demonstrated high degrees of swelling (Table 2); the hy-

drophilicity of these surfaces may contribute to reducing bacterial attachment. Surface charge can also influence bacterial attachment. Lower bacteria attachment on negatively charged LbL film surfaces compared to positively charged surfaces has previously been reported,[302] and attributed to repulsion between the negatively charged surface and the negative potential of the bacterial cell wall.[303] However, it has also been noted that positively charged surfaces can attract bacteria,[254,304] followed by a bactericidal effect through interaction with and disruption of the bacterial membrane.[305] This can lead to attached bacteria that are dead on the surface.[302] Indeed, we observed that dead bacteria accounted for approximately 40 to 60% of the total bacteria attached on the $(PLL/HA)_{50}$ coatings compared to 7% on uncoated glass (Fig. 3.11). Thus, HA may contribute to preventing bacterial attachment by influencing $(PLL/HA)_{50}$ film elasticity and potentially charge-based repulsion of bacteria, while PLL at the surface may attract bacteria, subsequently killing it for all PLL MWs examined. The overall effect is a decrease in bacterial attachment on the $(PLL/HA)_{50}$ film coated surfaces and increase in death of surface attached bacteria compared to uncoated surfaces.

Due to the high stability of $(PLL/HA)_{50}$ films formulated with PLL^{400}, we were interested in determining if these films had the ability to inhibit *S. aureus* attachment after being in a hydrated environment for an extended amount of time. We investigated attachment inhibition after preconditioning these coatings in bacteria media or $1\times$ PBS for 24 and 48 hours. At 48 hours, in particular, we had shown that PLL^{400} films were not effective in inhibiting planktonic bacterial growth. We found that these films reduced bacterial attachment when they were preconditioned in $1\times$ PBS but not in media (Fig. 3.7D). During preconditioning in bacteria media, proteins and sugars present in the media (e.g., beef extract, acid hydrosylate of casein, starch) could potentially adhere to the coatings, promoting bacterial attachment and masking attachment-inhibiting properties. This may also contribute to the loss in repeated planktonic bacteria inhibition efficacy for PLL^{400} films observed following 1 day. As a preliminary investigation of the protein adsorption capabilities of these

films, we incubated PLL^{30}, PLL^{90}, and PLL^{400} films with human plasma fibronectin followed by fibronectin antibody staining for fluorescence imaging of the surface; these films were compared with uncoated glass treated in the same way. We observed that PLL^{30} and PLL^{90} films showed significantly lower fluorescence (approximately 20 to 30%) compared to PLL^{400} films, which behaved similarly to uncoated glass (Fig. 3.12). The observed fluorescence on PLL^{400} films may either be due to fibronectin adsorption on the surface promoting antibody binding or direct antibody adsorption on the surface or a combination effect, as both are large proteins. Increased hydrophobicity can promote protein and cell attachment. However, our static water contact angle measurements showed that PLL^{90} and PLL^{400} coatings were similarly more hydrophobic than PLL^{30} coatings (Fig. 3.9), yet PLL^{400} appears more protein adhesive than PLL^{90}. It is likely that the multivalent characteristics of longer polymers (i.e., PLL^{400}), in addition to the increased charge density in PLL^{400} films, suggested by a higher ng PLL per nm film thickness (Table 2), could enhance protein adsorption compared to lower MW PLL. In fact, PLL with approximately 150 to 700 RUs or longer, is widely used to commercially coat tissue culture plates to aid in protein and cell attachment. The cell adhesive nature of certain PLL MWs has enabled its use in a variety of cell culture conditions. Hepatoyctes, fibroblasts, and embryonic stem cells have been successfully co-cultured on PLL and HA patterned surfaces.[241] Keratinocytes have been cultured successfully on $(PLL/HA)_{150.5}$ films.[286] HA containing hydrogels and coated surfaces are non-adhesive due to their high hydrophilicity, but incorporating PLL as the last layer has been shown to aid cells in adhering.[260,286] Despite their uses in cell culture, it is well known that polycations, including PLL, can be toxic to mammalian cells at high MW[306] and concentrations.[175,307,308] Our results indicated that while NIH 3T3 fibroblasts incubated in media exposed to PLL^{30} and PLL^{90} coatings remained similarly viable to untreated controls, cells exposed to media incubated in PLL^{400} coatings over 24 hours lost viability (Fig. 3.8). NIH 3T3 cells treated with non-film incorporated PLL^{400} at concentrations observed to release from $(PLL/HA)_{50}$ films also had significantly lower cell

viability. These results emphasize the importance of measuring the release concentration of polycations incorporated in LbL films.

3.6 Conclusion

We have shown that the commonly studied (PLL/HA) multilayer films are inherently antibacterial without any covalent modifications or addition of other antibacterial materials. Overall, we observed that over a 24 hour period $(PLL/HA)_{50}$ films assembled at all three PLL MWs examined in this work (PLL^{30}, PLL^{90}, and PLL^{400}) completely inhibited the growth of both gram-positive and gram-negative bacteria. However, we demonstrated that PLL MW dictates the number of times $(PLL/HA)_{50}$ coatings can be effectively utilized to inhibit planktonic bacterial growth upon repeated bacterial exposure. MW influences mobility of PLL within these films, limiting the ability of high MW PLL^{400} to diffuse to the film surface-bacteria interface or to be released from the films to kill surrounding bacteria. When PLL mobility within the film is not a limiting factor, the effect of PLL MW on film stability can explain the differences we observed in number of effective repeated uses; films assembled with PLL^{30} disintegrated and lost efficacy faster than those with higher MW PLL^{90}. All $(PLL/HA)_{50}$ films were capable of significantly reducing bacterial attachment compared to uncoated surfaces, critical in preventing biofilm formation. We found that PLL^{400} films, even though highly hydrated, promoted protein adhesion, likely due to PLL multivalency and cationic charge, which may contribute to its lack of repeated antibacterial efficacy. Additionally, PLL^{400} released from $(PLL/HA)_{50}$ films within 24 hours was cytotoxic to fibroblasts while PLL^{30} and PLL^{90} released from their respective films did not reduce cell viability. Therefore, there is a balance between polymer mobility, polymer biocompatibility, coating stability, and other surface interaction properties that dictate (PLL/HA) film antibacterial and anti-attachment properties and potential clinical use. The versatility of polymers and LbL self-assembly allows the design and formulation of an-

tibacterial coatings for varying needs. Potentially, films built with layers of different MW PLL could provide advantages of both high and low MW PLL; high MW PLL could provide a more stable coating, while lower MW PLL could provide a larger reservoir of mobile PLL that can diffuse out of the film to kill planktonic bacteria and interact with bacteria at the surface to promote contact killing.

3.7 Acknowledgments

The authors acknowledge financial support from the Office of Naval Research (N00014-14-1-0798) and Brown University. D.A. acknowledges support from a National Science Foundation Graduate Research Fellowship under Grant No. 1644760. We thank Brown University undergraduate researchers, Victor Paul Addonizio, Selena Tully, Sorathan Munckong, and Soobin Wang for their assistance. We acknowledge the use of the Microelectronics Core Facility for ellipsometry and profilometry and the Leduc Bioimaging Facility at Brown University for CLSM studies.

3.8 Supporting Information

The supporting information consists of a description of the experimental procedures for measuring film wettability and testing fibronectin adsorptions on film coated surfaces. Results from contact angle measurements are included. Supporting information also includes figures reporting further characterization of $(PLL/HA)_{50}$ films, which include water contact angle measurements, fibronectin adhesion, and live and dead bacteria attachment. Also included is a figure showing PLL concentration measured using both TNBSA and microdilution assay as a comparison of the two methods.

3.8.1 Methods

$(PLL/HA)_{50}$ Film Wettability

Film wettability was examined using a contact angle goniometer and DROPimage CA software (ramé-hart) to measure the static water contact angle on initially dry $(PLL/HA)_{50}$ coated glass using the sessile drop method. Images were taken immediately after the droplet was deposited onto the substrates to avoid film water absorption effects. At least four individual 2 μL droplets of water were imaged on a given film.

Examining Protein Adsorption on $(PLL/HA)_{50}$ Films

$(PLL/HA)_{50}$ coated glass and uncoated glass slides were incubated with 25 μg/mL fibronectin in 1$\times$ PBS, pH 7.4 for 2 hours. They were rinsed twice with 1$\times$ PBS before they were blocked with 10% v/v NGS (in 1$\times$ PBS) for 20 minutes at 25°C, rinsed in 1$\times$ PBS, and stained with rabbit anti-fibronectin antibody (1:100 in 1% NGS) overnight at 4°C. Substrates were then incubated with Alexa Fluor 594 goat anti-rabbit IgG secondary antibody (1:100 in 1$\times$ PBS) for 1.5 hours at 25°C, rinsed in 1$\times$ PBS, and imaged with a Nikon TiE inverted fluorescence microscope using a Plan Fluor 10$\times$/0.30 objective and a 545/30 excitation and 620/60 emission tetramethylrhodamine (TRITC) filter. Ten images were taken per substrate, with three repeats per condition. Mean fluorescence intensity per field of view was calculated using CellProfiler^{TM}.

3.8.2 Results

$(PLL/HA)_{50}$ Film Wettability

Static water contact angles for uncoated glass, and $(PLL/HA)_{50}$ with PLL^{30}, PLL^{90}, and PLL^{400} were found to be $34.9 \pm 2.9°$, $75.4 \pm 10.7°$, $106.3 \pm 6.8°$, and $97.6 \pm 3.8°$, respectively, as shown in Figure 3.9. These contact angle measurements were taken immediately following droplet contact with the surface due to the high absorption capability of the films. Overall, all three film architectures were found to be more hydrophobic than plain glass. PLL^{90} and PLL^{400} films had comparable water contact angles but were significantly more hydrophobic than PLL^{30} films.

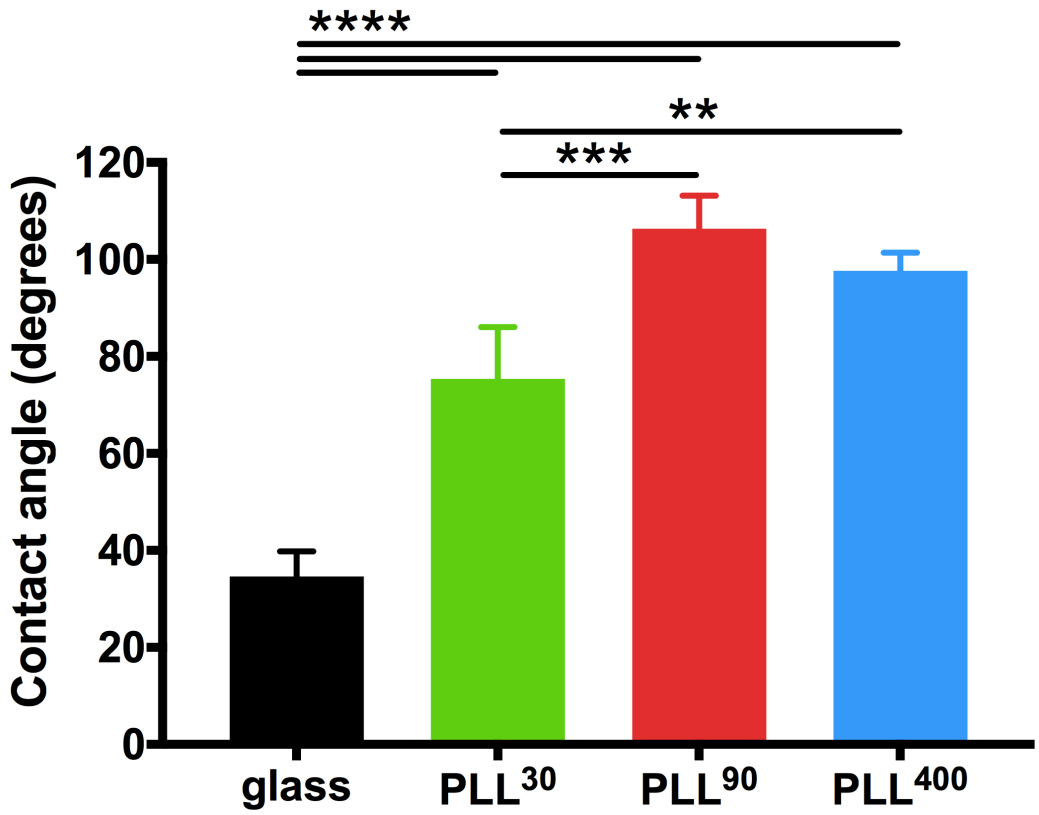

Figure 3.9: Static water contact angle measurements on uncoated glass and glass coated with $(PLL/HA)_{50}$ films assembled with PLL^{30}, PLL^{90}, and PLL^{400}. Results are shown as mean $\pm$ standard deviation. Statistical significance was examined using one-way ANOVA and Tukey's post-hoc analysis; ** $p < 0.01$; *** $p < 0.001$; **** $p < 0.0001$; n = 3.

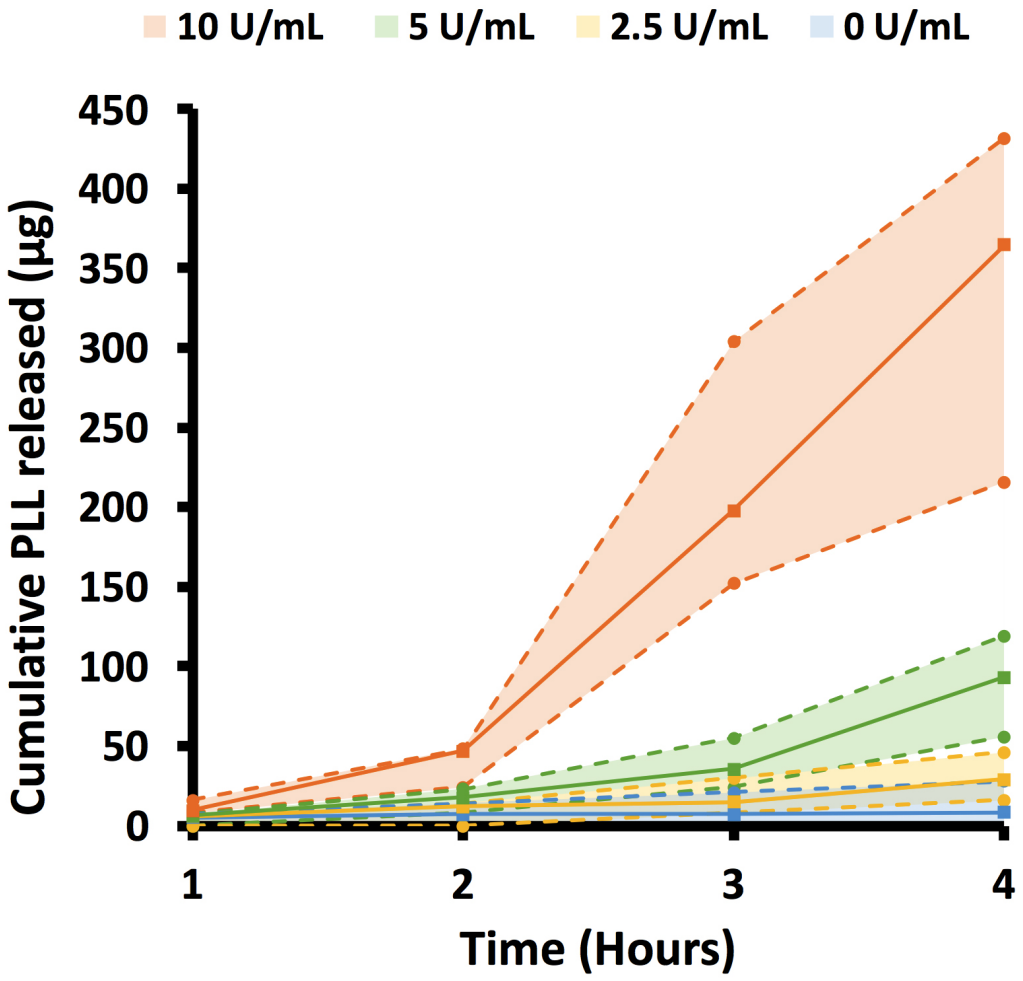

Figure 3.10: Comparison of PLL concentration in solutions in which $(PLL^{90}/HA)_{50}$ films were incubated with HAse (0, 2.5, 5, 10 U/mL) measured using TNBSA (data connected by solid lines) or back calculated using a microdilution assay (concentration range is the shaded region between data points connected with dotted lines). Experiments were conducted with 3 repeats.

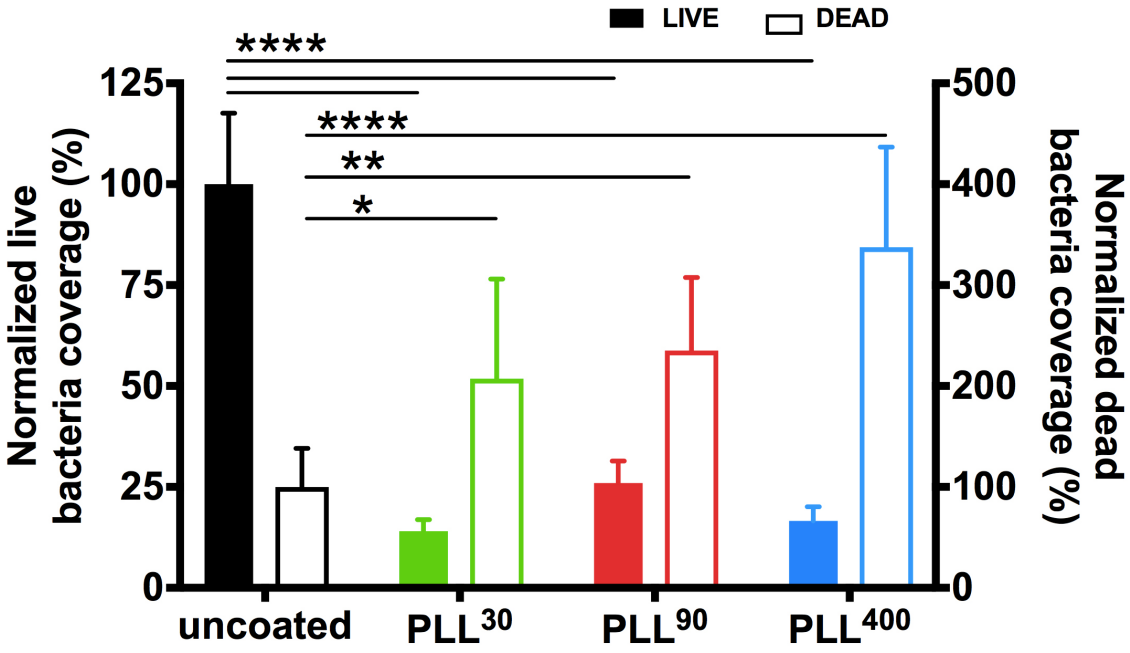

Figure 3.11: Percent area of $(PLL/HA)_{50}$ coated glass substrates covered with live and dead *S. aureus* normalized to percent area of uncoated glass with live and dead bacteria attached. Results are shown as mean ± standard deviation. Statistical significance was examined using one-way ANOVA and Tukey's post-hoc analysis; * $p < 0.05$; ** $p < 0.01$; **** $p < 0.0001$; n = 6 for film coated glass, n = 15 for uncoated glass.

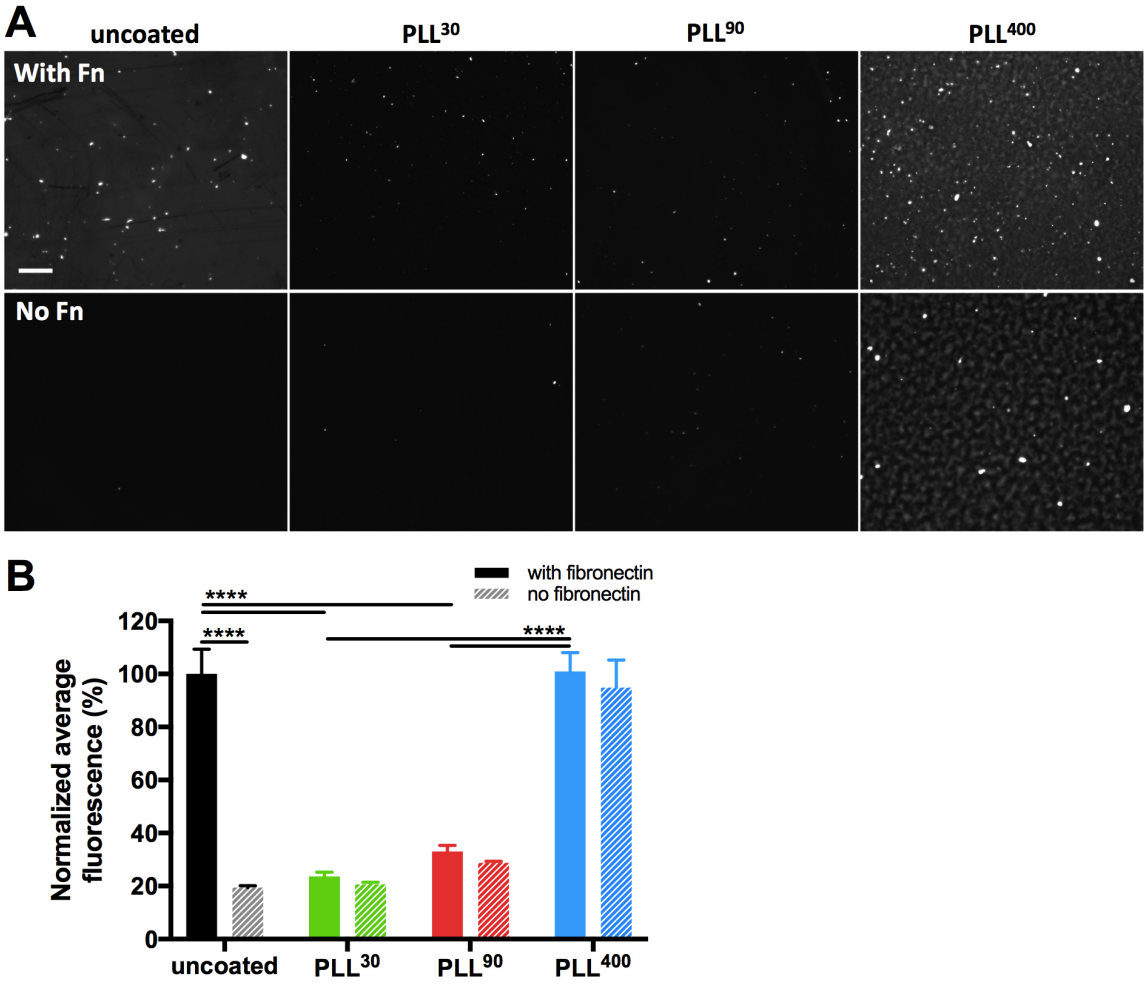

Figure 3.12: Fibronectin adsorption on uncoated and $(PLL/HA)_{50}$ coated glass. A) Representative fluorescence images of uncoated glass or glass coated with $(PLL/HA)_{50}$ films built with PLL^{30}, PLL^{90}, and PLL^{400} stained for fibronectin. Substrates were incubated with (top row) or without (bottom row) fibronectin in $1\times$ PBS for two hours before staining with anti-fibronectin primary antibodies and fluorescent secondary antibodies. Scale bar represents 200 μm. B) Average fluorescence per field of view is normalized to that of uncoated glass incubated with fibronectin. Results are shown as mean $\pm$ standard deviation. Statistical significance was examined among samples incubated with fibronectin and between the same type of sample with or without fibronectin incubation using one-way ANOVA and Tukey's post-hoc analysis; **** $p < 0.0001$; n = 3.

Chapter 4

A Chromogenic β-Lactamase Substrate for Diagnostic Biomaterials

---

Chapter 4 is a manuscript prepared for submission for peer review:

Alkekhia D.,* Safford H.,* Shukla S., Shukla A., "A chromogenic β-Lactamase substrate for diagnostic biomaterials", Editing manuscript, 2020.
* Authors contributed equally

4.1 Abstract

We report the synthesis of a chromogenic βL substrate that can be conjugated to polymers for the development of biomaterials with facile, visual βL detection functionality. Detection of βLs, bacterial enzymes which inactivate commonly used antibiotics (a major cause of antibiotic resistance), is important for promoting proper treatment of the infection. The βL substrate has a chromogenic leaving group on one end, and a functional group on the other allowing for conjugation to a variety of polymers. The substrate exhibited a color change from clear to yellow, even after its conjugation to polymers, in the presence of βLs as well as βL-producing bacteria. We formulated hydrogels, which incorporate the substrate covalently attached to the polymer backbone, that changed color in the presence of βL. These results demonstrate the potential of our substrate and our approach for developing diagnostic biomaterial, such as hydrogels for wound treatment, for point-of-care detection of βL producing bacteria.

4.2 Introduction

Wounds are highly prone to infection by bacteria, occurring in 10% of patients and costing approximately $8 billion in the United States alone.[309] These infections are further complicated by the prevalence of antibiotic resistant microbes, which according to a recent 2019 report by the Centers for Disease Control and Prevention (CDC), cause over 2.8 million illnesses and 35,000 deaths in the US, annually.[3] To effectively treat and eradicate wound infections, there is a critical need for clear and facile detection of the presence of antibiotic resistant bacteria. A major cause of resistance are βLs, enzymes produced by bacteria that cleave the β-lactam ring present in many common antibiotics including penicillins and cephalosporins, rendering these therapeutics ineffective.[18] Detecting the presence of βL-producing bacteria can aid in proper antibacterial agent choice and in containing pa-

tient transmission of resistant bacteria.

Most conventional detection methods, such as cultures and polymerase chain reaction (PCR), although potentially highly accurate are time consuming and are unable to provide a facile, visual infection indication without specialized instruments and trained personnel. There have been efforts in developing point-of-care testing with a visual indication of bacterial infection, such as paper-strips that change color due to electrostatic interaction with bacteria[56] and wound dressings that change color in the presence of lipase-producing bacteria[310]. Here, we focus on detecting βLs due to their specificity to bacteria and and in particular antibiotic resistant bacteria. Non-colorimetric βL hydrolysis indicators include luminescent ruthinium (i) probes,[311] fluorescent probes,[58,312] and fluorescence resonance energy transfer (FRET)-based probes[63]. However, these indicators require the use of external equipment. Alternatively, chromogenic βL substrates have been utilized for a visual color change in solution, on agar, or on discs, such as the commercially available CENTA[313,314], PADAC[315,316], and nitrocefin[18].

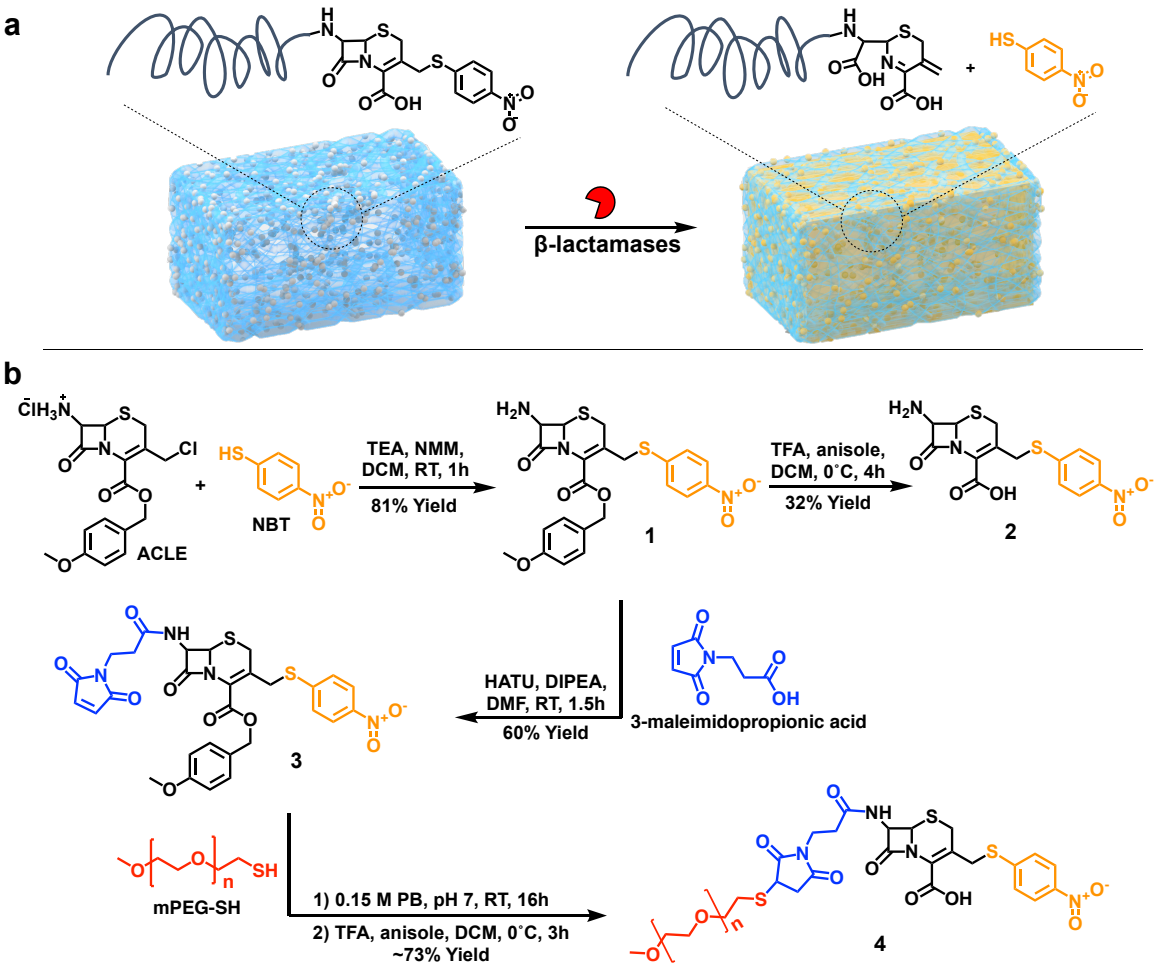

Scheme 4.1: a) Illustration of approach to develop βL-detecting hydrogels. b) Synthesis scheme of protected substrate **1**, its deprotection (**2**), or its functionalization with maleimide (**3**), followed by its conjugation to a polymer (e.g. PEG) (**4**) *via* thiol-maleimide click chemistry.

[a]ACLE: 7-amino-3-chloromethyl-3-cephem-4-carboxylic acid p-methoxybenzyl ester, NBT: 4-nitrobenzenethiol, TEA: triethylamine, NMM: 4-methylmorpholine, DCM: dichloromethane, TFA: trifluoroacetic acid, HATU: 1-[Bis(dimethylamino)methylene]-1H-1,2,3-triazolo[4,5-b]pyridinium 3-oxid hexafluorophosphate, DIPEA: N,N-diisopropylethylamine, DMF: dimethylformamide, mPEG-SH: methoxy-poly(ethylene glycol)-thiol, PB: sodium phosphate buffer

Our aim was to synthesize a chromogenic βL substrate which can be conjugated to polymers, providing a platform for a range of biomaterials (i.e., nanoparticles, hydrogels,

etc.) that incorporate a detection functionality (Scheme 4.1a). These biomaterials could potentially be placed on wounds to provide a color change *in situ* if an infection by βL-producing bacteria develops, promoting appropriate treatment. Conjugation to a polymer allows the formation of different types of biomaterials, even in combination with existing wound treatments, for developing multifunctional therapeutics with convenient application to injury sites. The conjugate could also sequester the indicator compound within the biomaterial, preventing its release before it is needed. Inspired by the structure of chromogenic βL substrate, CENTA[313,314], our approach was to develop a substrate with a chromophore leaving group at one end, and an easily modifiable group at another end, that can be conjugated to polymers while the carboxylic group βL recognition site remains protected during the reactions. Here, we report the development of a βL substrate that we have successfully conjugated to polymers and used to form hydrogels that changed color in response to βL and βL-producing bacteria.

4.3 Results and Discussion

To synthesize the protected β-lactam compound (**1**), we modified a cephalosporin derivative, 7-amino-3-chloromethyl-3-cephem-4-carboxylic acid p-methoxybenzyl ester (ACLE), with a chromophore, 4-nitrobenzenethiol (NBT), at the 3'-position (Scheme 4.1b). The primary amine at the 7'-position will be used to conjugate the substrate to polymers. The p-methoxybenzyl protecting group prevents modification of the cephalosporin's carboxylic group, which is an enzyme-substrate recognition site for some βLs.[317] Additionally, unlike CENTA's chromophore which has a carboxylic group susceptible to possible modification, here the chromophore is unmodified during chemical reactions.

Prior to conjugation to polymers, **1** was deprotected to yield substrate **2** (Scheme 4.1) to characterize its colorimetric and enzyme kinetic response in the presence of βLs. **2** was

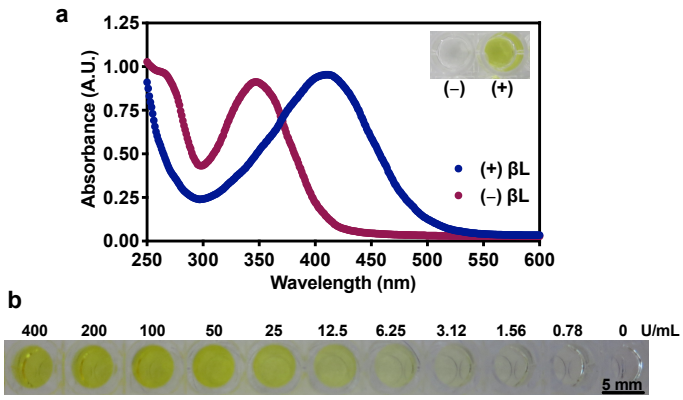

Figure 4.1: a) Absorbance spectra of substrate **2** incubated in 10% DMSO in 0.1 M sodium phosphate buffer (PB) with (+) or without (-) 200 U/mL βL-BC for 90 minutes at 37°C. Images of those solutions are in the inset. b) Images of solutions of **2** incubated with different concentrations of βL-BC (U/mL) (with 10% DMSO in PB) in a 96-well plate for 45 minutes at 37°C.

tested with βLs produced by *Bacillus cereus* (βL-BC), *Pseudomonas aeruginosa* (βL-PA), and *Enterobacter cloacae* (βL-EC) (penicillinases and cephalosphorinases that have different specificity towards β-lactams (EC 3.5.2.6)). These enzymes were chosen because of the prevalence of the bacteria that produce them in a variety of infections, including wounds.[318–321] Substrate **2** successfully changed color from clear to yellow when mixed with any of the three enzymes (insets in Figures 4.1a and S9). The βL responses were also observed on the ultraviolet–visible (UV-vis) spectra; as βLs cleave the β-lactam ring, its characteristic absorbance at 260 nm decreases, and the chromogenic leaving group is expelled (as suggested in Scheme 4.1a), causing a clear red shift in the wavelength of maximum absorbance (λ_{max}) from 345 to 410 nm as seen in Figures 4.1a for βL-BC and S9 for βL-PA and βL-EC. Furthermore, as seen in Figures 4.1b and S10a, respectively, the substrate color change and the shifts in the spectral scan are βL concentration dependant. The visual limit of detection of the concentrations we have tested seemed to be 3.12 units/mL (U/mL) for βL-BC. The absorbance at 410 nm was plotted in relation to βL concentration (Figure S10b), and the limit of detection based on absorbance signal was calculated to be 4.6 U/mL, which is similar to the visual limit.

Enzyme	Substrate	K_M (μM)	k_{cat} (s^{-1})	k_{cat}/K_M ($\mu M^{-1} s^{-1}$)
βL from *B. cereus*	Substrate **2**	866.80 ± 141.40	4.99 ± 0.57	0.0058 ± 0.0011
	CENTA	345.30 ± 36.08	16.50 ± 0.88	0.048 ± 0.0056
	Nitrocefin	450.70 ± 69.55	49.67 ± 4.35	0.11 ± 0.012
βL from *P. aeruginosa*	Substrate **2**	58.01 ± 9.54	0.66 ± 0.02	0.011 ± 0.002
	CENTA	12.63 ± 6.84	0.42 ± 0.02	0.033 ± 0.018
	Nitrocefin	178.80 ± 32.71	5.14 ± 0.37	0.029 ± 0.0056
βL from *E. cloacae*	Substrate **2**	n/a	n/a	n/a
	CENTA	68.88 ± 11.83	1.48 ± 0.062	0.021 ± 0.0038
	Nitrocefin	315.20 ± 26.75	9.04 ± 0.38	0.029 ± 0.0027

[a] n/a; not applicable

Table 4.1: Kinetic parameters of compound **2**, CENTA, and nitrocefin hydrolysis by three different βLs

Substrate-enzyme relationships were further characterized using Michaelis-Menten kinetics analysis. As shown in Table 4.1, parameters were determined for substrate **2**, as well as commercially available chromogenic substrates CENTA and nitrocefin as a comparison, with three different βLs. The measurements were conducted in 10% DMSO in PB (due to low aqueous solubility of **2** and nitrocefin), which decreased the efficiency of the enzymes compared to measurements in PB only solutions (not shown), but the values obtained for k_{cat}/K_M were within a similar range of values reported for CENTA, nitrocefin, and other substrates with βLs.[58,313] The k_{cat}/K_M values for substrate **2** were slightly lower compared to those of CENTA and nitrocefin for βL-BC and βL-PA, but with βL-EC, it was much lower, resulting mainly from a very low k_{cat}, indicating a low turnover number (thus reported as not applicable; n/a). This difference could arise from differences in the classes of the βLs tested and their substrate specificity. Although **2** required higher concentrations of βL-EC or longer incubation time compared to CENTA or nitrocefin, or compared to incubation with the two other βLs, it did still change color from clear to yellow.

To investigate potential antibacterial effects of the substrate, which could limit its usefulness in detecting such bacteria, minimum inhibitory concentrations (MIC) of **2** were

measured against several bacteria species. Of the bacteria tested (*Staphylococcus aureus*, methicillin-resistant *S. aureus* (MRSA), *Escherichia coli*, *P. aeruginosa*, *E. cloacae*, and *B. cereus*; Table S1), compound **2** was only antibacterial at the concentrations tested (up to 128 μg/mL) against *S. aureus* 25923, which is a non-βL producing species[322,323], and *S. aureus* 29213, which produces low amounts of βLs[323,324], at a minimum inhibitory concentration of 8 μg/mL. These effects were comparable to those observed for other chromogenic βL substrates, PADAC, CENTA, and nitrocefin, which were not antibacterial against gram-negative species but had some activity against *S. aureus* and some *Streptococci*.[314,315] **2** might have not exhibited an effect on the gram-positive MRSA and *B. cereus* at the tested concentrations due to their βL production.

After successfully synthesizing and characterizing substrate **2** and its response to βLs, we wanted to conjugate the βL substrate to a commonly used polymer to form diagnostic hydrogels. Poly(ethylene glycol) (PEG) was chosen as a model polymer because of its extensive use in biomaterials such as hydrogels, nanoparticles, and coatings for various biomedical applications given its biocompatiblity and tunability.[325,326] For facile conjugation of the βL substrate to polymers, we first functionalized the substrate with a maleimide group. This allows for polymer conjugation *via* modular click-chemistry under mild conditions such as maleimide-thiol Michael-type addition[92] or a furan-maleimide Diels-Alder reaction[327]. 3-maleimidopropionic acid was conjugated to **1** through amidation *via* its 7'-position primary amine yielding compound **3** (Scheme 4.1b). ^{1}H-NMR indicated the disappearance of the carboxylate proton on 3-maleimidopropionic acid (12.36 ppm), along with the appearance of the proton peaks of the newly formed amide (9.07 - 8.95 ppm) in the spectra of **3** (Figure S3). Next, we conjugated **3** to a linear, short PEG chain to investigate the effects of PEG addition on color change and enzyme kinetics. We conjugated **3** to methoxy-PEG-thiol (mPEG-SH) (1.7 kDa) *via* Michael-type addition forming **4** (Scheme 4.1b). The conjugation was confirmed using different characterization techniques. ^{1}H-NMR showed the disappearance of the maleimide protons at 7.00 ppm that are present in

compound **3** and the formation of a new signal at 4.02 ppm in compound **4**, indicating formation of the thiol-maleimide adduct (Figure S5); the other protons on the adduct would likely appear in the region of 2.4 - 3.2 ppm,[328] which in our case is obscured by the PEG repeat unit protons. Matrix-assisted laser desorption ionization-time of flight (MALDI-TOF) mass spectrometry demonstrated a shift in the molecular weight distribution of the conjugate compared to unmodified mPEG-SH (suggesting an average MW increase of $\sim$400 Da), indicating successful conjugation of **3** to PEG (Figure S4c). Conjugate **4** and unmodified mPEG-SH were also compared using size exclusion chromatography (SEC), where both eluted at similar times (as indicated by refractive index detector; not shown), however, while mPEG-SH has no absorbance signal, conjugate **4** had an absorbance at 345 nm, the substrate's characteristic λ_{max} (Figure S7), also indicating successful conjugation. In the presence of βL-BC, conjugate **4** changed color from clear to a bright yellow and the spectral scan showed a decrease in the peak at 260 nm and the expected red shift in λ_{max} (Figure S8). *Via* SEC, a decrease in the 345 nm absorbance signal where the conjugate eluted was evident after incubation with βL (Figure S7).

Furthermore, upon conjugation to the hydrophilic PEG, aqueous solubility of the substrate was improved, promoting its use in clinical situations, and allowing us to test the ability of the βL substrate-polymer conjugate to detect βL-producing bacteria (without DMSO, and at higher concentrations of the substrate). We incubated conjugate **4** at various concentrations with βL producing bacteria strains (*P. aeruginosa*[63], *E. cloacae*[63,329], and *B. cereus*[311]), as well as a non-pathogenic bacteria used as a non-βL producing bacteria control (*E. coli* DH5-α[311,329,330]). As shown in Figure 4.2a, the conjugate changes color when incubated with βL-producing bacteria, even at low concentrations of the conjugate (as low as 280 μg/mL; which is equivalent to approximately 47 μg/mL of **2**), while *E. coli* DH5-α did not cause a color change during the overnight incubation. At the highest concentration of conjugate **4** (4.5 mg/mL), the *B. cereus* solution appears clear as apposed to cloudy, suggesting a potential antibacterial concentration of conjugate **4** leading to bacteria

growth inhibition prior to sufficient βL production to cause a color change. This antibacterial effect against *B. cereus* was detected at a high concentration of the conjugate, where the equivalent concentration of compound **2**, approximately 750 μg/mL, was higher than the concentrations of **2** tested in the microdilution assay (up to 128 μg/mL; Table S1).

Having confirmed the responsiveness of the βL substrate-PEG conjugate to bacteria, we formulated a PEG hydrogel with substrate **3** covalently attached to the backbone, as a preliminary demonstration of a diagnostic biomaterial. As represented in Scheme S1, **3** was mixed with 4-arm-PEG-thiol to decorate on average one of the polymer's arms with the βL substrate, and then subsequently, the crosslinker maleimide-PEG-maleimide was added, leading to hydrogel formation. Control non-βL-responsive hydrogels were formed similarly but without adding **3**. After deprotection of the methoxybenzyl group, the hydrogels were extensively rinsed to remove any unbound **3** or organic solvents, and swelled in $1\times$ PBS. The increased swelling apparent in β-lactam-PEG hydrogels compared to control PEG hydrogels likely resulted from increased network defects due to incomplete gelation at sites where **3** was conjugated[331]. When both types of hydrogels were exposed to $1\times$ PBS with or without βL-BC, only the responsive PEG hydrogels incubated in βL changed color from clear to yellow, as seen in Figure 4.2b, indicating selective color change due to β-lactam compound hydrolysis by βLs.

To demonstrate the feasibility to tether the substrate to a range of polymers with varying molecular weights and properties, we tested the conjugation of the βL substrate to a naturally-occurring long, bulky polymer, gellan gum, which has been utilized in developing physically[267,332] and covalently[333,334] crosslinked hydrogels for biomedical applications. Preliminary positive results indicate that **3** was conjugated to the backbone of furan modified gellan *via* Diels-Alder click chemistry[327,335], and ionically crosslinked hydrogels formulated from the conjugate turned yellow in the presence of βL (not shown), indicating the versatility of our approach.

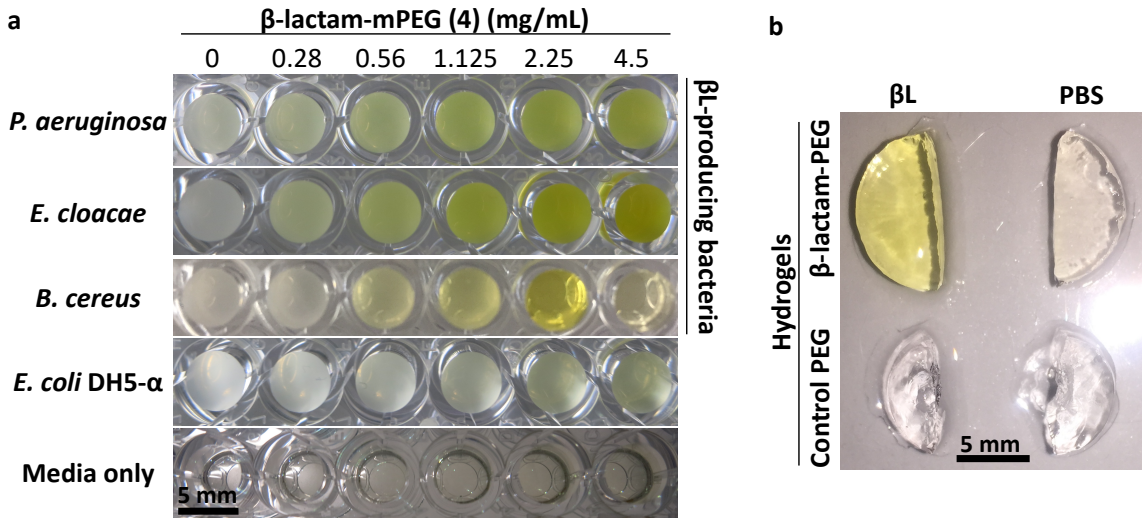

Figure 4.2: a) Images of solutions of various concentrations of conjugate **4** after overnight incubation with three βL-producing bacteria (*P. aeruginosa*, *E. cloacae*, *B. cereus*), one non-βL-producing (*E. coli*), or in broth only in 96-well plates. b) Images of 20% w/v β-lactam-PEG hydrogels and control PEG hydrogels after 15 minute-incubation in 1$\times$ PBS with (+) or without (-) 400 U/mL βL-BC.

In summary, we have developed a chromogenic βL substrate that can be covalently attached to polymers and changes color specifically in the presence of βLs and βL-producing bacteria. Kinetic analysis of the substrate demonstrated its response to βLs from different bacteria species. Hydrogels that we developed with the newly synthesized βL substrate tethered to the polymeric backbone demonstrated a color change from clear to bright yellow in the presence of βL. To our knowledge, this is the first time that a βL substrate has been conjugated to a polymer for direct and facile point-of-care colorimetric detection of infections by βL-producing bacteria. These conjugates could potentially be incorporated into multifunctional biomaterials for the enhanced prevention, detection, and treatment of bacterial infections.

4.4 Acknowledgement

This work was supported by the Office of Naval Research [grant number N00014-17-1-2120]. The authors thank Dr. Tun-Li Shen at the Mass Spectrometery Facility and Dr. Russell Hopson at the NMR Facility at Brown University for their technical support.

4.5 Supporting Information

4.5.1 Materials

7-amino-3-chloromethyl-3-cephem-4-carboxylic acid p-methoxybenzyl ester hydrochloride (ACLE) was purchased from AK Scientific (Union City, CA). 4-nitrobenzenethiol (NBT) and 3-maleimidopropionic acid were purchased from TCI Chemicals (Tokyo, Japan). Nitrocefin was purchased from P212121, LLC (Boston, MA). Deuterated dimethyl sulfoxide (DMSO-d6) and deuterium oxide were obtained from Cambridge Isotope Laboratories (Andover, MA). 2-(N-morpholino) ethanesulfonic acid (MES) buffer, triethylamine (TEA), 4-methylmorpholine (MMP), anhydrous dichloromethane (DCM), anhydrous dimethylformamide (DMF), hexanes, ethyl acetate, thin layer chromatography (TLC) Silica Gel 60 on glass plates, di-sodium hydrogen phosphate anyhydrous, sodium dihydrogen phosphate anhydrous, CENTA, dimethyl sulfoxide (DMSO), trifluoroacetic acid (TFA), anisole, βL from *B. cereus* (βL-BC; cat.# P0389, 28 kDa, 2817.8 U/mg protein, 4.72% protein), βL from *P. aeruginosa* (βL-PA; cat.# L6170, 30 kDa, 1080 U/mg protein, 1% protein), βL from *E. cloacae* (βL-EC; cat.# P4524, 20-26 kDa, 0.37 U/mg protein, 56.45% protein), phosphate buffered saline (PBS), sodium nitrate, cation-adjusted Muller-Hinton broth (CMHB), α-Cyano-4-hydroxycinnamic acid, 1-[Bis(dimethylamino)methylene]-1H-1,2,3-triazolo[4,5-b]pyridinium 3-oxid hexafluorophosphate (HATU), N,N-disopropylethylamine (DIPEA),

and hydrochloric acid (HCl) were acquired from Millipore Sigma (St. Louis, MO). Methanol, silica gel, tryptic soy broth (TSB), and SYLGARD 184 silicone elastomer kit were purchased from Thermo Fisher Scientific (Waltham, MA). Methoxy-poly(ethylene glycol)-thiol (mPEG-thiol) (average MW 1.7 kDa) was purchased from Laysan Bio, Inc (Arab, AL). Nitrocefin disks were obtained from Becton Dickinson (Franklin Lakes, NJ). *Staphylococcus aureus* strains 25923 and 29213, methicillin-resistant *S. aureus* (BAA-1707) (MRSA), *Escherichia coli* 25922, and *Enterobacter cloacae* 13047 were purchased from ATCC (Manassas, VA). *Pseudomonas aeruginosa* PA01 was generously donated by Walter Reed Army Institute of Research (Silver Spring, MD). textitE. coli DH5-α was purchase from Life Technologies (Carlsbad, CA). Ultra-high-purity nitrogen gas (99.999%; under N_2) was obtained from Corp Brothers, Inc. (Providence, RI). Repligen Biotech cellulose ester 500-1000 Da molecular weight cut-off (MWCO) dialysis tubing was obtained from Spectrum Labs Inc. (Rancho Dominguez, CA). Ultrapure deionized water (18.2 MΩ·cm, Millipore Sigma, Billerica, MA) was utilized in all experiments. Room temperature (RT) refereed to in this article is approximately 23°C.

4.5.2 Instrumentation

^{1}H-NMR was recorded on a Bruker DRX Avance 400 MHz spectrometer. ^{13}C-NMR and 2D-NMR were acquired on a Bruker Ascend 600 MHz spectrometer. Data for ^{1}H and ^{13}C NMR are reported with chemical shifts stated in δ in units of parts per million (ppm) relative to DMSO-d_6 (2.50 ppm). High resolution mass spectrometry (HRMS) electrospray ionization (ESI) was conducted on an Agilent 6530 liquid chromatography (LC)-MS. Matrix-assisted laser desorption ionization time-of-flight spectrometry (MALDI-TOF) was conducted using an AXIMA Performance equipped with a 50 Hz nitrogen laser. The matrix utilized was α-Cyano-4-hydroxycinnamic acid. Size exclusion chromatography (SEC) was performed on a 1260 Infinity II liquid chromatography system (Agilent Technologies,

Santa Clara, CA) equipped with multiple wavelength UV-Vis and refractive index detectors (Agilent Technologies, Santa Clara, CA). An Agilent AdvanceBio SEC 130 Å pore size (7.8 $\times$ 300 mm; 2.7 μm particle size) column was used under isocratic flow conditions with 100 mM sodium nitrate + 0.1% (v/v) trifluoroacetic acid (pH 6.5) as the mobile phase and at a flow rate of 0.35 mL/min. Ultraviolet-visible spectroscopy (UV-vis) spectral scans and kinetic experiments were performed using a BioTek® Cytation 3 microplate reader (Winooski, VT), unless specified otherwise, using 96-well UV-capable plates (Corning Inc., Corning, NY).

4.5.3 Substrate Synthesis and Characterization

Synthesis of 1

Substrate **1** was synthesized following a method modified from literature for a similar compound[80]. ACLE (600 mg, 1.48 mmol) was dissolved in anhydrous DCM (20 mL) and stirred at RT under N_2. TEA (390 μL, 2.8 mmol) was slowly added in three portions over a 20 minute time period to the ACLE mixture. NMM (200 μL, 1.8 mmol) and NBT (370 mg, 2.4 mmol) were added sequentially thereafter. The reaction was stirred at RT and monitored by TLC (30% hexanes/70% ethyl acetate). After 1 hour, DCM was evaporated using a Buchï rotary evaporator. The conjugate was purified using flash column chromatography (silica gel, 70% to 100% gradient ethyl acetate in hexanes as eluent) to yield substrate **1** (586 mg, 1.20 mmol, 81% yield, Δ_2 isomer $\sim$20%). HRMS-ESI: Calculated for $C_{22}H_{21}N_3O_6S_2^+$ $[M+H]^+$: 488.09; Found: 488.0948. ^{1}H-NMR (400 MHz, DMSO-d_6) δ (ppm): 8.08 - 8.04 (dd, J_1 = 2.0 Hz, J_1 = 6.2 Hz, 2H), 7.47 - 7.43 (dd, J_1 = 2.0 Hz, J_2 = 6.2 Hz, 2H), 7.34 - 7.26 (dd, J_1 = 2.0 Hz, J_2 = 5.8 Hz, 2H), 6.91 - 6.82 (dd, J_1 = 2.0 Hz, J_2 = 5.8 Hz, 2H), 5.20 - 5.07 (dd, J_1 = 11.8 Hz, J_2 = 28.9 Hz, 1H), 5.01 - 4.93 (dd, J_1 = 4.0, 5.0 Hz, J_2 = 19.4 Hz, 1H) 4.29 – 4.03 (dd, J_1 = 12.9 Hz, J_2 = 77.0 Hz, 2H) 3.75 - 3.65 (m,

4H) 3.53 - 3.45 (d, *J*= 17.9, 1H)

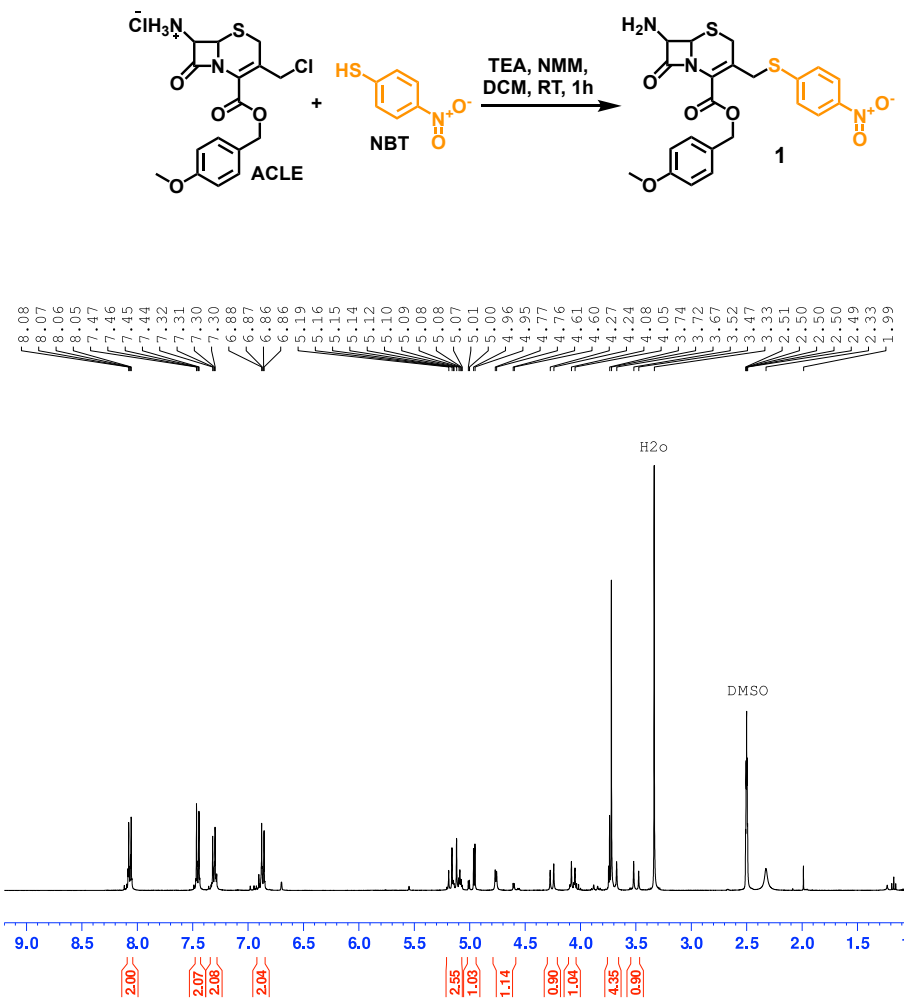

Figure 4.3: ^{1}H-NMR spectrum of compound **1** (DMSO-d_6, 400 MHz).

Synthesis of 2

Substrate **1** (70 mg, 0.14 mol) was deprotected in a solution of TFA:anisole:DCM (49 mL total) at a 1:1:5 volumetric ratio under N_2 on ice for 4 hours. DCM and TFA were evaporated under reduced pressure and anisole was removed by nitrogen bubbling. The deprotected conjugate was dissolved in DMSO at a concentration of approximately 8 mg/mL and diluted 1:10 in methanol. The suspension was left at 4°C overnight to precipitate, then

centrifuged at 5,000 rpm for 30 minutes at 4°C. The supernatant was removed and the pellet redissolved in DMSO to repeat the rinsing process once more. The final pellet was frozen and lyophilized (17 mg, 0.046 mmol, 32% yield, Δ_2 isomer ~10%). HRMS-ESI: Calculated for $C_{14}H_{13}N_3O_5S_2^+$ $[M+H]^+$: 368.03; Found: 368.0366 ^{1}H-NMR (400 MHz, DMSO-d_6) δ (ppm): 8.15 - 8.10 (dd, J_1 = 2.0 Hz, J_2 = 6.2 Hz, 2H), 7.58 - 7.53 (dd, J_1 = 2.0 Hz, J_2 = 6.2 Hz, 2H), 4.96 (d, J_1 = 5.0 Hz, 1H), 4.75 (d, J_1 = 5.0 Hz, 1H), 4.32 - 4.11 (dd, J_1 = 12.8 Hz, J_2 = 58.7 Hz, 2H), 3.72 - 3.44 (dd, J_1 = 17.8 Hz, J_2 = 85.3 Hz, 2H).

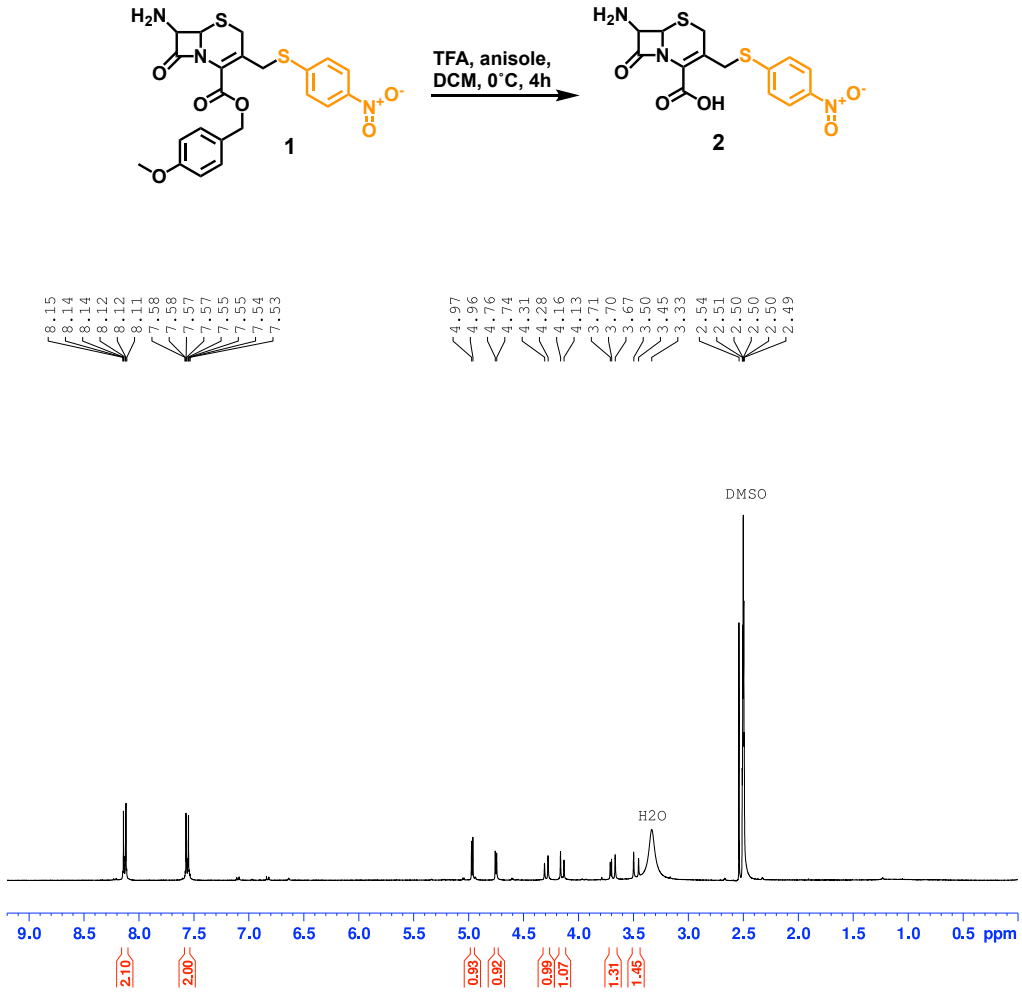

Figure 4.4: ^{1}H-NMR spectrum of compound **2** (DMSO-d_6, 400 MHz).

Synthesis of 3

Substrate **1** (151 mg, 0.31 mmol), 3-maleimidopropionic acid (344 mg, 1.24 mmol) and HATU (567 mg, 1.49 mmol) were dissolved in anhydrous DMF (4 mL). The mixture was stirred for 15 minutes under N_2 at RT before adding DIPEA (370 μL, 2.18 mmol), then the reaction was allowed to proceed for another 75 minutes and was monitored by TLC (20% ethyl acetate/80% hexanes). The crude reaction was transferred to a separatory funnel and partitioned between DCM and 0.1 M HCl to separate the layers. DCM was rinsed again with HCl and then rinsed twice with water. The organic layer was washed with brine and dried over sodium sulfate, filtered, and concentrated in vacuo. For further purification, the product was dissolved in DMSO at a concentration of approximately 50 mg/mL and diluted 1:3 in water. The suspension was left at 4°C overnight then centrifuged at 5,000 rpm for 20 minutes at 4°C. The supernatant was removed and the rinsing process was repeated once more. The final pellet was frozen and lyophilized (118 mg, 0.19 mmol, 60% yield, Δ_2 isomer ~40%). HRMS-ESI: calculated for $C_{29}H_{26}N_4O_9S_2^+$ $[M+H]^+$: 639.11; Found: 639.1218 ^{1}H-NMR (400 MHz, DMSO-d_6) δ (ppm): 9.07 - 8.95 (dd, J_1 = 7.5 Hz, J_1 = 40.8 Hz, 1H), 8.10 - 8.04 (dd, J_1 = 3.2 Hz, J_2 = 8.8 Hz, 2H), 7.48 - 7.44 (dd, J_1 = 5.2 Hz, J_2 = 8.4 Hz, 2H), 7.33 - 7.28(dd, J_1 = 3.4 Hz, J_2 = 2.4 Hz, 2H), 6.99 (s, 2H), 6.91 - 6.85 (dd, J_1 = 8.6 Hz, J_2 = 18.6 Hz, 2H), 5.64 - 5.33 (dd, textitJ_1 = 4.8, 3.7 Hz, J_2 = 8.4, 7.4 Hz, 1H), 5.22-5.05 (m, 3H), 4.26 - 3.85 (dd, textitJ_1 = 12.9, 14.6 Hz, J_2 = 73.6, 134.4 Hz, 2H), 3.75 - 3.69 (m, 4H), 3.65 - 3.55 (m, 2H), 3.53 (d, textitJ = 17.8 Hz, 1H) 2.48 - 2.41 (m, 2H).

Note: The non-β-responsive Δ_2 isomer has been reported in literature. Reaction conditions could be optimized to increase ratio of Δ_3 to Δ_2 isomer.[58,77,336]

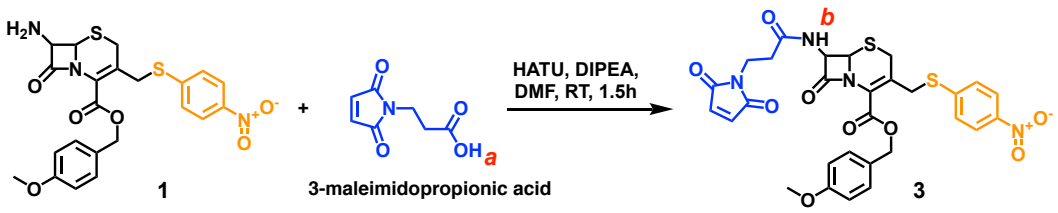

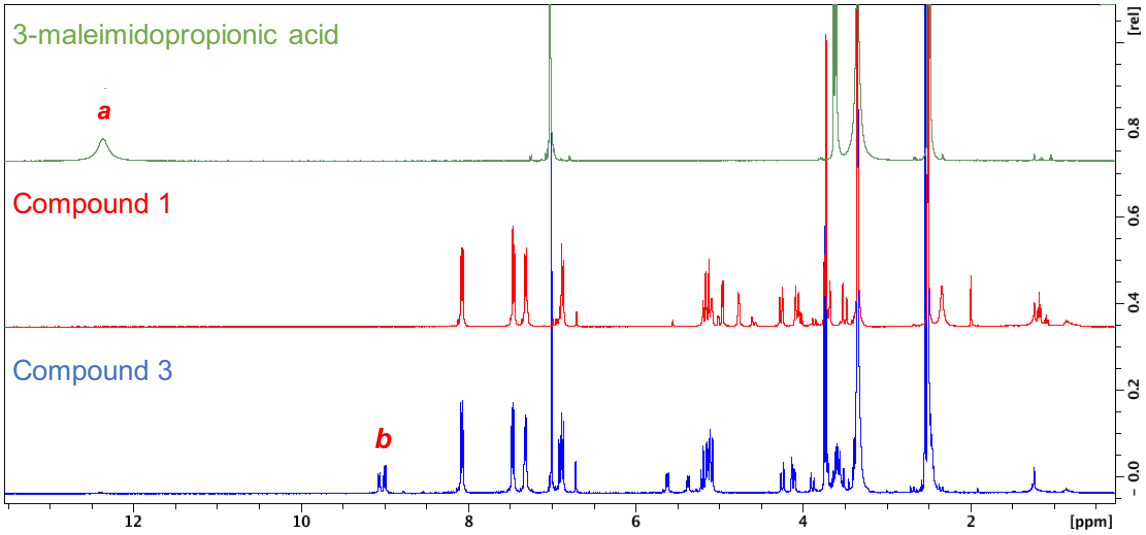

Figure 4.5: ^{1}H-NMR spectra of 3-maleimidopropionic acid, compound **1**, and compound **3** (DMSO-d_6, 400 MHz). Compound **3** spectrum includes the protons of compound 1 and of 3-maleimidopropionic acid minus the proton of the carboxylic acid (12.36 ppm), and the appearance of the newly formed amide (9.07 - 8.95 ppm).

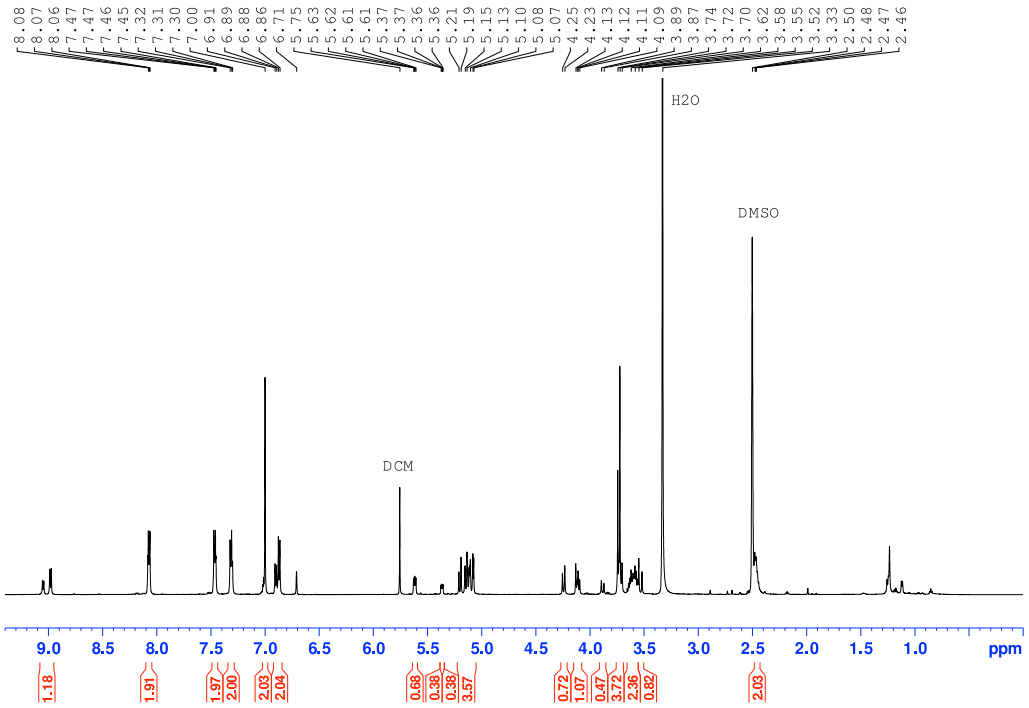

Figure 4.6: ^{1}H-NMR of compound **3** (DMSO-d_6, 400 MHz).

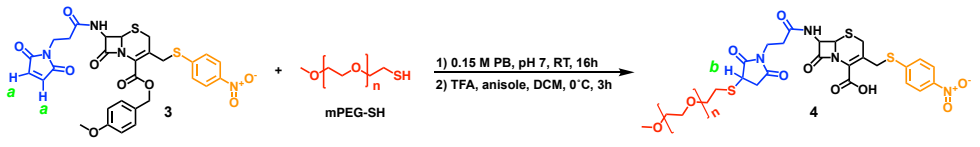

Synthesis of β-lactam-mPEG conjugate, 4

Product **3** (30 mg, 0.047 mmol) dissolved in DMSO (175 μL) was added to mPEG-thiol (40 mg, 0.023 mmol) dissolved in 0.15 M sodium phosphate buffer (PB; 1 mL; pH 7) and the solution was left spinning at RT for 16 hours. The product was then dialyzed in 500-1000 Da MWCO cellulose ester dialysis tubing in water for 6 hours, frozen, and lyophilized. The dried product was deprotected in a solution of TFA:anisole:DCM mixed at a 1:1:5 volumetric ratio (10.5 mL total) on ice for 3 hours. The DCM and TFA were evaporated under reduced pressure, then the product was precipitated and rinsed twice in cold diethyl ether (pelleted by centrifuging at 4,000$\times$g for 5 minutes at -10°C). Lastly, the conjugate was dialyzed in water for 24 hours, frozen, and lyophilized.

Conjugation was confirmed using ^{1}H-NMR (Figure 4.7), MALDI-TOF MS (Figure 4.8), and SEC (Figure 4.9) as described in the *Instrumentation* Section. Both SEC and NMR also indicated that any free, unconjugated **3** had been successfully removed. Response to βL-BC was characterized using SEC (Figure 4.9) and UV-vis spectroscopy (Figure 4.10).

4.5.4 Substrate 2 Incubation with βLs

For all βLs tested, 135 μL of each respective βL dissolved in 0.15 M PB (pH 7) was added to 15 μL of substrate **2** dissolved in DMSO for a final concentration of 0.2 mg/mL of **2**, 10% DMSO in PB, and different concentrations of enzymes. For all βLs tested, activity was reported by the vendor and one unit (U) was defined as hydrolyzing 1.0 μmole of benzylpenicillin per min at pH 7.0 at 25°C. Substrate **2** was incubated with 200 U/mL

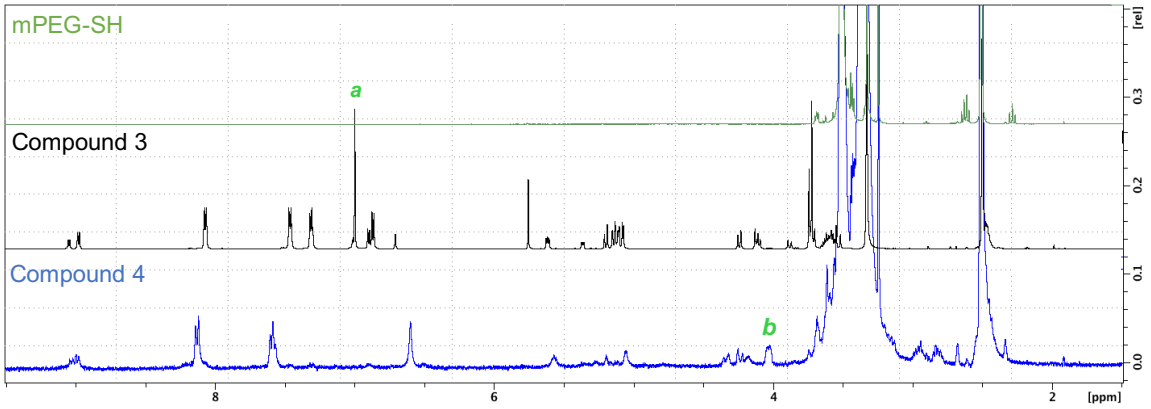

Figure 4.7: ^{1}H-NMR spectra of mPEG-SH, compound **3**, and compound **4** (DMSO-d_6, 400 MHz). Compound **4** spectra indicates presence of PEG repeat units, compound **3** protons minus those of the p-methoxybenzyl protecting group and the maleimide protons at 7.0 ppm. It also shows the appearance of one of the maleimide-thiol adduct protons at 4.02 ppm in compound **4**, suggesting successful conjugation. The other two protons on the adduct would likely appear in the region of 2.4 - 3.2 ppm,[328] obscured by the protons of the PEG repeat units.

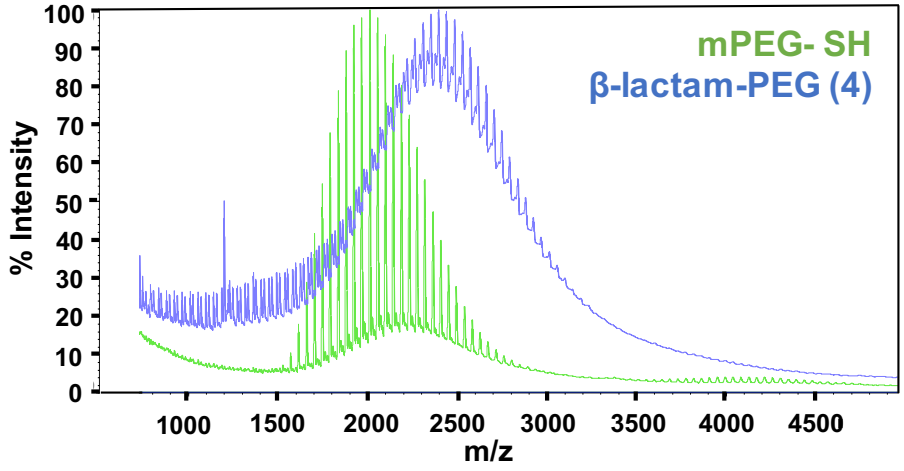

Figure 4.8: MALDI-TOF MS spectra of unmodified mPEG-SH (green) and β-lactam-PEG conjugate **4** (blue) demonstrating an increase in polymer mass upon conjugation of compound **3** to PEG.

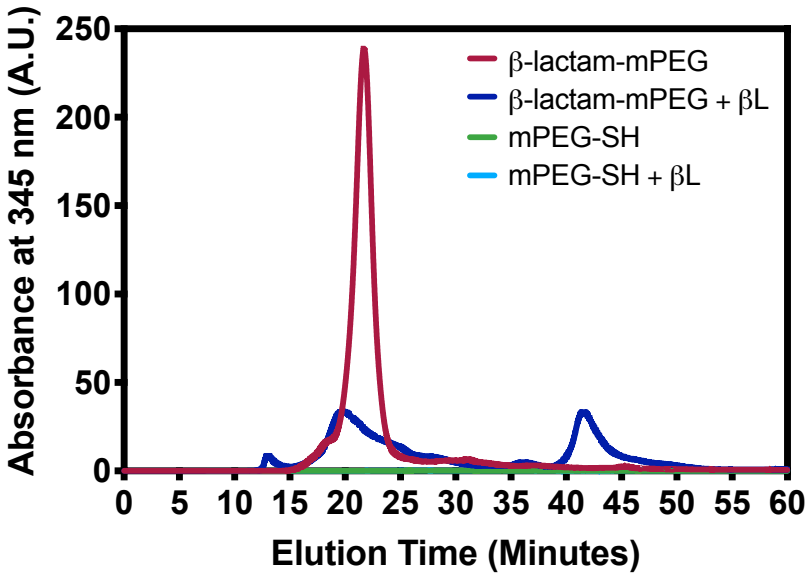

Figure 4.9: Size exclusion chromatograms of absorbance at 345 nm of 1 mg/mL mPEG-SH or β-lactam-PEG conjugate **4** incubated with or without 200 U/mL βL-BC in PBS for 3 hours at 37°C.

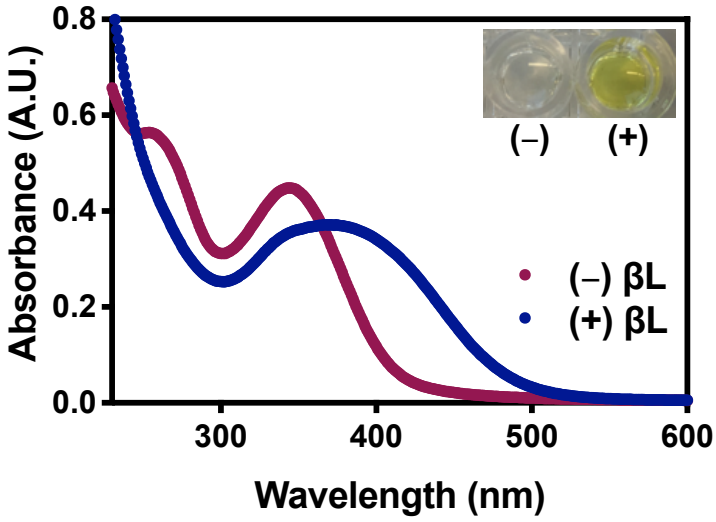

Figure 4.10: Spectral scan of **4** after incubation with or without βL-BC in PBS. 1 mg/mL of **4** was incubated with 200 U/mL βL-BC for 3 hours then diluted to 0.3 mg/mL before absorbance was measured in glass cuvettes using a PerkinElmer Lambda 950 spectrometer. Inset: Image of **4** incubated with (+) or without (-) βL in PB.

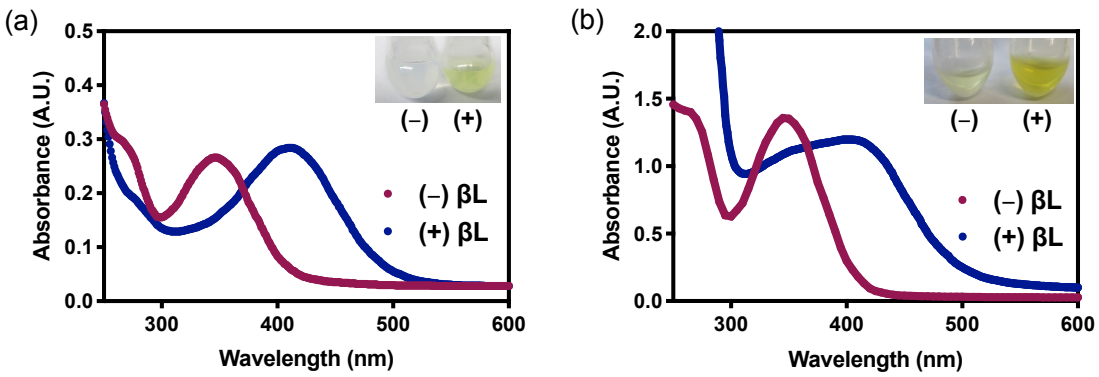

Figure 4.11: Absorbance spectrum of **2** incubated with (a) 50 U/mL of βL-PA after 90 minutes or (b) 1 U/mL of βL-EC after 3 hours. Insets: Images of **2** with (+) or without (-) βL in PB.

βL-BC for 30 minutes (Figure 1a), 50 U/mL βL-PA for 90 minutes (Figure 4.11a), or 1 U/mL βL-EC for 3 hours (Figure 4.11a) at 37°C before a UV-Visible spectral scan (from 230 to 600 nm) was conducted using a plate reader.

To study concentration dependent effects of βL, substrate **2** was incubated with 11 different concentrations (0.39 to 400 U/mL) of βL-BC as described above. After 45 minutes of incubation at 37°C, the absorbance spectra (Figure 4.12a) and absorbance at 410 nm (Figure 4.12b) were recorded. The plot of absorbance at 410 nm versus concentration was fit to a curve using linear regression and the limit of detection (LOD) was calculated using equation 4.1.

$$LOD = 3.3 \times \frac{standard\ deviation\ of\ blank}{slope} \tag{4.1}$$

4.5.5 Michelis-Menten Kinetics

Enzymatic activity of βL-BC, βL-PA, βL-EC against **2**, CENTA and nitrocefin was characterized. The three substrates were dissolved in DMSO at six different molar equiv-

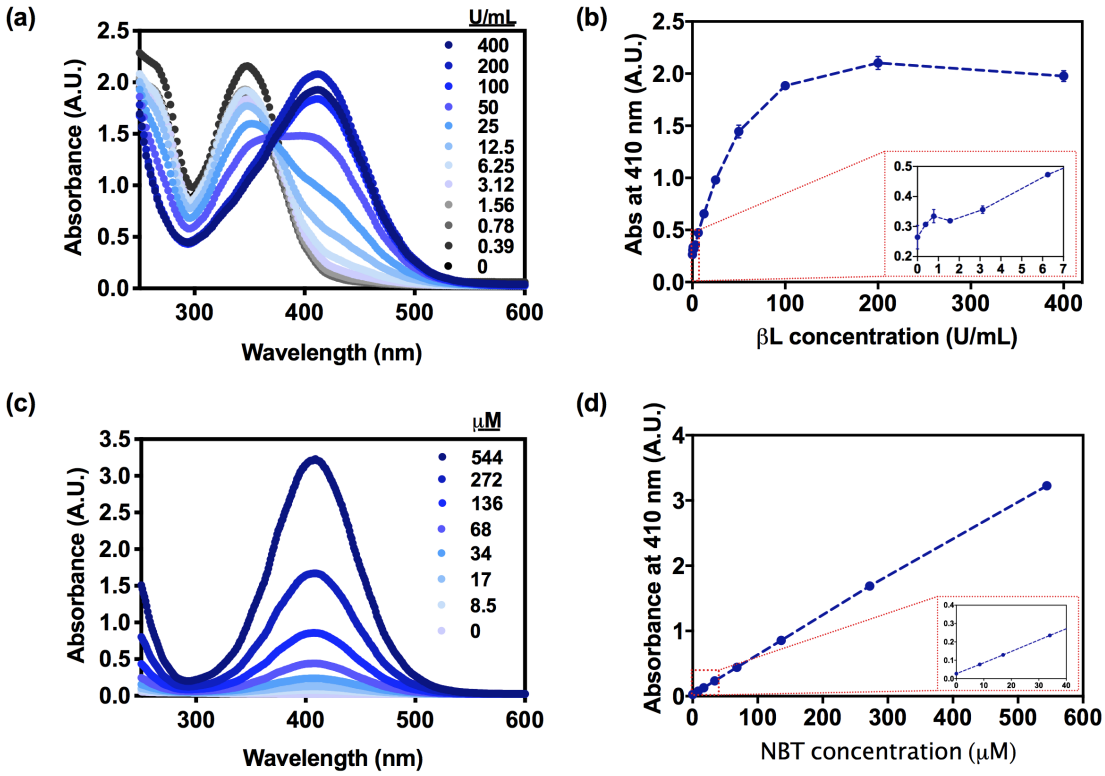

Figure 4.12: (a) Spectral scan of 0.2 mg/mL (544 μM) of **2** incubated with different concentrations (U/mL) of βL-BC or in PBS (with 10% DMSO) after 45 minutes at 37°C. (b) Absorbance signal at 410 nm as a function of βL concentration. Inset is a zoom in on lower concentrations of βL. (c) Spectral scan of different concentrations (μM) of 4-nitrobenzenethiol (NBT). (d) Absorbance signal at 410 nm as a function of NBT concentration. Inset is a zoom in on lower concentrations of NBT.

alent concentrations ranging from 0.68 to 5.4 mM (10×). Enzyme stocks (1.1×) were dissolved in 0.15 M PB (pH 7) at different concentrations (U/mL) for each substrate-βL combination and were warmed to 37°C. 15 μL of **2**, CENTA or nitrocefin followed by 135 μL of βL was added to 96-well plates to achieve final concentrations of 68 to 544 μM for substrates, different concentrations for βLs (reported in caption of Figure 4.13) in 10% DMSO in PB. Absorbance at 410, 405, and 485 nm, for **2**, CENTA, nitrocefin, respectively, were immediately monitored at 37°C over time. The change in absorbance was plotted against substrate concentration for each substrate and βL combination, and the initial slope of each curve was determined and taken as the initial velocity of the reaction.

The molar extinction coefficients of **2**, CENTA, and nitrocefin were also measured. 15 μL of each substrate at each concentration (in DMSO) and 135 μL of βL-BC (in 0.15 M PB, pH 7) was added to a 96-well plate to achieve final concentrations of 68 to 544 μM for substrates and 25 U/mL for βL-BC in 10% DMSO in PB. The change in absorbance at 410 nm for **2**, 405 nm for CENTA, and 485 nm for nitrocefin was monitored for 30 minutes. The maximum absorbance achieved for each substrate at each concentration was recorded and absorbance versus substrate concentration plots were generated for each substrate. The slope of each plot was determined and recorded as the extinction coefficient for each substrate. The coefficients were calculated as 1331, 6221, and 15068 $M^{-1}cm^{-1}$ for **2**, CENTA, and nitrocefin, respectively. The K_M, k_{cat}, and k_{cat}/K_M values were calculated through the initial velocities of the substrate and the direct fitting of the Michaelis-Menten curve[337] to the data using GraphPad Prism™ (Figure 4.13, Table 1).

4.5.6 Substrate 2 Minimum Inhibitory Concentration

Antibacterial effect of **2** was tested against different gram-positive and gram-negative bacteria (Table 4.2) in a microdilution assay. **2** was dissolved in DMSO at a concentration of 2.56 mg/mL and diluted to a concentration of 256 μg/mL in sterile 1× PBS. Substrate

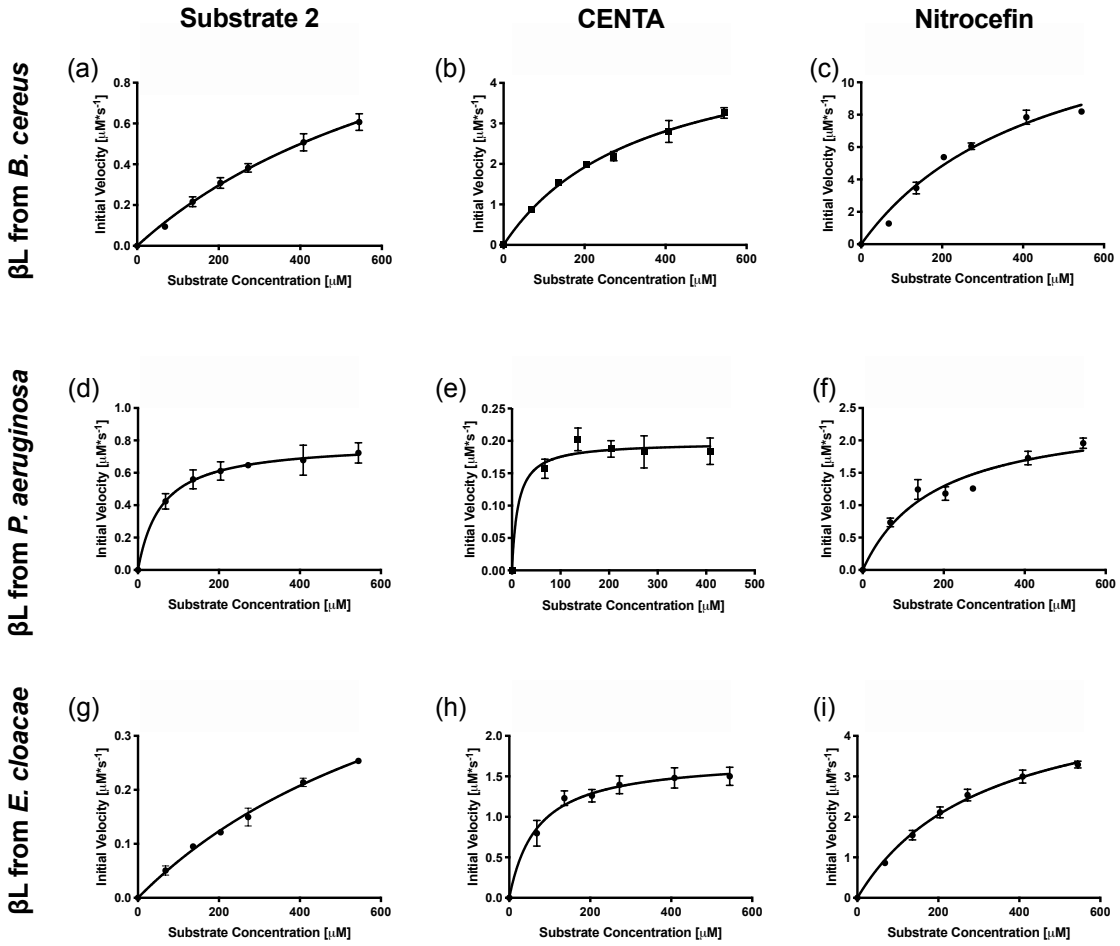

Figure 4.13: Michaelis-Menten kinetics charts of (a) **2**, (b) CENTA, and (c) nitrocefin with 25 U/mL βL-BC, (d) **2** with 25 U/mL, (e) CENTA with 10 U/mL, and (f) nitrocefin with 10 U/mL βL-PA, and (g) **2** with 1 U/mL, (h) CENTA with 0.01 U/mL, and (i) nitrocefin with 0.005 U/mL βL-EC.

Bacteria	MIC (μ g/mL)	Gram (+/-)
S. aureus 25923	8	+
S. aureus 29213	8	+
MRSA MW2	>128	+
B. cereus	>128	+
E. coli 25922	>128	-
P. aeruginosa PA01	>128	-
E. cloacae	>128	-

Table 4.2: MIC of **2** against different strains of bacteria

2 solutions and a control of 10% DMSO in CMHB or TSB were serially diluted 1:2 with CMHB or TSB in a 96-well plate. Bacteria were grown overnight, then diluted 1:1000, then added in their logarithmic growth phase to the wells at a final concentration of 10^5 CFU/mL. Positive controls of bacteria cultured in broth only and negative controls of CMHB or TSB without bacteria were included. After 16-18 hours of shaking at 100 rpm at 37°C, the optical density at 600 nm (OD_{600}) was measured using a plate reader. The normalized bacteria density was calculated using equation 4.2:

$$Normalized\,bacteria\,density = \frac{sample\,OD_{600} - negative\,control\,OD_{600}}{positive\,control\,OD_{600} - negative\,control\,OD_{600}} \tag{4.2}$$

The minimum inhibitory concentration (MIC) of **2** was determined as the lowest concentration of **2** in the range of concentrations over which the normalized bacteria density transitioned from zero to greater than zero.

4.5.7 Product 4 *in vitro* Bacteria Responsive Color Change

βL producing bacteria, *B. cereus*, *E. cloacae*, and *P. aeruginosa*, and non-βL producing bacteria, *E. coli* DH5-α, were grown overnight in 1$\times$ TSB, then diluted 1:1000 and grown

to mid-logarithmic growth phase. **4** was dissolved in 1× PBS at 9 mg/mL then serially diluted 1:2 in 50 μL of PBS in a 96-well plate. 50 μL of TSB or bacteria in TSB was added to each well to a final concentration of 10^7 CFU/mL. The final solutions were 50% TSB in PBS and were incubated shaking (100 rpm) at 37°C for 18-24 hours before digital images of the wells were taken (Figure 2a).

4.5.8 β-lactam-PEG Hydrogel Formation and βL-Responsive Color Change

20% w/v PEG hydrogels modified with substrate **3** were formed following similar previously reported procedures[331]. As depicted in Scheme 4.2, compound **3** (in DMSO) was incubated with 4-arm-poly(ethylene glycol)-thiol (PEG-4SH; 20 kDa) (in 0.1× PBS, pH 5) at a 4:1 thiol to maleimide molar ratio with shaking at 100 rpm at 37°C for 15 minutes. Subsequently, maleimide-PEG-maleimide (mal-PEG-mal; 2 kDa) (in DMSO) was added to the solution at a 1:1 thiol to maleimide molar ratio to form hydrogels; the mixture (50 μL) was briefly vortexed then quickly transferred to a 5 mm circular polydimethylsiloxane (PDMS) mold, and incubated at 37°C for 45 minutes. The control non-responsive hydrogels were formed similarly but without adding compound **3**. The hydrogels were rinsed in methanol then DCM (with shaking at room temperature), before TFA and anisole were added to deprotect the carboxylic acid (on ice for 4 hours). After the deprotection, the hydrogels were thoroughly rinsed in DCM then methanol. Before the hydrogels were incubated with βLs, they were rinsed and equilibrated in 1× PBS overnight at 4°C. The hydrogels were cut in half before 100 μL of PBS with or without 400 U/mL βL-BC were pipetted onto the hydrogels and a color change was apparent in a few minutes (Figure 2b).

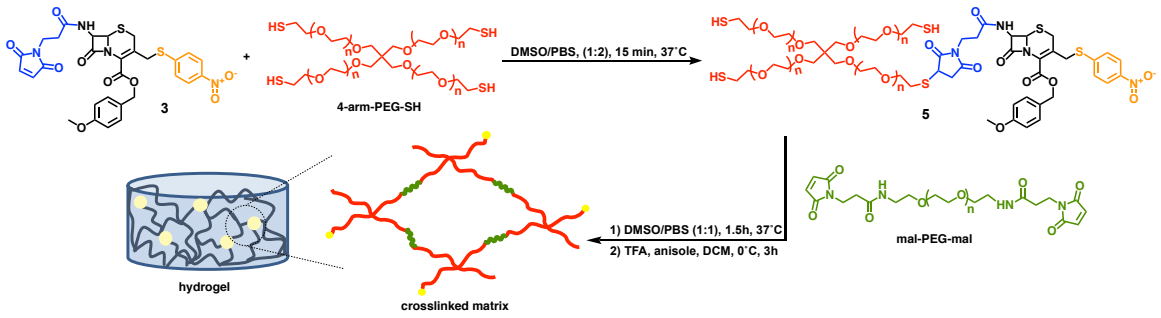

Scheme 4.2: Schematic of β-lactam-PEG hydrogel gelation.

Chapter 5

β-lactamase Responsive Hydrogels as a Platform for Bacteria Triggered Antibacterial Treatments

---

Chapter 5 is a manuscript prepared for submission for peer review:

Alkekhia D., LaRose C., Shukla A., "β-lactamase responsive hydrogels for bacteria triggered antibiotic delivery", In preparation, 2020.

5.1 Abstract

Antibiotic resistance is a major global health threat that has been associated with misuse and overuse of antibiotics. One of the main causes of resistance are β-lactamases (βLs), bacterial enzymes that hydrolyze the β-lactam present in the widely prescribed antibiotics including penicillins and cephalosporins inactivating them. Here, we developed hydrogels that degrade specifically in the presence of βL and βL-producing bacteria to provide a platform for bacteria triggered antibiotic delivery. The aim is to limit unnecessary exposure to antibacterial agents, and with the spatiotemporal control over their release, to localize delivery enhancing the drug concentration at the site infection and reducing off-site toxicity to the microbiome, potentially reducing susceptibility to antibiotic resistance development. A βL cleavable cephalosporin was functionalized with maleimides on both of its halves and used as a crosslinker in the synthesis of hydrogels by end-crosslinked polymerization with multiarm thiol-terminated poly(ethylene glycol) macromers *via* Michael-type addition. Only hydrogels containing the responsive moiety degraded by βLs, as demonstrated by a decrease in wet mass over time. Fluorescent polystyrene nanoparticles (NPs) encapsulated into the hydrogels as model cargo, were released at rates tracking hydrogel wet mass loss, indicating hydrogel surface erosion and degradation-controlled cargo release. Hydrogels demonstrated an on-off response when βL were added or removed, and lower degradation rates with increased polymer density, and different degradation rates when incubated with different types of βLs. The latter demonstrating βL-substrate hydrolysis kinetic controlled degradation. Responsive hydrogels also degraded and released NPs in the presence of βL-producing bacteria (*Bacillus cereus*, *Pseudomonas aeruginosa*) but remained stable when incubated with non-βL-producing bacteria (*Staphylococcus aureus*). Degradation rates were dependent on bacterial strain and culture conditions (shaking in solution, on agar, or on *ex vivo* porcine skin), ranging from approximately 21 hours to over a week.

5.2 Introduction

Bacterial antibiotic resistance is a major global health threat making bacterial infections among the leading causes of death.[1] A recent 2019 report by the Centers for Disease Control and Prevention (CDC) estimates over 2.8 million infections and over 35,000 deaths caused by antibiotic-resistance microbes annually in the US alone.[3] Overuse and misuse of antimicrobials, including antibiotics, has been associated with increased risk of antibacterial resistance development as well as other adverse drug events.[6] As the prevalence of antibiotic resistant bacteria continuously increases and development of new therapeutics remains stagnant, there is a critical need for new strategies and technologies for infection control.[200,201] One approach to improve management and treatment of infections is the development of biomaterials for controlled antibiotic delivery to enhance efficacy, reduce doses administered, and reduce off-site toxicity of current antibiotics. Self-regulated release of antimicrobials from biomaterials could potentially reduce susceptibility of bacteria towards developing antibiotic resistance by localizing antibiotic release at the site of infection and only when an infection arises, thus limiting unnecessary exposure and reducing toxicity.

Responsive materials, which undergo a change in material properties under specific stimuli, have been designed for different applications, such as diagnosis, tissue engineering, as well as drug delivery.[67] For antibacterial treatments, various types of material have been developed to respond to external stimuli including temperature, light, and magnetic fields.[338] Alternatively, biomaterial that does not require external interference and can respond to the native bacterial microenvironment, has been explored as self-defensive systems.[69] Among the most common examples in literature are pH responsive biomaterial[339] that can respond to the local decrease in pH[154] caused by various lactic and acetic acid producing bacteria.[73] Other triggers include bacterial toxins[74] and enzymes, such as lipases,[75]

proteases,[104] phosphatases and phospholipases,[76] and hyaluronidases.[199,203] Yet, some of these triggers are not necessarily bacteria specific. Acidic environments can be found in different locations in the body including uninfected wounds.[340] Some bacterial enzymes have mammalian analogs that cleave similar substrates that are also typically found in wounds. β-lactamases (βLs) on the other hand are specific to bacteria and are one of the major causes of antibiotic resistance.[17,18] These enzymes, which are produced by various gram-positive and gram-negative bacteria,[16] cleave the β-lactam ring present in many of the common antibiotics such as penicillins, cephalosporins, and carbapenems, inactivating the therapeutics.[17] This class of drugs is among the most commonly prescribed antibiotics around the world,[341] underscoring the importance of limiting their use, as well as the use of broad-spectrum late stage antibiotics, to preserve their efficacy.

An interesting characteristic of some cephalosporins is that hydrolysis of the amide bond in their β-lactam ring by βLs triggers the spontaneous release of a leaving group attached at the 3'-position, if present.[342] This property has been exploited in the development of βL responsive prodrugs,[343] such as compounds that are triggered by bacteria to release nitric acid[77] or antibiotics,[15,79] or activate photosensitizers for targeted photodynamic therapy.[80] Similar responsive compounds have also been synthesized for the detection of βL-producing bacteria utilizing luminescent ruthinium (i) probes,[311] fluorescent probes,[58,60,312] or fluorescence resonance energy transfer (FRET)-based probes.[63] Furthermore, βL responsive polymeric biomaterials such as vesicles for the delivery of antibiotics[81] or amphiphilic polymers for βL triggered hydrogelation as a detection mechanism have also been developed.[344] We wanted to utilize this molecular recognition to achieve a bacteria-triggered macroscopic change for the development of hydrogels or coatings that can be applied to larger surfaces such as wounds or medical devices and deliver encapsulated antibacterial agents selectively, when an infection arises. The goal is to limit unnecessary exposure to antibacterial agents and to localize their delivery to an infection site, potentially improving efficacy, reducing toxicity, and reducing susceptibility to bacterial antibiotic resistance

development.

Hydrogels have been used extensively for a variety of biomedical applications including treatment of wounds.[85] Their high water content make them an excellent candidate for hydrating the wound, enhancing autolytic debridement, taking up some exudate, filling deep and irregular wounds, and allowing gaseous exchange; all important factors for wound healing.[25] Hydrogels can also be loaded with antibacterial agents to prevent development of infections or growth factors to promote healing. Poly(ethylene glycol) (PEG) is among the most commonly used synthetic polymers in the formulation of biomaterials, including hydrogels.[28] These hydrogels are inherently hydrophilic, bioinert, anti-protein fouling, and non-degradable by mammalian enzymes, with minimal toxicity and inflammation *in vivo*.[345] PEG hydrogels thus offer a blank slate for engineering dynamic biofunctionality/flexible bio-design, such as selective sensitivity to enzymes.[346] The facile modification and versatility of PEG macromers has led to diversity in chemistries utilized to form hydrogels; the most common are free-radical polymerization and Michael-type addition.[28] The latter results in end-linking polymerization by simply mixing two components that carry reactive functional groups, providing better control over gelation and structure definition.[31] Michael addition thiol-ene chemistry proceeds at near physiological pH and temperatures, with selective reactivity that prevents potential reaction with therapeutics loaded into the hydrogels and eliminates the need for radicals, light, or toxic crosslinkers or catalyzers, adding to cargo preservation.[345] Studies have shown that the high efficiency of maleimide-thiol reaction (in comparison to other Michael acceptors) resulted in hydrogels with improved crosslinking kinetics and greater control over hydrogel mechanical properties.[90] PEG hydrogels have been rendered/designed to respond to their environment by the addition of enzyme-cleavable moieties, most commonly peptides, in the matrix's backbone, for drug delivery (e.g. delivery of proteins[101]) and tissue engineering applications (e.g. invasion[102] and modulation[347] of hydrogels by cells as their secreted enzymes cleave matrices).

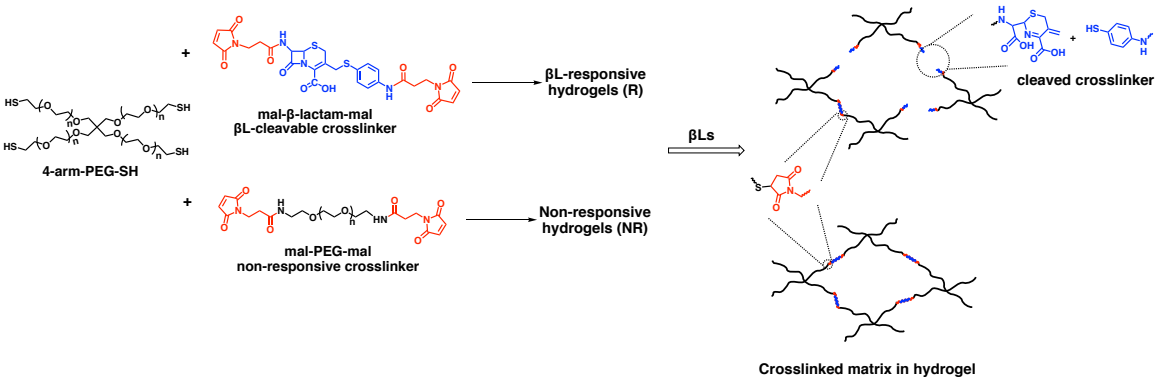

Scheme 5.1: Schematic of formation of βL responsive and non-responsive hydrogels, and the cleavage of the hydrogel backbone due to the hydrolysis of the β-lactam and expulsion of the leaving group by βLs.

Here we synthesized a βL cleavable compound, that is functionalized with maleimides on both ends, which participates as a crosslinker in thiol-ene Michael-type addition with multi-arm thiol terminated PEG building blocks to form βL-degradable hydrogels (Scheme 5.1). In the presence of βL, the β-lactam ring is cleaved leading to the expulsion of the second half of the crosslinker, which leads to cleavage of the matrix and degradation of the hydrogels. In this work, we demonstrate the selective degradation of βL responsive hydrogels in the presence of βLs and βL producing bacteria. Nanoparticles (NPs) loaded into the hydrogels were released solely upon hydrogel degradation in the presence of βL, indicating the potential use of this platform to control release of encapsulated antibacterial agents from prophylactic biomaterials (e.g., bandages) only in cases where an infection arises. Our studies also demonstrate how hydrogel composition (polymer density) and environmental factors such as βL concentration and specificity, and bacterial growth condition (e.g., in broth, on agar, on *ex vivo* porcine skin) can influence the rate of hydrogel degradation.

5.3 Materials and Methods

5.3.1 Materials

7-amino-3-chloromethyl-3-cephem-4-carboxylic acid p-methoxybenzyl ester hydrochloride (ACLE) was purchased from AK Scientific (Union City, CA). 3-maleimidopropionic acid was purchased from TCI Chemicals (Tokyo, Japan). Aminothiophenol (ATP), triethylamine (TEA), N-methylmorpholine (NMM), anhydrous dichloromethane (DCM), anhydrous dimethylformamide (DMF), hexanes, ethyl acetate (EtAc), thin layer chromatography (TLC) Silica Gel 60 on glass plates, dimethyl sulfoxide (DMSO), trifluoroacetic acid (TFA), anisole, βL from *B. cereus* (βL-BC; cat.# P0389, 28 kDa, 2817.8 U/mg protein, 4.72% protein), βL from *P. aeruginosa* (βL-PA; cat.# L6170, 30 kDa, 1080 U/mg protein, 1% protein), βL from *E. cloacae* (βL-EC; cat.# P4524, 20-26 kDa, 0.37 U/mg protein, 56.45% protein), collagenase from *Clostridium histolyticum*, phosphate buffered saline (PBS), calcium chloride dihydrate, 1-[Bis(dimethylamino)methylene]-1H-1,2,3-triazolo[4,5-b]pyridinium 3-oxid hexafluorophosphate (HATU), N,N-disopropylethylamine (DIPEA) were acquired from Millipore Sigma (St. Louis, MO). FluoSpheres carboxylate-modified microspheres (0.1 μm), silica gel, tryptic soy broth (TSB), sodium azide (0.5% W/V), and SYLGARD 184 silicone elastomer kit were purchased from Thermo Fisher Scientific (Waltham, MA). 4-arm-PEG-thiol was purchased from Laysan Bio, Inc (Arab, AL), Sigma, or JenKem (5 kDa). Deuterated acetone (acetone-$d_{6)}$ and chloroform ($CDCl_3$) were obtained from Cambridge Isotope Laboratories (Andover, MA). Nitrocefin disks were obtained from Becton Dickinson (Franklin Lakes, NJ). *Staphylococcus aureus* strains 25923, *Bacillus cereus* 13061, and *Pseudomonas aeruginosa* 27853 were purchased from ATCC (Manassas, VA). Ultra-high-purity nitrogen gas (99.999%; under N_2) was obtained from Corp Brothers, Inc. (Providence, RI). Ultrapure deionized water (18.2 MΩ·cm, Millipore Sigma, Billerica, MA) was

utilized in all experiments. Room temperature (RT) referred to in this article is approximately 23°C.

5.3.2 Instrumentation

^{1}H-NMR was recorded on a Bruker DRX Avance 400 MHz spectrometer and reported with chemical shifts stated as δ in units of parts per million (ppm) relative to $CDCl_3$ (7.26 ppm) or acetone-d_6 (2.05 ppm). High resolution mass spectrometry (HRMS) electrospray ionization (ESI) was conducted on an Agilent 6530 liquid chromatography (LC)-MS. Fluorescent spectroscopy were performed using a BioTek® Cytation 3 microplate reader (Winooski, VT), using 96-well black plates (Thermo Fisher Scientific, Waltham, MA).

5.3.3 Synthesis and characterization of βL-responsive crosslinker, mal-β-lactam-mal

Synthesis of compound 1

The core of the βL-responsive crosslinker was synthesized similarly to previous reports.[80] ACLE (600 mg, 1.48 mmol) was dissolved in anhydrous DCM (20 mL) and stirred on ice under N_2. TEA (400 μL, 2.8 mmol) was slowly added in three portions over a 20 minute time period to the ACLE mixture. NMM (200 μL, 1.8 mmol) and ATP (300 mg, 2.4 mmol) were added sequentially thereafter. The reaction was stirred on ice and monitored by TLC (30% EtAc/70% DCM). After 1 hour, the solvent was evaporated *in vacuo*, and the product was purified using column chromatography (silica gel, 20% to 80% gradient EtAC in DCM as eluent) to yield compound **1** as a white product (440 mg, 0.96 mmol, 65% yield). HRMS-ESI: Calculated for $C_{22}H_{23}N_3O_4S_2^+$ $[M+H]^+$: 458.1129; Found: 458.1199. ^{1}H-NMR (400 MHz, $CDCl_3$) δ (ppm): 7.31 (d, J= 8.5, 2H), 7.15 (d, J= 8.5, 2H), 6.88 (d, J= 8.5, 2H), 6.52 (d, J= 8.6, 2H), 5.10 - 4.94 (dd, J_1 = 11.9 Hz, J_2 = 43.1 Hz, 2H), 4.83 (d,

J= 4.9, 1H), 4.65 (d, J= 4.9, 1H), 4.19 - 3.51 (dd, J_1 = 13.3 Hz, J_2 = 245.2 Hz, 2H), 3.80 (s, 3H), 3.72 - 3.27 (dd, J_1 = 17.9 Hz, J_2 = 143.8 Hz, 2H).

Synthesis of protected mal-β-lactam-mal, Compound 2

Compound **1** (100 mg, 0.22 mmol), 3-maleimidopropionic acid (130 mg, 0.76 mmol) and HATU (350 mg, 0.92 mmol) were dissolved in anhydrous DMF (3 mL). The mixture was stirred for 15 minutes under N_2 at RT before adding DIPEA (227 μL, 1.3 mmol), then the reaction was allowed to proceed for another 75 minutes and was monitored by TLC (80% EtAc in DCM). The crude reaction was transferred to a separatory funnel and partitioned between DCM and water to separate the layers. The DCM fraction was washed again twice with water and once with brine, before it was dried over sodium sulfate, filtered, and concentrated *in vacuo*. The product was purified by flash chromatography (silica gel, 40-80% EtAc in DCM gradient) to afford a faint yellow product (132 mg, 0.17 mmol, 80% yield). HRMS-ESI: calculated for $C_{36}H_{33}N_5O_{10}S_2^+$ $[M+H]^+$: 760.1678; Found: 760.1746. ^{1}H-NMR (400 MHz, acetone-d_6) δ (ppm): 9.34 (s, 1H), 8.02 (d, J = 8.5, 1H), 7.59 (d, J = 8.7, 2H), 7.35 - 7.28 (dd, J_1 = 8.6 Hz, J_1 = 12.7 Hz, 4H), 6.91 (d, J = 8.7, 2H), 6.85 (d, J = 5.5, 4H), 5.71 - 5.66 (dd, J_1 = 4.7 Hz, J_2 = Hz, 1H), 5.06 - 4.88 (dd, J_1 = 12.0 Hz, J_2 = 49.2 Hz, 2H), 5.03 (d, J= 4.8, 1H), 4.29 (d, J = 13.3 Hz, 1H), 3.86 - 3.72 (m, 9H), 3.51 (d, J = 17.8 Hz, 1H), 2.71 - 2.60 (m, 4H).

Synthesis of mal-β-lactam-mal crosslinker

Compound **2** (125 mg, 0.16 mmol) was deprotected in a solution of TFA:anisole:DCM (42 mL total) at a 1:1:5 volumetric ratio under N_2 on ice for 1.5 hours and monitored by TLC (100% EtAc). Solvents were evaporated under reduced pressure. The deprotected crosslinker was dissolved in acetone and then precipitated in cold diethyl ether (8x volume) three times (centrifuged at 5,000 rpm for 10 minutes at 4°C) (57 mg, 0.09 mmol, 54%

yield). HRMS-ESI: Calculated for $C_{28}H_{25}N_5O_9S_2^+$ $[M+H]^+$: 640.1083; Found: 640.1152. ^{1}H-NMR (400 MHz, acetone-d_6) δ (ppm): 9.34 (s, 1H), 8.02 (d, J = 8.5, 1H), 7.57 (d, J = 8.6, 2H), 7.37 (d, J = 8.6, 2H), 6.85 (d, J = 5, 4H), 5.71 - 5.66 (dd, J_1 = 4.7 Hz, J_2 = 9 Hz, 1H), 5.03 (d, J= 4.8, 1H), 4.28 - 3.89 (dd, J_1 = 13.3 Hz, J_2 = 136.6 Hz, 2H), 3.84 - 3.69 (m, 5H), 3.51 (d, J = 17.7 Hz, 1H), 2.70 - 2.61 (m, 4H).

5.3.4 Hydrogel formation

The βL-degradable or non-degradable crosslinkers, mal-β-lactam-mal (639.11 Da) and mal-PEG-mal (494.5 Da), respectively, were dissolved in DMSO (4x concentration). 4-arm-PEG-thiol (20 kDa) was dissolved in 1$\times$ PBS pH 7 or in 0.1$\times$ PBS pH 4 for responsive or non-responsive hydrogels, respectively. These buffer concentrations and pH values were chosen to achieve similar gelation times between the two types of hydrogels. Increase in volume due to the presence of PEG was taken into account. For NP loaded hydrogels, 100 nm carboxylate coated fluorescent polystyrene NPs were briefly sonicated, vortexed, then added to the pre-gelation PEG solution at a final w/v concentration of 0.08% (1:20 dilution from stock solution), which is equivalent to approximately 135 $\times$ 10^{10} NPs/mL or $\sim$6.75 $\times$ 10^{10} NPs per gel. Hydrogels were formed by mixing the crosslinker and PEG at 1:1 maleimide:thiol stoichiometric ratio. PEG solutions were cooled on ice to aid in slowing the reaction initially and allow adequate mixing before transfer to the mold to increase uniformity/homogeneity of the hydrogels. The mixture was quickly vortexed and 50 μL was transferred into a 5 mm circular PDMS mold. Gelation occurred within minutes but the solutions were left for 1-2 hours at 37°C to ensure complete gelation. Hydrogels were swollen in 2 mL of 1$\times$ PBS (pH 7.4) shaking (100 rpm) at 37°C overnight to ensure removal of DMSO and any surface bound NPs, and to achieve equilibrium swelling before hydrogels were used in experiments.

5.3.5 Hydrogel equilibrium swelling and mesh size estimation

After hydrogels were formed, they were weighed as-made. The hydrogels were then swollen by incubation in 2 mL of 1× PBS, pH 7.4 at 37°C with shaking (100 rpm) for 48 hours, then pat dried and their wet mass was measured (W_w). The swollen gels were dried under vacuum at RT for 3 days, and the dry mass was weighed (W_d). The swelling ratio (Q_s) was calculated using equation 5.1. The swelling ratio was used to estimate the average mesh size using the Peppas-Miller expression based on the Flory–Rehner theory.[67,95]

$$Q_s = \frac{W_w - W_d}{W_d} \tag{5.1}$$

5.3.6 Hydrogel degradation by βL enzymes and NP release

Swollen hydrogels were incubated with 1 mL of βL enzyme in 24-well plates shaking (100 rpm) at 37°C. For all βLs tested, activity was reported by the vendor and one unit (U) was defined as hydrolyzing 1.0 μmole of benzylpenicillin per min at pH 7.0 at 25°C. At predetermined timepoints, hydrogels were removed from the solution, placed onto kimwipes to pat dry excess solution, then weighed. Simultaneously, 150 μL of the incubation solution was removed and fluorescence (excitation 580 nm, emission 607 nm) was measured to quantify the concentration of released NPs. The solution was placed back into the incubation wells for continued degradation and release. Standard curves of the NPs in PBS were produced to determine the concentration of NP released into the enzyme incubation solutions.

5.3.7 Hydrogel incubation with collagenases

To test potential non-specific degradation of hydrogels by collagenases, we set up an experiment similar to the incubation with βL as described in Section 3.6. However, 1 mM of calcium chloride (needed for collagenase activity) and 0.02% w/v sodium azide (to prevent bacteria growth) were added to the $1\times$ PBS, and the enzyme solutions were refreshed every 24 hours over the course of 1 week.

5.3.8 Hydrogel degradation by bacteria

Response of hydrogels was tested when incubated with βL-producing bacteria (*B. cereus* 13061[311] and *P. aeruginosa* 27853[63]) and non-βL-producing bacteria (*S. aureus* 25923[322,323]). For all assays, swollen responsive and nonresponsive hydrogels were sterilized via exposure to ultraviolet light in a Nuaire Class II Type A2 biosafety cabinet for 15 minutes.

To test hydrogel degradation by bacteria in solution, NP loaded hydrogels were placed in 12-well plates and 3 mL of 1×10^7 colony forming units (CFU)/mL bacteria in tryptic soy broth (TSB) was added. Controls included solutions of bacteria only, media only, and hydrogels in media only. Over time, digital images of the hydrogels in the wells were taken from the bottom of the plate, and subsequently 100 μL of the solution was removed and the fluorescence (excitation 580 nm, emission 607 nm) was measured to quantify NP release. Standard curves of the NPs in TSB were produced to determine the concentration of NP in the bacterial incubation solutions. The determined concentration was multiplied by the volume of incubation solution remaining to calculate the amount NP in the solution, and then that was normalized to the amount measured in the solutions after complete hydrogel degradation.

To test bacteria mediated degradation in a more dry environment, LB agar plates were streaked three times with cotton swab soaked into a solution of 1×10^8 CFU/mL bacteria, then hydrogels were placed on the infected agar and incubated at 37°C. Digital images of the hydrogels were taken daily.

We also tested responsiveness of hydrogels on infected *ex vivo* porcine skin. Cleaned, shaved, and frozen porcine skin was purchased from a butcher. The tissue was sterilized by soaking in 70% ethanol for 30 minutes then soaked in fresh 1× PBS three times before it was streaked three times using a cotton swab soaked into a solution of 1×10^7 CFU/mL bacteria. The hydrogels were placed on the infected tissue and then incubated at 37°C. Digital images of the hydrogels were taken daily.

5.3.9 Statistical analysis

Results are reported as mean ± standard deviation whenever appropriate. All experiments were repeated with three or more samples. Statistical significance was calculated using one-way and two-way analysis of variance (ANOVA; α = 0.05) with Tukey's post-hoc analysis on GraphPad PRISM™. A value of p <0.05 was considered statistically significant (*, p <0.05; **, p <0.01; ***, p <0.001; ****, p <0.0001)

5.4 Results and Discussion

5.4.1 Synthesis and Characterization of Hydrogels

To engineer βL-degradable hydrogels, we synthesized a βL-cleavable cephalosporin that is functionalized on both ends with maleimides (mal-β-lactam-mal) which can participate as a crosslinker in thiol-ene mediated PEG hydrogel polymerization, thus incorporating the responsive element in the backbone of the hydrogel's matrix, as illustrated in

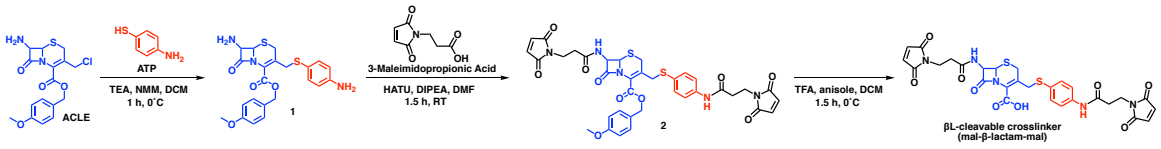

Scheme 5.2: Synthesis scheme of the βL-cleavable crosslinker.

Scheme 5.1. The βL-cleavable β-lactam compound 1 has been previously reported and incorporated as the core of different compounds for the detection[60,63] and treatment of infections.[80] Aminothiophenol (ATP), which is conjugated at the 3'-C site of ACLE (Scheme 5.2), acts as a leaving group that is expelled in the presence of βLs (as suggested in Scheme 5.1). The resulting compound has two amines, one on each half of the compound, which we functionalized with maleimides by conjugating 3-maleimidopropionic acid via amidation (forming compound 2). Post-functionalization with maleimides, the carboxylic acid on the β-lactam, which is an enzyme-substrate recognition site for some βLs,[348] was deprotected by the removal of the p-methoxybenzyl protecting group, resulting in the responsive crosslinker, mal-β-lactam-mal. ^{1}H NMR and HRMS confirmed the synthesis of the crosslinker (see Methods and Figures S1-3). To formulate non-βL-degradable control hydrogels, PEG functionalized with maleimides (mal-PEG-mal) was used as a crosslinker in place of mal-β-lactam-mal. The MW of mal-PEG-mal (494 Da) was chosen due to its similarity to that of the cephalosporin crosslinker (639 Da) to achieve comparable mesh size and physical properties among the responsive and non-responsive hydrogels, reducing unintended differences between the two type of hydrogels, other than the designed degradability of mal-β-lactam-mal crosslinked hydrogels.

The hydrogels were formed by mixing an equimolar ratio of thiols on the 4-arm-PEG-thiol to maleimides on the mal-β-lactam-mal or mal-PEG-mal crosslinkers. However, we observed that the two types of hydrogels demonstrated different crosslinking kinetics, which we hypothesize was due to the difference in the microenvironment of PEG thiols in the vicinity of the β-lactam versus PEG crosslinkers. Previous studies have shown that modulating the pK_a of the thiol could be achieved by placing positively or negatively

charged amino acids in close proximity to the thiols in a peptide sequence, either to increase the rate of slow acrylate-thiol Michael-type reactions[92] or to slow down the efficient maleimide-thiol reactions,[93,94] respectively. The β-lactam's carboxylic acid likely increases the pK_a of the thiols on the PEG arms, reducing the maleimide-thiol reaction rate between 4-arm-PEG-SH and the responsive cross-linker compared to the non-responsive crosslinker. An alternative explanation could be the lowered accessibility of the thiols to the maleimides on the β-lactam crosslinker, due to lower flexibility or increased hydrophobicity compared to PEG crosslinker.

Other ways the reactivity of the thiols can be modulated is through buffer strength and pH. These parameters have been investigated to slow down the highly efficient maleimide-thiol reaction enough to allow sufficient mixing of components to form uniform hydrogels.[93,94] Studies have shown that gelation conditions drastically influence properties of the resulting hydrogel, both microscopic[94] and macroscopic, such as swelling and stiffness,[92] but that unlike stoichiometric ratio and polymer density, pH and buffer concentration did not have as large of an effect on these properties.[92,94] Decreasing the pH decreases the availability of the reactive species, the thiolates (deprotonated sulfhydryl group), based on the Henderson-Hasselbalch equation. However, too slow of a reaction rate could decrease crosslinking efficiency, leading to more defects, and consequently larger mesh size, higher swelling, and reduced mechanical integrity.[91,92] Therefore, we empirically determined PBS concentration and pH for each type of hydrogel individually to allow appropriate time for mixing and transfer to molds before gelation starts. As shown in Table 5.1, the resulting responsive and non-responsive hydrogels had similar swelling ratios ($\sim$18) and average mesh sizes ($\sim$5 nm) (estimated using the Peppas-Miller modified expressions of the Flory-Rehner equation[67,95]), as expected given the similar MW of the two crosslinkers. Furthermore, the data suggests similar crosslinking efficiency under the chosen conditions.

To investigate the potential of this platform for selective, controlled antibiotic delivery,

Hydrogel	Swelling ratio	Mesh size (nm)
10% R	19.30 ± 2.27	5.10 ± 0.27
10% R + NP	17.90 ± 0.71	4.93 ± 0.09
10% NR	18.05 ± 0.78	4.93 ± 0.11
10% NR + NP	17.54 ± 0.42	4.94 ± 0.06

Table 5.1: Hydrogel swelling ratio and mesh size of responsive (R) and non-responsive (NR) hydrogels with (+ NP) or without NP loading. Data presented as average $\pm$ standard deviation; n = 3.

we loaded the hydrogels with fluorescent nanoparticles (NPs) as a model cargo. Given that most antibiotics are smaller in size than the hydrogels' average mesh size, we envisioned encapsulating antibacterial agents in a secondary carrier such as NPs that are larger than the hydrogel's mesh size and would prevent uncontrolled release of the therapeutic, and ensure triggered release only upon matrix cleavage by βLs. We mixed 100 nm fluorescent polystyrene NPs ($\sim$20-fold larger than estimated average mesh size) with the pre-polymer solution to physically entrap the NPs into the hydrogel mesh during gelation (Figure S4), and then monitored their release into incubation solutions (using fluorescence spectroscopy) as the hydrogels degraded. To investigate some of the potential effects of NP incorporation on hydrogel properties, we measured hydrogel degree of swelling and mesh size with and without NP incorporation. We found that addition of the NPs had no effect on either hydrogel property (Table 5.1).

5.4.2 β-lactamase Triggered Hydrogel Degradation and Nanoparticle Release

To test the triggered degradation of hydrogels and release of NPs, responsive and non-responsive NP-loaded hydrogels were incubated with βL from *Pseudomonas aeruginosa* (PA). Figure 5.1a includes images of the progression of degradation of a responsive hydrogel incubated with βL, while the non-responsive hydrogel showed no change in size or morphology, indicating selective cleavage of the β-lactam crosslinker. To further investi-

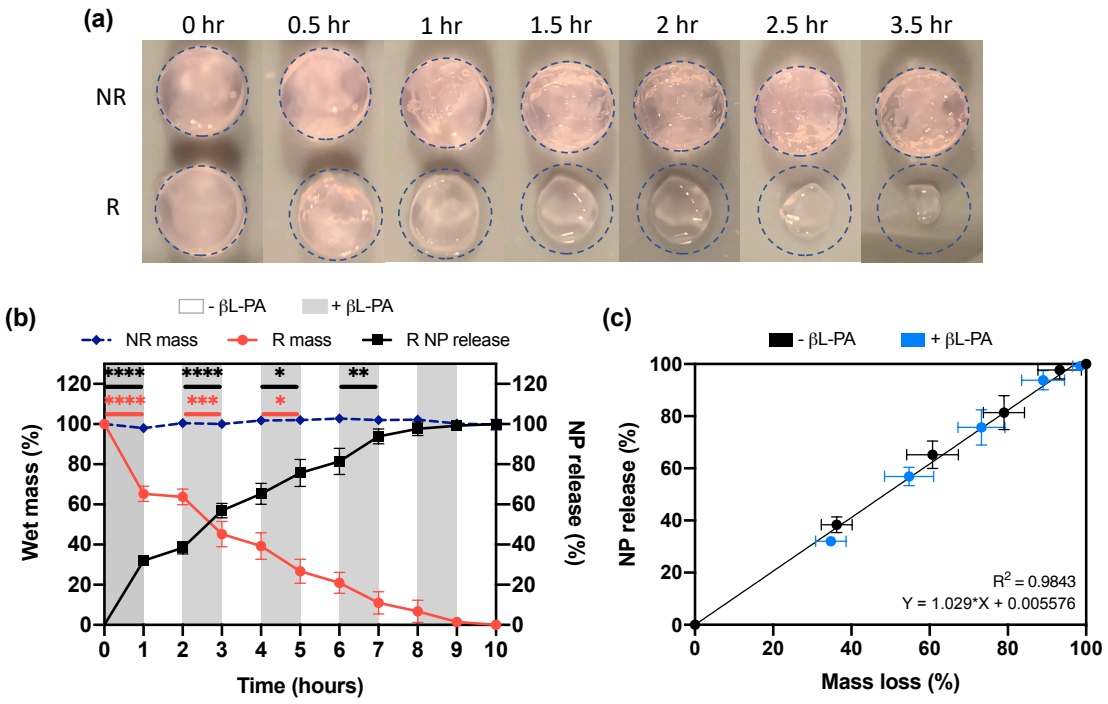

Figure 5.1: βL-triggered hydrogel degradation and NP release. (a) Digital pictures over time of responsive (R) and non-responsive (NR) NP-loaded hydrogels incubated with 50 U/mL βL from PA. The dotted circular overlay represents the hydrogel's original shape/size. Images are representative of three repeats. (b) Normalized wet mass and NP release from R and NR hydrogels with alternating incubation in solutions of 50 U/mL βL from *P. aeruginosa* (grey regions; + βL) or in PBS only (white regions; - βL) for 1 hour per incubation. (c) Normalized NP release as a function of normalized wet mass loss (each data point represents the same timepoint). Wet mass is normalized to initial mass after swelling and before addition of enzymes. NP release at a particular timepoint is normalized to the NP released at complete hydrogel degradation. Data presented as average $\pm$ standard deviation; n = 4. Statistical significance was tested using two-way ANOVA and Tukey's post-hoc analysis comparing consecutive timepoints; * $p < 0.05$; ** $p < 0.01$; *** $p < 0.001$; **** $p < 0.0001$.

gate the specificity of the hydrogel responsiveness, we wanted to incubate the hydrogels with other enzymes that could potentially be found in a wound environment. Collagenases, which cleave peptides in collagen, are produced by bacteria like *P. aeruginosa*[349] as a virulence factor, but also by mammalian cells during tissue remodeling and wound healing (such as matrix metalloproteinases (MMPs)).[350] Figure S5 demonstrates that both responsive and non-responsive hydrogels did not degrade when incubated with 0.1 or 1 mg/mL collagenase for a week, supporting specificity of hydrogel degradation. Responsive hydro-

gels did swell slowly over time however this is not expected to be due to the collagenase considering there was no significant difference in swelling between hydrogels incubated with 0.1 or 1 mg/mL collagenase; additionally no NP release was detected in any of the solutions.

We wanted to also investigate the feasibility of a triggered on-off response of these hydrogels, where degradation and cargo release would seize if the infection was cleared and βLs were no longer present, and would be re-initiated if an infection recurred. Therefore, we alternated incubating the hydrogels in solutions of βLs and blank $1\times$ PBS every hour. Change in hydrogel wet mass as well as NP release into the solutions was measured at each solution change. Figure 5.1b shows the stability of the non-responsive hydrogels, given no change in their wet mass observed over the experimental timescales. On the other hand, responsive hydrogels degraded in the presence of the βL, as demonstrated by the decrease in wet mass over time. The hydrogels did exhibit an on-off response when the enzyme was introduced or removed, respectively, which has also been demonstrated in other enzyme degradable hydrogels.[101] This effect was especially apparent in the earlier timepoints where changes in wet mass and NP release were occurring at a higher rate due to higher surface area. During incubation in buffer alone, any change in mass or NP release that occurred after the incubation was not statically significant from the previous timepoint. NP release from responsive hydrogels into the surrounding solution tracked hydrogel degradation rates, which is demonstrated clearly when the fractional NP release is plotted as a function of fractional mass loss in Figure 5.1c. These results indicate that NP release was solely degradation dependent. There was no detectable NP release from non-responsive hydrogels (fluorescence was below detection limit), further confirming the entrapment of NPs within the hydrogel matrix and release only upon degradation, indicating the potential of this platform to prevent uncontrolled release and achieve enzyme-triggered release of antibacterial agents.

Hydrogel degradation rates of enzyme-responsive hydrogels are dependent on enzyme concentration, degradation kinetics and concentration of the enzyme-labile moiety in the matrix, and polymer crosslinking density.[101,102] An increase in βL concentration led to more rapid degradation of the βLs responsive hydrogels, where 50 and 30 U/mL of βLs from PA resulted in complete degradation within approximately 4 and 8 hours, respectively (Figure 5.10). To probe the effect of enzyme specificity and efficiency in cleaving the β-lactam linker and degrading the hydrogel, we incubated the hydrogels with βLs collected from three different bacteria, from *Bacillus cereus* (BC), *P. aeruginosa* (PA), and *Enterococcus cloacae* (EC). Different concentrations of these enzymes in terms of their enzymatic activity towards benzylpenicillin (one unit (U) is defined as hydrolyzing 1 μmole of benzylpenicillin per min at pH 7.0 at 25°C) were chosen to achieve complete degradation in a few hours. The hydrogels degraded within 5 hours when incubated with 1 U/mL βL from EC, 8 hours with 30 U/mL βL from PA, and 9 hours with 400 U/mL with βL from BC (Figure 5.2). It was interesting that very different concentrations of the three βLs were required to achieve complete degradation in these time scales. The different degradation rates could result from differences in enzyme access to the β-lactam based on enzyme active site properties or hydrolysis catalytic efficiency. Different enzymes have different specificity and activity towards different antibiotics and β-lactam containing compounds.[351] For example, class C βLs are known to have a larger pocket size compared to other classes of βLs and could potentially accommodate polymers or bulky compounds near the β-lactam ring.[63] This property was exploited to achieve selective detection of class C βLs over other classes (such as class A βLs) using βL-responsive fluorescent compounds.[63] More studies are underway to investigate cleavage kinetics of the crosslinker and hydrogels by different types of βL to better understand and investigate potential changes in the β-lactam compound structure to allow recognition and efficient hydrolysis by a larger range of βLs.

For all degradation studies, an overall decrease in the rate of hydrogel degradation is observed over time, suggesting mass loss kinetics are proportional to the hydrogels' sur-

face area, and in turn suggesting surface erosion of hydrogels as opposed to bulk degradation.[97,352] Surface erosion is common in chemically degradable crosslinked PEG hydrogels, where enzyme hydrodynamic diameter is typically on the order of magnitude of the hydrogels' mesh size, which prevents or slows down enzyme penetration and diffusion into the hydrogel.[101] Based on crystallography studies, a class C 39 kDa βL was found to be $\sim 6 \times 5 \times 4$ nm in size,[353] which is close to our hydrogels' estimated average mesh size of ~ 5 nm.

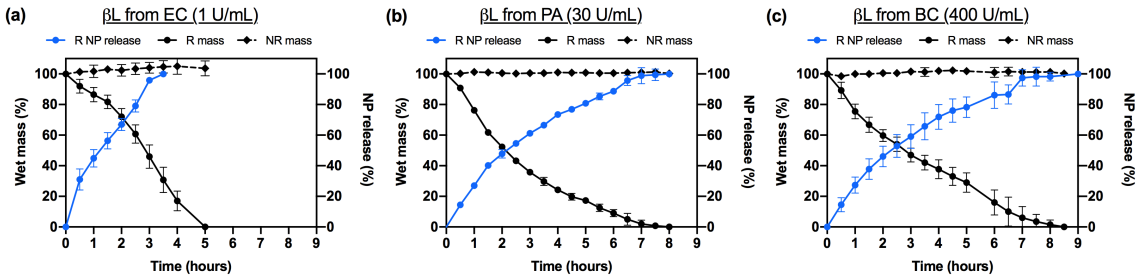

Figure 5.2: Hydrogel degradation and NP release by different βLs. Normalized wet mass and NP release from responsive (R) and non-responsive (NR) hydrogels incubated with βLs from (a) EC (1 U/mL), (b) PA (30 U/mL), and (c) BC (400 U/mL) over time. Wet mass is normalized to initial mass after swelling and before addition of enzymes. NP release is normalized to the fluorescence detected in the solutions after complete hydrogel degradation. Data presented as average $\pm$ standard deviation; n = 4.

Another parameter that could affect hydrogel degradation rate is polymer density; therefore, we investigated the degradation of hydrogels assembled with 5, 10, or 15% weight per volume (w/v) PEG. Higher PEG content led to slower degradation, with complete degradation by βL from PA achieved in approximately 13, 8, 3.5 hours for 15, 10, 5% w/v hydrogels, respectively (Figure 5.3a). Similar decrease in hydrogel degradation rates with increase in PEG concentration has been reported for other enzyme degradable PEG hydrogels, and has been associated with higher crosslinking density, smaller mesh size and reduced swelling.[92,354] As expected, change in polymer density affected hydrogel degradation rates but did not compromise the triggered NP release, as shown by the linear fit of fractional NP release plotted against fractional hydrogel mass loss in Figure 5.3b.

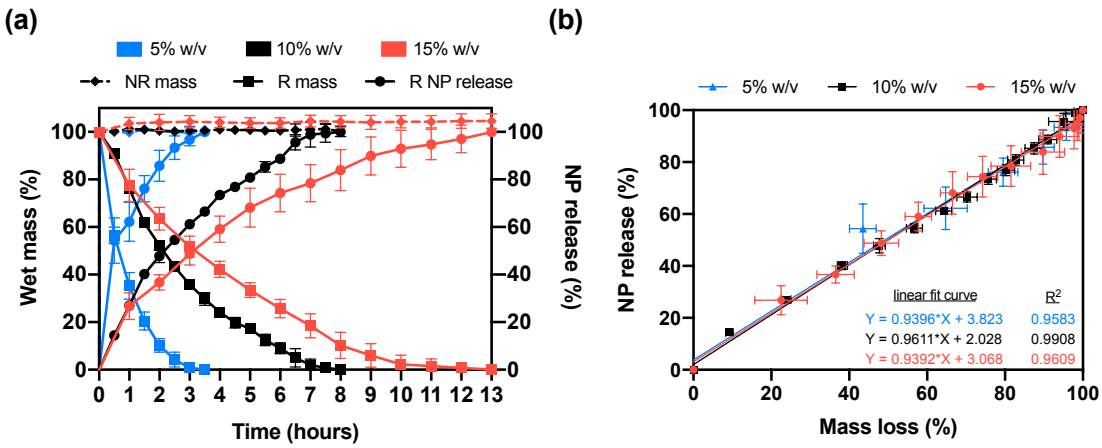

Figure 5.3: Effect of PEG content on hydrogel degradation rate. (a) Normalized wet mass and NP release from responsive (R) and non-responsive (NR) hydrogels with different PEG w/v% (5, 10, 15%) incubated with βL from *P. aeruginosa* (PA; 30 U/mL) over time. (b) Normalized NP release as a function of normalized wet mass loss (each data point represents one timepoint). Wet mass is normalized to initial mass after swelling and before addition of enzymes. NP release is normalized to the fluorescence detected in the solutions after complete hydrogel degradation. Data presented as average $\pm$ standard deviation; n = 4.

5.4.3 Bacteria triggered hydrogel degradation and nanoparticle release

βL degradable and non-degradable hydrogels loaded with fluorescent NPs were incubated in solutions of βL-producing (*B. cereus* 13061[311] and *P. aeruginosa* 27853[63]) and non-βL-producing bacteria (*S. aureus* 25923[322,323]) in their logarithmic growth phase. When incubated with *B. cereus*, the hydrogels degraded (as demonstrated by their decrease in size over time as shown in Figure 5.11), and NP release in the bacteria solutions (monitored *via* their fluorescence) increased as shown in Figure 5.4a. When incubated with *P. aeruginosa*, degradation of responsive hydrogels was completed within $\sim$42 hours (not shown), but NP release measurements were not possible due to the viscosity of *P. aeruginosa* solutions and their release of fluorescent metabolites such as pyocyanin[355,356] which could interfere with NP detection. On the other hand, no changes in hydrogel size or morphology were apparent, nor any NP release detected, during incubation with non-βL-

producing bacteria, *S. aureus*. Similarly, no changes were detected in non-responsive hydrogels incubated with any of the three bacteria strains. These results further confirmed the selective degradation of the responsive hydrogels by βLs.

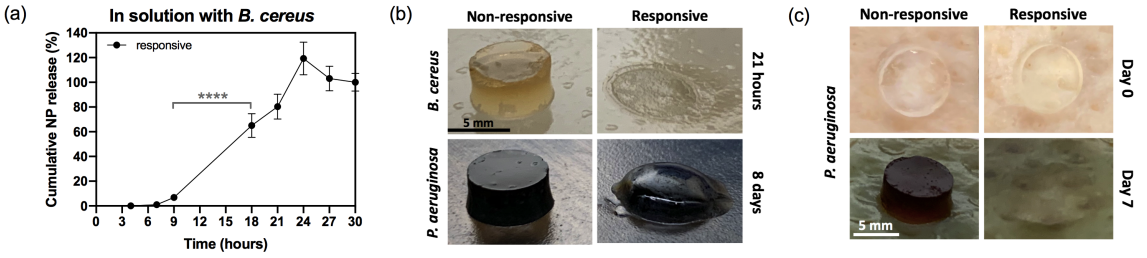

Figure 5.4: Hydrogel degradation by βL-producing bacteria. Normalized NP release from responsive (R) and non-responsive (NR) hydrogels incubated (a) in solutions of *B. cereus*. Data is presented as average $\pm$ standard deviation; n = 3. Statistical significance was tested using one-way ANOVA and Tukey's post-hoc analysis comparing consecutive timepoints; **** $p < 0.0001$. Images of unloaded R and NR hydrogels incubated on (b) agar infected with *B. cereus* (after 21 hours) or *P. aeruginosa* (after 8 days), or (c) on porcine *ex vivo* skin tissue infected with *P. aeruginosa* on day 0 (top) and day 7 (bottom).

To investigate hydrogel degradation in a drier environment, which would be more mimetic of a wound than shaking in solution, hydrogels were incubated on infected agar. Similar to the results seen in bacterial solutions, responsive hydrogels degraded on agar infected with *B. cereus* and *P. aeruginosa*, while non-responsive hydrogels did not (Figure 5.4b). Surprisingly the degradation of the hydrogel by *B. cereus* on agar was faster than in solution (within $\sim$21 hr versus in $\sim$30 hrs, respectively). However, the degradation of the hydrogels was much slower by *P. aeruginosa* on agar (Figure 5.12) than in solution ($\sim$8 days versus $\sim$42 hr, respectively). The green-blue color seen in the hydrogels is likely the pyocyanin secreted by *P. aeruginosa*,[355,356] which typically changes the color of media and agar, and seems to diffuse into the hydrogels. We had anticipated a slower degradation rate on agar and tissue than in solutions, as seen with *P. aeruginosa* but not *B. cereus*, due to the degradation front being limited to only one side of the hydrogel (assuming surface erosion). Additionally, static, drier conditions could lower diffusion of enzymes and clearance of degradation products from the surface of hydrogels compared to incubation in solution

with shaking. However, other factors such as media[357,358] and incubation conditions could affect the bacterial growth rate and enzyme production.

Furthermore, to more closely mimic a tissue infection, we tested the degradation of hydrogels on infected *ex vivo* porcine skin, which is commonly used as a model to study wound infections.[359] As shown in Figure 5.4c, degradation of responsive hydrogels on porcine skin was slower than in solution, but, interestingly, degradation induced by *P. aeruginosa* was faster ($\sim$6 days) than by *B. cereus* ($\sim$9 days, not shown), in contrast to what was observed in solution and on agar. One potential reason for faster degradation by *P. aeruginosa* might be higher growth rates of bacteria, which has been observed on an *ex vivo* human skin model infected with *P. aeruginosa* PAO1,[349] potentially resulting in a higher concentration of βLs. This high growth rate is hypothesized to be due to *P. aeruginosa*'s secretion of proteases such as collagenase, as mentioned earlier, that can cleave collagen abundant in the dermis and convert it into nutrients.[349] Again, non-responsive hydrogels remained stable, demonstrating the selective degradability of the hydrogels by βL-producing bacteria even when grown under different conditions. The differences in hydrogel degradation rates based on the strain of bacteria and the culture conditions warrants further investigation and *in vivo* testing to better mimic wound infections in terms of bacterial density and growth rate and secreted βL types and concentrations.

5.5 Conclusions

A βL cleavable cephalosporin was functionalized with maleimides on both of its halves and used as a crosslinker in the synthesis of hydrogels by end-crosslinked polymerization with multiarm thiol-terminated PEG macromers *via* Michael-type addition. The βL-degradable hydrogels degraded in the presence of βLs extracted from three different bacteria, exhibiting a decrease in wet mass over time accompanied with the release of fluorescent

polystyrene NPs loaded into the hydrogels as model cargo. The NP release tracked hydrogel degradation rates indicating degradation controlled release. Hydrogels incubated in collagenase, a common peptidase found in infected and non-infected wounds, did not degrade the hydrogels or release NPs. Control hydrogels lacking the responsive moiety also remained stable and did not release any detectable NPs into the surrounding βL solution, suggesting selective degradation of the responsive hydrogels by βLs. Responsive hydrogels also degraded in the presence of βL-producing bacteria but remained stable if they lacked the degradable motif or were incubated with non-βL-producing bacteria. Degradation rates differed based on bacteria strain (*B. cereus* vs. *P. aeruginosa*) and growth conditions (in solution, on agar, or on *ex vivo* porcine skin), which is likely correlated to the type and concentrations of βL secreted. The degradable hydrogels also demonstrated an on-off response when βLs were added or removed, respectively, supporting their triggered nature. These hydrogels have the potential to be used as injectable or pre-molded hydrogels for the bacteria triggered release of antibacterial agents, to reduce unnecessary exposure, localize delivery, and reduce off-site toxicity, potentially reducing susceptibility to bacterial antibiotic resistance development. Current studies include loading an antibacterial agent and testing the rate of hydrogel degradation and drug release in infected and non-infected clinical wound exudate. These studies will inform the drug loading needed for accurate dosing based on degradation rates.

5.6 Supplemental Information

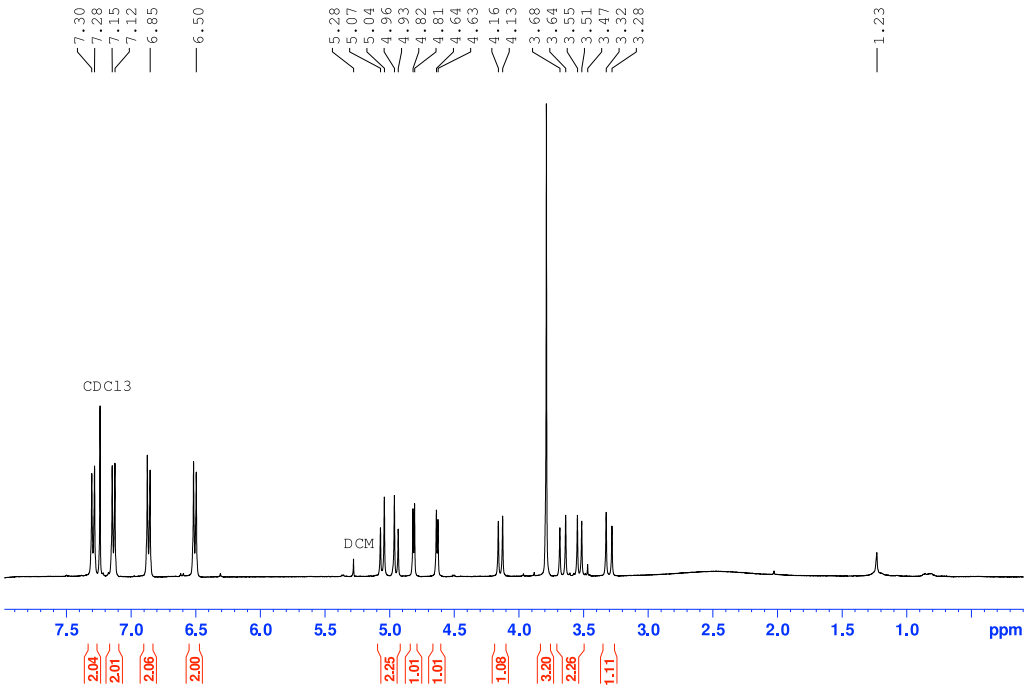

Figure 5.5: ^{1}H-NMR spectrum of compound **1** ($CDCl_3$, 400 MHz).

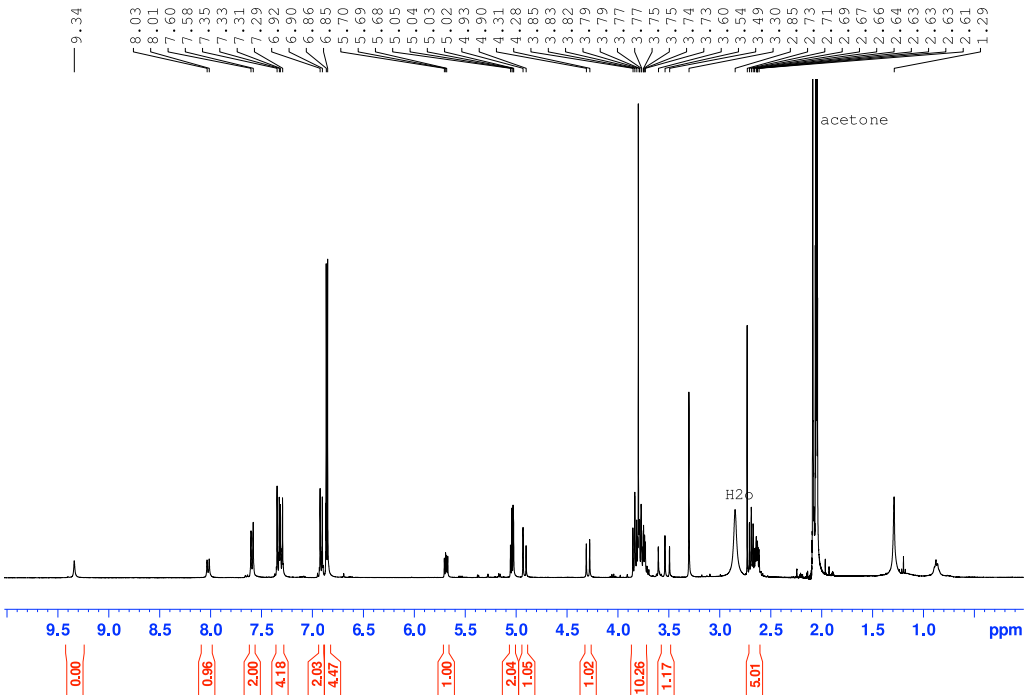

Figure 5.6: ^{1}H-NMR spectrum of compound **2** (acetone-d_6, 400 MHz).

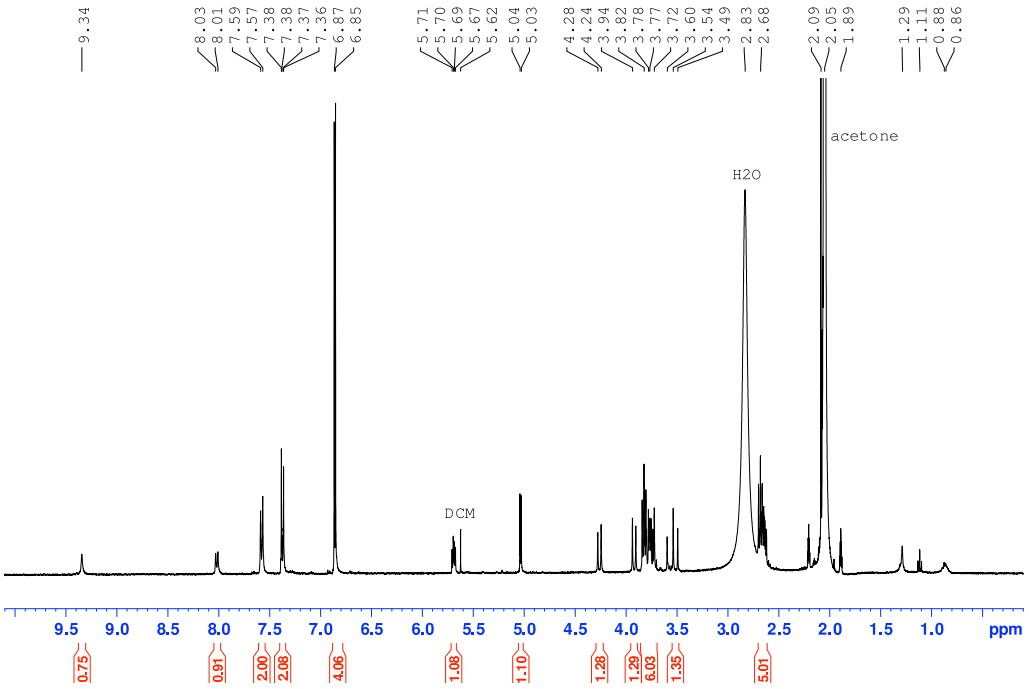

Figure 5.7: ^{1}H-NMR spectrum of the crosslinker, mal-β-lactam-mal (acetone-d_6, 400 MHz).

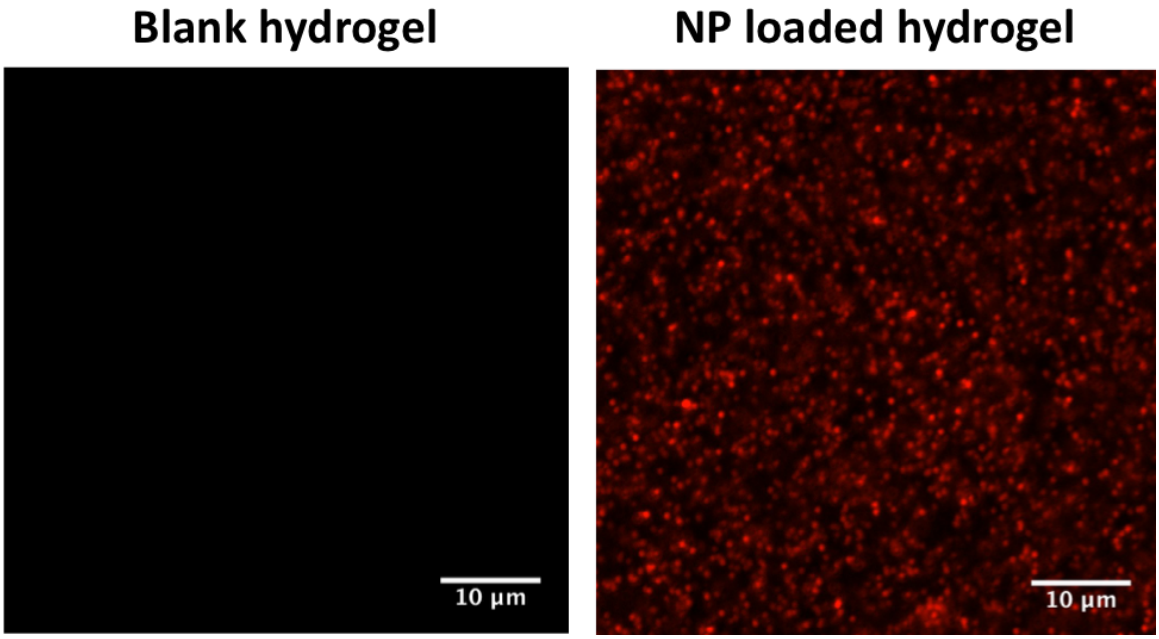

Figure 5.8: Confocal microscopy images of blank or NP-loaded, swollen hydrogels taken with a 25× water immersion objective using a 561 nm laser and 570 - 620 nm filter.

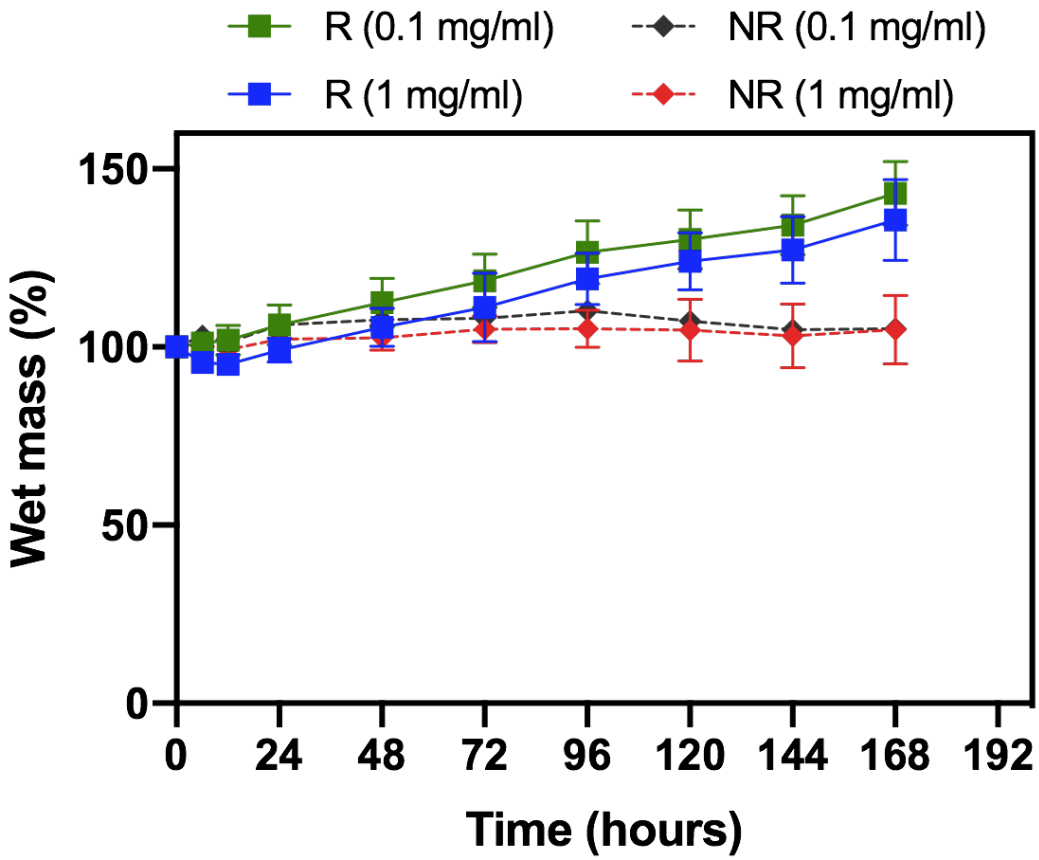

Figure 5.9: Incubation of hydrogels in collagenases. Normalized wet mass of responsive (R) and non-responsive (NR) hydrogels incubated with 0.1 or 1 mg/mL of collagenases over time. No NP release was detected. Data presented as average ± standard deviation; n = 3.

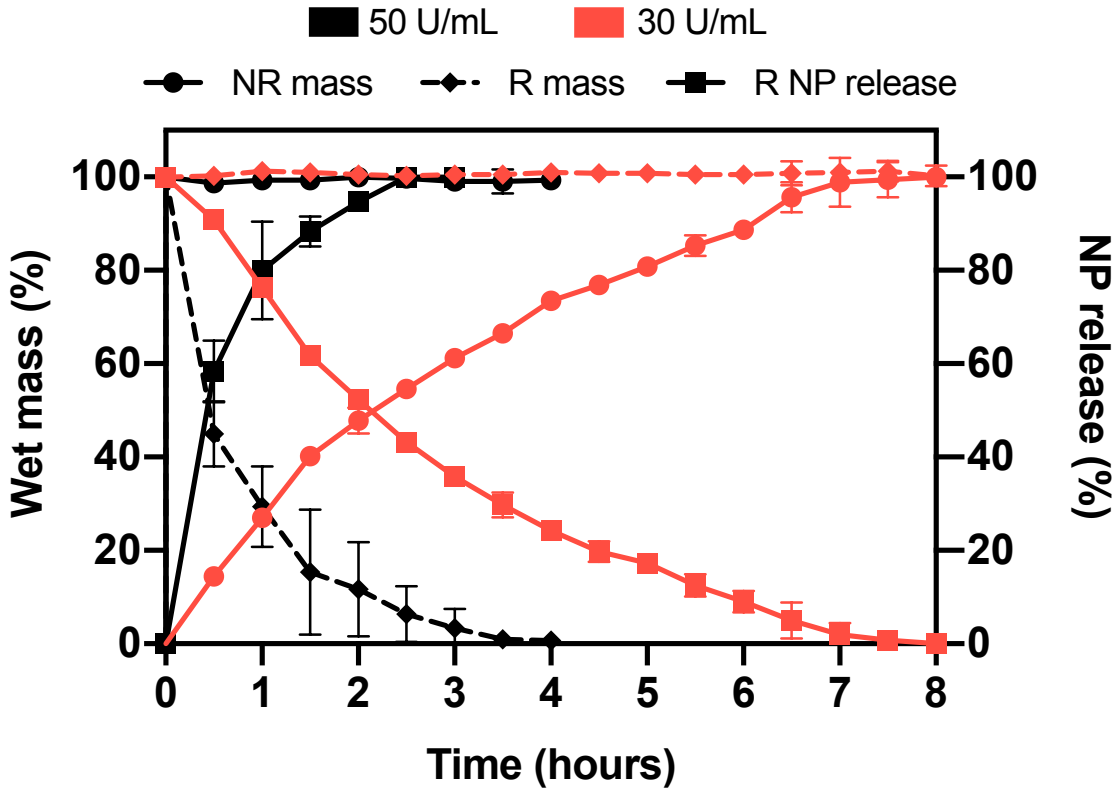

Figure 5.10: (a) Normalized wet mass and NP release from responsive (R) and non-responsive (NR) NP-loaded hydrogels incubated in solutions of 30 or 50 U/mL βL from *P. aeruginosa*. Wet mass is normalized to initial mass after swelling and before addition of enzymes. NP release is normalized to the fluorescence measured in the solutions after complete hydrogel degradation. Data presented as average $\pm$ standard deviation; n = 3 or 4.

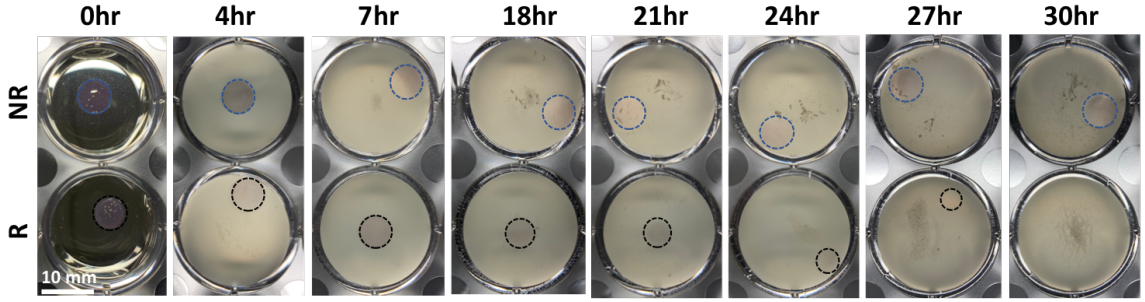

Figure 5.11: Digital images over multiple hours (from the bottom of the well plates) of responsive (R) and non-responsive (NR) NP-loaded hydrogels incubated with solutions of *B. cerues* at 37°C shaking at 100 rpm. The dotted circle overlay outlines the hydrogel's edge. Images are representative of three repeats. Note: The solution at 0 hours seems clear because at $1 \times 10_7$ CFU/mL, the media is not cloudy yet. The last image is at 30 hour after the bacteria solution has been removed for clearer view of hydrogels in the wells.

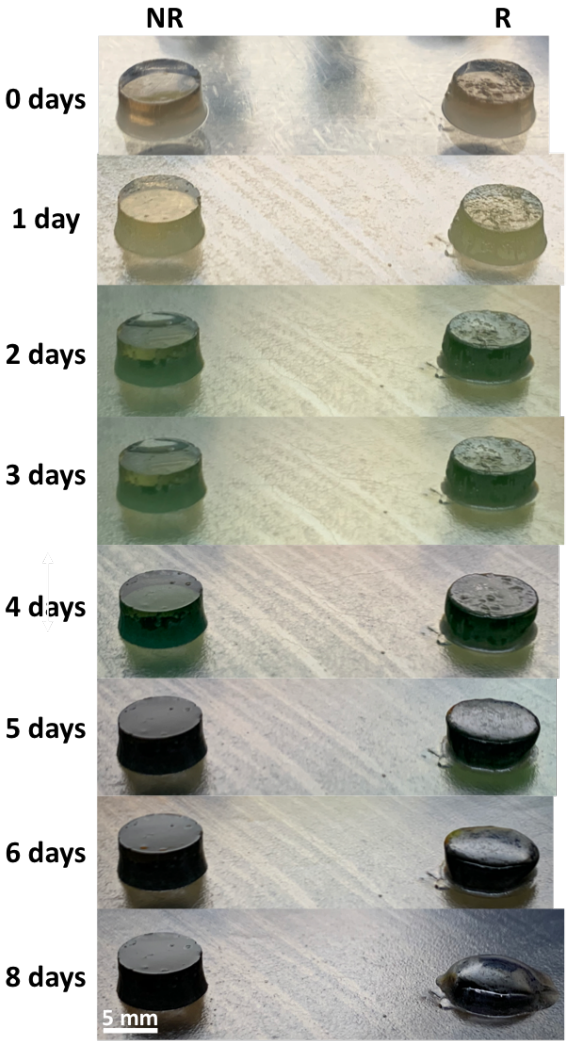

Figure 5.12: Digital images over multiple days of responsive (R) and non-responsive (NR) hydrogels incubated on agar streaked with *P. aeruginosa* at 37°C. Images are representative of one (skin) or two (agar) repeats.

Chapter 6

Conclusions

In this thesis we developed biomaterials for effective prevention, detection, and treatment of bacterial infections. The focus was on polymeric antibacterial coatings and βL responsive materials for the detection and effective treatment of antibiotic resistant bacteria infections. Below is a summary of the conclusions and a discussion of future steps and perspectives.

6.1 Polymeric Antibacterial Coatings

6.1.1 Conclusions

In chapter 2, we discussed the advantages that LbL self-assembly, with its versatility and modularity, can bring to the design of drug delivery systems for different biomedical applications. The focus of chapter 2.6 is LbL assembled biomaterials for bacterial infection prevention and treatment. We wanted to develop coatings that incorporated many of the advantageous properties reported. Therefore, we chose PLL as an antibiotic alternative, HA as a hydrophilic polyanionic polysaccharide, and LbL as a technique to form dynamic multilayer films (chapter 3). These films successfully inhibited planktonic bacterial growth ($>$99.8% inhibition) and reduced attachment to the coated surface (by $\sim$60–70% compared to non-film-coated surfaces) through anti-adhesive properties, contact killing, and release of PLL into the surrounding solution. This was the first study demonstrating the inherent antibacterial efficacy of (PLL/HA) films without any modification or incorporation of additional antibacterial therapeutics. They were effective in inhibiting the growth of both gram-positive (*S. aureus*, methicillin resistant *S. aureus*) and gram-negative (*P. aeruginosa*, *E. coli*) bacteria. By investigating the differences between films assembled using PLL of three different MWs, our studies revealed that the mobility of PLL within the films results in extended PLL release providing long-term antibacterial efficacy at certain PLL MWs. We found that even though the highest MW PLL examined resulted in more stable films,

these films were only effective over 24 hours, while films assembled with lower MW PLL could be used to inhibit growth over multiple bacterial exposures. High MW reduced PLL mobility limiting the fraction of PLL that can diffuse from the film to interact with bacteria. When PLL MW was low enough to allow its diffusion throughout the entirety of the film, there was a larger reservoir of mobile PLL that could be released over time; in this case, film dissolution timescales dictated the number of possible repeated uses (up to 5 uses for low MW PLL and up to 13 uses for medium MW PLL).

6.1.2 Future Perspectives

The different advantages of high and low MW PLL, such as more stable films and extended PLL release, respectively, could potentially be combined to provide longer lasting and/or slower releasing films. This warrants investigation into the effects of combining different MW PLL into one film. Assembly conditions, and whether different MW PLL are mixed together or incorporated at different stages of film assembly, will need to be optimized to control PLL loading into the film. For certain polyelectrolytes, a mixture of high and low MW polymer in the same deposition solution for short deposition times, could lead to low MW polymer outcompeting the high MW polymer and making up a higher portion of the polymers in the resulting film, due to their higher mobility. Alternatively, when different MW polymers are added at different assembly steps, due to the dynamic nature of LbL assembly, higher MW polymers can strip off or exchange lower MW polymers when the film is incubated in the solution of high MW polymer.[138] Assembly parameters such as solution ionic strength and deposition time can be regulated to achieve desired film architectures.[138,360] Similarly different types of antibacterial polymers with different MWs and structures could be incorporated into the films, such as antibacterial peptides, polymeric quaternary ammonium compounds, chitosan, etc., potentially providing synergy. Even antifungal peptides could be added for the prevention and treatment of polymicrobial in-

fections.

This approach of combining different MW polymers may potentially be used for temporally controlled release of different therapeutics from the same film. Multiple types of polymers could be used such as those that are functional themselves (like polycations as antimicrobials or for DNA transfection), or polymers with drugs tethered[50] or encapsulated within a polymeric host.[158] Consequently, these types of films could be utilized for most drug delivery application which benefit from temporal release of drugs, like delivery of an antibiotic followed by a growth factor for wound healing,[179] or a cancer drug resistance inhibitor followed by a chemotherapeutic.[198] These films can be used to assemble coatings on wound dressings, sponges, implants, other medical devices, or even to form hollow or coated NPs.

Other lessons gained from our studies were related to non-specific protein attachment of high MW polycations in LbL films. *In vivo* studies will be valuable to further inform the effects of proteins found in both infected and non-infected tissue on the films' antibacterial efficacy. This is important since our preliminary studies on fibronectin attachment and comparison of preincubation in $1\times$ PBS versus bacterial broth demonstrated that the highest MW PLL promoted protein adhesion which could have contributed to loss of antibacterial efficacy after 24 hours for this set of films. In fact, protein fouling is a major issue for almost all biomaterials for different applications, and the understanding that polymer MW and charge density influences the degree of protein adhesion could help mitigate this issue during the design process.

6.2 β-lactamase Responsive Biomaterials

6.2.1 Conclusions

Bacteria Diagnostic Biomaterials

In our initial efforts to synthesize a chromogenic βL substrate-polymer conjugate to be incorporated into biomaterials, we attached PEG to a commercially available substrate, CENTA. However, that resulted in loss of the βL responsive color change, which we expect is due to modification of the β-lactam carboxylate, which is an enzyme recognition site[348] and/or the carboxylate on the chromophore, affecting its color change once expelled. This motivated us to synthesize our own substrate which contains a chromophore lacking reactive groups and a maleimide functional group on the other end to allow facile attachment to polymers, while the β-lactam carboxylate remains protected during all chemical modifications. Using this approach, (chapter 4), we conjugated the substrate to both short linear and high MW multi-arm PEG while maintaining the substrate's responsiveness to βLs. Our product demonstrated a color change from clear to yellow in the presence of different βLs as well as βL-producing gram-positive (*B. cereus*), and gram-negative bacteria (*P. aeruginosa*, *E. cloacae*), but not when incubated with non-βLs producing bacteria (*E. coli* DH5-α). Similarly, PEG hydrogels with the βL substrate tethered to the polymeric backbone demonstrated this color change in the presence of βL, while control non-responsive hydrogels did not. One advantage of this approach is that conjugating the substrate to the polymer helps sequester the indicator compound within the biomaterial, preventing its release before it is needed. Additionally, our maleimide-β-lactam compound can be conjugated to polymers other than PEG, such as HA or gellan, to form a wide array of biomaterials. To our knowledge, this is the first time that a βL substrate has been conjugated to a polymer for direct and facile point-of-care colorimetric detection of infections

by βL-producing bacteria.

Bacteria Degradable Hydrogels

A βL cleavable cephalosporin was functionalized with maleimides on both of its halves and used as a crosslinker in the synthesis of end-crosslinked hydrogels with multiarm thiol-terminated PEG macromers *via* Michael-type addition. The βL-degradable hydrogels degraded in the presence of βLs extracted from three different bacteria, demonstrating a decrease in wet mass over time accompanied with the release of fluorescent polystyrene NPs loaded into the hydrogels as model cargo. The NP release tracked hydrogel degradation rates indicating degradation controlled release. Hydrogels incubated in collagenase, a common peptidase found in infected and non-infected wounds, did not degrade the hydrogels or release NPs. Control hydrogels lacking the responsive moiety also remained stable and did not release any detectable NPs into the surrounding βL solution, suggesting selective degradation of the responsive hydrogels by βLs.

The βL responsive hydrogels also degraded and released NP when incubated with βL-producing bacteria but remained stable with non-βL-producing bacteria. When tested under three different bacterial growth conditions (in solution, on agar, on *ex vivo* porcine skin), in an attempt to mimic various infection or wound environments, hydrogel degradation rates differed by different bacteria and under different conditions. The obvious differences in the three bacterial assays is the hydrated environment with shaking versus dry static incubation. With the first we would expect higher diffusion rates of the enzymes to the hydrogel, and faster clearance of the PEG degradation products from the surface of the hydrogel, potentially improving access of enzymes to the hydrogel. The other difference, under the assumption of surface erosion, is that degradation of the hydrogel proceeds from only one plane when incubated on agar or skin tissue versus from all surfaces when incubated in solution. However, there are other factors, requiring further investigation, which

affect bacteria growth rate and enzyme type and production rate, such as nutrients (type of media or tissue),[357,358] solution versus agar culture, static versus shaking, bacterial density (potentially affecting quorum sensing[361]). For example, an interesting observation was that the rate of degradation of hydrogels by *B. cerues* on agar was faster than in solutions. Another observation was that hydrogels incubated on porcine skin degraded faster when the skin was infected with *P. aeruginosa* than with *B. cereus*, which was opposite to what was seen in solution or on agar. This could potentially be explained by the faster growth and perhaps higher βL production by *P. aeruginosa* due to their release of collagenases which convert collagen abundant in skin into nutrients.[349]

Prior to the development of these responsive hydrogels, we first optimized gelation conditions gaining multiple insights. Initial approaches were to conjugate the βL responsive moiety to acrylate functionalized PEG chains to utilize the commonly used free-radical polymerization technique to form the hydrogels. However, after multiple attempts using different conjugation chemistry and reaction conditions, we hypothesized that differences in the size and hydrophilicity of the PEG (5 or 10 kDa) and βL cleaveable β-lactam compound ($\sim$400 Da) was preventing the attachment of two PEG chains per β-lactam compound; once one PEG is attached, it potentially aggregates around the hydrophobic compound and steric hindrance prevents attachment of a second PEG to the other side. Therefore, we investigated forming micelles from this seemingly amphiphilic conjugate with a cleavable cephalosporin on one end (appendix chapter A). Using thin film hydration we formed NPs that encapsulated the untethered β-lactam compound as a model cargo. We envisage loading the NPs with antibiotics that are similar in structure to β-lactam compound and would assemble in the hydrophobic core, resulting in NPs with a PEG shell for the delivery of antibiotics. These NPs could potentially also demonstrate βL responsive disassembly due to the cleavage of the β-lactam compound, leading to triggered release of the antibiotic. To develop the responsive hydrogels, we searched for an alternative gelation approach and turned to end-linked polymerization (chapter 5), where the thiol termi-

nated 4-arm-PEG macromer was mixed with the maleimide functionalized βL-degradable crosslinker during gelation. The hydrophobic crosslinker was not soluble in PBS but was soluble in DMSO, which is miscible with water, and the 25% of DMSO/PBS in the pre-gelation mixture did not affect gelation. With this approach and the rapid thiol-maleimide reaction, there were no issues of steric hindrance and gelation proceeded successfully.

6.2.2 Future Perspectives

The *in situ* gelation mechanism of the hydrogels discussed here can be used to formulate injectable hydrogels (e.g., into bone fractures[104]) and hydrogels that fill in irregular deep wounds.[362] However, conjugation of the substrates to polymers, as we have shown, allows the synthesis of different types of biomaterials other than hydrogels, such as NPs and films, as well as combining them with existing polymeric wound treatments to develop multifunctional therapeutics with convenient application to injury sites. For the diagnostic, the conjugate could also be covalently attached to surfaces or sprayed onto a surface to visually detect or test for infections on hospital surfaces or biomedical devices. In these cases, the diagnostic biomaterials could benefit from a more dramatic and distinguishable color change, which may be achieved by changing the chromophore attached at the C-3' position of the cephalosporin.

For βL degradable hydrogels, one of the main next steps is loading an antibacterial therapeutic and testing its release and activity against βL-producing bacteria. The loaded drug must remain entrapped in the hydrogel until the hydrogel is triggered to degrade and the drug must be effective against βL-producing bacteria. A promising approach would be to load NPs larger than the average mesh size, similar to the fluorescent polystyrene NPs we had loaded. These NPs could be carriers for antibiotics such as liposomes[363] and micelles[364], or have antibiotics conjugated to the surface (e.g., gentamicin[365] or vancomycin[366] functionalized NPs), or the NPs could be inherently antibacterial, such as cationic NPs (e.g.,

chitosan NPs[367]), or metallic NPs (e.g., silver NPs[368]). To advance these hydrogels even further, other types of therapeutics could be incorporated, in addition to antibacterial agents, to develop multifunctional treatments. For example, growth factors have been loaded and released from similar PEG hydrogels,[31] exhibiting preserved activity, so a combination of antibiotics and growth factors could be loaded to promote both wound healing and infection prevention and treatment. Given the modularity of the gelation mechanism, other cleavable motifs can be easily incorporated to provide hydrogels with dual or multi-responsive properties. However, portions of hydrogels loaded with antibacterials versus growth factors need to be separated to maintain purely βL-controlled release of antibiotics. 3D printing is one approach that could be used to form the stratified hydrogels.[369] Another interesting avenue would be encapsulation of probiotics, which have a gained a lot of attention as an alternative treatment to antibiotics to treat antibiotic resistant infections. Since Michael addition crosslinked hydrogels have shown positive results in encapsulation and delivery of mammalian cells from hydrogels *via* enzyme responsive cleavage of the matrix,[102,345,347] we might expect similar results for βL triggered release of bacterial cells.

There still remain a number of tests needed to optimize the βL responsive systems to ensure their efficacy *in vivo*. For both diagnostic and degradable biomaterials, gaining a better understanding of substrate hydrolysis kinetics by different types and classes of βLs is essential. The purified βLs and βL-producing bacteria used in our studies were commercially available and represent a range of βLs from gram-positive and gram-negative bacteria, but they are not thoroughly characterized. Therefore, current ongoing studies include the use of strains of bacteria transformed with plasmids of classified βLs (including the host strain that does not produce βLs as a control), as well as clinically relevant bacterial strain with characterized βLs. These studies will be important to better understand the specificity of the responsiveness. Ideally, the hydrogels would degrade selectively by βLs but by a wide range of βL classes.

Similarly, more extensive testing of nonspecific cleavage of the substrates by other enzymes that might be present in a wound is needed. As mentioned earlier, the hydrogels did not degrade in the presence of collagenases which are commonly found in infected and non-infected wounds and can cleave peptides. Preliminary testing using other enzymes secreted by microbes that could potentially be in an infected wound including bacterial lipases, bacterial α-amylase, and fungal secreted aspartyl proteinases, showed no changes in the hydrogels either. Only when incubated with trypsin, a pancreatic enzyme that cleaves amides, responsive hydrogels degraded within 6 hours, while non-responsive hydrogels did not. If there are trypsin-like enzymes in the wound, they might non-selectively degrade the hydrogel; this needs to be better investigated using more relevant *in vitro* and *in vivo* models to mimic the types and concentrations of enzymes in wounds.

Another critical factor is the concentration and enzymatic activity of βLs in wounds and whether they would cause a sufficient color change or degrade the hydrogels and release the drug at relevant timescales. It was difficult to find this type of information in the literature. Clinical samples of wound exudate of both uninfected and infected wounds, specifically those infected with βL-producing and non-producing bacteria, could inform both specificity and timescales of hydrogel degradation and drug release in *in vitro* studies. These tests would help inform hydrogel drug loading concentrations for appropriate dosing based on average rates of degradation. If needed, there are multiple ways to modulate the rate of degradation including, as demonstrated in our studies, changing polymer density, or as shown with other enzyme degradable PEG hydrogels, by changing PEG MW,[354] increasing the number of degradable motifs per crosslink,[103] or their overall concentration in the hydrogel.[101] An alternative approach would be to explore changes in the β-lactam compound structure to allow more efficient hydrolysis or recognition by a larger range of βLs. For example, increasing the distance between the β-lactam and the maleimide-thiol PEG conjugation site, might increase access of the enzyme or permit βLs with smaller active sites to hydrolyze the β-lactam. We could also test adding functional groups that are

known to play a role in enzyme recognition, such as the benzylic substituents at the C-7 amide, before the addition of the maleimide to see if that can enhance enzyme-substrate kinetics.[79,370]

Characterization of the mechanical properties of the hydrogels such as compression moduli, and how changing polymer density or MW and loading the hydrogels with NPs might affect their stiffness, is also important to ensure hydrogels are manageable during application and can withstand different pressures. Additional studies for drug loaded hydrogels would be investigating how forces exerted during application of gels for *in situ* gelation or applying a bandage potentially affect drug release. For the diagnostic hydrogels, tests should include investigating to what degree occupation of a portion of PEG arms with the substrate affects mechanical stability (higher swelling is visually clear for substrate modified hydrogels, suggesting lower stiffness), and what concentration of the chromogenic substrate is needed to produce a sufficient color change, there would need to be a balance between the two effects. Using PEG with more arms (8 versus 4) would allow higher ratios of functionalization with the substrate with a smaller effect on gelation efficiency and mechanical properties.[331]

Shelf-life of the biomaterials should be tested in terms of the stability of the hydrogels as well as the responsiveness of the cleavable moieties over times whether the hydrogels are stored hydrated or dried. Dehydrating the hydrogel to be stored without the need for cold storage would be ideal if two requirements are met: the hydrogel regains all of its structural and mechanical properties once reswollen and if the loaded antibacterial therapeutic also maintains its properties and efficacy.

The literature on infection treatment has seen a surge in bacteria responsive biomaterials, yet not many have reported testing of these biomaterials *in vivo*, which is where the field is lacking behind some other biomedical areas, like cancer therapeutics. Once the hydrogels have been loaded with a therapeutic and its triggered efficacy has been optimized,

in vivo studies could provide indications of the benefits of treatment with the βL controlled hydrogels, compared to non-responsive diffusion controlled hydrogels and to systemically administered antibiotics in terms of both eradicating bacterial infections and maintaining microbiome health.

6.3 Impact and Contributions

The studies in this thesis provide structure-property-function relationships that can inform development of technologies for polymeric multilayer films and enzyme degradable hydrogels in general, and antibacterial coatings and βL-responsive biomaterial in specific. With the (PLL/HA) films, we demonstrated how these commonly investigated films are inherently antibacterial, and more interestingly, that their antibacterial mechanism of action and repeated usage/extended efficacy is influenced by PLL MW. Our studies also emphasized the importance of testing the fouling and toxic properties of multilayer films and their components (particularly, high MW polycations) to ensure efficacy and biocompatibilty of such coatings. For the βL responsive material, we investigated βL substrate structures, polymer-small molecule conjugation chemistry, and hydrogel crosslinking chemistry to synthesize these responsive biomaterials. With these conjugates, we developed a platform that will allows us to answer many more questions. Using these building blocks, we can develop biomaterials of different scales (nano to macro) or multifunctionality depending on application needs. With the flexibility and versatility of polymers and our approach, there are many parameters that can be investigated and optimized to develop material with enhanced management of bacterial infections. Furthermore, bacteria-responsive diagnostics and therapeutics have the potential to bring us closer to personalized medicine to improve the treatment of the individual, while also protecting global communities from the threat of antibiotic resistance.

Appendices

Appendix A

Cephalosporin-PEG conjugate micelle-like nanoparticles

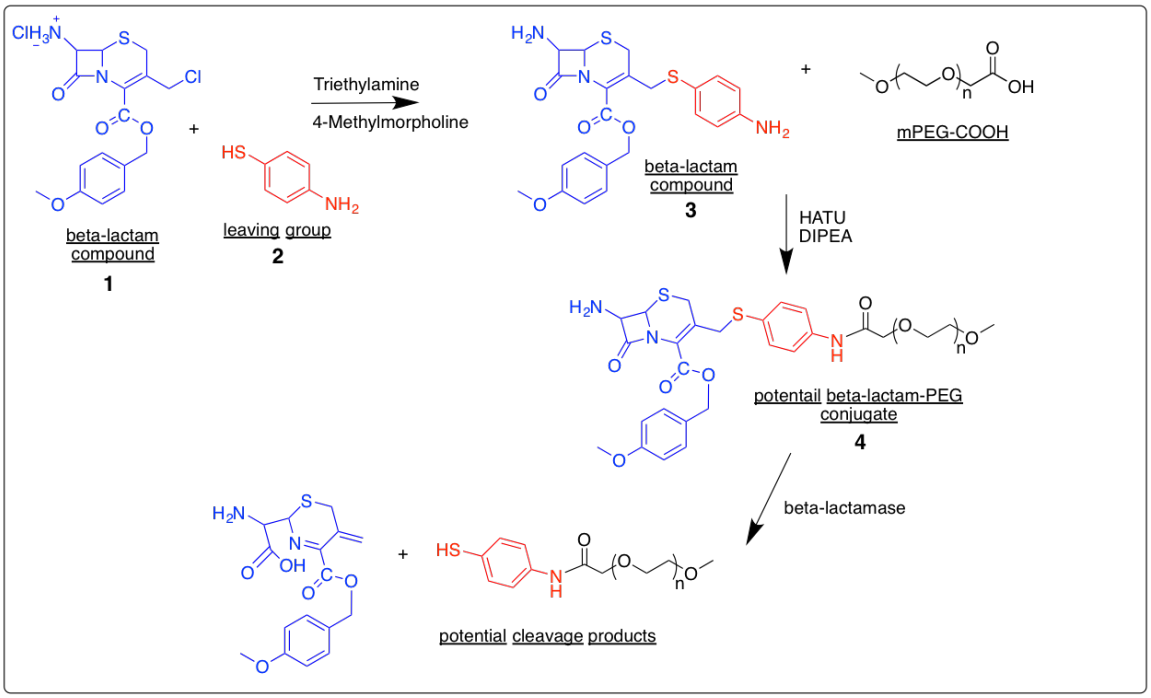

Figure A.1: Synthetic scheme of the β-lactam-PEG conjugate. Either amine on the β-lactam compound could be conjugated to the carboxylic acid on a PEG chain (one of the two possibilities is shown here). We have not detected a conjugate with 2 PEGs and 1 β-lactam. In the presence of βLs, the amide is hydrolyzed and the leaving group is expulsed. HATU: 1-[Bis(dimethylamino)methylene]-1H-1,2,3-triazolo[4,5-b]pyridinium 3-oxid hexafluorophosphate; DIPEA: N,N-Diisopropylethylamine.

To render synthetic polymers bacteria-responsive, we conjugated a βL cleavable cephalosporin to PEG (Scheme A.1). Due to the differences in polarity of the PEG and the β-lactam compound, we hypothesize the amphiphile we synthesized will self-assemble and would be able to entrap a functional antibiotic. When exposed to βLs, we anticipate the cleavage of the β-lactam compound will affect the polarity of the conjugate, leading to the disassembly of the self-assembled structures and release of the entrapped antibiotic.

The conjugate was characterized using proton nuclear magnetic resonance (^{1}H NMR) spectroscopy and matrix-assisted laser desorption ionization time-of-flight mass spectrometry (MALDI-TOF MS). The NMR spectrum of the conjugate (Figure A.2, c) contains both PEG (a) and β-lactam compound (b) protons. MALDI-TOF specta (Figure A.3) showed an increase in the molecular weight of the β-lactam-PEG conjugate compared to unmodified

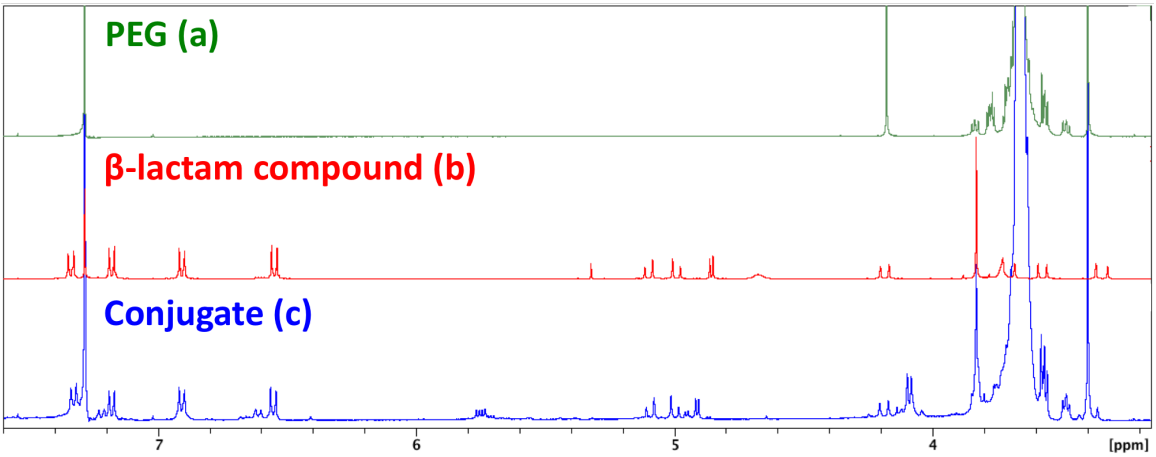

Figure A.2: ^{1}H NMR of the unmodified PEG (a), the β-lactam compound (b), and the β-lactam-PEG conjugate (c).

PEG, indicating successful conjugation. The effect of βL was studied by comparing conjugates with and without βL from *B. cereus* (penicillinase, pen'ase) using size-exclusion chromatography (SEC). SEC refractive index chromatogram shows a shift of the conjugate compared to the unmodified PEG, and then a shift again when exposed to the βL (Figure A.4a). No difference was apparent between unmodified PEG in 1 $\times$ PBS versus βL. An absorbance at 260 nm, characteristic of the β-lactam ring, is not presented in unmodified PEG but appears in the conjugate, again indicating conjugation (Figure A.4b). When incubated in βL, this absorbance from the conjugate is drastically reduced, confirming hydrolysis of the βL ring.

Once we confirmed successful conjugation and responsiveness to βL, we next formed nanoparticles (NPs) using the film hydration technique; the conjugate was dissolved in chloroform, which was evaporated under vacuum in a glass vial, then the conjugate was hydrated with water. Dynamic light scattering (DLS) results suggest the formation of particles with a hydrodynamic diameter of 246.8 $\pm$ 5.9 nm (Z-average $\pm$ stdev) and a polydispersity index of 0.16 $\pm$ 0.01 (Figure A.5a, "Blank"). Cryogenic transmission electron microscopy (cryo-TEM) images also indicate the formation of circular NP (Figure A.6). Their critical aggregation concentration (CAC) was determined using pyrene, a fluorescent

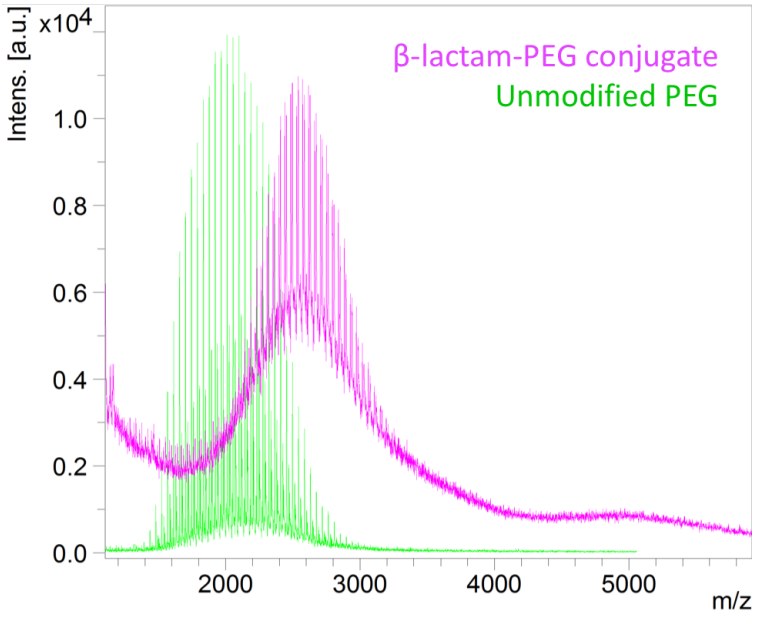

Figure A.3: MALDI-TOF spectra show a shift in molecular weight of conjugate compared to unmodified PEG, indicating successful conjugation.

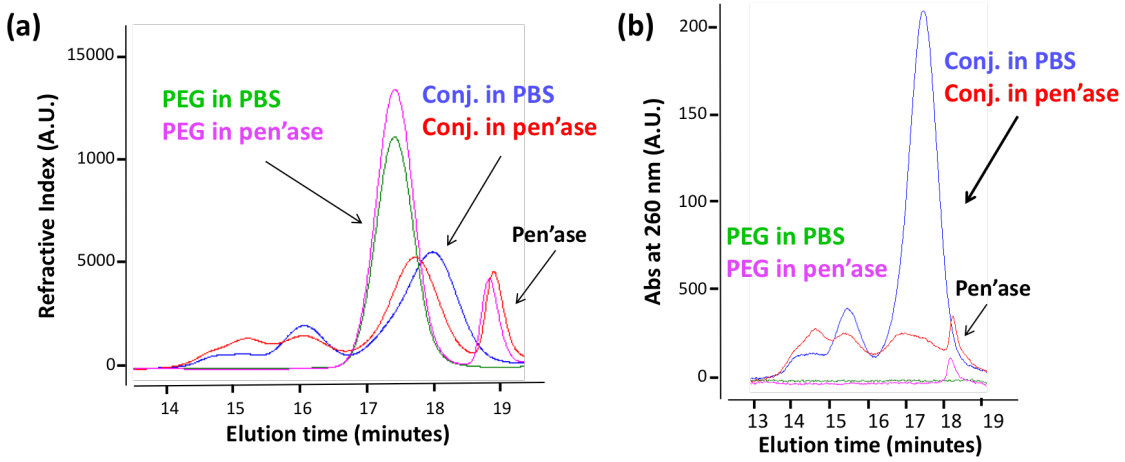

Figure A.4: SEC chromatograms of refractive index (a) and absorbance at 260 nm (b) of unmodfied PEG and β-lactam-PEG in 1 $\times$ PBS or βL from *B. cereus* (penicillinase, pen'ase)

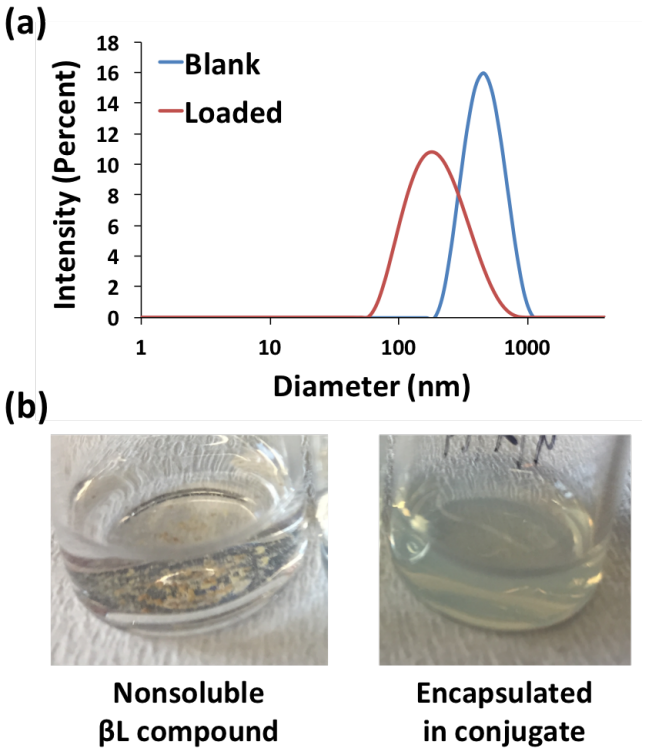

Figure A.5: (a) DLS shows a uniform size distribution of the β-lactam conjugate NPs with (Loaded) or without (Blank) free β-lactam compound encapsulated. (b) Images of solution of the β-lactam compound in 1 $\times$ PBS (left) or encapsulated in the NPs (right).

probe that is highly sensitive to the polarity of its microenvironment, and exhibits a change in fluorescence when it is entrapped in vesicles with a nonpolar core. Pyrene was dissolved in acetone which was evaporated in a glass vial, then the conjugates in chloroform were added at different amounts and also evaporated. Lastly, the mixture was rehydrated with water resulting in a pyrene concentration of 6×10^{-7} M and a range of concentrations of the conjugate. The ratio of two characteristic pyrene fluorescence peaks (371 nm/381 nm) was plotted against the log of the polymer concentration, and the transition point or the intersection of the two linear curves, which is suggested to be the CAC,[371] was determined to be 2.7×10^{-6} M or 7.9 μg/mL, which is in good agreement with other polymeric vesicles in literature (Figure A.7).

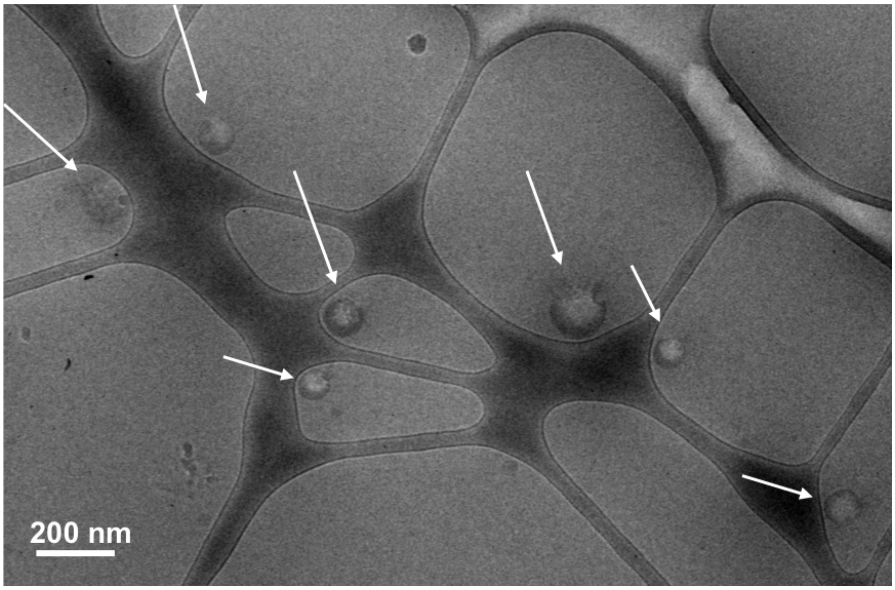

Figure A.6: Cryo-TEM images of β-lactam-PEG conjugate NPs loaded with free β-lactam compound. White arrows indicate a NP. We would like to thank Irene Andreu at the Rhode Island Consortium for Nanoscience and Nanotechnology for cryo-TEM imaging.

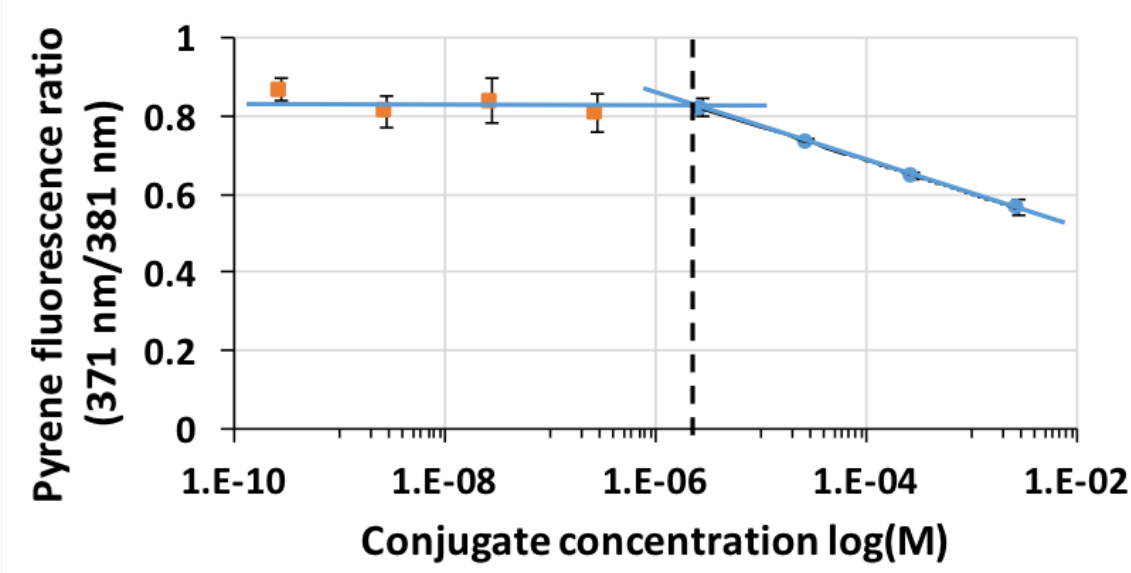

Figure A.7: Ratio of pyrene fluorescence intensity of peaks at 371 and 381 nm vs. log of conjugate concentration (M). The transition point (intersection) is approximated to be the CAC.

To explore the potential of loading a hydrophobic small molecule in the core of the NP, we first attempted encapsulating the free β-lactam compound (not conjugated to PEG) as a model cargo during NP formation. Figure A.5b shows an image of the non-soluble compound (no conjugate added) on the left, and on the right is an image of the solution of NPs formed in the presence of the small molecule as a homogeneous cloudy suspension without precipitation, suggesting enhanced solubility of the compound and its successful encapsulation. DLS of the β-lactam compound loaded NPs (177.3 $\pm$ 1.7 nm) was smaller than the blank hydrogel (Figure A.5a), potentially due the β-lactam compound helping form a tighter more hydrophobic core. Next, we will test the incorporation of antibiotics into the self-assembled particles, and then the NPs disassembly and drug release in response to βLs.

Our next steps for the β-lactam-PEG nanoparticles include confirming their responsiveness to βLs, and testing for a change in their stability and morphology. Next, the loading of different antibiotics (hydrophobic and hydrophilic) will be tested, and their release profile in the presence of the bacterial enzymes compared to physiological conditions will be optimized. Furthermore, their efficacy against bacteria and biocompatibility towards mammalian cells will be studied. One potential alternative approach that we could investigate if needed is conjugating a nonpolar compound such as palmitic acid to one side of the β-lactam compound and PEG to the other. Increasing the hydrophobicity and size of the nonpolar half of the amphiphilic polymer has been shown to increase the stability of the self-assembled vesicles, and we hypothesize could potentially have a more drastic effect on disassembly once the β-lactam is cleaved and the two halves are separated.

Appendix B

Polyelectrolyte Multilayer Films for Controlled Delivery of Chemotherapeutics

---

This chapter is in preparation to be submitted for peer review:

Wang S.,* Battigelli A.,* Fairman A., **Alkekhia D.**, Yang W., Antoci V., Moore D., and Shukla A., "Polyelectrolyte multilayer films for controlled delivery of chemotherapeutics", Editing manuscript, 2020.

* These authors contributed equally

B.1 Abstract

The Src homology 2 domain containing protein tyrosine phosphatase-2 (SHP2) is a key enzyme involved in pathways regulating tumor growth signaling. SHP2 has recently gained great interest as a promising cancer drug target and many SHP2 inhibitors are currently under development and investigation[372]. To address common complications of systemic administration of chemotherapeutics, such as off-target toxicity and reduced therapeutic efficacy, and maximize SHP2 inhibitor activity, we developed multilayer coatings for localized delivery of chemotherapeutics. Layer-by-layer (LbL) self-assembly is a technique harnessing complementary interactions between multivalent compounds to construct multilayer films, which could be formulated to serve as drug depots. Here, we have developed LbL films composed of chitosan (CHT) and poly-carboxymethyl-β-cyclodextrin (PβCD) for the delivery of a SHP2 inhibitor, SHP099, which has shown promise as a superior anticancer drug due to its low half-maximal inhibitory concentration (IC_{50}) against human esophageal cancer and breast adenocarcinoma cell proliferation *in vivo*. SHP099 was successfully loaded into multilayer films *via* host-guest interactions with PβCD. This complexation was characterized using nuclear magnetic resonance (NMR) spectroscopy, which confirmed the occurrence of the supramolecular assembly identifying the interaction of specific terminal protons present on the drug with the protons of the macrocycle. Assembled films demonstrated four days of detectable therapeutic drug release that inhibited colony formation of human breast adenocarcinoma cells *in vitro*. These films demonstrated potential clinical use as a localized cancer treatment with controlled, prolonged drug release, which could be utilized to formulate drug-loaded coatings of implants.

B.2 Introduction

Cancer is a disease marked by the uninhibited proliferation of cells that can spread into other tissue areas.[184] SHP2, a ubiquitously expressed oncoprotein, plays a key role in cell-growth-signaling pathways, regulating development, metabolism, and cell signaling across numerous species, but its overactivation has been associated with the development of numerous cancers and malignancies.[373,374] SHP2 has been validated as a target for cancer therapy[375], and there are many studies in this area to identify SHP2 allosteric inhibitors.[372,373,376] From these investigations, SHP099 has emerged as a promising drug candidate for cancer therapy,[377–379] and was chosen in this study from among numerous SHP2 inhibitors for its demonstrated high-target specificity and reduced off-target cytotoxicity against receptor-tyrosine-kinase-driven (RTK-driven) cancers in *in vitro* models.[373]

With most chemotherapy, systemically administered drugs circulate until they reach the tumor site where they inhibit intracellular growth pathways, blocking the progression of cancer.[380] However, this lack of specific tumor targeting causes unintended toxic accumulation in healthy tissue, resulting in adverse side effects[381,382] and reducing therapeutic efficacy against the tumor.[380] There is, therefore, a need for controlled release of anticancer drugs through localized delivery systems to minimize harmful systemic toxicities and maximize chemotherapeutic potential.[381] Polymeric drug delivery systems have been of interest because of their structural and compositional tunability, as well as their ability to deliver drugs to target sites at therapeutically relevant concentrations.[380] One technique that has been used to construct such delivery systems is layer-by-layer (LbL) self-assembly in which multilayer film formation is driven by multivalent interactions between complementary species.[383] Specifically, the LbL technique of dip-coating substrates with polyelectrolytes involves alternate dipping in solutions of cationic and anionic polymers, facilitating adsorption through electrostatic interactions.[384] Among LbL assembly's advantages there

is the ability to readily and conformally coat different substrates under mild aqueous conditions, promoting its use in various biomedical applications[385]. For example, LbL assembly has been used to develop cell coatings for tissue engineering,[111] responsive drug-delivering implant coatings,[178,386] and nanoparticles layered with MRI contrast and luminescent agents to enhance diagnostic imaging.[174]

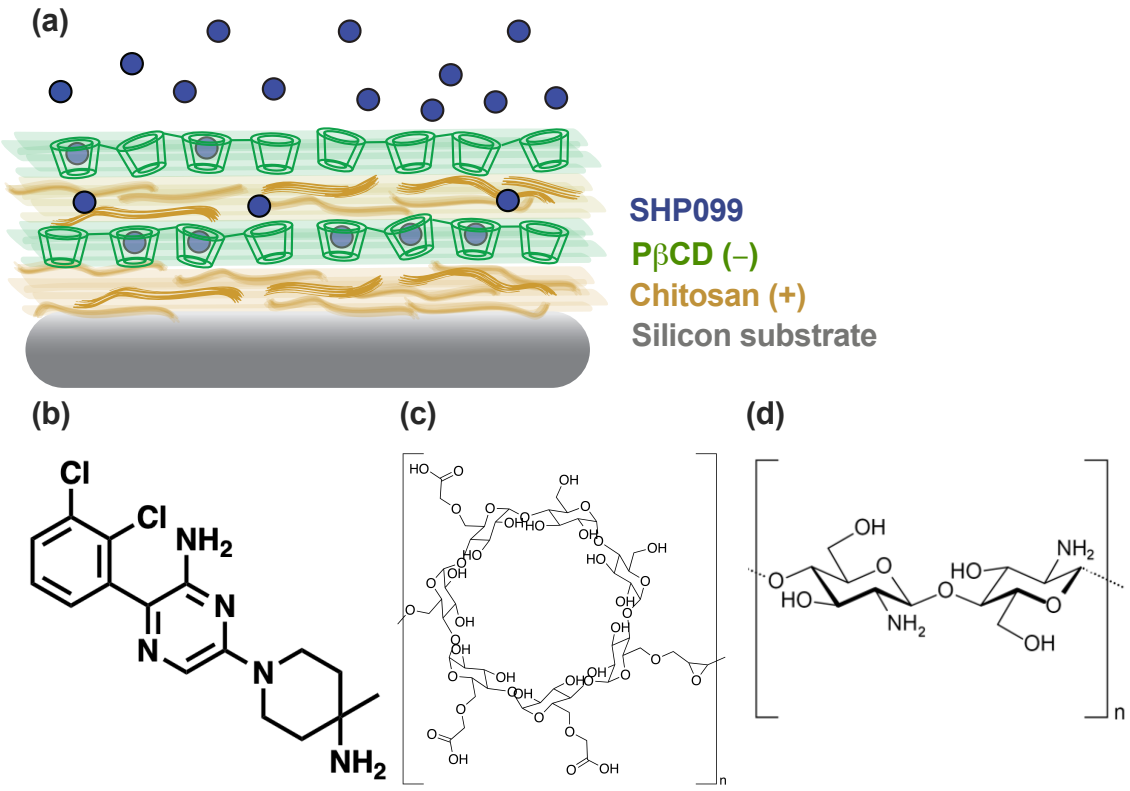

Figure B.1: (a) Schematic of layer-by-layer self-assembled film $(\text{CHT/P}\beta\text{CD-SHP099})_{25}$ on silicon substrate. Chemical structure of SHP099 (b), PβCD (c), and CHT (d).

In this study, LbL self-assembly was used to develop films with alternating layers of chitosan (CHT), a polycation, and poly-carboxymethyl-β-cyclodextrin (PβCD), a polyanion, for loading and localized delivery of SHP099.[387] Chitosan is a natural polymer derived from the exoskeleton of shellfish,[388] and is commonly used in LbL applications due to its biocompatible, biodegradable, and antimicrobial properties.[389]

To ensure efficient drug loading and controlled release into and from the films, CDs

were chosen as carriers for their known ability to encapsulate small hydrophobic molecules in their hydrophobic core pocket.[390] Polymerized formulations of CDs or CD-modified polymers have been utilized in multiple LbL systems where they have been used for example to concurrently incorporate and release antibiotics and non-steroidal anti-inflammatory drugs (NSAIDs),[391] build biodegradable drug eluting platforms targeting infections,[392] or construct nanocarriers for gene delivery[393]. Here, we investigated PβCD-SHP099 complexation then assembled (CHT/PβCD-SHP099)$_{25}$ films to explore their ability to load and release SHP099 and inhibit the proliferation of human breast adenocarcinoma cells *in vitro*.

B.3 Materials and Methods

B.3.1 Chemicals and Materials

Chitosan (CHT, $\geq$ 75% deacetylated), poly(sodium-4-styrenesulfonate) (SPS, average molecular weight $\sim$70,000 Da), methanol, sodium acetate buffer, and 1$\times$ Dulbecco's phosphate-buffered saline (1$\times$ PBS, pH 7.4) were purchased from Sigma Aldrich (St. Louis, MO). Linear poly(ethyleneimine) (LPEI, molecular weight $\sim$45,000 Da) was obtained from Polysciences, Inc. (Warrington, PA), and sodium hydroxide (NaOH) was obtained from Thermo Fisher Scientific (Waltham, MA). Poly-carboxymethyl-β-cyclodextrin (PβCD, average molecular weight $\sim$153,000 Da) was purchased from Cyclo Lab (Budapest, Hungary), while SHP099 dihydrochloride was purchased from ChemieTek (Indianapolis, IN). Deuterium oxide (D_2O) was purchased from Cambridge Isotope Laboratories (Tewksbury, MA). Cell counting kit-8 (CCK8) was purchased from Dojindo Molecular Technologies, Inc. (Rockville, MD). Silicon was purchased from WAFERPRO (San Jose, CA). MDA-MB-468 human breast adenocarcinoma cells and NIH 3T3 murine fibroblasts were obtained from ATCC (Manassas, VA). RPMI 1640 medium containing L-glutamine, HEPES, phenol red, sodium pyruvate, high glucose, and low sodium bicarbonate was pur-

chased from Thermo Fisher Scientific (Waltham, MA), and supplemented with 10% fetal bovine serum (FBS) (Corning Inc., Corning, NY) and 1% penicillin-streptomycin (Caisson Laboratories, Smithfield, UT). 4% paraformaldehyde was purchased from Electron Microscopy Sciences (Hatfield, PA). 0.01% TWEEN® was purchased from Sigma Aldrich (St. Louis, MO). 0.2% crystal violet was purchased from Millipore Sigma (St. Louis, MO). 33% acetic acid was purchased from Fisher Scientific (Hampton, NH). Ultrapure water (18.2 MΩ·cm MilliQ water, EMD Millipore, Taunton, MA) was used in all experiments. Room temperature referred to this paper is 21-23°C.

B.3.2 Characterizing PβCD-SHP099 guest-host complexation using nuclear magnetic resonance

Solutions of 3.08 mg/mL SHP099, 20.08 mg/mL PβCD, and SHP099 with PβCD (3.08 mg/mL, 20.08 mg/mL, respectively) were prepared in D_2O for all nuclear magnetic resonance (NMR) studies. SHP099 and PβCD were mixed in D_2O at approximately 700 rpm for 1.5 h at room temperature to allow PβCD-SHP099 interaction. One-dimensional (1D) proton (^{1}H) NMR spectra were acquired using a Bruker DRX Avance 400 MHz spectrometer. Two-dimensional (2D) nuclear Overhauser effect spectroscopy (NOESY) and diffusion ordered spectroscopy (DOSY) experiments were performed using a Bruker Ascend 600 MHz spectrometer.

B.3.3 (CHT/PβCD-SHP099) film assembly and characterization

Layer-by-layer film assembly.

Following similar protocols,[199] silicon substrates ($\sim 0.7 \times 2.5$ cm) were prepared for assembly by first rinsing three times in methanol, then three times in ultrapure water, and, finally, drying with a stream of air. Dried substrates were plasma etched using air in a

Harrick PDC-32G plasma cleaner operated at a high radio frequency level (12 MHz) for 1 min. Substrates were then immediately submerged in a bath of LPEI (10 mM, pH 4.25). Using an adapted Zeiss-Microm DS-50 programmable slide stainer, all substrates were initially coated with ten (LPEI/SPS) bilayers to facilitate the subsequent assembly of the (CHT/PβCD) films. Each layer was assembled by submerging the substrates in a bath of LPEI for 5 min, followed by three baths of ultrapure water for 10, 20, and 30 seconds, and then a bath of SPS (10 mM, pH 4.75) for 5 min, followed by three additional baths of ultrapure water for 10, 20, and 30 seconds. This process was repeated ten times.

(CHT/PβCD)$_n$ films (n represents the number of bilayers) were assembled using a Biolin Scientific KSV Nima dip coater. Substrates were first submerged in CHT (1 mg/mL in 0.1 M sodium acetate buffer, pH 6) for 10 min, followed by a 1 min rinse in a sodium acetate wash bath (0.1 M, pH 6) with gentle agitation, then submerged in a PβCD solution (20.08 mg/mL in 0.1 M sodium acetate buffer, pH 6) either with or without pre-incubation with SHP099 (3.08 mg/mL) for 10 min to develop "loaded pre-assembly" or "loaded post-assembly" films (described below), followed, by another rinse in sodium acetate. This process was repeated multiple times to build up (CHT/PβCD)$_n$ films. Films were stored dry at 4°C for use in subsequent experiments. For all substrates, film formed on the non-plasma-treated surface of the substrate was removed using 1 mM NaOH before any further experiments were performed.

In the cases where SHP099 was incorporated during film assembly ("loaded pre-assembly"), PβCD-SHP099 complex solutions were prepared before film assembly by mixing SHP099 and PβCD (at a 1:2 molar ratio relative to the molar mass of PβCD repeat units) in sodium acetate buffer (0.1 M, pH 6) at approximately 700 rpm for 1.5 h at room temperature to allow PβCD-SHP099 interaction.

We tested another method of drug loading where SHP099 was loaded *post*-assembly into (CHT/PβCD)$_{25}$ films. Films were assembled as described above using PβCD alone,

then the films were soaked in 2 mL solutions of 3.075 mg/mL SHP099 in sodium acetate buffer (0.1 M, pH 6) at room temperature for 24 h, shaking at 50 rpm.

Film growth characterization.

$(CHT/P\beta CD\text{-}SHP099)_n$ and $(CHT/P\beta CD)_n$ film growth was examined by measuring dry film thickness for n = 5, 10, 15, 20, and 25 bilayers using a Veeco Dektak 3 surface profilometer and for films with thicknesses below 200 nm, a J.A. Woollam M-2000 ellipsometer was used. For profilometry measurements, films were scratched at 3 different locations along the length of each substrate and the average step height between the uncoated silicon surface and the film was determined at each scratch. Scan lengths of 2000 μm were utilized. Ellipsometry measurements were taken using a 632.8 nm laser at three incidence angles: 55°, 65°, and 75°. The refractive index for the films was set to 1.55. Measurements were taken at 10 different locations on the substrate.

Drug loading quantification.

To quantify SHP099 loading in $(CHT/P\beta CD\text{-}SHP099)_{25}$, films were first disrupted in 50 μL of 1 M NaOH (15 min incubation), solutions were diluted in 950 μL of 1$\times$ PBS (pH 7.4), then absorbance was measured at 350 nm (SHP099s characteristic wavelength of maximum absorbance (λ_{max})) using a BioTek® cytation 3 plate reader. Standard curves of SHP099 were produced and used to quantify the amount of SHP099 encapsulated in the films.

B.3.4 SHP099 release and film thickness change over time

To determine the release profile of SHP099 from $(CHT/P\beta CD\text{-}SHP099)_{25}$ films, substrates were incubated in 500 μL 1$\times$ PBS at 37°C, and solutions were refreshed with 1$\times$

PBS at hourly or daily time-points. Drug release for each time-point was subsequently determined via ultraviolet-visible (UV-Vis) spectroscopy, as described in Section *Drug loading quantification*. To determine film thickness at each time-point, the films were removed from their 1× PBS incubation solutions, dried with a gentle stream of nitrogen, and measured for thickness using a profilometer and ellipsometer (as described in Section *Film growth characterization*), before they were replaced in fresh solutions for further incubation.

B.3.5 Clonogenic assays of *in vitro* cell proliferation

To study the effects of SHP099 released over time from (CHT/PβCD-SHP099)$_{25}$ films on cancer cell growth, the film coated silicon wafers were first sterilized via exposure to ultraviolet light in a Nuaire Class II Type A2 biosafety cabinet for 15 min per side. Then they were incubated coated-side down in 0.5 mL of cell culture medium (described below) at 37°C. At each time-point, the medium was removed, frozen at -20°C for future testing with cells, and fresh medium was added to the substrates.

MDA-MB-468 human breast adenocarcinoma cells were cultured in RPMI 1640 medium with 10% fetal bovine serum (FBS) and 1% penicillin/streptomycin at 37°C and 5% CO_2. Cells were then seeded in 96-well plates at a seeding density of approximately 800 cells/cm^2; after 24 h of incubation, cells were treated with SHP099 at concentrations ranging from 1.25 to 50 μM; the same concentration range of SHP099 with PβCD at a 1:2 molar ratio as in film assembly conditions; PβCD at concentrations ranging from 0.0089 to 0.89 μM; or film incubated cell media collected at time-points throughout 96 h of incubation (as described above). PβCD-SHP099 solutions were prepared by combining solutions of each component and shaking for 1 h at 37°C to allow PβCD-SHP099 interaction before cell treatment. SHP099, SHP099-PβCD mixture, and PβCD solutions were prepared from stock solutions that were made in 1× PBS to allow full dissolution of either or both solutes

and then diluted in media to reach a final concentration of 10% PBS before incubation with cells. Cell incubation solutions were refreshed every 3-4 days. Cells were grown in a 10% PBS in growth media or in growth media only as positive controls.

After 14 days of cell treatment, cells were washed with 0.01% PBS-TWEEN three times, fixed with 4% paraformaldehyde for 15 min at room temperature, washed again with PBS-TWEEN three times, then stained with 0.2% v/v crystal violet solution in water under shaking for 30 min at room temperature. Cells were first thoroughly washed with water to remove excess crystal violet solution, and then their stains were dissolved in 33% v/v acetic acid with rocking for 5 min at room temperature, and the absorbance was measured at 595 nm to characterize cell proliferation. Acetic acid alone were used as a negative control. Results were normalized to trimmed averages (which exclude statistical outliers beyond 1.5× the interquartile range) of controls of cells treated with 10% 1× PBS in growth media or growth media alone using Eq. 1.

$$Normalized\,cell\,viability = \frac{sample\ abs\ -\ negative\ control\ abs}{positive\ control\ abs\ -\ negative\ control\ abs} \tag{B.1}$$

B.3.6 Statistical Analysis

Results are reported as mean ± standard deviation whenever appropriate. All experiments were repeated with three or more samples. Statistical significance was calculated using one-way analysis of variance (ANOVA; α = 0.05) with Tukey's post-hoc analysis and Sidak's multiple comparison test on GraphPad PRISM™. A value of $p < 0.05$ was considered statistically significant (*, $p < 0.05$; **, $p < 0.01$; ***, $p < 0.001$; ****, $p < 0.0001$).

B.4 Results and Discussion

B.4.1 Characterizing PβCD-SHP099 host-guest complexation using nuclear magnetic resonance

To understand the nature of the interactions occurring between SHP009 and PβCD, a combination of 1 and 2D ^{1}H-NMR techniques were used (Fig. B.2).

Initial 1D ^{1}H-NMR studies were conducted on SHP099, PβCD, and on a 2:1 mixture of SHP099-PβCD solutions at film assembly conditions (3.08 mg/mL SHP099, 20.08 mg/mL PβCD). Isolated ^{1}H-NMR spectra of SHP099 clearly display a set of aromatic and heteroaromatic resonances in the range of 8.00 to 7.00 ppm and the remaining piperidinyl and methyl resonances at 4.00-1.7 and 1.4 ppm, respectively. On the other hand, the NMR spectrum of PβCD shows a very broad set of resonances concentrated in the area between 6.00-5.00 and 4.5 to 3.00 ppm. Such broad resonances are a direct consequences of the polymeric nature of PBβD. Interestingly, when a 2:1 mixture of SHP099 and PβCD was investigated, it was possible to observe a broadening of the aromatic and heteroaromatic signal of SHP099 (Fig. B.2a). We ascribe such behavior to the changing in nature of the SHP099 which, upon complexation, would become an integral part of the polymeric structure of PβCD causing an increase on its nuclei relaxation times. Minor differences are also present in chemical shifts of the proton resonance of SHP009 when isolated and in the presence of PβCD. Specifically, downfield shifts of 0.05 and 0.04 ppm were observed for the multiplets of protons 6 and 8, and for proton 7 of SHP099, once mixed with equimolar quantities of PβCD (Fig. B.2a). Additional downfield shifts of 0.02 and 0.06 were also observed in signals corresponding to proton 1 and 2 of SHP099, respectively (Fig. B.2a). These chemical shifts variation are comparable with the formation of a cyclodextrin inclusion complex.[394,395] Resonances of protons 3 and 4 (at 3.28 and 4.00 ppm, respectively)

Proton label	SHP099 only	SHP099-PβCD	Difference
1	1.4	1.42	0.02
2	1.89	1.95	0.06
3	3.28	masked	masked
4	4.00	masked	masked
5	7.47	7.47	0
6	7.34	7.39	0.05
7	7.62	7.66	0.04
8	7.34	7.39	0.05

Table B.1: NMR shifts. (Units: ppm)

were masked by the signal from PβCD, while no shifts were observed for proton 5 (at 7.47 ppm) which is on the pyrazine of the SHP099 structure (Fig. B.2a). The observed shifts of protons 1, 2, 6, 7 and 8, but not of proton 5, suggest drug interaction with PβCD on either or both ends of the drug molecule (i.e. on the phenyl or piperidinyl group).

To better understand the structure of the PβCD-SHP099 host-guest complex, 2D NOESY was performed on the SHP099-PβCD complex solution. In this case, a second evidence of an intermolecular interaction between the cyclodextrin cavity and SHP099 was found. Indeed, a direct coupling was detected between the methyl group of SHP099 and the cyclodextrin resonances of PβCD, indicating close proximity ($<$5 Å) between the two groups. A similar type of coupling is also observed between PβCD and proton 2 of SHP099, further highlighting their spatial proximity.

Additionally, 2D-DOSY, a technique that is conventionally used to analyze mixtures of molecules in solution,[396] was performed to further investigate the complexation. Such technique is able to give important information about the diffusion coefficients and therefore the volume/radius of a molecular species formed upon host-guest complexation.[396] figure B.2c shows a 2D-DOSY plot with the diffusion coefficients of the resonance of SHP099 when in solution alone (blue spectra) and when in presence of PβCD. In the first case, the diffusion coefficients (D0) are higher than PβCD diffusion coefficients shown in the PβCD-SHP099 mixture spectra (red) due to the lower molecular volume. However, in the

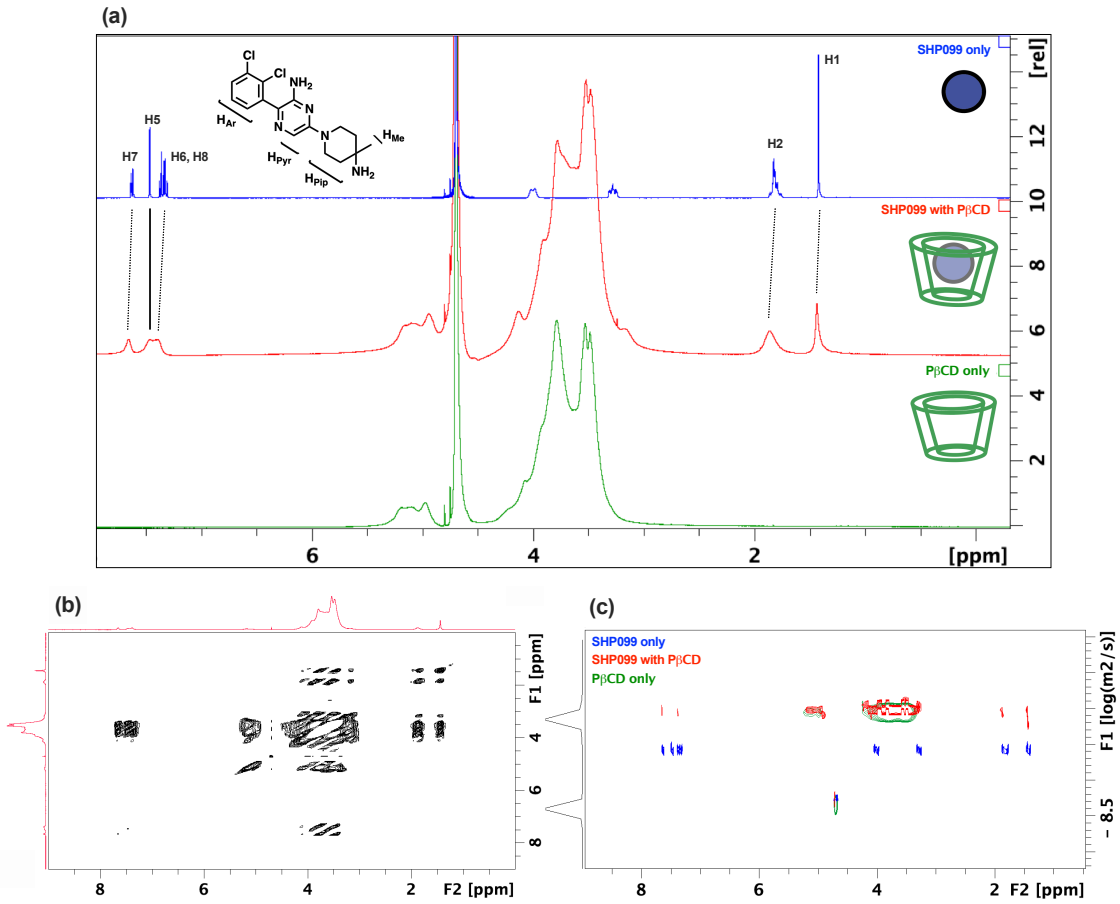

Figure B.2: (a) Comparison of 1D ^{1}H-NMR spectra for solutions of SHP099 (blue), SHP099-PβCD mixture solution (red), and PβCD (green) dissolved in D_2O. (b) 2D NOESY spectra of SHP099-PβCD mixture. (c) DOSY spectra of SHP099, SHP099-PβCD mixture or PβCD.

mixture, the diffusion coefficient of SHP099 proton 1 (1.4 ppm) decreases (compared to SHP099 alone) to that of the PβCD-SHP099. The decrease in diffusion rates confirms the formation of inclusion complexes deduced from chemical shifts observed in 1D ^{1}H-NMR and NOESY NMR experiments.

B.4.2 Characterization of SHP099 loading and release from (CHT/PβCD-SHP099)$_{25}$ films

Film growth was characterized by measuring the thickness of films with increasing numbers of bilayers. SHP099 was pre-encapsulated into CD, by mixing the solutions for

1.5 h, to allow complexation. Measurements demonstrated that film thickness increased with increasing number of bilayers; however, smaller increases in thickness per bilayer were observed at earlier stages of film assembly compared to later stages (Fig. B.3a). This behavior may be attributed to the formation of islets - small "islands" of deposited film, as opposed to uniform layers - initially formed on the surface of the substrate during early stages of bilayer deposition, as observed in other LbL film studies.[257,397,398] As additional layers are deposited, these islets grow and begin to coalesce until they form a uniform film surface, thus facilitating a constant thickness increment at each deposition step at later stages of assembly.

We then investigated the incorporation of SHP099 into the multilayered film using two different methods: loading SHP099 either pre-film assembly (SHP099 pre-incubated with PβCD to allow complexation) or post-film assembly (by soaking assembled (CHT/PβCD)$_{25}$ films in SHP099 solution). A comparison of their respective drug loading and release profiles was conducted to determine which method yielded optimal results (e.g., higher drug loading, lower bolus release, extended release at biologically relevant concentrations). Interestingly, the films assembled using PβCD complexed with SHP099 pre-assembly were more than twice as thick as the films loaded with SHP099 post-assembly (4.76 ± 0.17 μm vs. 2.26 ± 0.25 μm, respectively), yet they resulted in very similar SHP099 loading (123.77 ± 8.80 μg vs. 127.18 ± 9.12 μg, respectively) (Fig. B.3b). Furthermore, we found no statistically significant difference in the thickness of post-assembly loaded films before and after incubation in SHP099 solution, indicating that post-assembly loading of SHP099 does not affect film thickness. When SHP099 is loaded pre-film assembly, it could potentially reduce electrostatic repulsion between PβCD carboxylic acids, promoting incorporation of a larger amount of polymer. This might be similar to the effect of increasing the ionic strength of LbL assembly solutions, which leads to ionic shielding and thicker film formation (up to a limit before salts completely prevent assembly).[135,136] Another possibility is drug guest molecules acting as "crosslinks" bridging two PβCD if

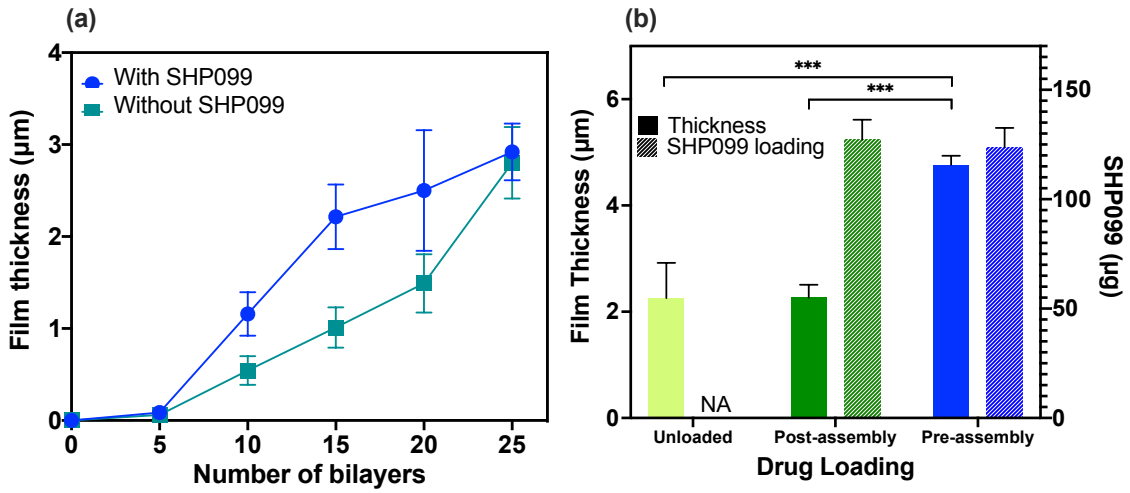

Figure B.3: (a) Average film thickness of (CHT/PβCD) films, with and without SHP099, with increasing number of assembled bilayers. (b) Thickness (left axis) and SHP099 load (right axis) of pre- or post-assembly loaded $(CHT/P\beta CD)_{25}$ films, before (unloaded) and after (pre- and post-assembly) complexation with SHP099. Results are reported as mean $\pm$ standard deviation; statistical significance was examined using one-way ANOVA and Tukey's post-hoc analysis, n=3, α=0.05, ***p$<$0.001. NA: not applicable.

each half of the same guest molecule was incorporated into two hosts on two different PβCD chains, providing an additional assembly mechanism, leading to thicker films compared to films without SHP099 or film with SHP099 introduced after film assembly.

Although drug loading was similar in both cases, we wanted to investigate any differences in drug release, which was examined under physiologically relevant conditions (in 1$\times$ PBS, pH 7.4 at 37°C), that might be caused by drug loading method. Periodically, film eluent was removed, and the incubation solution was refreshed to quantify the amount of SHP099 released over time (Fig. B.4). For both loading methods, at all measured time-points (Fig. B.4b), $(CHT/P\beta CD\text{-}SHP099)_{25}$ films were able to release SHP099 at concentrations well above its established IC_{50} for human esophageal and breast adenocarcinoma cell proliferation inhibition via the p-ERK pathway (0.25 μM).[373] The inset in figure B.4a shows that for $(CHT/P\beta CD\text{-}SHP099)_{25}$ films loaded both pre- or post-assembly, most of the release occurred in the first 5 h of incubation in 1$\times$ PBS. However, when SHP099-PβCD was complexed pre-assembly, the films released 66 $\pm$ 1% of their total SHP099

load in the first 5 h, while films loaded post-assembly demonstrated higher release leading to 93.73 $\pm$ 1.40% of their total load being released in that time. After the initial 24 h, films loaded pre-assembly continued to release between 2.51 $\pm$ 0.09 to 9.11 $\pm$ 0.73 μM of SHP099 between daily time-points over 4 days at which point SHP099 release fell below our determined lowest detection limit using UV-Vis spectroscopy (Fig. B.4b). Films loaded post-assembly continued to release SHP099 between the first and the second day but at lower concentrations compared to the other films (between 0.049 $\pm$ 0.034 to 0.512 $\pm$ 0.18 μM), after which SHP099 release fell below the lowest detection limit. At the end of their respective incubation periods with detectable SHP099 release (2 days for post-assembly loaded films and 4 days for pre-assembly loaded films), post-assembly and pre-assembly loaded films had released 93.95 $\pm$ 1.40% and 69.30 $\pm$ 0.82% of their total load, respectively (Fig. B.4a). These results demonstrate that, as compared to SHP099 loading pre-film assembly, loading post-assembly led to a greater bolus release resulting in overall release for a shorter period of time, which is not suitable for applications where burst drug release should be avoided and a more gradual, extended release profile is desired (Fig. B.4a, b).

The rapid release demonstrated by post-assembly loaded films could potentially be due to some SHP099 being adsorbed to the polyelectrolytes of the films *via* electrostatic interactions, as opposed to encapsulated within the PβCD pocket, as hypothesized for SHP099-PβCD pre-incubated solutions, which would have steadied drug release due to the additional interactions formed inside the pocket. It has also been previously demonstrated that bolus release is characteristic of films in which a considerable quantity of the released component occupies the films' top layers[399]. It is possible that more SHP099 is present in the outermost layers for films loaded post-assembly due to a lack of interdiffusion which could explain the faster release from these films compared to pre-assembly loaded films, where SHP099 is likely incorporated into the multilayers within the PβCD core at each deposition step. Due to the more desirable SHP099 release profile from pre-assembly loaded films, those films were used in subsequent experiments.

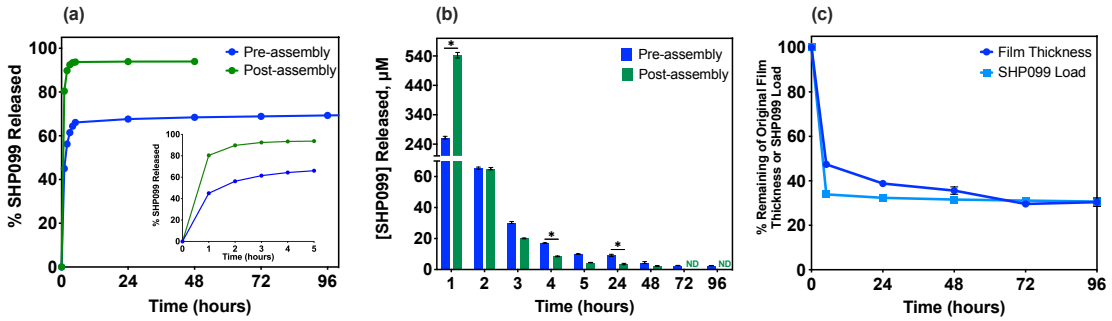

Figure B.4: (a) Percent cumulative release of SHP099 from (CHT/PβCD-SHP099)$_{25}$ films with SHP099 loaded pre-assembly or post-assembly incubated in 1$\times$ PBS, pH 7.4 at 37°C. Inset: Zoom of release in first 5 h. (b) Concentration of SHP099 released from pre-assembly loaded or post-assembly loaded films over time. (c) Percent of pre-assembly loaded (CHT/PβCD-SHP099)$_{25}$ film's initial thickness or drug load remaining over time. Results are reported as mean $\pm$ standard deviation; statistical significance was examined using one-way ANOVA and Sidak's multiple comparison test, α=0.05, *p$<$0.0332; n=3. ND: Not detectable.

To elucidate the mechanisms of drug release, we monitored changes in thickness of (CHT/PβCD-SHP099)$_{25}$ films loaded pre-assembly (S.I. Fig. S1 and Fig. B.4c). Film thickness changed at rates comparable to changes in the rate of SHP099 release. Within 5 h of incubation in 1$\times$ PBS, the thickness of these films decreased by 49.06 $\pm$ 16.96%, which was accompanied by a 66.1 $\pm$ 1% decrease in drug load, as mentioned previously. After 5 h of incubation, these films demonstrated a more gradual decrease in thickness, resulting in an additional 20% loss of their initial thickness between 5 h and 96 h, which was associated with approximately an additional 3% decrease of initial drug load. Therefore, films with SHP099 displayed analogous changes in thickness and release profiles at the end of their respective incubation periods (both $\sim$70% decrease from initial values), characterized by rapid initial decreases followed by more gradual decreases at later time-points (Fig. B.4). We therefore hypothesize that SHP099 release may be attributed to dissolution of the films caused by differences in pH and ionic strength between film assembly conditions (0.1 M sodium acetate buffer, pH 6) and film incubation conditions (0.01 M PBS, pH 7.4).

To elucidate any potential effect of SHP099 on film dissolution, we also compared the

changes in thickness of films assembled without SHP099 ((CHT/PβCD)$_{25}$) (S.I. Fig. S1). Similarly to films with SHP099, films lacking drug, exhibited a decrease in thickness by $52.59 \pm 1.18\%$ within 5 h of incubation in $1\times$ PBS, followed by a more gradual decrease in thickness after the initial 5 h of incubation, losing an additional 24% of initial film thickness between 5 and 96 h. These results demonstrate no apparent effect of the presence of SHP099 on film dissolution, indicating that film disassembly is indeed likely due to difference in incubation solution pH and ionic strength.

B.4.3 Inhibition of cell proliferation *in vitro*

The anticancer efficacy of the composite material was examined by studying the effect of the film release solution collected at hourly or daily time-points (similar to drug release assay) on MDA-MB-468 colony formation. Despite apparent film dissolution, it is possible that SHP099 molecules still interact with PβCD core in the release solutions. In order to elucidate how SHP099's efficacy against cells might be affected by its potential interaction or encapsulation within PβCD, we compared the effects of either free SHP099 or SHP099 pre-incubated with PβCD on cancer cell proliferation *in vitro*.

Compared to untreated controls (Fig. B.5b), density of cancer cell colonies (stained with crystal violet) was visibly reduced in groups treated with both free SHP099 and complexed PβCD-SHP099 (Fig. B.5a). Further, both of these treatment groups exhibited increased inhibition of colony formation with increased concentrations of SHP099. As expected, there was no observable difference in colony density for groups treated with any concentration of PβCD alone compared to untreated controls (Fig. B.5a). Colony density visibly increases with increasing time-points which correspond to decreasing concentrations of drug released from films at these times, as previously shown (Fig. B.4b). Nonetheless, even for the sample where the cells were treated with the release solution from the last time-point (96 h), a visible decrease in colony density was observed.

We then quantified colony density after dissolving the crystal violet stain. A statistically significant reduction in colony formation of MDA-MB-468 cells was observed in all control groups containing SHP099 (Fig. B.5c). In general, inhibition of cell proliferation increased with increasing concentrations of SHP099. This concentration dependant effect was apparent regardless of PβCD presence; for each SHP099 concentration, no statistically significant difference was observed for colony formation in samples treated with or without pre-incubation with PβCD.

Concentrations of PβCD alone were tested to verify that any inhibitory effects seen in SHP099-PβCD solutions were indeed due to SHP099 and not PβCD. No statistically significant differences in colony growth were seen in cells treated with any of the tested concentrations of PβCD when compared to the untreated controls (Fig. B.5c), indicating PβCD alone had no inhibitory effect on cell growth.

When cells were treated with media in which (CHT/PβCD-SHP099)$_{25}$ films were incubated for specified duration, cell colony formation was significantly lower compared to the untreated controls, and similar to inhibition observed with the control SHP099 solutions, indicating that SHP099 loading and release from the films did not seem to negatively affect its activity. However, there was no significant difference in colony formation between cells treated with the release solutions collected at different incubation intervals, indicating that the differences in concentrations of SHP099 measured in those release solutions (Fig B.4) does not translate to drastic differences in anticancer activity, and that a high enough concentration of SHP099 was released at all incubation time-points tested. Nevertheless, cell growth was inhibited to as low as 9.81 $\pm$ 1.64% compared to control when treated with solutions that were incubated with films for 1 h (Fig. B.5d). Cell growth inhibition declined with later time-point release solutions, increasing to 20.86 $\pm$ 14.46% of untreated controls remaining when treated with solutions containing drug release from the last time point analysed (96 h) of the release assay (Fig. B.5d).

In summary, SHP099 release from (CHT/PβCD-SHP099)$_{25}$ films was shown to reduce human breast adenocarcinoma cell growth compared to untreated controls, confirming the potential of these films to prevent cancerous cell growth in cancer patients. It is important to note once more that the release assays were conducted by refreshing the incubation solution of films at each time-point, such that the release concentrations were not cumulative, but rather reflective of release in between two time-points. As initial investigation of potential toxicity associated with released SHP099, the effect of different concentrations of SHP099 on noncancerous cells was investigated. Fibroblasts (NIH 3T3 cells) were incubated for two weeks with the same concentrations of SHP099 used for the controls on MDA-MB-468 (1.25 μM - 50 μM) cells and a viability assay was conducted (S.I. Fig. S2). No significant effect on the cells was observed at the lowest concentrations used (from 1.25 to 2.5 μM) compared to the untreated controls. Higher concentrations had a minimal effect on fibroblasts, except for the highest concentration (50 μM) which was highly toxic and no cell survival was detected. Concentrations of that order of magnitude were observed only after 1 h of drug release and a possible solution to decrease this toxicity would require an initial rinse of the substrate to eliminate the burst release of the drug. Future work may explore the incubation of cells directly onto the films to investigate influence of cells on films and on drug release, material biocompatibility, and the ability of cells to adhere and grow on these substrates.

B.5 Conclusions

Systemic drug delivery is responsible for many of the severe side effects of chemotherapy treatment endured by cancer patients, while simultaneously reducing the maximum potential efficacy of the chemotherapeutic, thus creating a need for localized and extended drug delivery. To these ends, we have assembled polyelectrolyte multilayer films with the biocompatible polymers CHT and PβCD, loaded with the chemotherapeutic, SHP099,

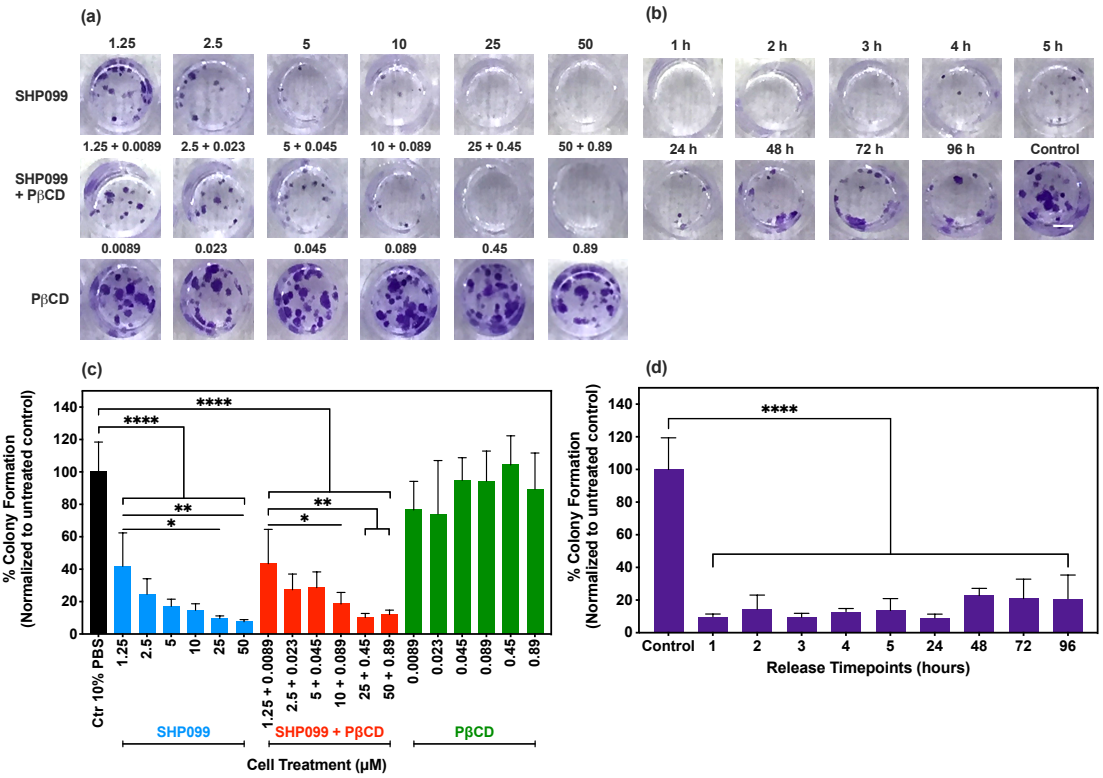

Figure B.5: Representative images of crystal violet-stained MDA-MB-468 cell colonies after 14 days of growth in media containing (a) SHP099, SHP099-PβCD mixture, or PβCD solutions in 10% PBS or (b) solutions of drug released from (CHT/PβCD-SHP099)$_{25}$ films into media between time-points of release assay, or untreated cells control. Concentrations of each control group in and time-point of the release assay at which the release solution was collected are given above each well image. Scale bar represents 2 mm. Normalized MDA-MB-468 cell colony formation after treatment for 14 days with (c) varying concentrations of SHP099, PβCD-SHP099, or PβCD or (d) release solutions from (CHT/PβCD-SHP099)$_{25}$ films in comparison to untreated cell controls. Results are reported as means $\pm$ standard deviations. Statistical significance was examined using one-way ANOVA and Tukey's post-hoc analysis compared to untreated controls, n $\geq$ 3, α=0.05, ****p$<$0.0001.

into the CD cavities. Drug release from our films was above the half-maximal inhibitory concentration required for SHP099 to block cell growth pathways for at least four days, reflecting in the films' ability to impede human breast adenocarcinoma cell growth *in vitro*. Our results also indicated the advantage of pre-encapsulation of the drug within PβCD cavity, to achieve stronger drug-polymer interaction leading to more gradual and extended release of SHP099 from the films over time, compared to release from films loaded with SHP099 post film assembly. These results demonstrate that (CHT/PβCD-SHP099)$_{25}$ films hold promising potential in clinical applications, such as surgical implant coatings that can lower the chances of tumor recurrence from residual cancerous tissue following primary tumor resection. The versatility of PβCD drug encapsulation creates the opportunity for multi-drug loading into (CHT/PβCD) films, such that the synergistic effects of combination therapy with multiple anticancer drugs may amplify the films' inhibitory effect on cancerous cell growth.

Acknowledgements

The authors thank Russell Hopson at the NMR Facility at Brown University for his technical expertise and assistance in conducting and analyzing 2D NMR experiments, and acknowledge the use of the Microelectronics Core Facility at Brown University for profilometery and ellipsometry.

B.6 Supplementary Information

B.6.1 (CHT/Pβ)$_{25}$ and (CHT/PβCD-SHP099)$_{25}$ *in vitro* dissolution in 1$\times$ PBS

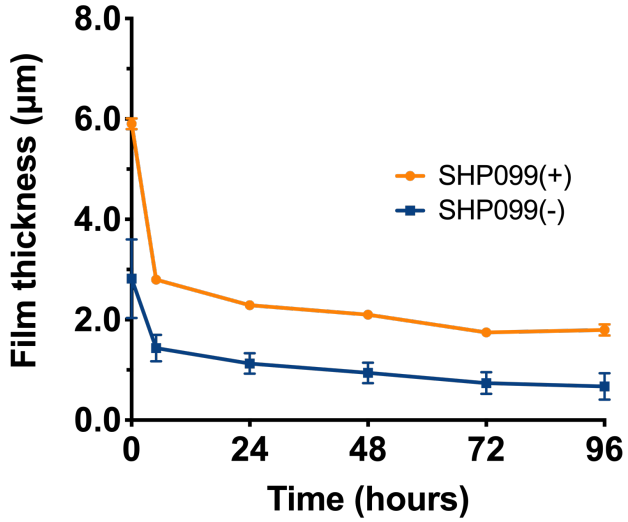

[t].3 [t].3

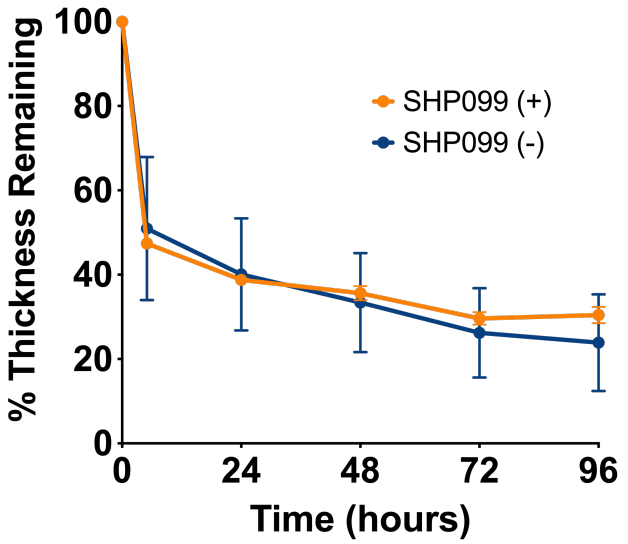

Figure B.6: (a) Thickness of (CHT/PBCD)$_{25}$ films with (+) or without (–) SHP099 incubated in 1$\times$ PBS at 37°C over time. (b) Percent of initial thickness remaining of (CHT/PβCD)$_{25}$ films with (+) or without (–) SHP099 incubated in 1$\times$ PBS at 37°C over time. Results are reported as mean $\pm$ standard deviation; n=3.

B.6.2 SHP099 *in vitro* cytocompatibility

Cytocompatibility of SHP099 was assessed for NIH 3T3 murine fibroblasts. NIH 3T3 cells were cultured in DMEM (containing 4 mM l-glutamine, 4500 mg/L glucose, 1 mM sodium pyruvate, and 1500 mg/L sodium bicarbonate) with 10% calf bovine serum and 1% penicillin–streptomycin at 37°C and 5% CO_2. Cells were then seeded in 96-well plates at a seeding density of approximately 2500 cells/cm^2. After 24 h, cells were treated with increasing concentration of SHP099 (from 1.25 to 50 M), similarly to the clonogenic assays. Cell viability was measured using CCK8 following the vendor's protocol. Briefly, after 24 h of SHP099 incubation with the cells, the solutions were removed and 100 L of CCK8 reagent was added. After 2 h of incubation at 37°C, absorbance at 450 nm was measured using a BioTek® Cytation 3 plate reader. Positive controls of cells grown in DMEM and negative controls lacking cells were included. Normalized cell viability was calculated using Eq. (B.2).

$$Normalized\ cell\ viability = \frac{sample\ abs\ -\ negative\ control\ abs}{positive\ control\ abs\ -\ negative\ control\ abs} \tag{B.2}$$

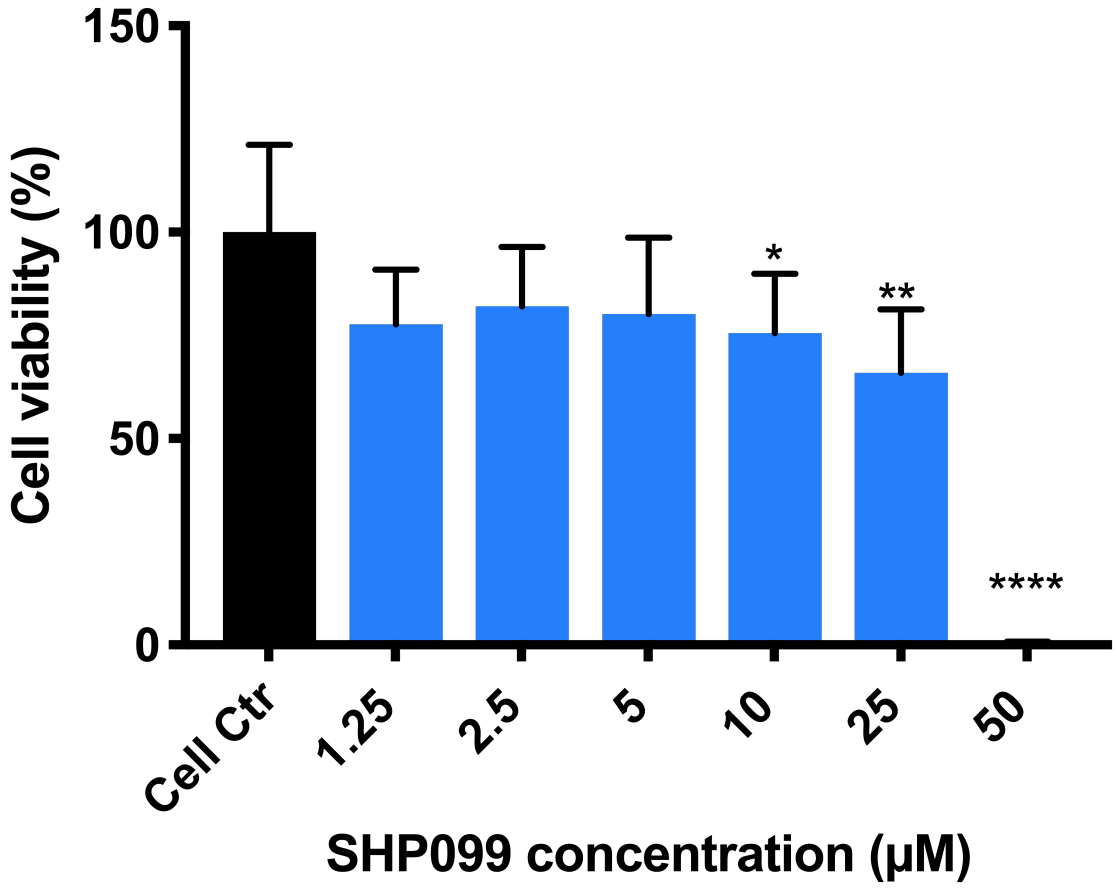

Figure B.7: NIH 3T3 fibroblast viability in media incubated with increasing concentration of SHP099 for 14 days to assess biocompatibility of the drug on non cancer cells. Viability and statistical significance are shown relative to untreated cells. Statistical significance was examined using one-way ANOVA; *¡ 0.05; **¡ 0.01; ****p¡ 0.0001; n=3.

B.6.3 2D NMR of Controls

[t].9

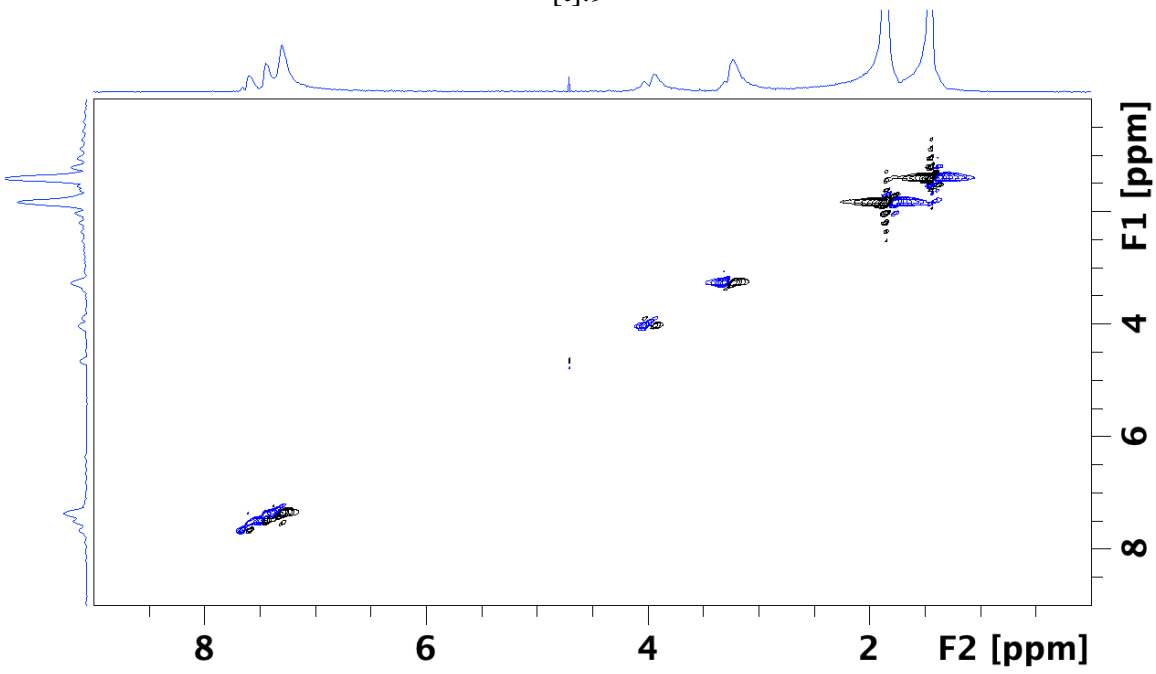

[t].9

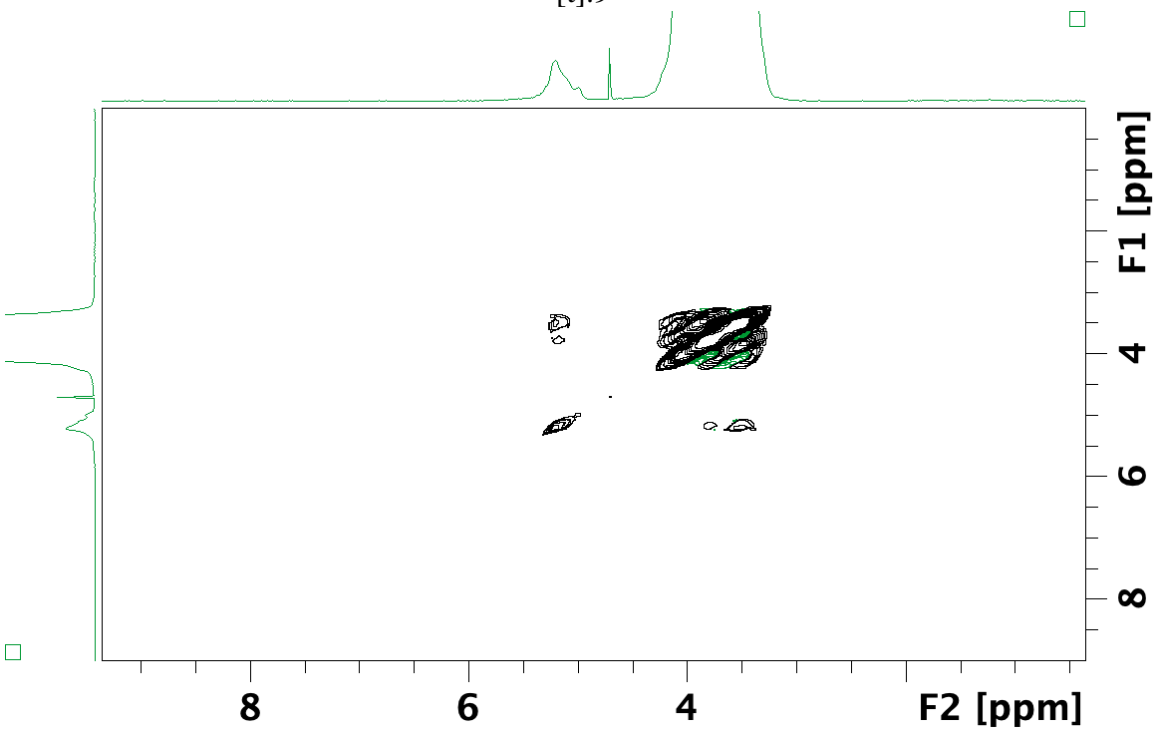

Figure B.8: 2D NOESY NMR of SHP099 and PβCD dissolved in D_2O.

Bibliography

1. Klevens, R. M. *et al.* Estimating health care-associated infections and deaths in U.S. Hospitals, 2002. *Public Health Reports* **122,** 160–166 (Mar. 2007).
2. Figueroa, M. *et al. Polyhydroxyanthraquinones as quorum sensing inhibitors from the guttates of Penicillium restrictum and their analysis by desorption electrospray ionization mass spectrometry* tech. rep. 6 (2014), 1351–1358.
3. CDC, C. f. D. C. & Prevention. *Antibiotic resistance threats in the United States* tech. rep. (2019).
4. Ligon, B. L. Penicillin: Its Discovery and Early Development. *Seminars in Pediatric Infectious Diseases* **15,** 52–57 (2004).
5. Brooks, B. D. & Brooks, A. E. Therapeutic strategies to combat antibiotic resistance. *Advanced Drug Delivery Reviews* **78,** 14–27 (Oct. 2014).
6. Llor, C. & Bjerrum, L. Antimicrobial resistance: Risk associated with antibiotic overuse and initiatives to reduce the problem. *Therapeutic Advances in Drug Safety* **5,** 229–241 (Dec. 2014).
7. Huang, K. S. *et al.* Recent advances in antimicrobial polymers: A mini-review. *International Journal of Molecular Sciences* **17,** 1578 (Sept. 2016).
8. Park, S. C., Park, Y. & Hahm, K. S. The role of antimicrobial peptides in preventing multidrug-resistant bacterial infections and biofilm formation. *International Journal of Molecular Sciences* **12,** 5971–5992 (Sept. 2011).
9. Fox, J. L. Antimicrobial peptides stage a comeback. *Nature Biotechnology* **31,** 379–382 (May 2013).
10. Kilcher, S. & Loessner, M. J. *Engineering Bacteriophages as Versatile Biologics* Oct. 2018.
11. Miró-Canturri, A., Ayerbe-Algaba, R. & Smani, Y. Drug repurposing for the treatment of bacterial and fungal infections. *Frontiers in Microbiology* **10,** 41 (Jan. 2019).
12. Gwisai, T. *et al.* Repurposing niclosamide as a versatile antimicrobial surface coating against device-associated, hospital-acquired bacterial infections. *Biomedical Materials (Bristol)* **12** (2017).

13. Roy, R., Tiwari, M., Donelli, G. & Tiwari, V. Strategies for combating bacterial biofilms: A focus on anti-biofilm agents and their mechanisms of action. *Virulence* **9,** 522–554 (Dec. 2018).

14. Drawz, S. M. & Bonomo, R. A. *Three decades of β-lactamase inhibitors* Jan. 2010.

15. Liu, R. *et al.* A Synthetic Dual Drug Sideromycin Induces Gram-Negative Bacteria to Commit Suicide with a Gram-Positive Antibiotic. *Journal of Medicinal Chemistry* **61,** 3845–3854 (May 2018).

16. Wilke, M. S., Lovering, A. L. & Strynadka, N. C. *β-Lactam antibiotic resistance: A current structural perspective* Oct. 2005.

17. Zhang, H. M. & Hao, Q. Crystal structure of NDM-1 reveals a common β-lactam hydrolysis mechanism. *FASEB Journal* **25,** 2574–2582 (Aug. 2011).

18. Livermore, D. M. & Brown, D. F. J. Detection of β-lactamase-mediated resistance. *Journal of Antimicrobial Chemotherapy* **48,** 59–64 (July 2001).

19. Zygmunt, D. J., Stratton, C. W. & Kernodle, D. S. Characterization of four beta-lactamases produced by Staphylococcus aureus. *Antimicrobial Agents and Chemotherapy* **36,** 440–445 (Feb. 1992).

20. Chow, C., Xu, H. & Blanchard, J. S. Kinetic characterization of hydrolysis of nitrocefin, cefoxitin, and meropenem by β-lactamase from mycobacterium tuberculosis. *Biochemistry* **52,** 4097–4104 (2013).

21. Imsande, J., Gillin, F. D., Tanis, R. J. & Atherly, A. G. Properties of penicillinase from Bacillus cereus 569. *Journal of Biological Chemistry* **245,** 2205–2212 (1970).

22. Giwercman, B., Jensen, E. T., Hoiby, N., Kharazmi, A. & Costerton, J. W. Induction of β-lactamase production in Pseudomonas aeruginosa biofilm. *Antimicrobial Agents and Chemotherapy* **35,** 1008–1010 (1991).

23. Zhao, W.-H. & Hu, Z.-Q. β-Lactamases identified in clinical isolates of ¡i¿Pseudomonas aeruginosa¡/i¿. *Critical Reviews in Microbiology* **36,** 245–258 (2010).

24. Anderl, J. N., Franklin, M. J. & Stewart, P. S. Role of antibiotic penetration limitation in Klebsiella pneumoniae biofilm resistance to ampicillin and ciprofloxacin. *Antimicrobial Agents and Chemotherapy* **44,** 1818–1824 (July 2000).

25. Boateng, J. S., Matthews, K. H., Stevens, H. N. & Eccleston, G. M. *Wound healing dressings and drug delivery systems: A review* 2008.

26. Liu, Y. *et al.* Nanotechnology-based antimicrobials and delivery systems for biofilm-infection control. *Chemical Society Reviews* **48,** 428–446 (Jan. 2019).

27. Campoccia, D., Montanaro, L. & Arciola, C. R. A review of the biomaterials technologies for infection-resistant surfaces. *Biomaterials* **34,** 8533–8554 (2013).

28. Nuttelman, C. R. *et al.* Macromolecular monomers for the synthesis of hydrogel niches and their application in cell encapsulation and tissue engineering. *Progress in Polymer Science (Oxford)* **33,** 167–179 (2008).

29. Stebbins, N. D., Ouimet, M. A. & Uhrich, K. E. Antibiotic-containing polymers for localized, sustained drug delivery. *Advanced Drug Delivery Reviews* **78,** 77–87 (Nov. 2014).

30. Immordino, M. L., Dosio, F. & Cattel, L. Stealth liposomes: Review of the basic science, rationale, and clinical applications, existing and potential. *International Journal of Nanomedicine* **1,** 297–315 (2006).

31. Lin, C. C. & Anseth, K. S. PEG hydrogels for the controlled release of biomolecules in regenerative medicine. *Pharmaceutical Research* **26,** 631–643 (2009).

32. Guggenbichler, J. P., Assadian, O., Boeswald, M. & Kramer, A. Incidence and clinical implication of nosocomial infections associated with implantable biomaterials - catheters, ventilator-associated pneumonia, urinary tract infections. *GMS Krankenhaushygiene interdisziplinär* **6,** Doc18 (2011).

33. Bartlett, J. G. Treating foot infections in diabetic patients: A randomized, multicenter, open-label trial of linezolid versus ampicillin-sulbactam/amoxicillin-clavulanate. *Infectious Diseases in Clinical Practice* **12,** 267–268 (Apr. 2004).

34. Hall-Stoodley, L., Costerton, J. W. & Stoodley, P. Bacterial biofilms: From the natural environment to infectious diseases. *Nature Reviews Microbiology* **2,** 95–108 (Feb. 2004).

35. Hetrick, E. M. & Schoenfisch, M. H. Reducing implant-related infections: Active release strategies. *Chemical Society Reviews* **35,** 780–789 (2006).

36. Davies, D. Understanding biofilm resistance to antibacterial agents. *Nature Reviews Drug Discovery* **2,** 114–122 (Feb. 2003).

37. Arciola, C. R., Campoccia, D., Speziale, P., Montanaro, L. & Costerton, J. W. *Biofilm formation in Staphylococcus implant infections. A review of molecular mechanisms and implications for biofilm-resistant materials* Sept. 2012.

38. Drekonja, D. M., Kuskowski, M. A., Wilt, T. J. & Johnson, J. R. Antimicrobial urinary catheters: A systematic review. *Expert Review of Medical Devices* **5,** 495–506 (July 2008).

39. Giavaresi, G. *et al.* Efficacy of antibacterial-loaded coating in an in vivo model of acutely highly contaminated implant. *International Orthopaedics* **38,** 1505–1512 (July 2014).

40. Schmidmaier, G., Lucke, M., Wildemann, B., Haas, N. P. & Raschke, M. Prophylaxis and treatment of implant-related infections by antibiotic-coated implants: a review. *Injury* **37,** 105–12 (May 2006).

41. Metcalf, D. G., Parsons, D. & Bowler, P. G. Clinical safety and effectiveness evaluation of a new antimicrobial wound dressing designed to manage exudate, infection and biofilm. *International Wound Journal* **14,** 203–213 (Feb. 2017).

42. Bloom, H. L. & Hirsh, D. Clinical use of antibacterial mesh envelopes in cardiovascular electronic device implantations. *Medical Devices: Evidence and Research* **8,** 71 (2015).

43. Cloutier, M., Mantovani, D. & Rosei, F. Antibacterial Coatings: Challenges, Perspectives, and Opportunities. *Trends in Biotechnology* **33,** 637–652 (Nov. 2015).

44. Wu, P. & Grainger, D. W. Drug/device combinations for local drug therapies and infection prophylaxis. *Biomaterials* **27,** 2450–2467 (2006).

45. Busscher, H. J. *et al.* Biomaterial-Associated Infection: Locating the Finish Line in the Race for the Surface. *Science Translational Medicine* **4,** 10–153 (Sept. 2012).

46. Séon, L., Lavalle, P., Schaaf, P. & Boulmedais, F. Polyelectrolyte Multilayers: A Versatile Tool for Preparing Antimicrobial Coatings. *Langmuir* **31,** 12856–12872 (Nov. 2015).

47. Carmona-Ribeiro, A. M. & de Melo Carrasco, L. D. Cationic antimicrobial polymers and their assemblies. *International Journal of Molecular Sciences* **14,** 9906–9946 (May 2013).

48. Zhuk, I. *et al.* Self-defensive layer-by-layer films with bacteria-triggered antibiotic release. *ACS Nano* **8,** 7733–7745 (Aug. 2014).

49. Chen, W. H. *et al.* Mesoporous silica-based versatile theranostic nanoplatform constructed by layer-by-layer assembly for excellent photodynamic/chemo therapy. *Biomaterials* **117,** 54–65 (Feb. 2017).

50. Hsu, B. B., Park, M.-H., Hagerman, S. R. & Hammond, P. T. Multimonth controlled small molecule release from biodegradable thin films. *Proceedings of the National Academy of Sciences* **111,** 12175–12180 (Aug. 2014).

51. Engler, A. C. *et al.* Effects of side group functionality and molecular weight on the activity of synthetic antimicrobial polypeptides. *Biomacromolecules* **12,** 1666–1674 (May 2011).

52. Milović, N. M., Wang, J., Lewis, K. & Klibanov, A. M. Immobilized N-alkylated polyethylenimine avidly kills bacteria by rupturing cell membranes with no resistance developed. *Biotechnology and Bioengineering* **90,** 715–722 (2005).

53. Dark, P. M., Dean, P. & Warhurst, G. *Bench-to-bedside review: the promise of rapid infection diagnosis during sepsis using polymerase chain reaction-based pathogen detection.* 2009.

54. Goldberg, B., Sichtig, H., Geyer, C., Ledeboer, N. & Weinstock, G. M. *Making the leap from research laboratory to clinic: Challenges and opportunities for next-generation sequencing in infectious disease diagnostics* Dec. 2015.

55. Yager, P., Domingo, G. J. & Gerdes, J. Point-of-Care Diagnostics for Global Health. *Annual Review of Biomedical Engineering* **10,** 107–144 (Aug. 2008).

56. Creran, B. *et al.* Detection of bacteria using inkjet-printed enzymatic test strips. *ACS Applied Materials and Interfaces* **6,** 19525–19530 (Nov. 2014).

57. Quesada-González, D. & Merkoçi, A. Nanomaterial-based devices for point-of-care diagnostic applications. *Chemical Society Reviews* **47,** 4697–4709 (2018).

58. Van Berkel, S. S. *et al.* Assay Platform for Clinically Relevant Metallo-β-lactamases. *Journal of Medicinal Chemistry* **56,** 6945–6953 (Sept. 2013).

59. Cheng, Y. *et al.* Fluorogenic probes with substitutions at the 2 and 7 positions of cephalosporin are highly BlaC-specific for rapid mycobacterium tuberculosis detection. *Angewandte Chemie - International Edition* **53,** 9360–9364 (Aug. 2014).

60. Xiao, J. M. *et al.* Novel fluorescent cephalosporins: Synthesis, antimicrobial activity and photodynamic inactivation of antibiotic resistant bacteria. *European Journal of Medicinal Chemistry* **59,** 150–159 (2013).

61. Mao, W., Wang, Y., Qian, X., Xia, L. & Xie, H. A Carbapenem-Based Off–On Fluorescent Probe for Specific Detection of Metallo-β-Lactamase Activities. *ChemBioChem* **20,** 511–515 (Feb. 2019).

62. Shao, Q. & Xing, B. Enzyme responsive luminescent ruthenium(ii) cephalosporin probe for intracellular imaging and photoinactivation of antibiotics resistant bacteria. *Chemical Communications* **48,** 1739–1741 (2012).

63. Chan, H. L. *et al.* Unique Fluorescent Imaging Probe for Bacterial Surface Localization and Resistant Enzyme Imaging. *ACS Chemical Biology* **13,** 1890–1896 (July 2018).

64. Tosh, P. K. & McDonald, L. C. Infection control in the multidrug-resistant era: Tending the human microbiome. *Clinical Infectious Diseases* **54,** 707–713 (Mar. 2012).

65. Nandi, S. K. *et al.* Local antibiotic delivery systems for the treatment of osteomyelitis - A review. *Materials Science and Engineering C* **29,** 2478–2485 (2009).

66. Min, J. *et al.* Designer Dual Therapy Nanolayered Implant Coatings Eradicate Biofilms and Accelerate Bone Tissue Repair. *ACS Nano* **10,** 4441–4450 (Apr. 2016).

67. Koetting, M. C., Peters, J. T., Steichen, S. D. & Peppas, N. A. Stimulus-responsive hydrogels: Theory, modern advances, and applications. *Materials Science and Engineering R: Reports* **93,** 1–49 (2015).

68. Badeau, B. A. & DeForest, C. A. Programming Stimuli-Responsive Behavior into Biomaterials. *Annual Review of Biomedical Engineering* **21,** 241–265 (2019).

69. Li, X. *et al. Recent developments in smart antibacterial surfaces to inhibit biofilm formation and bacterial infections* 2018.

70. Radovic-Moreno, A. F. *et al.* Surface charge-switching polymeric nanoparticles for bacterial cell wall-targeted delivery of antibiotics. *ACS Nano* **6,** 4279–4287 (2012).

71. Pornpattananangkul, D. *et al.* Stimuli-responsive liposome fusion mediated by gold nanoparticles. *ACS Nano* **4,** 1935–1942 (2010).

72. Gao, W. *et al.* Hydrogel containing nanoparticle-stabilized liposomes for topical antimicrobial delivery. *ACS Nano* **8,** 2900–2907 (2014).

73. Smith, S. M. D-lactic acid production as a monitor of the effectiveness of antimicrobial agents. *Antimicrobial Agents and Chemotherapy* **35,** 237–241 (Feb. 1991).

74. Pornpattananangkul, D. *et al.* Bacterial toxin-triggered drug release from gold nanoparticle-stabilized liposomes for the treatment of bacterial infection. *Journal of the American Chemical Society* **133,** 4132–4139 (2011).

75. Xiong, M. H. *et al.* Lipase-sensitive polymeric triple-layered nanogel for "on-demand" drug delivery. *Journal of the American Chemical Society* **134,** 4355–4362 (Mar. 2012).

76. Xiong, M. H. *et al.* Bacteria-responsive multifunctional nanogel for targeted antibiotic delivery. *Advanced Materials* **24,** 6175–6180 (Dec. 2012).

77. Yepuri, N. R. *et al.* Synthesis of cephalosporin-3-diazeniumdiolates: Biofilm dispersing NO-donor prodrugs activated by β-lactamase. *Chemical Communications* **49,** 4791–4793 (May 2013).

78. Zaengle-Barone, J. M. *et al.* Copper Influences the Antibacterial Outcomes of a β-Lactamase-Activated Prochelator against Drug-Resistant Bacteria. *ACS Infectious Diseases* **4,** 1019–1029 (June 2018).

79. Evans, L. E. *et al.* Exploitation of Antibiotic Resistance as a Novel Drug Target: Development of a β-Lactamase-Activated Antibacterial Prodrug. *Journal of Medicinal Chemistry* **62,** 4411–4425 (May 2019).

80. Zheng, X. *et al.* Exploiting a bacterial drug-resistance mechanism: A light-activated construct for the destruction of MRSA. *Angewandte Chemie - International Edition* **48,** 2148–2151 (Mar. 2009).

81. Li, Y., Liu, G., Wang, X., Hu, J. & Liu, S. Enzyme-Responsive Polymeric Vesicles for Bacterial-Strain-Selective Delivery of Antimicrobial Agents. *Angewandte Chemie - International Edition* **55,** 1760–1764 (Jan. 2016).

82. Hoare, T. R. & Kohane, D. S. Hydrogels in drug delivery: Progress and challenges. *Polymer* **49,** 1993–2007 (2008).

83. Simões, S. Modular Hydrogels for Drug Delivery. *Journal of Biomaterials and Nanobiotechnology* **03,** 185–199 (2012).

84. Ng, V. W. *et al.* Antimicrobial hydrogels: A new weapon in the arsenal against multidrug-resistant infections. *Advanced Drug Delivery Reviews* **78,** 46–62 (2014).

85. Caló, E. & Khutoryanskiy, V. V. Biomedical applications of hydrogels: A review of patents and commercial products. *European Polymer Journal* **65,** 252–267 (Apr. 2015).

86. Abu-gnim, C. *et al. PHARMACEUTICAL COMPOSITIONS CONTAINING MUPIROCIN* 2000.

87. Francesko, A. *et al.* Bottom-up Layer-by-Layer Assembling of Antibacterial Free-standing Nanobiocomposite Films. *Biomacromolecules* **19,** 3628–3636 (2018).

88. Ifkovits, J. L. & Burdick, J. A. Review: Photopolymerizable and Degradable Biomaterials for Tissue Engineering Applications. *Tissue Engineering* **13,** 2369–2385 (2007).

89. Jiang, Y., Chen, J., Deng, C., Suuronen, E. J. & Zhong, Z. Click hydrogels, microgels and nanogels: Emerging platforms for drug delivery and tissue engineering. *Biomaterials* **35,** 4969–4985 (June 2014).

90. Phelps, E. A. *et al.* Maleimide cross-linked bioactive PEG hydrogel exhibits improved reaction kinetics and cross-linking for cell encapsulation and in situ delivery. *Advanced Materials* **24,** 64–70 (2012).

91. Macdougall, L. J., Pérez-Madrigal, M. M., Arno, M. C. & Dove, A. P. Nonswelling Thiol–Yne Cross-Linked Hydrogel Materials as Cytocompatible Soft Tissue Scaffolds. *Biomacromolecules* **19,** 1378–1388 (May 2018).

92. Lutolf, M. P. & Hubbell, J. A. Synthesis and physicochemical characterization of end-linked poly(ethylene glycol)-co-peptide hydrogels formed by Michael-type addition. *Biomacromolecules* **4,** 713–722 (2003).

93. Jansen, L. E., Negrón-Piñeiro, L. J., Galarza, S. & Peyton, S. R. Control of thiol-maleimide reaction kinetics in PEG hydrogel networks. *Acta Biomaterialia* **70,** 120–128 (Apr. 2018).

94. Darling, N. J., Hung, Y.-S., Sharma, S. & Segura, T. Controlling the kinetics of thiol-maleimide Michael-type addition gelation kinetics for the generation of homogenous poly(ethylene glycol) hydrogels. *Biomaterials* **101,** 199–206 (Sept. 2016).

95. Canal, T. & Peppas, N. A. Correlation between mesh size and equilibrium degree of swelling of polymeric networks. *Journal of Biomedical Materials Research* **23,** 1183–1193 (Oct. 1989).

96. Huang, X. & Brazel, C. S. On the importance and mechanisms of burst release in matrix-controlled drug delivery systems. *Journal of Controlled Release* **73,** 121–136 (2001).

97. Kamaly, N., Yameen, B., Wu, J. & Farokhzad, O. C. Degradable controlled-release polymers and polymeric nanoparticles: Mechanisms of controlling drug release. *Chemical Reviews* **116,** 2602–2663 (Feb. 2016).

98. Li, J. & Mooney, D. J. Designing hydrogels for controlled drug delivery. *Nature Reviews Materials* **1,** 16071 (Dec. 2016).

99. Cruise, G. M., Scharp, D. S. & Hubbell, J. A. Characterization of permeability and network structure of interfacially photopolymerized poly(ethylene glycol) diacrylate hydrogels. *Biomaterials* **19,** 1287–1294 (July 1998).

100. DuBose, J. W., Cutshall, C. & Metters, A. T. Controlled release of tethered molecules via engineered hydrogel degradation: Model development and validation. *Journal of Biomedical Materials Research - Part A* **74,** 104–116 (2005).

101. Aimetti, A. A., Machen, A. J. & Anseth, K. S. Poly(ethylene glycol) hydrogels formed by thiol-ene photopolymerization for enzyme-responsive protein delivery. *Biomaterials* **30,** 6048–6054 (2009).

102. Lutolf, M. P. *et al.* Synthetic matrix metalloproteinase-sensitive hydrogels for the conduction of tissue regeneration: Engineering cell-invasion characteristics. *Proceedings of the National Academy of Sciences of the United States of America* **100,** 5413–5418 (Apr. 2003).

103. Sokic, S. & Papavasiliou, G. Controlled Proteolytic Cleavage Site Presentation in Biomimetic PEGDA Hydrogels Enhances Neovascularization ¡i¿In Vitro¡/i¿. *Tissue Engineering Part A* **18,** 2477–2486 (2012).

104. Johnson, C. T. *et al.* Hydrogel delivery of lysostaphin eliminates orthopedic implant infection by Staphylococcus aureus and supports fracture healing. *Proceedings of the National Academy of Sciences* **115,** E4960–E4969 (May 2018).

105. Iler, R. Multilayers of colloidal particles. *Journal of Colloid and Interface Science* **21,** 569–594 (June 1966).

106. Decher, G. & Hong, J. .-. Buildup of ultrathin multilayer films by a self-assembly process, 1 consecutive adsorption of anionic and cationic bipolar amphiphiles on charged surfaces. *Makromolekulare Chemie. Macromolecular Symposia* **46,** 321–327 (June 1991).

107. Saurer, E. M. *et al.* Polyelectrolyte multilayers promote stent-mediated delivery of DNA to vascular tissue. *Biomacromolecules* **14,** 1696–1704 (May 2013).

108. Shukla, A., Fang, J. C., Puranam, S. & Hammond, P. T. Release of vancomycin from multilayer coated absorbent gelatin sponges. *Journal of Controlled Release* **157,** 64–71 (Jan. 2012).

109. Krogman, K. C., Cohen, R. E., Hammond, P. T., Rubner, M. F. & Wang, B. N. Industrial-scale spray layer-by-layer assembly for production of biomimetic photonic systems. *Bioinspiration and Biomimetics* **8,** 045005 (Nov. 2013).

110. Shukla, A. & Almeida, B. Advances in cellular and tissue engineering using layer-by-layer assembly. *Wiley Interdisciplinary Reviews: Nanomedicine and Nanobiotechnology* **6,** 411–421 (Sept. 2014).

111. Liu, T. *et al.* Biomedical Applications of Layer-by-Layer Self-Assembly for Cell Encapsulation: Current Status and Future Perspectives. *Advanced Healthcare Materials* **8,** 1800939 (Jan. 2019).

112. Fukuda, Y. *et al.* Layer-by-layer cell coating technique using extracellular matrix facilitates rapid fabrication and function of pancreatic β-cell spheroids. *Biomaterials* **160,** 82–91 (Apr. 2018).

113. Cai, X., Gao, X., Wang, L., Wu, Q. & Lin, X. A layer-by-layer assembled and carbon nanotubes/gold nanoparticles-based bienzyme biosensor for cholesterol detection. *Sensors and Actuators, B: Chemical* **181,** 575–583 (2013).

114. Barsan, M. M., David, M., Florescu, M., Ţugulea, L. & Brett, C. M. A new self-assembled layer-by-layer glucose biosensor based on chitosan biopolymer entrapped enzyme with nitrogen doped graphene. *Bioelectrochemistry* **99,** 46–52 (Oct. 2014).

115. Tang, T. *et al.* Harnessing the layer-by-layer assembly technique to design biomaterials vaccines for immune modulation in translational applications. *Biomaterials Science* **7,** 715–732 (2019).

116. Costa, R. R., Alatorre-Meda, M. & Mano, J. F. *Drug nano-reservoirs synthesized using layer-by-layer technologies* Nov. 2015.

117. Shukla, A., Fang, J. C., Puranam, S., Jensen, F. R. & Hammond, P. T. Hemostatic multilayer coatings. *Advanced Materials* **24,** 492–496 (Jan. 2012).

118. Pérez-Anes, A. *et al.* Bioinspired Titanium Drug Eluting Platforms Based on a Poly-β-cyclodextrin-Chitosan Layer-by-Layer Self-Assembly Targeting Infections. *ACS Applied Materials and Interfaces* **7,** 12882–12893 (June 2015).

119. Turvey, M. E. *et al.* Microneedle-based intradermal delivery of stabilized dengue virus. *Bioengineering & Translational Medicine* **4,** e10127 (May 2019).

120. Anselmo, A. C. *et al.* Monocyte-mediated delivery of polymeric backpacks to inflamed tissues: A generalized strategy to deliver drugs to treat inflammation. *Journal of Controlled Release* **199,** 29–36 (2015).

121. Luo, G.-F. *et al.* Encapsulation of an Adamantane-Doxorubicin Prodrug in pH-Responsive Polysaccharide Capsules for Controlled Release. *ACS Applied Materials & Interfaces* **4,** 5317–5324 (Oct. 2012).

122. Borges, J. & Mano, J. F. Molecular interactions driving the layer-by-layer assembly of multilayers. *Chemical Reviews* **114,** 8883–8942 (Aug. 2014).

123. Izquierdo, A., Ono, S. S., Voegel, J. C., Schaaf, P. & Decher, G. Dipping versus spraying: Exploring the deposition conditions for speeding up layer-by-layer assembly. *Langmuir* **21,** 7558–7567 (2005).

124. Kharlampieva, E., Kozlovskaya, V., Chan, J., Ankner, J. F. & Tsukruk, V. V. Spin-assisted layer-by-layer assembly: Variation of stratification as studied with neutron reflectivity. *Langmuir* **25,** 14017–14024 (Dec. 2009).

125. Hong, X. *et al.* Fabrication of magnetic luminescent nanocomposites by a layer-by-layer self-assembly approach. *Chemistry of Materials* **16,** 4022–4027 (2004).

126. Kantak, C., Beyer, S., Yobas, L., Bansal, T. & Trau, D. A 'microfluidic pinball' for on-chip generation of Layer-by-Layer polyelectrolyte microcapsules. *Lab on a Chip* **11,** 1030–1035 (Feb. 2011).

127. DeRocher, J. P., Mao, P., Han, J., Rubner, M. F. & Cohen, R. E. Layer-by-Layer Assembly of Polyelectrolytes in Nanofluidic Devices. *Macromolecules* **43,** 2430–2437 (Mar. 2010).

128. Kantak, C., Beyer, S., Yobas, L., Bansal, T. & Trau, D. A 'microfluidic pinball' for on-chip generation of Layer-by-Layer polyelectrolyte microcapsules. *Lab on a Chip* **11,** 1030 (Feb. 2011).

129. Andres, C. M. & Kotov, N. A. Inkjet deposition of layer-by-layer assembled films. *Journal of the American Chemical Society* **132,** 14496–14502 (Oct. 2010).

130. Sung, Y. Y. & Rubner, M. F. Micropatterning of polymer thin films with pH-sensitive and cross-linkable hydrogen-bonded polyelectrolyte multilayers. *Journal of the American Chemical Society* **124,** 2100–2101 (2002).

131. Clark, S. L., Montague, M. & Hammond, P. T. Selective deposition in multilayer assembly: SAMs as molecular templates. *Supramolecular Science* **4,** 141–146 (Mar. 1997).

132. Richardson, J. J., Björnmalm, M. & Caruso, F. Technology-driven layer-by-layer assembly of nanofilms. *Science* **348,** aaa2491–aaa2491 (2015).

133. Richardson, J. J. *et al.* Innovation in Layer-by-Layer Assembly. *Chemical Reviews* **116,** 14828–14867 (Dec. 2016).

134. Salomäki, M., Vinokurov, I. A. & Kankare, J. Effect of temperature on the buildup of polyelectrolyte multilayers. *Langmuir* **21,** 11232–11240 (Nov. 2005).

135. Dubas, S. T. & Schlenoff, J. B. Factors controlling the growth of polyelectrolyte multilayers. *Macromolecules* **32,** 8153–8160 (Nov. 1999).

136. Dubas, S. T. & Schlenoff, J. B. Polyelectrolyte multilayers containing a weak polyacid: Construction and deconstruction. *Macromolecules* **34,** 3736–3740 (2001).

137. Schönhoff, M. & Bieker, P. Linear and exponential growth regimes of multilayers of weak polyelectrolytes in dependence on pH. *Macromolecules* **43,** 5052–5059 (June 2010).

138. Sui, Z., Salloum, D. & Schlenoff, J. B. Effect of Molecular Weight on the Construction of Polyelectrolyte Multilayers: Stripping versus Sticking. *Langmuir* **19,** 2491–2495 (Mar. 2003).

139. Porcel, C. *et al.* Influence of the polyelectrolyte molecular weight on exponentially growing multilayer films in the linear regime. *Langmuir* **23,** 1898–1904 (2007).

140. Selin, V., Ankner, J. F. & Sukhishvili, S. A. Nonlinear Layer-by-Layer Films: Effects of Chain Diffusivity on Film Structure and Swelling. *Macromolecules* **50,** 6192–6201 (Aug. 2017).

141. Fu, J. & Schlenoff, J. B. Driving Forces for Oppositely Charged Polyion Association in Aqueous Solutions: Enthalpic, Entropic, but Not Electrostatic. *Journal of the American Chemical Society* **138,** 980–990 (Jan. 2016).

142. Ghostine, R. A., Markarian, M. Z. & Schlenoff, J. B. Asymmetric growth in polyelectrolyte multilayers. *Journal of the American Chemical Society* **135,** 7636–7646 (2013).

143. Fares, H. M. & Schlenoff, J. B. Diffusion of Sites versus Polymers in Polyelectrolyte Complexes and Multilayers. *Journal of the American Chemical Society* **139,** 14656–14667 (2017).

144. Michaels, A. S. & Miekka, R. G. Polycation-polyanion complexes: Preparation and properties of poly-(vinylbenzyltrimethylammonium) poly-(styrenesulfonate). *Journal of Physical Chemistry* **65,** 1765–1773 (Oct. 1961).

145. Ladam, G. *et al.* In situ determination of the structural properties of initially deposited polyelectrolyte multilayers. *Langmuir* **16,** 1249–1255 (2000).

146. Clark, S. L., Montague, M. F. & Hammond, P. T. Ionic Effects of Sodium Chloride on the Templated Deposition of Polyelectrolytes Using Layer-by-Layer Ionic Assembly. *Macromolecules* **30,** 7237–7244 (Nov. 1997).

147. Castleberry, S. A. *et al.* Self-Assembled Wound Dressings Silence MMP-9 and Improve Diabetic Wound Healing in Vivo. *Advanced Materials* **28,** 1809–1817 (Mar. 2016).

148. Truong-Phuoc, L. *et al.* Layer-by-Layer Photocatalytic Assembly for Solar Light-Activated Self-Decontaminating Textiles. *ACS Applied Materials and Interfaces* **8,** 34438–34445 (Dec. 2016).

149. Jia, Z. *et al.* Triple-Bioinspired Burying/Crosslinking Interfacial Coassembly Strategy for Layer-by-Layer Construction of Robust Functional Bioceramic Self-Coatings for Osteointegration Applications. *ACS Applied Materials and Interfaces* **11,** 4447–4469 (Jan. 2019).

150. Correa, S., Boehnke, N., Deiss-Yehiely, E. & Hammond, P. T. Solution Conditions Tune and Optimize Loading of Therapeutic Polyelectrolytes into Layer-by-Layer Functionalized Liposomes. *ACS Nano* **13,** 5623–5634 (May 2019).

151. Caruso, F. Nanoengineering of particle surfaces. *Advanced Materials* **13,** 11–22 (Jan. 2001).

152. Schneider, G. & Decher, G. From functional core/shell nanoparticles prepared via layer-by-layer deposition to empty nanospheres. *Nano Letters* **4,** 1833–1839 (Oct. 2004).

153. Pavlukhina, S. *et al.* Small-molecule-hosting nanocomposite films with multiple bacteria-triggered responses. *NPG Asia Materials* **6,** e121–e121 (Aug. 2014).

154. Albright, V. *et al.* Self-defensive antibiotic-loaded layer-by-layer coatings: Imaging of localized bacterial acidification and pH-triggering of antibiotic release. *Acta Biomaterialia* **61,** 66–74 (Oct. 2017).

155. Zhang, J. & Ma, P. X. Cyclodextrin-based supramolecular systems for drug delivery: Recent progress and future perspective. *Advanced Drug Delivery Reviews* **65,** 1215–1233 (Aug. 2013).

156. Junthip, J. *et al.* Layer-by-layer coating of textile with two oppositely charged cyclodextrin polyelectrolytes for extended drug delivery. *Journal of Biomedical Materials Research - Part A* **104,** 1408–1424 (June 2016).

157. Jing, J. *et al.* Cyclodextrin/paclitaxel complex in biodegradable capsules for breast cancer treatment. *Chemistry of Materials* **25,** 3867–3873 (Oct. 2013).

158. Huang, T. *et al.* Molecularly Selective Regulation of Delivery Fluxes by Employing Supramolecular Interactions in Layer-by-Layer Films. *Chemistry - An Asian Journal* **13,** 1067–1073 (Apr. 2018).

159. Wang, B. *et al.* A self-defensive antibacterial coating acting through the bacteria-triggered release of a hydrophobic antibiotic from layer-by-layer films. *Journal of Materials Chemistry B* **5,** 1498–1506 (Feb. 2017).

160. Zhang, H., Wang, D., Zuo, X. & Gao, C. UV-Responsive Multilayers with Multiple Functions for Biofilm Destruction and Tissue Regeneration. *ACS Applied Materials and Interfaces* **11,** 17283–17293 (2019).

161. Zhu, Z., Gao, N., Wang, H. & Sukhishvili, S. A. Temperature-triggered on-demand drug release enabled by hydrogen-bonded multilayers of block copolymer micelles. *Journal of Controlled Release* **171,** 73–80 (Oct. 2013).

162. Shah, N. J. *et al.* Surface-mediated bone tissue morphogenesis from tunable nanolayered implant coatings. *Science Translational Medicine* (2013).

163. Lin, M. *et al.* Facial Layer-by-Layer Engineering of Upconversion Nanoparticles for Gene Delivery: Near-Infrared-Initiated Fluorescence Resonance Energy Transfer Tracking and Overcoming Drug Resistance in Ovarian Cancer. *ACS Applied Materials and Interfaces* **9,** 7941–7949 (Mar. 2017).

164. Kim, J. O. *et al.* Layer-by-layer coated lipid-polymer hybrid nanoparticles designed for use in anticancer drug delivery. *Carbohydrate Polymers* **102,** 653–661 (Feb. 2014).

165. Feng, W. *et al.* Effect of pH-responsive alginate/chitosan multilayers coating on delivery efficiency, cellular uptake and biodistribution of mesoporous silica nanoparticles based nanocarriers. *ACS Applied Materials and Interfaces* **6,** 8447–8460 (June 2014).

166. Dreaden, E. C. *et al.* Bimodal tumor-targeting from microenvironment responsive hyaluronan layer-by-layer (LbL) nanoparticles. *ACS Nano* **8,** 8374–8382 (2014).

167. Li, J. *et al.* Biospecific Self-Assembly of a Nanoparticle Coating for Targeted and Stimuli-Responsive Drug Delivery. *Advanced Functional Materials* **25,** 1404–1417 (Mar. 2015).

168. Deng, Z. J. *et al.* Layer-by-layer nanoparticles for systemic codelivery of an anticancer drug and siRNA for potential triple-negative breast cancer treatment. *ACS Nano* **7,** 9571–9584 (Nov. 2013).

169. Shukla, A., Fang, J. C., Puranam, S. & Hammond, P. T. Release of vancomycin from multilayer coated absorbent gelatin sponges. *Journal of Controlled Release* **157,** 64–71 (Jan. 2012).

170. Demuth, P. C. *et al.* Polymer multilayer tattooing for enhanced DNA vaccination. *Nature Materials* **12,** 367–376 (Apr. 2013).

171. Wang, X. *et al.* Microenvironment-Responsive Magnetic Nanocomposites Based on Silver Nanoparticles/Gentamicin for Enhanced Biofilm Disruption by Magnetic Field. *ACS Applied Materials and Interfaces* **10,** 34905–34915 (Oct. 2018).

172. Tao, B. *et al.* BMP2-loaded titania nanotubes coating with pH-responsive multilayers for bacterial infections inhibition and osteogenic activity improvement. *Colloids and Surfaces B: Biointerfaces* **177,** 242–252 (May 2019).

173. Choi, K. Y. *et al.* Binary Targeting of siRNA to Hematologic Cancer Cells In Vivo Using Layer-by-Layer Nanoparticles. *Advanced Functional Materials* **29,** 1900018 (May 2019).

174. Correa, S., Dreaden, E. C., Gu, L. & Hammond, P. T. Engineering nanolayered particles for modular drug delivery. *Journal of Controlled Release* **240,** 364–386 (2016).

175. Jeong, H. *et al.* In vitro blood cell viability profiling of polymers used in molecular assembly. *Scientific Reports* **7,** 9481 (Aug. 2017).

176. Selin, V., Ankner, J. & Sukhishvili, S. Ionically Paired Layer-by-Layer Hydrogels: Water and Polyelectrolyte Uptake Controlled by Deposition Time. *Gels* **4,** 7 (Jan. 2018).

177. Guo, X., Carter, M. C. D., Appadoo, V. & Lynn, D. M. Tunable and Selective Degradation of Amine-Reactive Multilayers in Acidic Media. *Biomacromolecules,* acs.biomac.9b00756 (Aug. 2019).

178. Wood, K. C., Chuang, H. F., Batten, R. D., Lynn, D. M. & Hammond, P. T. Controlling interlayer diffusion to achieve sustained, multiagent delivery from layer-by-layer thin films. *Proceedings of the National Academy of Sciences* **103,** 10207–10212 (July 2006).

179. Min, J., Braatz, R. D. & Hammond, P. T. Tunable staged release of therapeutics from layer-by-layer coatings with clay interlayer barrier. *Biomaterials* **35,** 2507–2517 (Mar. 2014).

180. Delcea, M., Möhwald, H. & Skirtach, A. G. Stimuli-responsive LbL capsules and nanoshells for drug delivery. *Advanced Drug Delivery Reviews* **63,** 730–747 (Aug. 2011).

181. Nam, K. *et al.* Size-controlled synthesis of polymerized DNA nanoparticles for targeted anticancer drug delivery. *Chemical Communications* **55,** 4905–4908 (Apr. 2019).

182. Morton, S. W. *et al.* Osteotropic therapy via targeted layer-by-layer nanoparticles. *Advanced Healthcare Materials* **3,** 867–875 (2014).

183. Bonner, D. K. *et al.* Intracellular trafficking of polyamidoamine-poly(ethylene glycol) block copolymers in DNA delivery. *Bioconjugate Chemistry* **22,** 1519–1525 (Aug. 2011).

184. Jemal, A. *et al.* Cancer Statistics, 2007. *CA: A Cancer Journal for Clinicians* **57,** 43–66 (Jan. 2007).

185. Mariotto, A. B., Robin Yabroff, K., Shao, Y., Feuer, E. J. & Brown, M. L. Projections of the cost of cancer care in the United States: 2010-2020. *Journal of the National Cancer Institute* **103,** 117–128 (Jan. 2011).

186. Cavaletti, G. & Marmiroli, P. Chemotherapy-induced peripheral neurotoxicity. *Current Opinion in Neurology* **28,** 500–507 (Oct. 2015).

187. Dreaden, E. C. *et al.* Tumor-targeted synergistic blockade of MAPK and PI3K from a layer-by-layer nanoparticle. *Clinical Cancer Research* **21,** 4410–4419 (Oct. 2015).

188. Liu, X. Q. & Picart, C. Layer-by-Layer Assemblies for Cancer Treatment and Diagnosis. *Advanced Materials* **28,** 1295–1301 (Feb. 2016).

189. Yan, Y., Zuo, X. & Wei, D. Concise Review: Emerging Role of CD44 in Cancer Stem Cells: A Promising Biomarker and Therapeutic Target. *STEM CELLS Translational Medicine* **4,** 1033–1043 (Sept. 2015).

190. Mattheolabakis, G., Milane, L., Singh, A. & Amiji, M. M. Hyaluronic acid targeting of CD44 for cancer therapy: from receptor biology to nanomedicine. *Journal of Drug Targeting* **23,** 605–618 (Sept. 2015).

191. Smith, M. R. Rituximab (monoclonal anti-CD20 antibody): mechanisms of action and resistance. *Oncogene* **22,** 7359–7368 (Oct. 2003).

192. Li, X., Kim, J., Yoon, J. & Chen, X. Cancer-Associated, Stimuli-Driven, Turn on Theranostics for Multimodality Imaging and Therapy. *Advanced Materials* **29,** 1606857 (June 2017).

193. Wu, Z., Lin, X., Zou, X., Sun, J. & He, Q. Biodegradable protein-based rockets for drug transportation and light-triggered release. *ACS Applied Materials and Interfaces* **7,** 250–255 (Jan. 2015).

194. Katagiri, K., Nakamura, M. & Koumoto, K. Magnetoresponsive smart capsules formed with polyelectrolytes, lipid bilayers and magnetic nanoparticles. *ACS Applied Materials and Interfaces* **2,** 768–773 (Mar. 2010).

195. Jain, R. K. & Stylianopoulos, T. Delivering nanomedicine to solid tumors. *Nature Reviews Clinical Oncology* **7,** 653–664 (Nov. 2010).

196. Such, G. K., Yan, Y., Johnston, A. P. R., Gunawan, S. T. & Caruso, F. Interfacing Materials Science and Biology for Drug Carrier Design. *Advanced Materials* **27,** 2278–2297 (Apr. 2015).

197. Li, Q. L. *et al.* Mesoporous silica nanoparticles coated by layer-by-layer self-assembly using cucurbit[7]uril for in vitro and in vivo anticancer drug release. *Chemistry of Materials* **26,** 6418–6431 (Nov. 2014).

198. Gu, L., Deng, Z. J., Roy, S. & Hammond, P. T. A combination RNAi-chemotherapy layer-by-layer nanoparticle for systemic targeting of KRAS/P53 with cisplatin to treat non–small cell lung cancer. *Clinical Cancer Research* **23,** 7312–7323 (2017).

199. Alkekhia, D. & Shukla, A. Influence of poly-l-lysine molecular weight on antibacterial efficacy in polymer multilayer films. *Journal of Biomedical Materials Research - Part A* **107,** 1324–1339 (June 2019).

200. United Nations. *NO TIME TO WAIT: SECURING THE FUTURE FROM DRUG-RESISTANT INFECTIONS. REPORT TO THE SECRETARY-GENERAL OF THE UNITED NATIONS* tech. rep. (2019).

201. Aslam, B. *et al.* Antibiotic resistance: a rundown of a global crisis. *Infection and Drug Resistance* **Volume 11,** 1645–1658 (Oct. 2018).

202. Laloyaux, X. *et al.* Temperature-responsive polymer brushes switching from bactericidal to cell-repellent. *Advanced Materials* **22,** 5024–5028 (Nov. 2010).

203. Francesko, A. *et al.* Bacteria-responsive multilayer coatings comprising polycationic nanospheres for bacteria biofilm prevention on urinary catheters. *Acta Biomaterialia* **33,** 203–212 (2016).

204. Menzel, E. J. & Farr, C. Hyaluronidase and its substrate hyaluronan: Biochemistry, biological activities and therapeutic uses. *Cancer Letters* **131,** 3–11 (1998).

205. Ibberson, C. B. *et al.* Staphylococcus aureus hyaluronidase is a CodY-regulated virulence factor. *Infection and Immunity* **82,** 4253–4264 (2014).

206. Wang, B. *et al.* Construction of High Drug Loading and Enzymatic Degradable Multilayer Films for Self-Defense Drug Release and Long-Term Biofilm Inhibition. *Biomacromolecules* **19,** 85–93 (2018).

207. Wei, T., Tang, Z., Yu, Q. & Chen, H. Smart Antibacterial Surfaces with Switchable Bacteria-Killing and Bacteria-Releasing Capabilities. *ACS Applied Materials and Interfaces* **9,** 37511–37523 (2017).

208. Xu, Q. *et al.* Bacterial self-defense antibiotics release from organic-inorganic hybrid multilayer films for long-term anti-adhesion and biofilm inhibition properties. *Nanoscale* **9,** 19245–19254 (2017).

209. Pletzer, D., Mansour, S. C. & Hancock, R. E. W. Synergy between conventional antibiotics and anti-biofilm peptides in a murine, sub-cutaneous abscess model caused by recalcitrant ESKAPE pathogens. *PLOS Pathogens* **14** (ed Yeaman, M. R.) e1007084 (June 2018).

210. Wu, Y. *et al.* Layer-by-Layer (LBL) Self-Assembled Biohybrid Nanomaterials for Efficient Antibacterial Applications. *ACS Applied Materials and Interfaces* **7,** 17255–17263 (2015).

211. Dafe, A., Etemadi, H., Zarredar, H. & Mahdavinia, G. R. Development of novel carboxymethyl cellulose/k-carrageenan blends as an enteric delivery vehicle for probiotic bacteria. *International Journal of Biological Macromolecules* **97,** 299–307 (Apr. 2017).

212. Wang, M. *et al.* Enhanced viability of layer-by-layer encapsulated Lactobacillus pentosus using chitosan and sodium phytate. *Food Chemistry* **285,** 260–265 (July 2019).

213. Anselmo, A. C., McHugh, K. J., Webster, J., Langer, R. & Jaklenec, A. Layer-by-Layer Encapsulation of Probiotics for Delivery to the Microbiome. *Advanced Materials* **28,** 9486–9490 (2016).

214. Zhang, S., Xing, M. & Li, B. Biomimetic layer-by-layer self-assembly of nanofilms, nanocoatings, and 3D scaffolds for tissue engineering. *International Journal of Molecular Sciences* **19,** 1641 (June 2018).

215. Zeng, J. & Matsusaki, M. Layer-by-layer assembly of nanofilms to control cell functions. *Polymer Chemistry* **10,** 2960–2974 (June 2019).

216. Oliveira, M. B., Hatami, J. & Mano, J. F. Coating Strategies Using Layer-by-layer Deposition for Cell Encapsulation. *Chemistry - An Asian Journal* **11,** 1753–1764 (June 2016).

217. Sutrisno, L. *et al.* Fabrication of hyaluronidase-responsive biocompatible multilayers on BMP2 loaded titanium nanotube for the bacterial infection prevention. *Materials Science and Engineering C* **89,** 95–105 (2018).

218. Lin, B. J. *et al.* Cytokine loaded layer-by-layer ultrathin matrices to deliver single dermal papilla cells for spot-by-spot hair follicle regeneration. *Journal of Materials Chemistry B* **4,** 489–504 (Jan. 2016).

219. Zhang, P., Chiu, Y. C., Tostanoski, L. H. & Jewell, C. M. Polyelectrolyte Multilayers Assembled Entirely from Immune Signals on Gold Nanoparticle Templates Promote Antigen-Specific T Cell Response. *ACS Nano* **9,** 6465–6477 (June 2015).

220. He, Y. *et al.* Synthetic Charge-Invertible Polymer for Rapid and Complete Implantation of Layer-by-Layer Microneedle Drug Films for Enhanced Transdermal Vaccination. *ACS Nano* **12,** 10272–10280 (Oct. 2018).

221. Duong, H. T. T. *et al.* Smart vaccine delivery based on microneedle arrays decorated with ultra-pH-responsive copolymers for cancer immunotherapy. *Biomaterials* **185,** 13–24 (Dec. 2018).

222. He, Y. *et al.* Synthetic Lift-off Polymer beneath Layer-by-Layer Films for Surface-Mediated Drug Delivery. *ACS Macro Letters* **6,** 1320–1324 (Nov. 2017).

223. Boucher, H. W. *et al.* Bad bugs, no drugs: no ESKAPE! An update from the Infectious Diseases Society of America. *Clinical infectious diseases : an official publication of the Infectious Diseases Society of America* **48,** 1–12 (Jan. 2009).

224. Boucher, H. W. *et al.* 10 '20 progress - Development of new drugs active against gram-negative bacilli: An update from the infectious diseases society of America. *Clinical Infectious Diseases* **56,** 1685–1694 (June 2013).

225. Yewale, V. N. *Antimicrobial resistance - A ticking bomb!* tech. rep. 3 (WHO, 2014), 171–172.

226. Reardon, S. Antibiotic resistance sweeping developing world. *Nature* **509,** 141–142 (2014).

227. Grosman, R., Vlach, O. & Leznar, M. Infections associated with surgical treatment of idiopathic scoliosis. *Acta Chirurgiae Orthopaedicae et Traumatologiae Cechoslovaca* **69,** 175–178 (Apr. 2002).

228. Stewart, P. S. & Costerton, J. W. Antibiotic resistance of bacteria in biofilms. *Lancet* **358,** 135–138 (Apr. 2001).

229. Hsu, S. H., Tseng, H. J. & Lin, Y. C. The biocompatibility and antibacterial properties of waterborne polyurethane-silver nanocomposites. *Biomaterials* **31,** 6796–6808 (Sept. 2010).

230. Wang, R., Neoh, K. G., Kang, E. T., Tambyah, P. A. & Chiong, E. Antifouling coating with controllable and sustained silver release for long-term inhibition of infection and encrustation in urinary catheters. *Journal of Biomedical Materials Research - Part B Applied Biomaterials* **103,** 519–528 (Apr. 2015).

231. Schaer, T. P., Stewart, S., Hsu, B. B. & Klibanov, A. M. Hydrophobic polycationic coatings that inhibit biofilms and support bone healing during infection. *Biomaterials* **33,** 1245–1254 (Feb. 2012).

232. Lin, J. *et al.* Durably Antibacterial and Bacterially Antiadhesive Cotton Fabrics Coated by Cationic Fluorinated Polymers. *ACS Applied Materials and Interfaces* **10,** 6124–6136 (Feb. 2018).

233. Palumbo, F. S. *et al.* A polycarboxylic/amino functionalized hyaluronic acid derivative for the production of pH sensible hydrogels in the prevention of bacterial adhesion on biomedical surfaces. *International Journal of Pharmaceutics* **478,** 70–77 (Jan. 2015).

234. Konai, M. M., Bhattacharjee, B., Ghosh, S. & Haldar, J. *Recent Progress in Polymer Research to Tackle Infections and Antimicrobial Resistance* June 2018.

235. Falagas, M. E. & Bliziotis, I. A. Pandrug-resistant Gram-negative bacteria: the dawn of the post-antibiotic era? *International Journal of Antimicrobial Agents* **29,** 630–636 (June 2007).

236. Paterson, D. L. Resistance in gram-negative bacteria: Enterobacteriaceae. *American Journal of Infection Control* **34,** S20–S28 (June 2006).

237. Santajit, S. & Indrawattana, N. *Mechanisms of Antimicrobial Resistance in ESKAPE Pathogens* 2016.

238. Siedenbiedel, F. & Tiller, J. C. Antimicrobial polymers in solution and on surfaces: Overview and functional principles. *Polymers* **4,** 46–71 (2012).

239. Ren, K., Ji, J. & Shen, J. Construction and enzymatic degradation of multilayered poly-L-lysine/DNA films. *Biomaterials* **27,** 1152–1159 (Mar. 2006).

240. Zhu, X. *et al.* Polyion multilayers with precise surface charge control for antifouling. *ACS Applied Materials and Interfaces* **7,** 852–861 (Jan. 2015).

241. Khademhosseini, A. *et al.* Layer-by-layer deposition of hyaluronic acid and poly-L-lysine for patterned cell co-cultures. *Biomaterials* **25,** 3583–3592 (Aug. 2004).

242. Delihas, N., Riley, L. W., Loo, W., Berkowitz, J. & Poltoratskaia, N. High sensitivity of Mycobacterium species to the bactericidal activity by polylysine. *FEMS Microbiology Letters* **132,** 233–237 (1995).

243. Conte, M., Aliberti, F., Fucci, L. & Piscopo, M. Antimicrobial activity of various cationic molecules on foodborne pathogens. *World Journal of Microbiology and Biotechnology* **23,** 1679–1683 (2007).

244. SHIMA, S., MATSUOKA, H., IWAMOTO, T. & SAKAI, H. Antimicrobial action of .EPSILON.-poly-L-lysine. *The Journal of Antibiotics* **37,** 1449–1455 (1984).

245. Dubois, A. V. *et al.* Poly-L-lysine compacts DNA, kills bacteria, and improves protease inhibition in cystic fibrosis sputum. *American Journal of Respiratory and Critical Care Medicine* **188,** 703–709 (Sept. 2013).

246. Some, S. *et al.* Dual functions of highly potent graphene derivative-poly-l-lysine composites to inhibit bacteria and support human cells. *ACS Nano* **6,** 7151–7161 (2012).

247. Li, P. *et al.* Cationic peptidopolysaccharides show excellent broad-spectrum antimicrobial activities and high selectivity. *Advanced Materials* **24,** 4130–4137 (Aug. 2012).

248. Polo, L. *et al.* Polylysine-porphycene conjugates as efficient photosensitizeers for the inactivation of microbial pathogens. *Journal of Photochemistry and Photobiology B: Biology* **59,** 152–158 (2000).

249. Tomé, J. P. C. *et al.* Synthesis and Antibacterial Activity of New Poly-S-lysinePorphyrin Conjugates. *Journal of Medicinal Chemistry* **47,** 6649–6652 (2004).

250. Decher, G. Fuzzy nanoassemblies: Toward layered polymeric multicomposites. *Science* **277,** 1232–1237 (Aug. 1997).

251. Gates, S. J. & Shukla, A. Layer-by-layer assembly of readily detachable chitosan and poly(acrylic acid) polyelectrolyte multilayer films. *Journal of Polymer Science, Part B: Polymer Physics* **55,** 127–131 (Jan. 2017).

252. Shukla, A., Fuller, R. C. & Hammond, P. T. Design of multi-drug release coatings targeting infection and inflammation. *Journal of Controlled Release* **155,** 159–166 (Oct. 2011).

253. Shukla, A. *et al.* Controlling the release of peptide antimicrobial agents from surfaces. *Biomaterials* **31,** 2348–2357 (Mar. 2010).

254. Etienne, O. *et al.* Multilayer polyelectrolyte films functionalized by insertion of defensin: A new approach to protection of implants from bacterial colonization. *Antimicrobial Agents and Chemotherapy* **48,** 3662–3669 (2004).

255. Jiang, B. & Li, B. Polypeptide nanocoatings for preventing dental and orthopaedic device-associated infection: PH-induced antibiotic capture, release, and antibiotic efficacy. *Journal of Biomedical Materials Research - Part B Applied Biomaterials* **88,** 332–338 (Feb. 2009).

256. Wittmer, C. R. *et al.* Multilayer nanofilms as substrates for hepatocellular applications. *Biomaterials* **29,** 4082–4090 (Oct. 2008).

257. Picart, C. *et al.* Buildup mechanism for poly(L-lysine)/hyaluronic acid films onto a solid surface. *Langmuir* **17,** 7414–7424 (2001).

258. Picart, C. *et al.* Molecular basis for the explanation of the exponential growth of polyelectrolyte multilayers. *Proceedings of the National Academy of Sciences* **99,** 12531–12535 (Oct. 2002).

259. Szarpak, A. *et al.* Designing hyaluronic acid-based layer-by-layer capsules as a carrier for intracellular drug delivery. *Biomacromolecules* **11,** 713–720 (Mar. 2010).

260. Yamanlar, S., Sant, S., Boudou, T., Picart, C. & Khademhosseini, A. Surface functionalization of hyaluronic acid hydrogels by polyelectrolyte multilayer films. *Biomaterials* **32,** 5590–5599 (2011).

261. Yao, Q. *et al.* Bacterial infection microenvironment-responsive enzymatically degradable multilayer films for multifunctional antibacterial properties. *Journal of Materials Chemistry B* **5,** 8532–8541 (2017).

262. Saha, N., Monge, C., Dulong, V., Picart, C. & Glinel, K. Influence of polyelectrolyte film stiffness on bacterial growth. *Biomacromolecules* **14,** 520–528 (Feb. 2013).

263. Lichter, J. A. & Rubner, M. F. Polyelectrolyte multilayers with intrinsic antimicrobial functionality: The importance of mobile polycations. *Langmuir* **25,** 7686–7694 (July 2009).

264. Mutschler, A. *et al.* Unexpected Bactericidal Activity of Poly(arginine)/Hyaluronan Nanolayered Coatings. *Chemistry of Materials* **28,** 8700–8709 (Dec. 2016).

265. Grotzky, A., Manaka, Y., Fornera, S., Willeke, M. & Walde, P. Quantification of α-polylysine: A comparison of four UV/Vis spectrophotometric methods. *Analytical Methods* **2,** 1448–1455 (2010).

266. Leclercq, L., Boustta, M., Rixte, J. & Vert, M. Degradability of poly(l-lysine) and poly(dl-aminoserinate) complexed with a polyanion under conditions modelling physico-chemical characteristics of body fluids. *Journal of Colloid and Interface Science* **350,** 459–464 (Oct. 2010).

267. Shukla, S. & Shukla, A. Tunable antibiotic delivery from gellan hydrogels. *Journal of Materials Chemistry B* **6,** 6444–6458 (2018).

268. Lavalle, P. *et al.* Modeling the Buildup of Polyelectrolyte Multilayer Films Having Exponential Growth. *The Journal of Physical Chemistry B* **108,** 635–648 (2004).

269. Li, S. *et al.* A DNA nanorobot functions as a cancer therapeutic in response to a molecular trigger in vivo. *Nature Biotechnology* **36,** 258–264 (Mar. 2018).

270. Harding, J. L. & Reynolds, M. M. Combating medical device fouling. *Trends in Biotechnology* **32,** 140–146 (2014).

271. Vaara, M., Siikanen, O., Apajalahti, J., Frimodt-Møller, N. & Vaara, T. Susceptibility of carbapenemase-producing strains of Klebsiella pneumoniae and Escherichia coli to the direct antibacterial activity of NAB739 and to the synergistic activity of NAB7061 with rifampicin and clarithromycin. *Journal of Antimicrobial Chemotherapy* **65,** 942–945 (Sept. 2010).

272. Vaara, M. & Vaara, T. Polycations as outer membrane-disorganizing agents. *Antimicrobial Agents and Chemotherapy* **24,** 114–122 (1983).

273. Hae Cho, C. A. *et al.* Molecular Weight and Charge Density Effects of Guanidinylated Biodegradable Polycarbonates on Antimicrobial Activity and Selectivity. *Biomacromolecules* **19,** 1389–1401 (May 2018).

274. Locock, K. E. S. *et al.* Guanylated polymethacrylates: A class of potent antimicrobial polymers with low hemolytic activity. *Biomacromolecules* **14,** 4021–4031 (Nov. 2013).

275. Lienkamp, K., Kumar, K. N., Som, A., Nüsslein, K. & Tew, G. N. "Doubly selective" antimicrobial polymers: How do they differentiate between bacteria? *Chemistry - A European Journal* **15,** 11710–11714 (Nov. 2009).

276. Porcel, C. *et al.* From Exponential to Linear Growth in Polyelectrolyte Multilayers. *Langmuir* **22,** 4376–4383 (2006).

277. Li, B. & Webster, T. J. Bacteria antibiotic resistance: New challenges and opportunities for implant-associated orthopedic infections. *Journal of Orthopaedic Research* **36,** 22–32 (Jan. 2018).

278. Martínez-Pastor, J. C., Vilchez, F., Pitart, C., Sierra, J. M. & Soriano, A. Antibiotic resistance in orthopaedic surgery: Acute knee prosthetic joint infections due to extended-spectrum beta-lactamase (ESBL)-producing Enterobacteriaceae. *European Journal of Clinical Microbiology and Infectious Diseases* **29,** 1039–1041 (Aug. 2010).

279. Weiner, L. M. *et al.* Antimicrobial-Resistant Pathogens Associated with Healthcare-Associated Infections: Summary of Data Reported to the National Healthcare Safety Network at the Centers for Disease Control and Prevention, 2011-2014. *Infection Control and Hospital Epidemiology* **37,** 1288–1301 (Nov. 2016).

280. Peleg, A. Y. & Hooper, D. C. Hospital-acquired infections due to gram-negative bacteria. *The New England journal of medicine* **362,** 1804–13 (May 2010).

281. Proctor, R. A. *et al. Small colony variants: A pathogenic form of bacteria that facilitates persistent and recurrent infections* 2006.

282. Kujawa, P., Moraille, P., Sanchez, J., Badia, A. & Winnik, F. M. Effect of molecular weight on the exponential growth and morphology of hyaluronan/chitosan multilayers: A surface plasmon resonance spectroscopy and atomic force microscopy investigation. *Journal of the American Chemical Society* **127,** 9224–9234 (2005).

283. Hübsch, E. *et al.* Controlling the growth regime of polyelectrolyte multilayer films: Changing from exponential to linear growth by adjusting the composition of polyelectrolyte mixtures. *Langmuir* **20,** 1980–1985 (2004).

284. Picart, C. *et al.* Controlled degradability of polysaccharide multilayer films in vitro and in vivo. *Advanced Functional Materials* **15,** 1771–1780 (Nov. 2005).

285. Jang, Y., Seo, J., Akgun, B., Satija, S. & Char, K. Molecular weight dependence on the disintegration of spin-assisted weak polyelectrolyte multilayer films. *Macromolecules* **46,** 4580–4588 (June 2013).

286. Monteiro, I. P., Shukla, A., Marques, A. P., Reis, R. L. & Hammond, P. T. Spray-assisted layer-by-layer assembly on hyaluronic acid scaffolds for skin tissue engineering. *Journal of Biomedical Materials Research - Part A* **103,** 330–340 (Mar. 2015).

287. Richert, L. *et al.* Improvement of Stability and Cell Adhesion Properties of Polyelectrolyte Multilayer Films by Chemical Cross-Linking. *Biomacromolecules* **5,** 284–294 (2004).

288. Hart, M. E., Hart, M. J. & Roop, A. J. Genotypic and phenotypic assessment of hyaluronidase among type strains of a select group of Staphylococcal species. *International Journal of Microbiology* (2009).

289. Starr, C. R. & Engleberg, N. C. Role of hyaluronidase in subcutaneous spread and growth of group A streptococcus. *Infection and Immunity* **74,** 40–48 (Jan. 2006).

290. Makris, G., Wright, J. D., Ingham, E. & Holland, K. T. The hyaluronate lyase of Staphylococcus aureus - A virulence factor? *Microbiology* **150,** 2005–2013 (June 2004).

291. Baier, G. *et al.* Enzyme responsive hyaluronic acid nanocapsules containing polyhexanide and their exposure to bacteria to prevent infection. *Biomacromolecules* **14,** 1103–1112 (2013).

292. Wang, B. L., Ren, K. F., Chang, H., Wang, J. L. & Ji, J. Construction of degradable multilayer films for enhanced antibacterial properties. *ACS Applied Materials and Interfaces* **5,** 4136–4143 (May 2013).

293. Cado, G. *et al.* Self-defensive biomaterial coating against bacteria and yeasts: Polysaccharide multilayer film with embedded antimicrobial peptide. *Advanced Functional Materials* **23,** 4801–4809 (Apr. 2013).

294. Chua, P. H., Neoh, K. G., Kang, E. T. & Wang, W. Surface functionalization of titanium with hyaluronic acid/chitosan polyelectrolyte multilayers and RGD for promoting osteoblast functions and inhibiting bacterial adhesion. *Biomaterials* **29,** 1412–1421 (Apr. 2008).

295. Harris, L. G., Patterson, L. M., Bacon, C., Ap Gwynn, I. & Richards, R. G. Assessment of the cytocompatibility of different coated titanium surfaces to fibroblasts and osteoblasts. *Journal of Biomedical Materials Research - Part A* **73,** 12–20 (Apr. 2005).

296. Richert, L., Arntz, Y., Schaaf, P., Voegel, J. C. & Picart, C. Ph Dependent Growth of Poly(L-Lysine)/Poly(L-Glutamic) Acid Multilayer Films and Their Cell Adhesion Properties. *Surface Science* **570,** 13–29 (Oct. 2004).

297. Engler, A. J., Richert, L., Wong, J. Y., Picart, C. & Discher, D. E. Surface probe measurements of the elasticity of sectioned tissue, thin gels and polyelectrolyte multilayer films: Correlations between substrate stiffness and cell adhesion. *Surface Science* **570,** 142–154 (Oct. 2004).

298. Kolewe, K. W., Zhu, J., Mako, N. R., Nonnenmann, S. S. & Schiffman, J. D. Bacterial Adhesion Is Affected by the Thickness and Stiffness of Poly(ethylene glycol) Hydrogels. *ACS Applied Materials and Interfaces* **10,** 2275–2281 (Jan. 2018).

299. Kolewe, K. W., Peyton, S. R. & Schiffman, J. D. Fewer Bacteria Adhere to Softer Hydrogels. *ACS Applied Materials and Interfaces* **7,** 19562–19569 (2015).

300. Song, F. *et al.* How Bacteria Respond to Material Stiffness during Attachment: A Role of Escherichia coli Flagellar Motility. *ACS Applied Materials and Interfaces* **9,** 22176–22184 (2017).

301. Lichter, J. A. *et al.* Substrata mechanical stiffness can regulate adhesion of viable bacteria. *Biomacromolecules* **9,** 1571–1578 (June 2008).

302. Guo, S. *et al.* Tailoring Polyelectrolyte Architecture to Promote Cell Growth and Inhibit Bacterial Adhesion. *ACS Applied Materials and Interfaces* **10,** 7882–7891 (Mar. 2018).

303. Zhuk, A. *et al.* Chain conformation and dynamics in spin-assisted weak polyelectrolyte multilayers. *Langmuir* **31,** 3889–3896 (Apr. 2015).

304. Colville, K., Tompkins, N., Rutenberg, A. D. & Jericho, M. H. Effects of poly(L-lysine) substrates on attached escherichia coli bacteria. *Langmuir* **26,** 2639–2644 (2010).

305. Wang, B. *et al.* Construction of High Drug Loading and Enzymatic Degradable Multilayer Films for Self-Defense Drug Release and Long-Term Biofilm Inhibition. *Biomacromolecules* **19,** 85–93 (2018).

306. Choksakulnimitr, S., Masuda, S., Tokuda, H., Takakura, Y. & Hashida, M. *In vitro cytotoxicity of macromolecules in different cell culture systems* tech. rep. 3 (1995), 233–241.

307. Fischer, D., Li, Y., Ahlemeyer, B., Krieglstein, J. & Kissel, T. In vitro cytotoxicity testing of polycations: Influence of polymer structure on cell viability and hemolysis. *Biomaterials* **24,** 1121–1131 (Mar. 2003).

308. Sgouras, D. & Duncan, R. Methods for the evaluation of biocompatibility of soluble synthetic polymers which have potential for biomedical use: 1 - Use of the tetrazolium-based colorimetric assay (MTT) as a preliminary screen for evaluation of in vitro cytotoxicity. *Journal of Materials Science: Materials in Medicine* **1,** 61–68 (July 1990).

309. Tognetti, L. *et al.* Bacterial skin and soft tissue infections: review of the epidemiology, microbiology, aetiopathogenesis and treatment. *Journal of the European Academy of Dermatology and Venereology* (2012).

310. Singh, H. *et al.* Lipase-Responsive Electrospun Theranostic Wound Dressing for Simultaneous Recognition and Treatment of Wound Infection. *ACS Applied Bio Materials* **2,** 2028–2036 (May 2019).

311. Shao, Q. & Xing, B. Enzyme responsive luminescent ruthenium(ii) cephalosporin probe for intracellular imaging and photoinactivation of antibiotics resistant bacteria. *Chemical Communications* **48,** 1739–1741 (2012).

312. Xie, H. *et al.* Fluorogenic Probes with Substitutions at the 2 and 7 Positions of Cephalosporin are Highly BlaC-Specific for Rapid Mycobacterium tuberculosis Detection. *Angewandte Chemie International Edition* **53,** 9360–9364 (Aug. 2014).

313. Bebrone, C. *et al.* CENTA as a Chromogenic Substrate for Studying -Lactamases. *Antimicrobial Agents and Chemotherapy* **45,** 1868–1871 (June 2001).

314. Jones, R. N., Wilson, H. W., Novick, W. J., Barry, A. L. & Thornsberry, C. In vitro evaluation of CENTA, a new beta-lactamase-susceptible chromogenic cephalosporin reagent. *Journal of Clinical Microbiology* **15,** 954–958 (May 1982).

315. Jones, R. N., Wilson, H. W. & Novick, W. J. In vitro evaluation of pyridine-2-azo-p-dimethylaniline cephalosporin, a new diagnostic chromogenic reagent, and comparison nitrocefin, cephacetrile, and other beta-lactam compounds. *Journal of Clinical Microbiology* **15,** 677–683 (Apr. 1982).

316. Kobayashi, S., Arai, S., Hayashi, S. & Sakaguchi, T. Simple assay of beta-lactamase with agar medium containing a chromogenic cephalosporin, pyridinium-2-azo-p-dimethylaniline chromophore (PADAC). *Antimicrobial Agents and Chemotherapy* **32,** 1040–1045 (July 1988).

317. Morandi, F. *et al.* Nanomolar Inhibitors of AmpC β-Lactamase. *Journal of the American Chemical Society* **125,** 685–695 (Jan. 2003).

318. Bodey, G. P., Bolivar, R., Fainstein, V. & Jadeja, L. Infections Caused by Pseudomonas aeruginosa. *Clinical Infectious Diseases* **5,** 279–313 (2011).

319. Davin-Regli, A. & PagÃs, J.-M. Enterobacter aerogenes and Enterobacter cloacae; versatile bacterial pathogens confronting antibiotic treatment. *Frontiers in Microbiology* **6,** 392 (May 2015).

320. Bottone, E. J. Bacillus cereus, a Volatile Human Pathogen. *Clinical Microbiology Reviews* **23,** 382–398 (Apr. 2010).

321. Mirsalehian, A. *et al.* Detection of AmpC-β-lactamases producing isolates among carbapenem resistant P. aeruginosa isolated from burn patient. eng. *Iranian journal of microbiology* **6,** 306–10 (Oct. 2014).

322. Khan, S., Sallum, U. W., Zheng, X., Nau, G. J. & Hasan, T. Rapid optical determination of β-lactamase and antibiotic activity. *BMC Microbiology* **14,** 84 (2014).

323. Lee, S. *et al.* Clinical Implications of Cefazolin Inoculum Effect and β-Lactamase Type on Methicillin-Susceptible Staphylococcus aureus Bacteremia. *Microbial Drug Resistance* **20,** 568–574 (Dec. 2014).

324. Kernodle, D. S., McGraw, P. A., Stratton, C. W. & Kaiser, A. B. *Use of extracts versus whole-cell bacterial suspensions in the identification of Staphylococcus aureus β-lactamase variants* tech. rep. 3 (1990), 420–425.

325. Zhu, J. Bioactive modification of poly(ethylene glycol) hydrogels for tissue engineering. eng. *Biomaterials* **31,** 4639–4656 (June 2010).

326. Hamley, I. W. PEG-peptide conjugates. *Biomacromolecules* **15,** 1543–1559 (2014).

327. Gandini, A. The furan/maleimide Diels-Alder reaction: A versatile click-unclick tool in macromolecular synthesis. *Progress in Polymer Science* **38,** 1–29 (Jan. 2013).

328. Northrop, B. H., Frayne, S. H. & Choudhary, U. Thiol-maleimide "click" chemistry: Evaluating the influence of solvent, initiator, and thiol on the reaction mechanism, kinetics, and selectivity. *Polymer Chemistry* **6,** 3415–3430 (Apr. 2015).

329. Aw, J. *et al.* Enzyme-responsive reporter molecules for selective localization and fluorescence imaging of pathogenic biofilms. *Chemical Communications* **53,** 3330–3333 (Mar. 2017).

330. Boschi, L. *et al.* The Legionella (Fluoribacter) gormanii metallo-β-lactamase: A new member of the highly divergent lineage of molecular-subclass B3 β-lactamases. *Antimicrobial Agents and Chemotherapy* **44,** 1538–1543 (June 2000).

331. Kim, J. *et al.* Characterization of the crosslinking kinetics of multi-arm poly(ethylene glycol) hydrogels formed via Michael-type addition. *Soft Matter* **12,** 2076–2085 (Feb. 2016).

332. Du, H., Hamilton, P., Reilly, M. & Ravi, N. Injectable in situ Physically and Chemically Crosslinkable Gellan Hydrogel. *Macromolecular Bioscience* **12,** 952–961 (July 2012).

333. Annaka, M., Ogata, Y. & Nakahira, T. Swelling Behavior of Covalently Cross-Linked Gellan Gels. *The Journal of Physical Chemistry B* **104,** 6755–6760 (July 2000).

334. Osmałek, T., Froelich, A. & Tasarek, S. Application of gellan gum in pharmacy and medicine. *International Journal of Pharmaceutics* **466,** 328–340 (May 2014).

335. Gauthier, M. A. & Klok, H.-A. Peptide/protein–polymer conjugates: synthetic strategies and design concepts. *Chemical Communications* **0,** 2591 (June 2008).

336. Botta, M. *et al.* Experimental and theoretical investigations on the cephalosporin 3- 2 isomerization. *ELECTRONIC JOURNAL OF THEORETICAL CHEMISTRY* **1,** 52–59 (1996).

337. English, B. P. *et al.* Ever-fluctuating single enzyme molecules: Michaelis-Menten equation revisited. *Nature Chemical Biology* **2,** 87–94 (2006).

338. Canaparo, R. *et al. Recent developments in antibacterial therapy: Focus on stimuli-responsive drug-delivery systems and therapeutic nanoparticles* 2019.

339. Zhuk, I. *et al.* Self-Defensive Layer-by-Layer Films with Bacteria-Triggered Antibiotic Release. *ACS nano,* 7733–7745 (Aug. 2014).

340. Dissemond, J., Witthoff, M., Brauns, T. C., Haberer, D. & Goos, M. pH-wert des milieus chronischer wunden: Untersuchungen im rahmen einer modernen wundtherapie. *Hautarzt* **54,** 959–965 (Oct. 2003).

341. Cars, O., Mölstad, S. & Melander, A. Variation in antibiotic use in the European Union. *Lancet* **357,** 1851–1853 (June 2001).

342. Page, M. I. & Proctor, P. Mechanism of B-Lactam Ring Opening in Cephalosporins. *Journal of the American Chemical Society* **106,** 3820–3825 (1984).

343. Perez-Inestrosa, E. *et al.* Cephalosporin chemical reactivity and its immunological implications. *Current Opinion in Allergy and Clinical Immunology* **5,** 323–330 (2005).

344. Yang, Z. *et al.* Using β-lactamase to trigger supramolecular hydrogelation. *Journal of the American Chemical Society* **129,** 266–267 (Jan. 2007).

345. García, A. J. PEG-maleimide hydrogels for protein and cell delivery in regenerative medicine. *Annals of Biomedical Engineering* **42,** 312–322 (Feb. 2014).

346. Zhu, J. Bioactive modification of poly(ethylene glycol) hydrogels for tissue engineering. *Biomaterials* **31,** 4639–4656 (2010).

347. Lutolf, M. P., Raeber, G. P., Zisch, A. H., Tirelli, N. & Hubbell, J. A. Cell-responsive synthetic hydrogels. *Advanced Materials* **15,** 888–892 (June 2003).

348. Morandi, F. *et al.* Nanomolar Inhibitors of AmpC β-Lactamase. *Journal of the American Chemical Society* **125,** 685–695 (Jan. 2003).

349. Schaudinn, C. *et al.* Development, standardization and testing of a bacterial wound infection model based on ex vivo human skin. *PLoS ONE* **12** (ed Dague, E.) e0186946 (Nov. 2017).

350. Nwomeh, B. C., Liang, H.-X., Cohen, I. & Yager, D. R. MMP-8 Is the Predominant Collagenase in Healing Wounds and Nonhealing Ulcers. *Journal of Surgical Research* **81,** 189–195 (Feb. 1999).

351. DM, L. beta-Lactamases in Laboratory and Clinical Resistance DAVID. *Clinical Microbiology Reviews* **8,** 557–584 (1995).

352. Lin, C. C. & Metters, A. T. Hydrogels in controlled release formulations: Network design and mathematical modeling. *Advanced Drug Delivery Reviews* **58,** 1379–1408 (2006).

353. Oefner, C. *et al.* Refined crystal structure of β-lactamase from Citrobacter freundii indicates a mechanism for β-lactam hydrolysis. *Nature* **343,** 284–288 (1990).

354. Van Dijk, M., Van Nostrum, C. F., Hennink, W. E., Rijkers, D. T. & Liskamp, R. M. Synthesis and characterization of enzymatically biodegradable peg and peptide-based hydrogels prepared by click chemistry. *Biomacromolecules* **11,** 1608–1614 (June 2010).

355. Lau, G. W., Ran, H., Kong, F., Hassett, D. J. & Mavrodi, D. Pseudomonas aeruginosa Pyocyanin Is Critical for Lung Infection in Mice. *Infection and Immunity* **72,** 4275–4278 (July 2004).

356. Lau, G. W., Hassett, D. J., Ran, H. & Kong, F. The role of pyocyanin in Pseudomonas aeruginosa infection. *Trends in Molecular Medicine* **10,** 599–606 (Dec. 2004).

357. Sundararajan, S., Kannan, C. N. & Chittibabu, S. Alkaline protease from Bacillus cereus VITSN04: Potential application as a dehairing agent. *Journal of Bioscience and Bioengineering* **111,** 128–133 (Feb. 2011).

358. Glatz, B. A. & Goepfert, J. M. Extracellular factor synthesized by Bacillus cereus which evokes a dermal reaction in guinea pigs. *Infection and Immunity* **8,** 25–29 (1973).

359. Yang, Q. *et al.* Development of a novel ex vivo porcine skin explant model for the assessment of mature bacterial biofilms. *Wound Repair and Regeneration* **21,** 704–714 (Sept. 2013).

360. Soltwedel, O. *et al.* Influence of polycation (PDADMAC) weight on vertical diffusion within polyelectrolyte multilayers during film formation and postpreparation treatment. *Macromolecules* **45,** 7995–8004 (Oct. 2012).

361. Swift, S. *et al.* Quorum sensing as a population-density-dependent determinant of bacterial physiology. *Advances in Microbial Physiology* **45,** 199–270 (2001).

362. Griffin, D. R., Weaver, W. M., Scumpia, P. O., Di Carlo, D. & Segura, T. Accelerated wound healing by injectable microporous gel scaffolds assembled from annealed building blocks. *Nature Materials* **14,** 737–744 (2015).

363. Applications, C. in. January, 455–490 (2013).

364. Forier, K. *et al.* Lipid and polymer nanoparticles for drug delivery to bacterial biofilms. *Journal of Controlled Release* **190,** 607–623 (Sept. 2014).

365. Quan, K. *et al.* Homogeneous Distribution of Magnetic, Antimicrobial-Carrying Nanoparticles through an Infectious Biofilm Enhances Biofilm-Killing Efficacy. *ACS Biomaterials Science & Engineering,* acsbiomaterials.9b01425 (Dec. 2019).

366. Pichavant, L. *et al.* Vancomycin Functionalized Nanoparticles for Bactericidal Biomaterial Surfaces. *Biomacromolecules* **17,** 1339–1346 (Apr. 2016).

367. De Paz, L. E., Resin, A., Howard, K. A., Sutherland, D. S. & Wejse, P. L. Antimicrobial effect of chitosan nanoparticles on Streptococcus mutans biofilms. *Applied and Environmental Microbiology* **77,** 3892–3895 (June 2011).

368. Yuan, P., Ding, X., Yang, Y. Y. & Xu, Q. H. Metal Nanoparticles for Diagnosis and Therapy of Bacterial Infection. *Advanced Healthcare Materials* **7,** 1701392 (July 2018).

369. Jung, J. W., Lee, J. S. & Cho, D. W. Computer-Aided multiple-head 3D printing system for printing of heterogeneous organ/tissue constructs. *Scientific Reports* **6,** 21685 (Feb. 2016).

370. Neu, H. C. β-Lactam Antibiotics: Structural Relationships Affecting in Vitro Activity and Pharmacologic Properties. *Clinical Infectious Diseases* **8,** S237–S259 (July 1986).

371. Topel, Ö., Çakir, B. A., Budama, L. & Hoda, N. Determination of critical micelle concentration of polybutadiene-block- poly(ethyleneoxide) diblock copolymer by fluorescence spectroscopy and dynamic light scattering. *Journal of Molecular Liquids* **177,** 40–43 (2013).

372. Bagdanoff, J. T. *et al.* Optimization of Fused Bicyclic Allosteric SHP2 Inhibitors. *Journal of Medicinal Chemistry* **62,** 1781–1792 (Feb. 2019).

373. Chen, Y. N. P. *et al.* Allosteric inhibition of SHP2 phosphatase inhibits cancers driven by receptor tyrosine kinases. *Nature* **535,** 148–152 (July 2016).

374. Tajan, M., de Rocca Serra, A., Valet, P., Edouard, T. & Yart, A. SHP2 sails from physiology to pathology. *European Journal of Medical Genetics* **58,** 509–525 (Oct. 2015).

375. Zeng, L.-F. *et al.* Therapeutic Potential of Targeting the Oncogenic SHP2 Phosphatase. *Journal of Medicinal Chemistry* **57,** 6594–6609 (Aug. 2014).

376. Fodor, M. *et al.* Dual Allosteric Inhibition of SHP2 Phosphatase. *ACS Chemical Biology* **13,** 647–656 (2018).

377. Zhao, M. *et al.* SHP2 inhibition triggers anti-tumor immunity and synergizes with PD-1 blockade. *Acta Pharmaceutica Sinica B* **9,** 304–315 (Mar. 2019).

378. Garcia Fortanet, J. *et al.* Allosteric Inhibition of SHP2: Identification of a Potent, Selective, and Orally Efficacious Phosphatase Inhibitor. *Journal of Medicinal Chemistry* **59,** 7773–7782 (2016).

379. Sun, X. *et al.* Selective inhibition of leukemia-associated SHP2 E69K mutant by the allosteric SHP2 inhibitor SHP099. *Leukemia* **32,** 1246–1249 (May 2018).

380. De Souza, R., Zahedi, P., Allen, C. J. & Piquette-Miller, M. *Polymeric drug delivery systems for localized cancer chemotherapy* Aug. 2010.

381. Wolinsky, J. B., Colson, Y. L. & Grinstaff, M. W. Local drug delivery strategies for cancer treatment: Gels, nanoparticles, polymeric films, rods, and wafers. *Journal of Controlled Release* **159,** 14–26 (Apr. 2012).

382. Yi, H. G. *et al.* A 3D-printed local drug delivery patch for pancreatic cancer growth suppression. *Journal of Controlled Release* **238,** 231–241 (Sept. 2016).

383. Smith, R. C., Riollano, M., Leung, A. & Hammond, P. T. Layer-by-layer platform technology for small-molecule delivery. *Angewandte Chemie - International Edition* **48,** 8974–8977 (Nov. 2009).

384. Martin, A. *et al.* Multilayered textile coating based on a β-cyclodextrin polyelectrolyte for the controlled release of drugs. *Carbohydrate Polymers* **93,** 718–730 (Apr. 2013).

385. Shukla, A. & Almeida, B. Advances in cellular and tissue engineering using layer-by-layer assembly. *Wiley Interdisciplinary Reviews: Nanomedicine and Nanobiotechnology* **6,** 411–421 (Sept. 2014).

386. Deshmukh, P. K. *et al.* Stimuli-sensitive layer-by-layer (LbL) self-assembly systems: Targeting and biosensory applications. *Journal of Controlled Release* **166,** 294–306 (Mar. 2013).

387. Tang, K. & Besseling, N. A. M. Formation of polyelectrolyte multilayers: Ionic strengths and growth regimes. *Soft Matter* **12,** 1032–1040 (Jan. 2016).

388. Pillai, C. K., Paul, W. & Sharma, C. P. Chitin and chitosan polymers: Chemistry, solubility and fiber formation. *Progress in Polymer Science (Oxford)* **34,** 641–678 (July 2009).

389. Berger, J. *et al.* Structure and interactions in covalently and ionically crosslinked chitosan hydrogels for biomedical applications. *European Journal of Pharmaceutics and Biopharmaceutics* **57,** 19–34. arXiv: `9809069v1 [gr-qc]` (2004).

390. Crini, G. Review: A history of cyclodextrins. *Chemical Reviews* **114,** 10940–10975 (Nov. 2014).

391. Shukla, A., Fuller, R. C. & Hammond, P. T. Design of multi-drug release coatings targeting infection and inflammation. *Journal of Controlled Release* **155,** 159–166 (Oct. 2011).

392. Pérez-Anes, A. *et al.* Bioinspired Titanium Drug Eluting Platforms Based on a Poly-β-cyclodextrin-Chitosan Layer-by-Layer Self-Assembly Targeting Infections. *ACS Applied Materials and Interfaces* **7,** 12882–12893 (June 2015).

393. Zhang, J. & Ma, P. X. Cyclodextrin-based supramolecular systems for drug delivery: Recent progress and future perspective. *Advanced Drug Delivery Reviews* **65,** 1215–1233 (Aug. 2013).

394. Schneider, H.-J., Hacket, F., Rüdiger, V. & Ikeda, H. *NMR Studies of Cyclodextrins and Cyclodextrin Complexes* tech. rep. 5 (2002), 1755–1786.

395. Zhao, R., Sandström, C., Zhang, H. & Tan, T. NMR Study on the Inclusion Complexes of β-Cyclodextrin with Isoflavones. *Molecules* **21,** 372 (Mar. 2016).

396. Ferrazza, R., Rossi, B. & Guella, G. DOSY-NMR and raman investigations on the self-aggregation and cyclodextrin complexation of vanillin. *Journal of Physical Chemistry B* **118,** 7147–7155 (2014).

397. Ren, K., Ji, J. & Shen, J. Tunable DNA release from cross-linked ultrathin DNA/PLL multilayered films. *Bioconjugate Chemistry* **17,** 77–83 (Jan. 2006).

398. Richert, L. *et al.* Layer by Layer Buildup of Polysaccharide Films: Physical Chemistry and Cellular Adhesion Aspects. *Langmuir* **20,** 448–458 (2004).

399. Shukla, A., Avadhany, S. N., Fang, J. C. & Hammond, P. T. Tunable vancomycin releasing surfaces for biomedical applications. *Small* **6,** 2392–2404 (Nov. 2010).